UNIVERSITY OF OKLAHOMA

GRADUATE COLLEGE

REMOTE SENSING ANALYSIS OF CROPLANDS, WOODY PLANT ENCROACHMENT AND CARBON FLUXES OF WOODY SAVANNA

A DISSERTATION

SUBMITTED TO THE GRADUATE FACULTY

in partial fulfillment of the requirements for the

Degree of

DOCTOR OF PHILOSOPHY

By

JIE WANG
Norman, Oklahoma
2017

REMOTE SENSING ANALYSIS OF CROPLANDS, WOODY PLANT ENCROACHMENT AND CARBON FLUXES OF WOODY SAVANNA

A DISSERTATION APPROVED FOR THE
DEPARTMENT OF MICROBIOLOGY AND PLANT BIOLOGY

BY

_____
Dr. Xiangming Xiao, Chair

_____
Dr. Jeffrey Basara

_____
Dr. Yiqi Luo

_____
Dr. Jean Steiner

_____
Dr. Heather McCarthy

This dissertation is dedicated to my family for their unconditional love and support, to my impressive study journey in U.S and to my youth.

Acknowledgements

Four years ago, I was so lucky to be a student of Prof. Xiangming Xiao. Now, I would like to express my deepest gratitude to my advisor, Prof. Xiangming Xiao, for his guidance, encouragement and caring during my Ph.D. study. Without his continuous instruction and support, it is impossible for me to finish my Ph.D study on time with so many difficulties.

I would like to thank other members of my advisory committee, Prof. Jeffrey Basara, Prof. Yiqi Luo, Pro. Heather McCarty and Prof. Jean Steiner for their instruction and help in my study over last four year.

I would like to thank all members of EOMF for their company and help in last four years. This big family supported me through an impressive period.

I would like to express my heartfelt thanks to my beloved family for their consistent loving and trust all through these years. I owe my heartfelt thanks to my friends for their support and caring.

Last, I acknowledge research grants for the support to my Ph.D. study and appreciate the staffs of the Center for Spatial Analysis for their assistance.

Table of Contents

List of Tables

List of Figures

Abstract

Since 1990s, much attention has been paid to Land use/land cover change (LULCC) studies because it is an important component of global change. The vegetation change is a critical factor of land cover changes, which interacts with climate, ecosystem processes, biogeochemical cycles and biodiversity. Remote sensing is a good tool to detect the changes of land use and land cover. To date, most of studies on vegetation changes have been conducted at biome scales, but have not examined changes at the species level. This lack of studies on species inhibits analysis of ecosystem functions caused by the shifts of vegetation types. This dissertation aims to explore the potential of remote sensing images to produce long-term products on specific vegetation type and study the interactions between vegetation type, climate and gross primary production.

In Chapter 2, a simple algorithms was developed to identify paddy rice by selecting a unique temporal window (flooding/transplanting period) at regional scale using time series Landsat-8 images. A wheat-rice double-cropped area from China was selected as the study area. The resultant paddy rice map had overall accuracy and Kappa coefficient of 89.8% and 0.79, respectively. In comparison with the National Land Cover Data (China) from 2010, the resultant map had a better detection of the changes in the paddy rice fields. These results demonstrate the efficacy of using images from multiple sources to generate paddy rice maps for two-crop rotation systems.

Chapter 3 developed a pixel and phenology-based mapping algorithm, and used it to analyze PALSAR mosaic data in 2010 and all the available Landsat 5/7 data during 1984-2010. This study analyzed 4,233 images covering more than 10 counties in the central region of Oklahoma, and generated eastern redcedar forest maps for 2010 and five

historical time periods: the late 1980s (1984-1989), early 1990s (1990-1994), late 1990s (1995-1999), early 2000s (2000-2004), and late 2000s (2005-2010). The resultant maps clearly illustrated an increase in red cedar encroachment within the study area at an annual rate of ~8% during 1984-2010.

Chapter 4 investigates the dynamics of juniper encroachment on the grasslands of Oklahoma by generating multi-period maps of juniper encroachment from 1984 to 2010 at a 30-m spatial resolution. The juniper forest maps in 1984 to 2010 were produced by the algorithms developed in Chapter 3. The resultant maps revealed the spatio-temporal dynamics of juniper forest encroachment at state and county scales. This study also characterized the juniper forest encroachment by geographical pattern and soil conditions. The resultant maps can be used to support studies on ecosystem processes, sustainability, and ecosystem services.

Chapter 5 compared dynamics of major climatic variables, eddy covariance tower-based GPP, and vegetation indices (VIs) over the last decade in a deciduous savanna and an evergreen savanna under a Mediterranean climate. The relationships were also examined among VIs, GPP, and major climatic variables in dry, normal, and wet hydrological years. GPP of these two savanna sites were also simulated using a light-use efficiency based Vegetation Photosynthesis Model (VPM). The results of this study help better understanding the eco-physiological response of evergreen and deciduous savannas, and also suggest the potential of VPM to simulate interannual variations of GPP in different types of Mediterranean-climate savannas.

Chapter1: Introduction

1.1 Research background

Land Use/Cover changes (LUCC) have gained much attentions from global environmental change research in recent several decades. Long-term studies revealed that these land surface changes impact the environment though modifying biosphere extensively. For example, LUCC affects regional climates by modifying surface albedo and the surface-atmosphere energy exchanges (Pielke *et al.*, 2002). LUCC directly shapes the Earth's ecosystems and affects the carbon cycles by effects on carbon sources and sinks, which further impacts the global climate. (Woodwell *et al.*, 1983; Houghton *et al.*, 1985). Land use practices also changed the consumption of freshwater among irrigation, industry, and domestic consumption. Land cover changes altered the partitioning of precipitation into runoff, evapotranspiration, and ground water (Foley *et al.*, 2005). In addition, LUCC have numerous impacts on ecosystem productions and services. Primary concerns are biodiversity, ecosystem and soil degradation (Lambin & Geist, 2008). Therefore, knowledge about LUCC is important to understand global change and overcome the ecological problems (eg. habitat loss, deterioration of environmental quality).

Producing accurate land use and land cover data sources is a prerequisite to get the land use/cover patterns and dynamics over spatial and temporal scales. Remote sensing can provide land surface information consistently and continuously for large scales, ranging from regional to global. Over the last few decades, numerous projects of LUCC have been launched to measure the land cover changes based on remote sensing technology. The main LULC products included the 1-km global land cover characteristics

database from the project of the International Geosphere-Biosphere Program, Data and Information Systems (IGBP-DIScover) (Loveland et al., 2000), the global land cover database for the year 2000 (GLC2000) produced by the European Commission's Joint Research Centre (Bartholome & Belward, 2005), the 1-km Global Land Cover Facility (GLCF) products from Advanced Very High Resolution Radiometer (AVHRR) (Hansen et al., 2000), the 1-km and 500-m global land cover mapping from moderate resolution imaging spectroradiometer (MODIS) (Friedl et al., 2002; Friedl et al., 2010), and the global land cover with finer resolution at 30-m from Landsat TM and ETM+ data (Gong et al., 2013). These products have play critical roles in understanding the complicated intercations between human activities and global change. However, these products have been generated using the classification schemes at biome-level and only record the natural land cover types, such as forest, cropland and grassland. The plant species information in forest, cropland or grassland was not provided in these LUCC datasets. In addition, these products are generated for one period and have not been updated continuously with specific time intervals.

LUCC datasets at species level are limited for all ecosystems ranging from cropland, grassland to forest. It is needed to input plant types to accurately assess and predict food security, biodiversity and biogeochemical. Recently, some efforts have been made to generate plant type maps using remote sensing images over agricultural ecosystem, including paddy rice (Xiao et al., 2005; Xiao et al., 2006), wheat (Ren et al., 2008), maize (Zhong et al., 2014), soybean (Zhong et al., 2014), cotton (Zhang et al., 2008), and rubber plantations (Dong et al., 2013). The majority of these studies were conducted using MODIS data with coarse spatial resolution (500m or 1km), which may

cause large uncertainties from mixed pixels. Therefore, it is still needed to explore the potential to produce the plant type maps using finer-resolution images (eg. 30-m Landsat) and monitor the vegetation changes at species level with long term satellite observations.

Land cover change directly influences ecosystem structure and is a land surface forcing of climate change (Mahmood et al., 2010). Thus, the dominate species shifts will altered the microclimate and ecosystem processes, including water, carbon, and nutrient cycles (Williams et al., 2013; Caterina et al., 2014). The interactions among vegetation, ecosystem processes and climate change are complex and vary with vegetation types. Understanding the relationship among these biotic and abiotic factors would provide insights for ecosystem service assessment, ecosystem management, conservation planning, and biodiversity assessment. Processed-based vegetation models have been widely to examine the responses of terrestrial ecosystem functions to climate change (Cramer et al., 2001). However, remote sensing methods provide a new way to understand this problem based on observation data (Chambers et al., 2007). Subsequently, a number of Production Efficiency Models (PEMs) have been developed to estimate the gross primary production (GPP) of ecosystem using remote sensing and climate data, including the Global Production Efficiency Model (GLO-PEM) (Prince & Goward, 1995), the Terrestrial Uptake and Release of Carbon model (TRUC) (Ruimy et al., 1996), the MODIS Daily Photosynthesis model (PSN) (Running et al., 2000), and the Vegetation Photosynthesis Model (VPM) (Xiao et al., 2004). The VPM is a satellite-based PEMs that developed based on the concept of chlorophyll. This model was use to explore the potential of satellite-based PEMs to simulate seasonal dynamic and interannual variation of the GPP in ecosystems with different vegetation types under various climate.

1.2 Overall research objectives

The goal of this dissertation is to improve the application of moderate remote sensing into studies on vegetation changes from biome level to species level on regional and global scales during long period. I am also interested in how these changes affected the ecosystem processes, climate, biodiversity and other ecological services. My dissertation focuses on three ecosystems of agriculture, grassland and savanna across the mid-low latitude regions (30°N ~ 40°N) in Southeastern China, Southern USA and Southwestern Spain. The study areas are under temperate or Mediterranean climate.

1.3 Organization of the dissertation

This dissertation has six chapters, including an introduction, four theme chapters, and one summary. Chapters 2, 3, 5 have been published on three peer-reviewed journals, and Chapter 4 has been submitted to one peer-reviewed journal.

Chapter 2 explores the potential utility of integrating time series optical images (Landsat-8, MODIS) and radar images (PALSAR) in mapping paddy rice planting areas. A pixel and phenology-based algorithms is developed based on the unique spectral signature within a specific phenological window of paddy rice fields. This simple and robust algorithms successfully extracts paddy rice plants from two-crop rotation agricultural ecosystem. The discussion focuses on the advantages of the integration of multi-source remote sensing data in the identification of fragmented paddy rice fields, and the uncertainties in the resultant 30-m paddy rice map.

Chapter 3 explores the potential to monitor the long-term eastern redcedar encroachment into the grassland using moderate spatial resolution images from Landsat. This chapter examines the backscatter and spectral signatures of eastern redcedar on

PALSAR and Landsat images, and develops an algorithms to map eastern redcedar dynamics in long-term period. The discussion focuses on the source errors, uncertainties, potential and regional implications of this algorithms to map the historical eastern redcedar encroachment.

Chapter 4 evaluates the spatial and temporal dynamics of juniper species (eastern redcedar and ashe juniper) encroachment on grasslands in Oklahoma. This chapter generated 30-m juniper forest maps from 1984 to 2010 in Oklahoma based on the algorithms developed in Chapter 3. We characterized the encroachment processes of juniper forest by administrative boundaries (eg. state and county level), geographical patterns (eg. Latitude, Longitude and elevation) and soil setting. The discussion focuses on the encroachment characteristics of juniper forest and the relationship between juniper encroachment and soil features.

Chapter 5 compares the eco-physiological response of two functional savannas (deciduous and evergreen) to temporal variations in biophysical factors (eg. precipitation, temperature) under similar Mediterranean climate based on long-term flux tower and remote sensing data. Using these data, this chapter also examines the interactions of climate, vegetation growth, and gross primary production (GPP). Finally, we simulated GPP of these two savanna sites using a light-use efficiency based Vegetation Photosynthesis Model (VPM). This chapter aims to provide some information to accurate simulate GPP in different types of Mediterranean-climate savannas. The discussion focuses on the seasonality of two savannas in vegetation indices, GPP and phenology, different responses to interannual variations of precipitation, and the roles of parameters in VPM to accurate simulate GPP.

1.4 List of Publications from the Dissertation

Chapter 2

Wang, J., Xiao, X.M., *et a*l. (2015). Mapping paddy rice planting area in wheat-rice double-cropped areas through integration of Landsat-8 OLI, MODIS, and PALSAR images. *Scientific Reports*, *5*, 10088.

Chapter 3

Wang, J., Xiao, X.M., *et al*. (2017). Mapping the dynamics of eastern red cedar encroachment into grasslands during 1984-2010 through PALSAR and time series Landsat images. *Remote Sensing of Environment, 190,* 223-246

Chapter 4

Wang, J., Xiao, X.M., *et al*. (2017). Spatio-temporal dynamics of juniper forest encroachment into grasslands during 1984-2010 based on PALSAR and Landsat images. (Submitted)

Chapter 5

Wang, J., Xiao, X.M., *et al*. (2016). Canopy and climate controls of gross primary production of Mediterranean-type deciduous and evergreen oak savannas. *Agricultural and Forest Meteorology, 226*, 132-147.

Chapter 2: Mapping paddy rice planting area in wheat-rice double-cropped areas through integration of Landsat-8 OLI, MODIS, and PALSAR images

Abstract

As farmland systems vary over space and time (season and year), accurate and updated maps of paddy rice are needed for studies of food security and environmental problems. We selected a wheat-rice double-cropped area from fragmented landscapes along the rural–urban complex (Jiangsu Province, China) and explored the potential utility of integrating time series optical images (Landsat-8, MODIS) and radar images (PALSAR) in mapping paddy rice planting areas. We first identified several main types of non-cropland land cover and then identified paddy rice fields by selecting pixels that were inundated only during paddy rice flooding periods. These key temporal windows were determined based on MODIS Land Surface Temperature and vegetation indices. The resultant paddy rice map was evaluated using regions of interest (ROIs) drawn from multiple high-resolution images, Google Earth, and in-situ cropland photos. The estimated overall accuracy and Kappa coefficient were 89.8% and 0.79, respectively. In comparison with the National Land Cover Data (China) from 2010, the resultant map better detected changes in the paddy rice fields and revealed more details about their distribution. These results demonstrate the efficacy of using images from multiple sources to generate paddy rice maps for two-crop rotation systems.

2.1 Introduction

Studies on paddy rice fields aim to provide direct or indirect information for researches on food security, water resource management, and environmental

sustainability. Paddy rice fields provide one of the main staple foods for more than half of the world's population with 11% of cultivated land (Khush 2005). In Asia, the majority of rice agriculture relies on irrigation, accounting for 70% of global fresh water withdrawals (SAMAD et al. 1992). Determining the area of paddy rice fields is an important component of obtaining more accurate information about agricultural water use to effectively manage fresh water resources (Brisco et al. 2013). In addition, as a kind of cultivated wetland, seasonally flooded paddy fields contribute 10–13% of the atmosphere's anthropogenic methane (Zhang et al. 2011). Meanwhile, paddy rice fields are changing at a breakneck pace due to dramatic encroachment by expanding cities (Woolston 2014) and the potentially reduced availability of water resources caused by climate change (Dayton 2014). Therefore, it is urgently necessary to update and refine information about paddy rice planting areas in order to efficiently and accurately estimate crop production (Doraiswamy et al. 2005), manage water resources (Rosenzweig et al. 2004; Wu et al. 2010b) and monitor greenhouse gas emissions (Li et al. 2005).

At the global and regional scales, several early studies of ecosystems and land cover have involved mapping paddy rice fields based on agricultural census data. In the late 1980s and early 1990s, several paddy rice datasets with coarse spatial resolution were produced to analyze global climate and greenhouse gas emission (Aselmann and Crutzen 1989; Matthews et al. 1991). In the years following, two global cropland datasets representing crop patterns in the early 1990s and in the year 2000 were created at a spatial resolution of 5 arc minutes (~10 km) (Leff et al. 2004; Monfreda et al. 2008). At the regional scale, a rice dataset for Asia was developed at the beginning of the 1980s (Huke 1982). In recent years, several studies on paddy rice planting areas were conducted by

combining agricultural census data at the national scale (Frolking et al. 2002; Liu et al. 2013). Although most of the crop datasets were produced with input from multiple sources, these datasets were developed mainly by relying on statistics with coarse spatial resolution that were supplied by administrative units. Given the limitations of this spatial and temporal information, it is a challenge to apply these datasets to finer spatial research and to update them year to year.

Remote sensing is an efficient technique to acquire temporal and spatial cropland information repeatedly and consistently (Thenkabail et al. 2012). Historically, two main kinds of satellites have been used to map paddy rice fields: microwave and optical. Microwave satellites can penetrate through clouds and are thus superior for mapping paddy rice in regions dominated by long-term cloudy and rainy weather (Bouvet and Thuy 2011; Miyaoka et al. 2013; Shao et al. 2001; Zhang et al. 2009), but available synthetic aperture radar (SAR) imagery is limited (Zhang et al. 2009) or expensive (Li et al. 2012). Commonly used optical sensors are the Multispectral Scanner System/Thematic Mapper/Enhanced Thematic Mapper Plus (MSS/TM/ETM+), the Moderate Resolution Imaging Spectroradiometer (MODIS) (Bridhikitti and Overcamp 2012; Gumma et al. 2014; Son et al. 2014; Sun et al. 2009; Xiao et al. 2006a; Xiao et al. 2005b), NOAA's Advanced Very High Resolution Radiometer (AVHRR) (Bachelet 1995; Fang et al. 1998), and SPOT High Resolution Geometrical/High Resolution Visible Infrared/VEGETATION (HRG/HRVIR/VGT) (Chen et al. 2011; Thi et al. 2012; Xiao et al. 2002a). Owing to continuous archiving and free to acquire, MODIS and Landsat have been the prevalent data sources of mapping paddy rice fields over the last several years.

Optical image classification techniques often use either individual image(s) or individual pixel(s) of time series data as input, here namely image-based methods and pixel-based methods. Image-based methods quantify the relationships (such as similarities or differences in spectra or texture) among all the pixels in an image for classification or object detection. These image-based methods have been applied to paddy rice mapping using single or multi-temporal optical images (e.g., MODIS and Landsat) at regional scales (Akbari et al. 2006; Gumma et al. 2011; Li et al. 2012; Panigrahy and Parihar 1992). For image-based methods, collection of training samples (pixels) from ground reference data in each corresponding year remains a challenge (Zhong et al. 2014a). Pixel-based methods rely primarily on the time series data for a pixel. These methods track the seasonal dynamics of a type of land cover and provide phenology information about the land surface. Several pixel-based algorithms have been developed to classify cropland using various optical images (e.g., MODIS, Landsat, SPOT, and FORMOSAT-2) (Chen et al. 2011; Shiu et al. 2012; Zhong et al. 2014a; Zhong et al. 2011). To take into account the phenology of paddy rice, a pixel- and phenology-based algorithm using time series data of vegetation indices has been proposed. This was successfully applied to VGT and MODIS data for southern China and South and Southeast Asia (Xiao et al. 2006a; Xiao et al. 2005b). Due to the high temporal resolution and continuous observation, MODIS data have frequently been combined with pixel- and phenology-based algorithms to track paddy rice phenology in order to map paddy rice areas or detect the intensity of paddy rice fields (Bridhikitti and Overcamp 2012; Peng et al. 2011; Sakamoto et al. 2009; Son et al. 2014; Sun et al. 2009; Torbick et al. 2011). However, MODIS-based phenology information cannot capture the sub-pixel dynamics

of small paddy rice fields in heterogeneous and fragmented agricultural landscapes (Biradar and Xiao 2011; Son et al. 2014). This could be improved by using Landsat images with 30-m spatial resolution. Nevertheless, more research is needed to document the combination of Landsat images with pixel- and phenology-based algorithms for paddy rice mapping, especially in the case of Landsat 8 OLI images.

Reduced Landsat data availability caused by cloud cover or other problems may result in the failure of Landsat time series with 16-day intervals to distinguish the crops and trees. This problem is obvious in regions with double or multiple rotation agricultural systems, where cropland tends to be covered by plants year round, resulting in unavoidable confusion with natural evergreen forest. Fortunately, this problem can be solved by the Phased Array Type L-band Synthetic Aperture Radar (PALSAR) onboard the Advanced Land Observing Satellite (ALOS), given its capacity for forest detection (Dong et al. 2013a; Shimada et al. 2014b). The current study, which involves mapping paddy rice planting areas at a 30-m spatial resolution, has two aims: (1) to develop a pixel- and phenology-based algorithm by integrating time series optical images (Landsat-8, MODIS) and radar images (PALSAR) to map paddy rice planting areas in wheat-rice agricultural systems; and (2) to evaluate the potential utility of Landsat-8 OLI data in identifying fragmented paddy rice fields in complex agricultural landscapes. The case study area is located at the Yangzi-Huaihe Plain, China, which is characterized by a two-crop rotation (wheat and rice) agricultural system and intermixture of rural and urban landscapes (Figure 2.1).

2.2 Materials and methods

2.2.1 Study area

This study focused on a coastal area (33°06′14″ - 35°06′15″ N, 118°04′58″ - 120°03′28″ E), composed of the northeast Jiangsu province and the southeast Shandong province, a part of the Yangzi-Huaihe plain of China, at OLI image path 120 and row 36 (Figure 2.1). The area is flat with an average elevation of about 17 meters. It is comprised of 19 counties, three in the Shandong province and the rest in the Jiangsu province. Only seven counties, belonging to the Jiangsu province, are located completely within the research area.

Within a warm temperate and sub-humid monsoon climate zone[1], there is a long crop growing season in the test area. Records of averages for three years (2010-2012) from four local National Weather Stations demonstrate that the 8-day mean air temperature is usually higher than 10 ˚C from late March to early November (Figure 2.2 (a)) and precipitation mainly occurs from late June to late September. The crop growing season is around DOY (Day of Year) 110 to 295, according to the criterion that the first and last date of the 8-day night Land Surface Temperature (LSTnight) is greater than 5˚C (Figure 2.2 (b), (c)), calculated from the MYD11A2 product in 2010. Limited by temperature and precipitation, there is one rice crop per year in this area. However, two-crop rotation systems are dominant. In the southern part of the test area within the Jiangsu province, the double cropping system mainly consists of a winter wheat and paddy rice rotation, a rapeseed and paddy rice crop rotation[2], or a winter wheat and corn rotation. In the northern test area within the Shandong province, the double cropping system is mainly a winter wheat and corn rotation.

According to three years-worth (2010-2012) of observation records from two agricultural meteorology and phenology stations (Ganyv and Lvxian), a local crop calendar was made for three main crops: winter wheat, paddy rice, and corn (Figure 2.3). Varying both inter-annually and inter-regionally, winter wheat generally matures in early or mid-June, and the fields are flooded within 1-2 weeks after a quick harvest of winter wheat. One week to 10 days later, usually in mid-to-late June, rice seedlings are transplanted in this flooded soil. The harvest of rice usually happens in late October and then the next crop rotation begins. After the harvest of winter wheat, corn, as another dominant crop, is usually sown in late June and harvested in late September. Therefore, from June to October, paddy rice, corn, and other crops (peanut, soybean) constitute mixed agricultural landscapes. The surface water bodies in this region include mainly lakes, rivers, and salt ponds, as well as fish and aquaculture ponds.

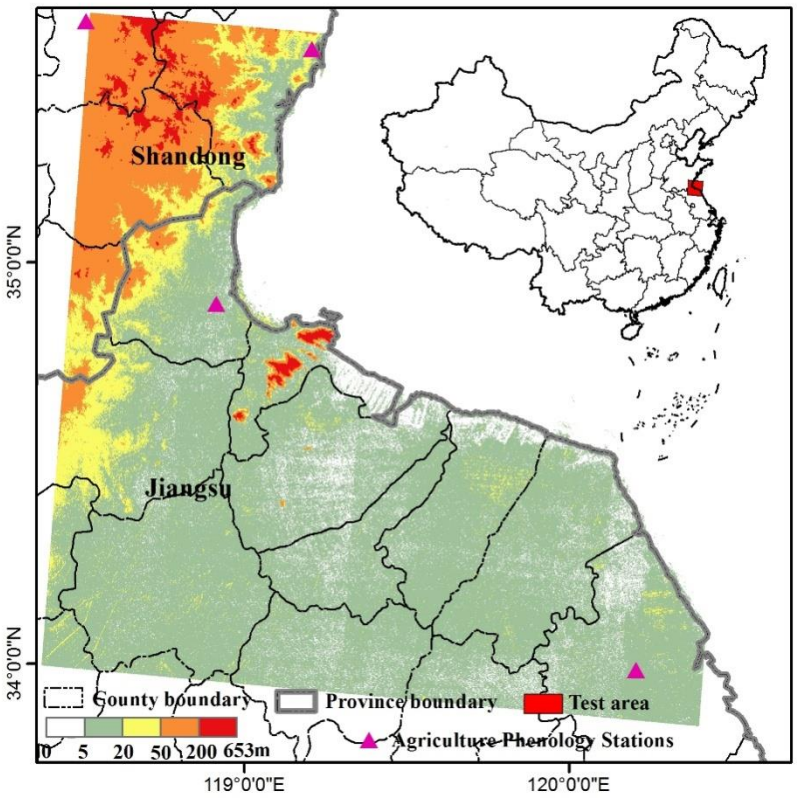

Figure 2.1 Black rectangle shows the location of the test area in the Yangzi-Huaihe Plain covering the northeastern Jiangsu province and the southeastern Shandong province of China. The average elevation of this area is about 17m. Four black triangles represent the agriculture phenology stations provided by the China Meteorological Data Sharing Service System (http://cdc.cma.gov.cn/home.do). This map created in ArcMap 10.1.

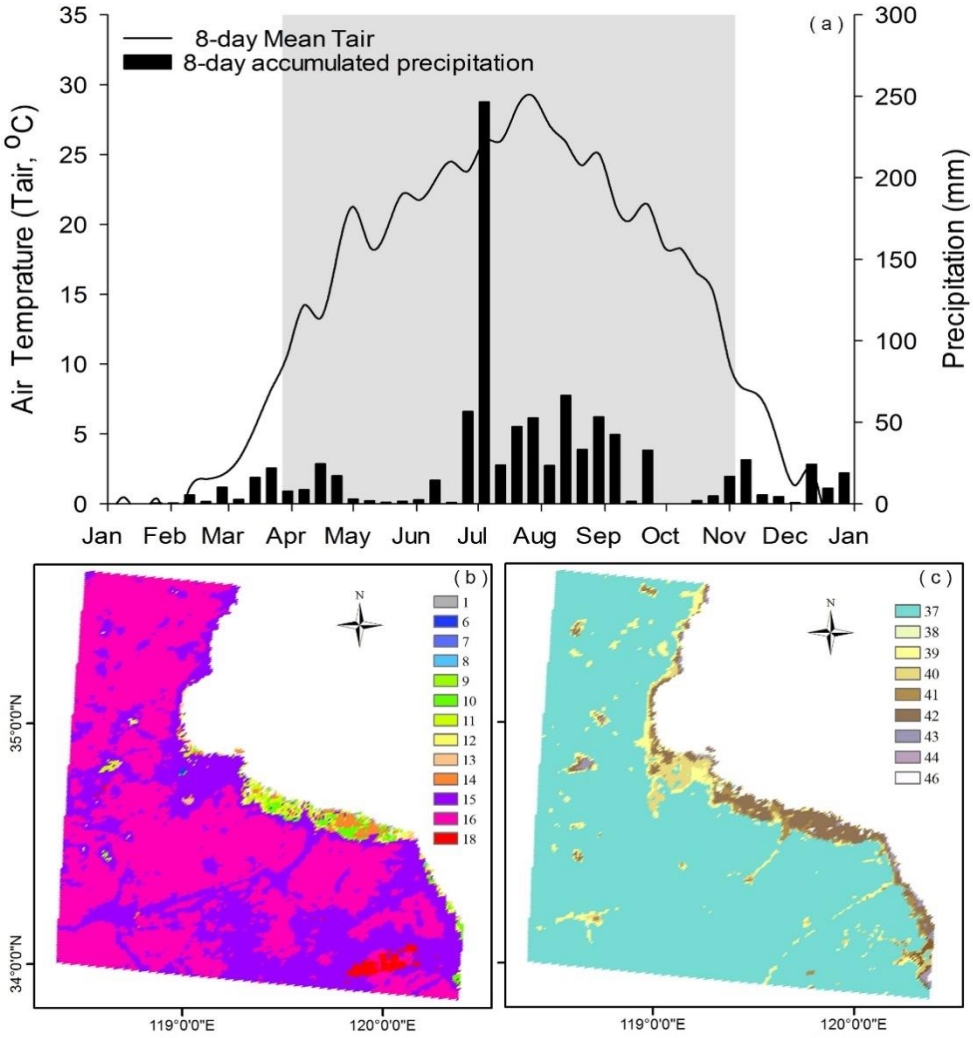

Figure 2.2 (a) The seasonal dynamics of 8-day accumulation precipitation and 8-day mean air temperature, which were calculated from mean observations of four meteorological stations: Ganyu (34.833 °N, 119.117 °E), Sheyang (33.767 °N, 120.25 °E), Lvxian (35.433 °N, 119.533 °E), Rizhao (35.583 °N, 118.833 °E), with the period of Tair ≥10 °C highlighted. Figure 2.2 (b), the first date when 8-day night Land Surface Temperature (LSTnight) was greater than 5˚C. Figure 2.2(c) the last date when 8-day LSTnight was greater than 5˚C. They were calculated from the MYD11A2 product in 2010. Figure (a) created in SigmaPlot 12.0, Figure (b & c) created in ArcMap 10.1.

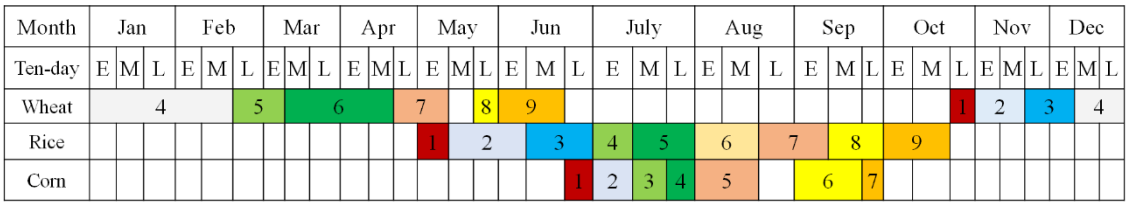

Winter wheat: 1. Sowing, 2. Seeding, 3. Tillering, 4. Stop growing, 5. Reviving, 6. Stem elongation, 7. Heading, 8. Milk stage, 9. Mature/Harvest
Rice: 1. Sowing, 2. Seeding, 3. Flooding/Transplanting, 4. Reviving, 5. Tillering, 6. Booting, 7. Heading, 8. Milk stage, 9. Mature/Harvest
Corn: 1. Sowing, 2. Seeding/Three leaves, 3. Seven leaves, 4. Stem elongation, 5. Heading, 6. Milk stage, 7. Mature/Harvest

Figure 2.3 Three main crop calendars include winter wheat, rice and corn, which were collected based on two agriculture phenology stations: Ganyu (34.833 °N, 119.117 °E) and Lvxian (35.433 °N, 119.533 °E). Figure created in Excel 2013.

2.2.2 Landsat-8 image data and process

The Landsat-8 satellite, launched on February 11, 2013, by NASA, carries two sensors, the Operational Land Imager (OLI) and the Thermal Infrared Sensor (TIRS). The OLI collects images with six narrower heritage bands and two newly specified bands: a deep blue band (Band 1, 0.43-0.45μm) observing ocean color in coastal zones and a shortwave infrared band (band 9, 1.36-1.39μm) detecting cirrus clouds. Images are collected at 16-day intervals with 15-meter panchromatic and 30-meter multi-spectral spatial resolutions. TIRS measures land surface emitted radiance in two thermal infrared bands with a spatial resolution of 100 m. These two sensors provide images with 12-bit radiometric resolution and higher signal-to-noise.

In this study, 12 standard level 1T data products (path/row 120/36), acquired from April 21, 2013, to December 01, 2013, were obtained from USGS by EarthExplorer (http://earthexplorer.usgs.gov/) (Table 2.1). The Landsat-8 level 1 GeoTIFF data products have finished radiometric calibration, systematic geometric correction, precision correction, and parallax error correction (Roy et al. 2014).

Table 2.1 A list of Landsat-8 images acquired in 2013 used in this study (Path/Row: 114/27). The valid percentage for each image was calculated based on cloud/cloud shadow masks generated by Fmask.

Date	DOY	Valid percentage (%)
April 21	111	99.2
May 23	143	57.5
June 08	159	35.5
June 24	175	65.2
July 10	191	71.9
July 26	207	30.5
August 11	223	88.2
August 27	239	98.6
September 12	255	28.7
September 28	271	28.7
November 15	319	98.4
December 1	335	98.6

Atmospheric correction was carried out for each image by using the updated Landsat Ecosystem Disturbance Adaptive Processing System (LEDAPS) routine. The LEDAPS project ingests and calibrates digital numbers to at-sensor radiance and then to surface reflectance after atmospheric correction by using the 6S approach (Masek et al. 2006). This radiative transfer code has an accuracy better than 1% over a range of atmospheric stressing conditions (Ju et al. 2012).

Clouds and associated cloud shadows obstruct the view of the land surface, frequently bringing false information into the land cover analyses (Goodwin et al. 2013; Huang et al. 2010). To remove these interference factors, Fmask (Function of mask) code was used to generate cloud and cloud shadow masks for each of the Landsat-8 images. Fmask is one of the detection methods based on clouds' physical properties at a global scale. Cloud shadow layers are generated by a sequential processing, including darkening effect identification of the cloud shadow in the NIR band, segmentation of potential cloud layer, and geometric match of the potential cloud shadow. The average detection accuracy

for clouds and for cloud shadows is more than 96% and 70%, respectively (Zhu and Woodcock 2012).

In this paper, a good quality observation means that the pixels in each image are not covered by clouds or cloud shadows. Using the cloud and cloud shadow masks, the quality of each image and its percentage of good observations were obtained and calculated (Table 2.1). From April to December, there were eight valid, informative images with a percentage of good observations larger than 50%.

Four vegetation indices were calculated from the surface reflectance. As a vegetation measure, Normalized Difference Vegetation Index (NDVI) (Tucker 1979) successfully monitors seasonal and inter-annual changes in vegetation growth and activity (Huete et al. 2002). Enhanced Vegetation Index (EVI) was developed to improve vegetation monitoring in high biomass regions (Huete et al. 2002; Huete et al. 1997a). Both can provide green-related vegetation information. Land Surface Water Index (LSWI), developed by SWRI and NIR spectral bands, is a water-sensitive vegetation index, tracking water thickness in vegetation and soil (Xiao et al. 2002b; Xiao et al. 2005d). Normalized Difference Snow Index (NDSI) was developed to detect snow automatically (Hall et al. 1995; Hall et al. 2002).

$$NDVI = \frac{\rho_{NIR} - \rho_{red}}{\rho_{NIR} + \rho_{red}} \tag{2.1}$$

$$EVI = 2.5 \times \frac{\rho_{NIR} - \rho_{red}}{\rho_{NIR} + 6 \times \rho_{red} - 7.5\rho_{blue} + 1} \tag{2.2}$$

$$LSWI = \frac{\rho_{NIR} - \rho_{SWIR}}{\rho_{NIR} + \rho_{SWIR}} \tag{2.3}$$

$$NDSI = \frac{\rho_{green} - \rho_{SWIR}}{\rho_{green} + \rho_{SWIR}} \quad (2.4)$$

Owing to high surface reflectance in the visible spectral bands, snow cover could potentially impact the seasonal dynamics of vegetation indices, especially in winter and spring (Xiao et al. 2005b). In this research, snow cover masks were generated based on the MODIS snow product algorithm (Hall et al. 1995; Hall et al. 2002). Snow-covered pixels were identified through NDSI > 0.4 and NIR > 0.11 from each Landsat-8 image.

2.2.3 Field survey data

To estimate the classification accuracy of this work, a field survey was conducted in the summer from July 21, 2013, to August 7, 2013. In general, the croplands were fragmented and agricultural landscapes were heterogeneous. In this survey, field photos were taken at 16 sites with GPS cameras (Figure 2.4), including 6 paddy rice fields, 2 cornfields, 1 mixture cropland of paddy rice and corn, and 7 other croplands (e.g. peanut fields). The sites with large croplands were chosen for taking photos. At each sample site, at least five photos were taken from within the croplands, one each towards the four cardinal directions (north, east, south and west) and a vertical-down view. All the photos taken over that summer were submitted to the field photo library of the Earth Observation and Modeling Facility at the University of Oklahoma (http://www.eomf.ou.edu/photos/browse/) as public property; they can be used by anyone who is interested. During this field trip, we talked to local farmers to gather additional information on the cropping calendar, crop rotation, and management practices such as fertilization and irrigation. From the field photo library, we also selected field photos from an additional 20 sites that were taken by other people.

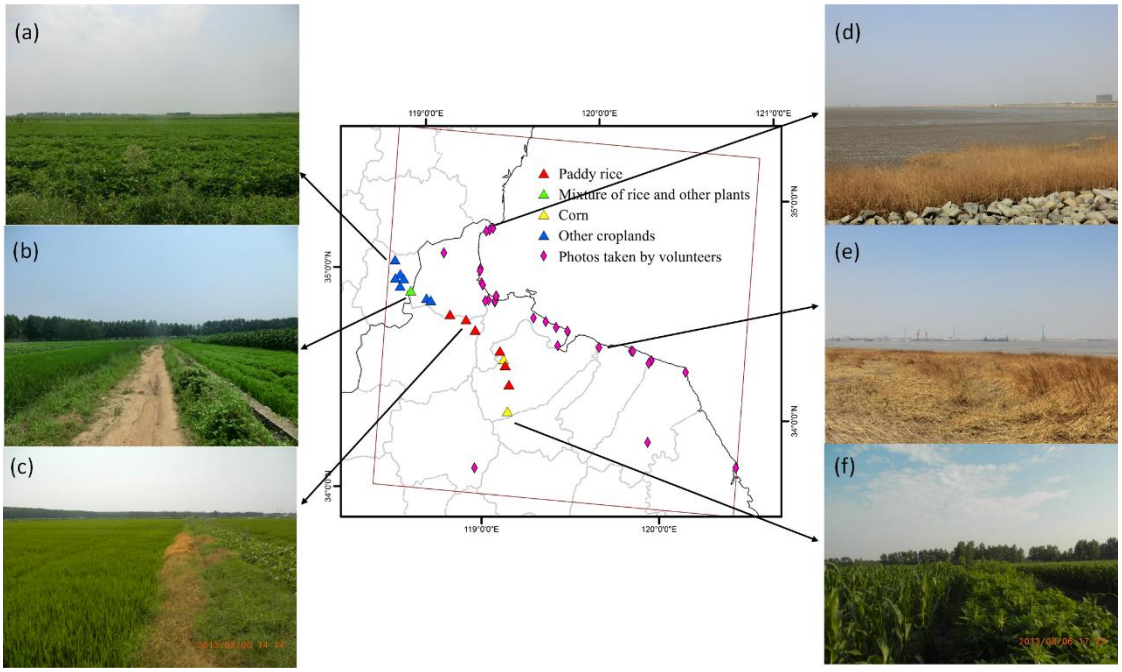

Figure 2.4 Ground truth photos of different land cover types, collected by field campaigns in 2013 and volunteers of EOMF photo library (http://www.eomf.ou.edu/photos/). (a & b & c & f)- Four cropland photos taken during field campaigns in 2013 (08/06/2013) present other croplands, a mixture of rice and other plants, paddy rice fields and corn lands, respectively; (d & e)-Two photos were provided by volunteers, which were uploaded to the EOMF photo library on 06/07/2013. These two photos show the mixture of vegetation and water.

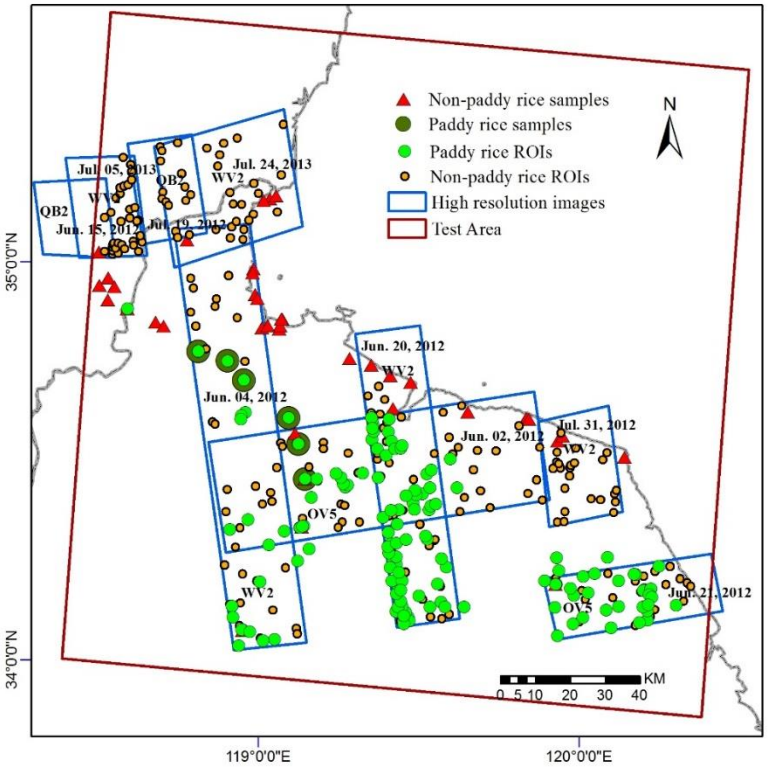

Figure 2.5 Spatial distribution of ROIs used for accuracy validation of the results in this research. ROIs were drawn according to field samples, high resolution images, and Google Earth. Here, points were used to identify the location of each ROI polygon. Blue polygons show the temporal and spatial information of high resolution images used in this work. Map created in ArcMap 10.1.

2.2.4 High-resolution images

Google Earth images were not enough to visually interpret ROIs as it lacked images within key time windows. We also ordered multiple high-resolution images from 2012 and 2013 from the NASA Goddard Space Flight Center, including WorldView-2 (WV2), OrbView5 (OV5), and QuickBird2 (QB2). The WV2 satellite sensor provides a 0.5m panchromatic band and eight multispectral bands with 1.8m resolution at Nadir (http://www.satimagingcorp.com/satellite-sensors/worldview-2.html). The OV5 collects a 0.41m panchromatic and four 1.65 m multispectral images at Nadir (http://www.satimagingcorp.com-/satellite-sensors/geoeye-1.html). The QB2 provides a 0.61m panchromatic and four 2.4m multispectral images at Nadir (http://www.satimagingcorp.com/satellite-sensors/quickbird.html). Figure 2.5 showed the distribution of high-resolution images used in this study as well as acquisition time and satellite sensors. Then, according to the reference information, we generated a series of random sampling points and interpreted them into ROIs. In total, 15,751 Landsat-8 pixels were acquired, including 7,388 paddy rice pixels (173 ROIs) and 8,363 non-paddy rice pixels (427 ROIs) (Figure 2.5).

2.2.5 2010 National Land Cover Data

The NLCD was developed by the Chinese Academy of Sciences using remote sensing and geographic information system techniques (Liu et al. 2014; Zhang et al. 2014). The 2010 1:100,000 NLCD was interpreted from 2010 Landsat TM digital images

by using the human-computer interactive interpretation method. For the areas that do not have TM data, the China–Brazil Earth Resources Satellite (CBERS) and the Huanjing-1 satellite (HJ-1) were used as supplemental data to fill gaps. To ensure high-quality and consistent NLCD, nationwide field surveys and uniform quality control were conducted before and after the development of each dataset. A classification system of 25 land cover classes was applied in the NLCD project, including paddy land and upland. The visual interpretation vector dataset was converted into a 1-km gridded database. Each 1-km gridded cell had the percentage of the area of various land-use types within it.

2.2.6 Maps of non-cropland land cover types

It is necessary to map some major non-cropland land covers, including water bodies, built-up and barren lands, forests, permanently flooded regions during the growing season (Figure 2.6). In practice, these land cover types potentially affect the seasonal dynamics of vegetation indices and the accuracy of the paddy rice detection algorithm.

Water bodies have lower NDVI and EVI and higher LSWI values. Similar to the water body extraction algorithm based on MODIS (Xiao et al. 2005), pixels in each image meeting the condition NDVI < 0.1 and NDVI < LSWI were extracted as water. Persistent water bodies were then composed of the pixels that were identified as water in all the good quality observations throughout the plant growing season.

Built-up and barren lands have high reflectance at visible and near infrared bands and low moisture content. Based on these physical features, a simple algorithm was put forward for built-up/barren lands, that is, LSWI < 0. Then, we calculated the frequency of a pixel identified as barren/built-up lands in the Landsat-8 time series (the total number

of good quality observations). Permanent built-up/barren land mask was made up by pixels with a frequency of ≥ 90%.

Forest cover can be mapped from optical images or microwave images. Because of frequent cloud cover and 16-day revisit cycle, there is no sufficient number of Landsat images available in 2013 to distinguish croplands and forests. Previous studies showed that the cloud-free L-band synthetic aperture radar (SAR) is the most advantageous for forest detection (Dong et al. 2013). In this research project, the Phased Array Type L-band Synthetic Aperture Radar (PALSAR-50m) Forest/Non-forest (FNF) classification map from 2010, provided by Japan Aerospace Exploration Agency (JAXA), were resampled to generate a 30 m forest mask. These PALSAR 50 m products are free to the public at the official ALOS Kyoto and Carbon Initiative website (http://www.eorc.jaxa.jp/ALOS/en/palsar_fnf/data/index.htm) (Dong et al. 2012). Compared to the ground truth data, these forest/non-forest products yielded 84% total accuracy on average (Shimada et al. 2011). This forest mask includes evergreen and deciduous forests.

Unlike seasonally flooded paddy rice fields, some lands remain flooded during the whole growing season. Therefore, it is necessary to distinguish between these two kinds of flooded lands. First, this work identified the flooded pixels for each Landsat-8 image following the rule LSWI – EVI ≥ 0 or LSWI – NDVI ≥ 0. Then, a map of the permanently flooded lands was produced from the pixels flooded in all the good-quality observations throughout the growing season.

According to the seasonal dynamics of MODIS-based vegetation indices (Figure 2.7 (a)) and Landsat-8 datasets (Table 2.1), seasonally flooded pixels were further divided

into three phases: flooded from mid-April to early June, from mid-June to early July, and from late July to early November. From mid-April to early June, flooded signals mainly appeared in natural wetlands, some aquaculture areas, and irrigation channels. From mid-June to early July, paddy rice fields begin flooding and transplanting with significant flooded signals. From late July to early November, flooded signals disappear from paddy rice fields and they may appear in the irrigation channels of croplands.

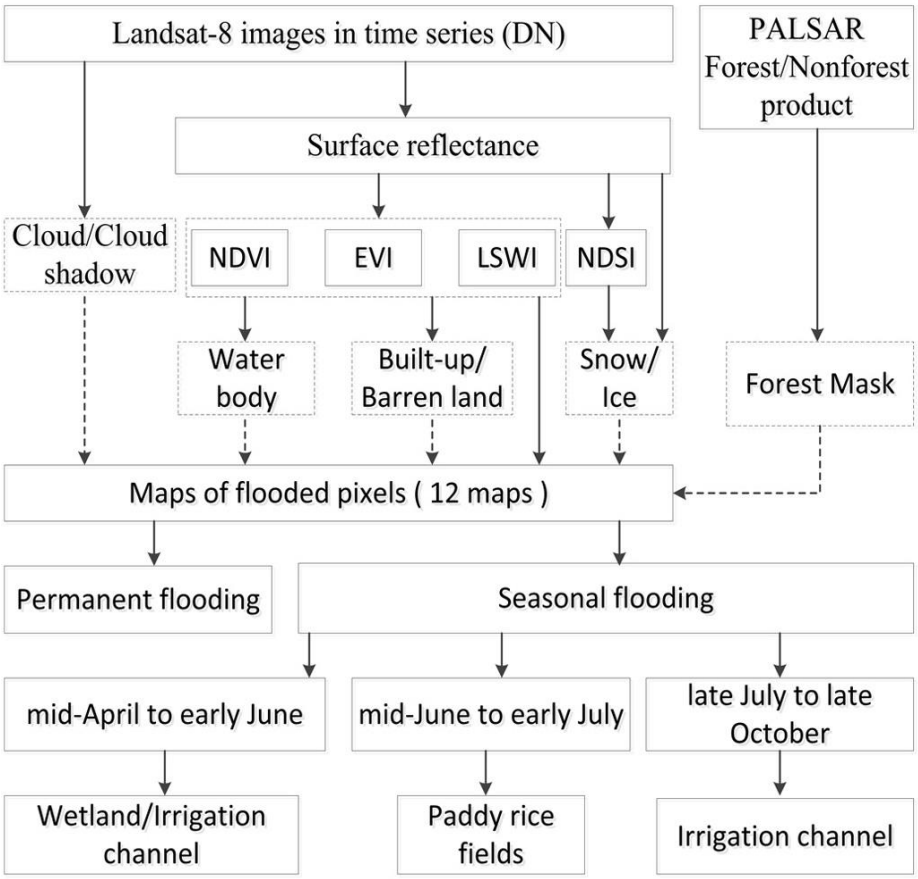

Figure 2.6 The workflow for mapping paddy rice planting area in a doubling agricultural system (Yangzi-Huaihe Plain) using Landsat-8 images from 2013. PALSAR 50 m FNF product was used as forest mask. Vegetation indices algorithms were used to detect non-croplands and flooded croplands. Figure created in Microsoft Visio 2010.

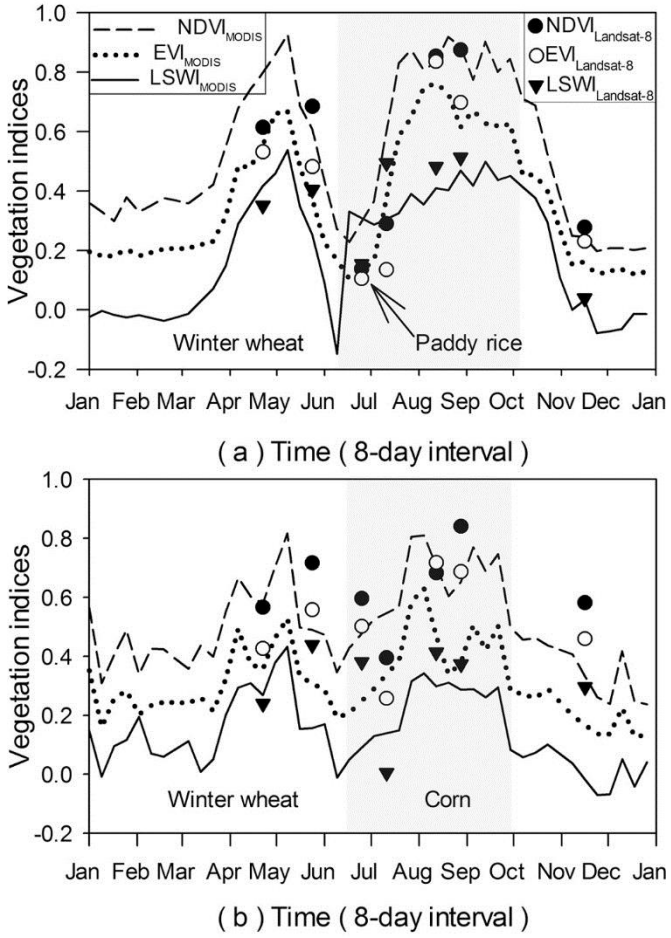

Figure 2.7 The seasonal dynamics of the Normalized Difference Vegetation Index (NDVI), Enhanced Vegetation Index (EVI), and Land Surface Water Index (LSWI), extracted from MOD09A1 product in 2012 and Landsat-8 images with good quality observations in 2013, for two-crop rotation agricultural systems. (a) Winter wheat and paddy rice rotation (34.286˚N, 119.642˚E), (b) winter wheat and corn rotation (34.237˚N, 119.232˚E).

2.2.7 Algorithms for identifying inundation and paddy rice fields

Paddy rice is usually planted in flooded fields. Three periods can be differentiated during paddy rice growth. In the flooding periods, the land surface of paddy rice fields is covered by water with a depth of 2-15 cm and green paddy rice plants. About 50 to 60 days later, most of the cropland surface is covered by the canopies of paddy rice plants. At the end of the growth period prior to harvesting, there is a decrease in the number of leaves and a decrease of leaf and stem moisture content.

The phenological features of main crops in the study area were investigated through MOD09A1 8-day composite vegetation indices time series (Figure 2.7), obtained from the MODIS data portal at the Earth Observation and Modeling Facility (EOMF), University of Oklahoma (http://www.eomf.ou.edu/visualization/gmap/). To get reliable vegetation index time series data, the bad-quality observations were gap-filled through a three-step gap-filling procedure (Jin et al. 2013). Figure 2.7 (a & b) show that the largest difference between paddy rice and other crops is the flooded signal during the growing season.

The phenological features of main crops were also investigated via the dynamics of three vegetation indices based on Landsat-8 time series images. Figure 2.7(a) shows that LSWI is larger than EVI in early July. Figure 2.7(a & b) indicate that despite a 16-day revisit, it is possible to detect the difference between paddy rice and corn from the Landsat-8 images. According to the seasonal dynamics of NDVI, EVI, and LSWI and the finer spatial resolution of Landsat-8 images, an algorithm was proposed to extract paddy rice fields from 30 m Landsat-8 images: $LSWI - NDVI \geq 0$ or $LSWI - EVI \geq 0$. According to the dynamics of MODIS vegetation indices, Landsat-8 images acquired within the flooding periods were used to map paddy rice fields. In this study, the flooding periods of paddy rice fields was from mid-June to early July, composed by the flooding/transplanting period and the reviving period of paddy rice calendar.

2.2.8 Accuracy assessment and comparison

We used ground truth data (field photos (Figure 2.4)), Google Earth (GE), and high-resolution images to locate and digitize Regions of Interest (ROIs). Google Earth displays high-resolution images, which have been used to validate land cover

classification in several studies (Cohen et al. 2010; Luedeling and Buerkert 2008; Montesano et al. 2009). However, GE images were not enough to visually interpret ROIs as it lacked images within key time windows. We also ordered multiple high-resolution images from 2012 and 2013 from the NASA Goddard Space Flight Center, including WorldView-2 (WV2), OrbView5 (OV5), and QuickBird2 (QB2). According to the reference information, we generated a series of random sampling points and interpreted them into ROIs. In total, 15,751 Landsat-8 pixels were acquired, including 7,388 paddy rice pixels (173 ROIs) and 8,363 non-paddy rice pixels (427 ROIs) (Figure 2.5).

The accuracy of the paddy rice map produced in this study was assessed by using the "Ground Truth ROIs" method in ENVI software. We obtained a confusion matrix between the paddy rice map and the ROI data, and producer's accuracy, user's accuracy, overall accuracy, and the Kappa coefficient. We estimated the accuracy of a paddy rice map using only good quality observations during the flooding/transplanting period. Finally, according to the cloud/cloud shadow masks from June 24 and July 10, we selected 3,610 paddy rice pixels (199 ROIs) and 3,113 non-paddy rice pixels (85 ROIs) located in good observation regions that were then used to validate the final paddy rice map.

We compared our results with the 1 km gridded 2010 National Land Cover Data, China (hereafter referred to as NLCD2010) to analyze their differences and the dynamics of paddy rice fields. The paddy rice map was compared with NLCD2010 at two scales. At the regional level, we analyzed the variations of paddy rice fields in spatial distribution and planting areas. At the pixel level, correlation analysis was used to compare these two datasets in regard to the estimation of paddy rice planting areas.

2.3 Results

2.3.1 Spectral signatures of flooded pixels and other land cover types

Different characteristics of vegetation indices are the basis for distinguishing flooded paddies from other land cover types. Figure 2.8 shows one example of the maps of EVI, NDVI, LSWI, LSWI-EVI, and LSWI-NDVI on Julian day 191 (July 10, 2013). At this time, paddy rice fields are in the midst of the flooding periods (including flooding/transplanting period and reviving period of paddy rice calendar), covered by a mixture of water and plants. Some uplands (e.g. corn fields) are going through the seeding or three leaves periods, covered by soil or by a mixture of soil and plants. The scatterplot graphs (Figure 2.9 (a & b)) show that EVI and NDVI mainly cluster between 0 and 0.3 for both the paddies and the uplands. The tremendous discrepancy between the two is that paddies cluster with LSWI-EVI ≥ 0 or LSWI-NDVI ≥ 0 and uplands cluster with LSWI-EVI < 0 or LSWI-NDVI < 0. Water bodies have LSWI-EVI ≥ 0 or LSWI-NDVI ≥ 0, but their EVI and NDVI are close to or less than zero. Other vegetation like forests or shrubs have higher EVI or NDVI (larger than 0.4) and lower LSWI-EVI or LSWI-NDVI (less than 0). Figure 2.9(c) shows that more paddy fields are detected by using LSWI-EVI ≥ 0 than LSWI-NDVI ≥ 0. In this image, about 10% of the pixels are flooded.

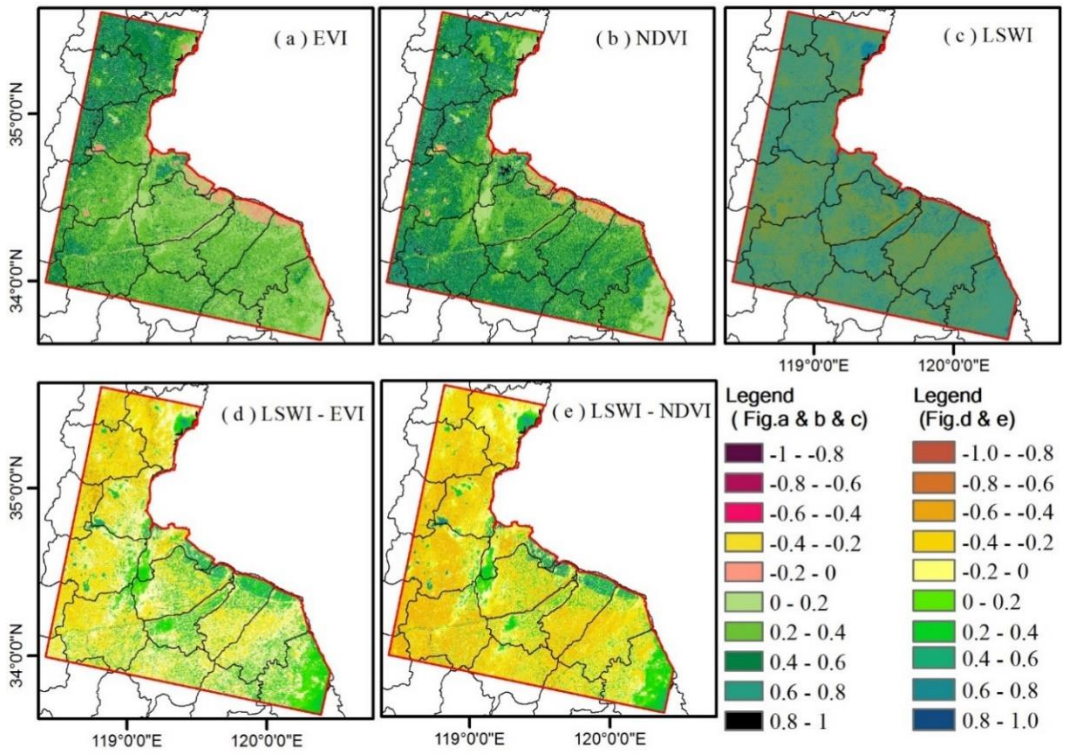

Figure 2.8 Spatial characteristics of vegetation indices during the flooding/transplanting period in the test area, only including the terrestrial area. (a & b & c & d & e) show the mappings of EVI, NDVI, LSWI, LSWI-EIV, and LSWI-NVI on Julian day 191, July 10, 2013. All these maps created in ArcMap 10.1.

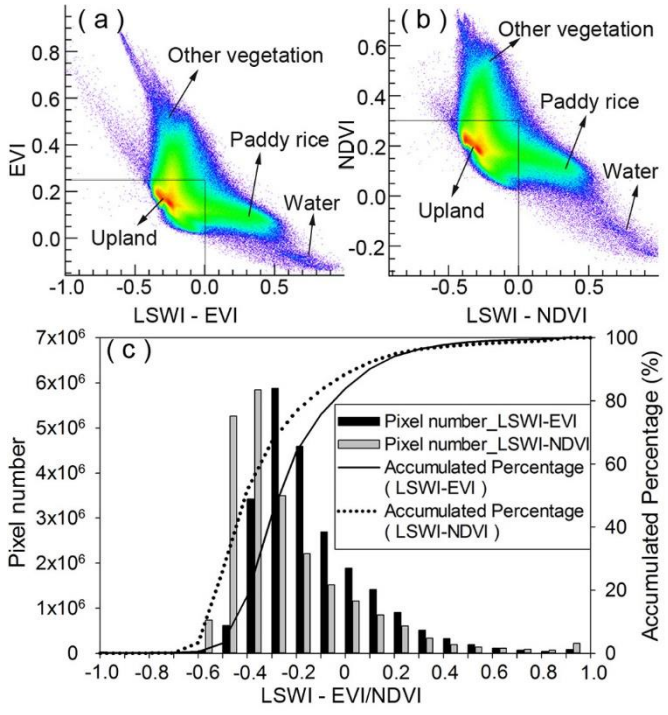

Figure 2.9 (a & b) show the gathering of four main objects (paddy rice fields, uplands, other vegetation, and water) in two-dimensional scatter plots: EVI and LSWI-EVI, and NDVI and LSWI-NDVI on Julian day 191(July 10, 2013). (c) Frequency histograms of LSWI-EVI and LSWI-NDVI. It shows that LSWI-EVI ≥ 0 detects more paddy rice fields than LSWI-NDVI ≥ 0. (a & b) created in ENVI 5.0, (c) created in Sigmaplot 12.0.

2.3.2 Spatio-temporal dynamics of paddy rice fields

Two Landsat-8 images (June 24 & July 10, 2013) were acquired during the flooding periods. Figure 2.10 (a & b) show the original images with bands combination: R: SWIR1, G: NIR, B: Green. Figure 2.10 (c & d) and (e & f) represent relevant paddy rice maps identified by the criteria LSWI-NDVI ≥ 0 and by LSWI-EVI ≥ 0, respectively. Figure 2.10 (g & h) are the combined paddy rice maps identified by the criteria LSWI-NDVI ≥ 0 or LSWI-EVI ≥ 0. They also show cloud/cloud shadow, water body, built-up/barren land, and forest masks. Because of less cloud/cloud shadow cover, the image quality on July 10 is better than the one on June 24 and more paddy rice fields are detected from it.

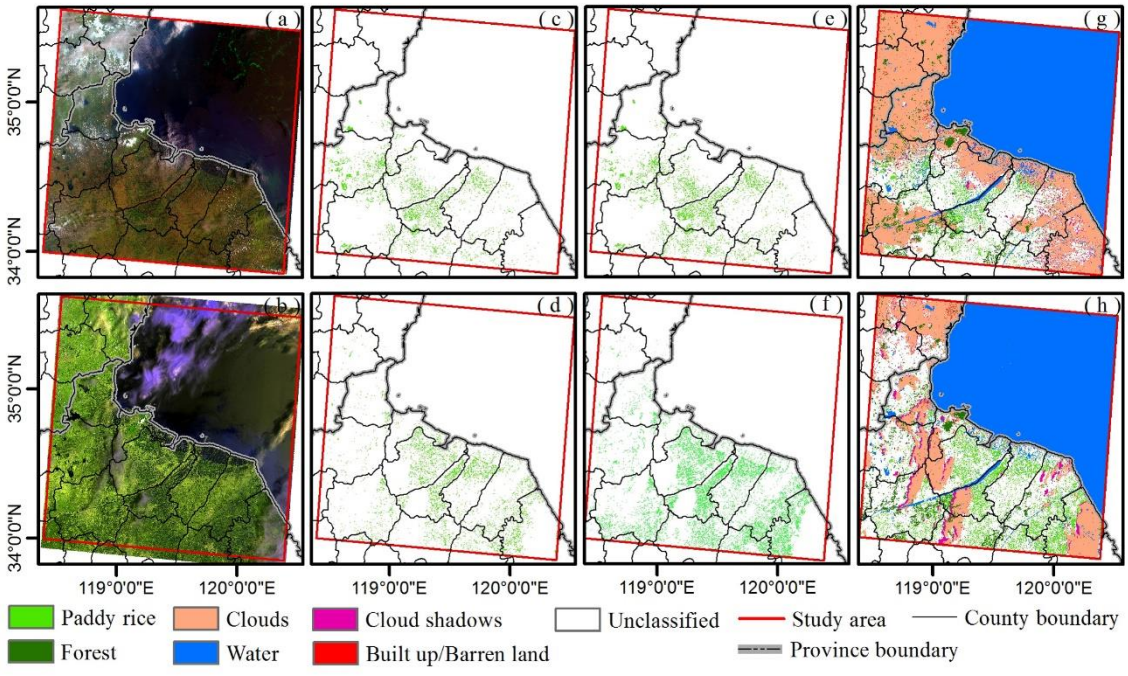

Figure 2.10 (a & b) Landsat-8 images after atmospheric correction on June 24, 2013, and July 10, 2013 (R,G,B = SWIR, NIR, Green); (c & d) Flooding pixels identified by the criteria LSWI-NDVI ≥ 0; (e & f) Flooding pixels identified by the criteria LSWI – EVI ≥ 0; (g & h) Paddy rice mappings identified by the criteria LSWI-NDVI ≥ 0 or LSWI - EVI ≥ 0. Clouds/cloud shadows, water, built-up/barren land, forest are all shown. Map created in ArcMap 10.1. (a & b) were downloaded from Earth Resources Observation and Science (EROS) Center, USGS (http://earthexplorer.usgs.gov/).

2.3.3 Spatial distribution of paddy rice fields

Figure 2.11 shows the spatial distribution of paddy rice fields in 2013 at 30 m spatial resolution, which integrates the paddy rice maps from June 24 and July 10. Few paddy rice fields are detected within the Shandong Province. However, in the Jiangsu Province, paddy rice fields are distributed widely and extensively. The paddy rice planting area is estimated to be approximately 2406.0 km^2, accounting for 37.55% of the study area. Additionally, this map reveals that the rice agriculture here is mainly conducted in small or medium size croplands. We used the Fragstats software 4.2 (http://www.umass.edu/landeco/research/fragstats/downloads/fragstats_downloads.html#diagnostic) to evaluate the fragmentation of the paddy rice fields. In this map, the total number of paddy field patches is 180,135, and the mean patch size of paddy fields is 0.0238 km^2 (~154 m×154 m).

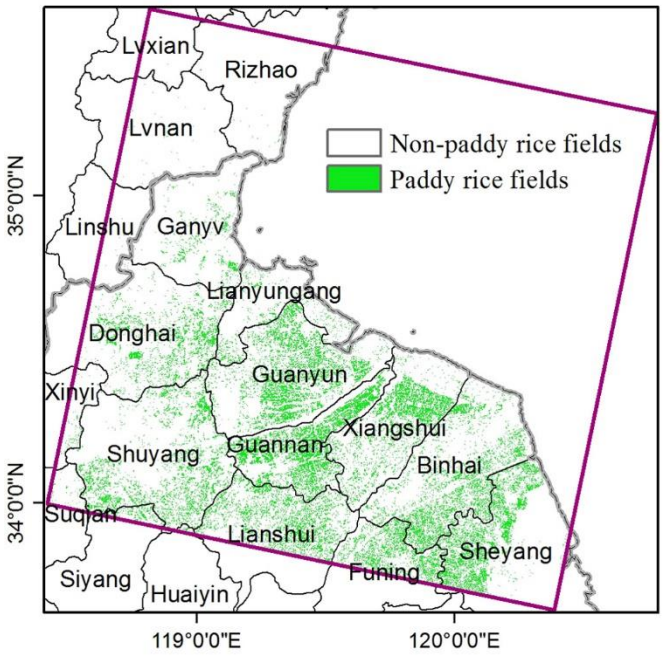

Figure 2.11 The paddy rice planting area map at 30 m spatial resolution, identified through the criteria LSWI - NDVI ≥ 0 or LSWI - EVI ≥ 0 from Landsat-8 images on June 24, 2013, and July 10, 2013. The total number of paddy rice plots is 180,135, and the mean paddy rice field size is 0.0238 km2 (~154 m*154 m). Map created in ArcMap 10.1.

2.3.4 Evaluation of Landsat-derived rice map

In this work, 3,610 paddy rice pixels (199 ROIs) and 3,113 non-paddy rice pixels (85 ROIs), located in good observation regions, were employed to calculate the confusion matrix (Table 2.2).

The validation showed the paddy rice/non-paddy rice map has a reasonably high accuracy. The paddy rice planting area in this map yielded 83.13% producer accuracy and 97.53% user accuracy. The non-paddy rice area in this map has 97.56% producer accuracy and 83.30% user accuracy. The overall accuracy and Kappa coefficient of this map are 89.81% and 0.79, respectively.

Table 2.2 Accuracy assessment of the 30 m Landsat-8 paddy rice map using ROIs (Regions of Interest) in the Yangzi-Huaihe Plain, southeast China.

	Ground Truth			
	Paddy rice	Non-paddy rice	Total	User Acc.
paddy rice	3001	76	3077	97.5%
Non-Paddy rice	609	3037	3646	83.3%
Total	3610	3113	6723	
Pro. Acc	83.1%	97.6%		
Overall accuracy	89.8%	Kappa coefficient	0.79	

2.3.5 Comparison to other available datasets

To compare this result with NLCD 2010 Paddy data, the 30 m Landsat-8 paddy rice planting area mapping was resampled to have 1 km spatial resolution ($Paddy_{Landsat\text{-}8}$, Figure 2.12(a)). In general, the spatial aggregation of paddy rice fields in both mappings (Figure 2.12(a & c)) was consistent except for two areas marked with blue circles (A & B). Furthermore, $Paddy_{Landsat\text{-}8}$ revealed more details about paddy rice field patterns than $Paddy_{NLCD2010}$ data (Figure 2.12(c)).

The total area of paddy rice planting in 2013 estimated by $Paddy_{Landsat\text{-}8}$ was 2406.0 km^2. It was far less than the paddy rice area (4,986.96 km^2) in 2010 estimated by $Paddy_{NLCD2010}$. Just considering the paddy rice fields in good observation regions, the paddy rice area from $Paddy_{Landsat\text{-}8}$ was 1,311.14 km^2, 12.17% lower than that (1,492.85 km^2) from $Paddy_{NLCD2010}$. Figure 2.12(b) shows the cloud/cloud shadow masks of images on June 24 and July 23, 2013. For the difference marked by the blue circle A, one obvious explanation is cloud contamination on June 24, 2013 (Figure 2.12(b)). Likewise, visual analysis showed a large difference occurred in the blue circle B (Figure 2.12(a & c)).

$Paddy_{Landsat\text{-}8}$ detected some paddy rice fields in this area, while NLCD2010 data classified these croplands as uplands (Figure 2.12(d)). One WordView-2 image (Figure 2.12(e)) on June 20, 2012, its location marked by the black rectangle, was used to judge the performance of these two results. It shows there are abundant flooding signals in the croplands that should be classified as paddies rather than uplands.

At the pixel level, the regression analysis was carried out to compare these two datasets for the paddy rice area estimate. R-square was 0.56 without considering the grey points gathering on X-axis (Figure 2.12(f)). One possible reason for this difference was that $Paddy_{Landsat\text{-}8}$ detected new paddy rice fields that were absent in $Paddy_{NLCD2010}$, just as the paddy rice fields within the blue circle B. In addition, owing to $Paddy_{NLCD2010}$ referring to the paddy rice planting area in 2010 and $Paddy_{Landsat\text{-}8}$ focusing on that in 2013, there were uncertainties due to paddy rice changes in actual agricultural practice or rapid Land Use/Land cover changes.

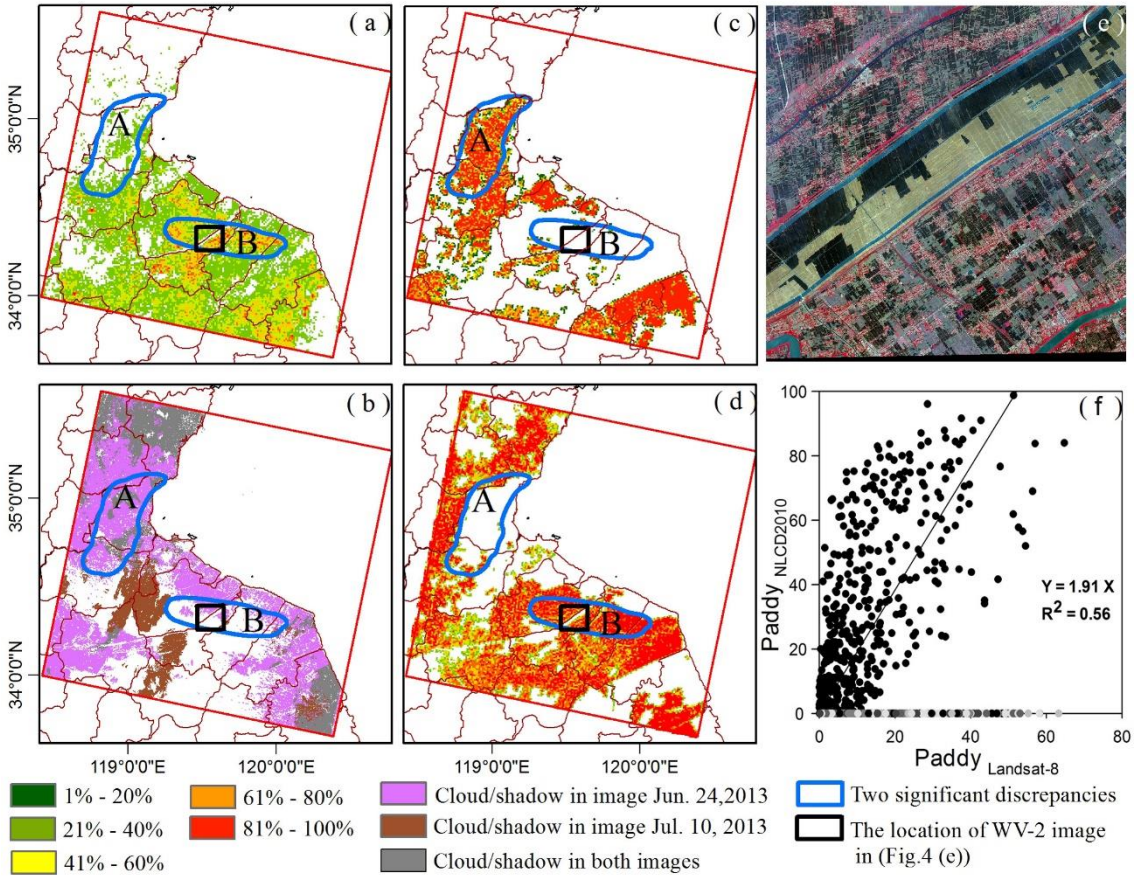

Figure 2.12 (a) 1 km Landsat-8 paddy rice map (PaddyLandsat-8), and different colors presenting the occupation levels of paddy rice fields in given pixels; (b) The cloud/cloud shadow masks for images on June 24 and July 10, 2013; (c) Paddy rice map of 1 km NLCD2010 dataset (PaddyNLCD2010); two significant discrepancies between PaddyLandsat-8 and PaddyNLCD2010 are marked with blue circles (A & B); (d) Upland map of 1 km NLCD2010 dataset; (e) WorldView-2 image from June 20, 2012, the location of which is marked by the black rectangle in (a & b & c & d). It shows abundant flooded signals in the croplands, which should be classified as paddy rice fields just as in the results of this study, rather than uplands in NLCD2010. (f) Pixel-level comparison between these two datasets. The solid line was drawn from the regression analysis of all the points except the grey ones gathering on the X-axis. These grey points reveal that PaddyLandsat-8 detected new paddy rice fields that were absent in PaddyNLCD2010. Maps (a & b & c & d & e) created in ArcMap 10.1 and Map (f) created in SigmaPlot 12.0. Image (e) was provided by NASA for use in the NASA projects.

2.4 Discussion

In this study, multi-source remote sensing data including Landsat-8, MODIS, and PALSAR were used to identify paddy rice fields from the rotation agricultural system of winter wheat and paddy rice. 30 m Landsat OLI images provide more details about the distribution of paddy rice fields (Figure 2.12(a)), and they are also helpful in identifying paddy rice from heterogeneous crops, which are common in this study area (Figure 2.4). MODIS-based LST_{night} images have the ability to track the growing season, which is consistent with the results of climate observations (Figure 2.2). The dynamics of MODIS-based vegetation indices give it the ability to detect the flooding signals (including flooding/transplanting and reviving periods) of paddy rice fields (Figure 2.6(a)) and yield results consistent with the crop calendar (Figure 2.3). Therefore, MODIS-based LST_{night} and vegetation indices (VI) dynamics can help automatically select Landsat-8 images for paddy rice planting area mapping. PALSAR data have advantages in mapping forest, which can be used to generate forest masks in paddy rice mapping to solve the mixture of croplands and forest, especially in the areas with long growing seasons. Therefore, the combination of multi-source remote sensing data makes it possible to map paddy rice fields automatically in complicated agricultural systems.

The integration of Landsat-8, MODIS, and PALSAR data also showed some advantages in the identification of fragmented paddy rice fields. The mean patch size of paddy fields in the study area was 154 m × 154 m in 2013. In terms of relatively small and even fragmented rice fields, the Landsat-8 images with finer spatial resolution (30 m) were better than the MODIS satellite data (500 m) in reducing mixed-pixel problems. In last several decades, the croplands in this study area were becoming fragmented rapidly,

because of high population pressure, rapid economic development, urbanization, and limited arable lands. In 1983, the mean farmland area was about 14 km^2, reduced to 6 km^2 in 2000(Ou 2004). In neighboring districts, the mean patch size of paddy rice fields also showed rapid diminution, declining from ~12 km^2 in 1990 to ~1.4 km^2 by 2006(Long et al. 2009). At the same time, the minimum patch area was also reduced from $2x10^{-4}$ km^2 in 1990 to $5x10^{-5}$ km^2 in 2006. Cropland fragmentation is common in Asia (Shiu et al. 2012). In China, the crop land area per household was 5.3×10^{-3} km^2 divided into 6.06 plots on average (Tan et al. 2006). The net cultivated area per capita was lower than 6×10^{-4} km^2 in Bangladesh (Rahman and Rahman 2009), and the average rice field was 1.1×10^{-2} km^2 in Taiwan (Chen et al. 2011). Therefore, the integration of multi-source remote sensing data has the potential to provide more valuable information for updating and refining paddy rice maps in Asia.

We recognized that the paddy rice map identified in this study was affected by several potential factors. The first source of uncertainty was the limited availability of images from the 16-day revisit Landsat-8 satellite that detected the flooded signals of paddy rice fields. In the study area, the flooding periods usually lasted around three weeks, from mid to late June or early July. Therefore, the flooded signals of paddy rice fields could only be observed by one or two images. This shortage of image data could be remedied in the future by using multi-year Landsat-8 data and other optical sensors, such as Landsat TM/ETM+, and Sentinel-2A/B (Berger et al. 2012; Drusch et al. 2012). Secondly, paddy rice planting area mapping based on Landsat-8 images did not avoid the impacts of clouds and their shadows, just as the other optical sensors, MODIS, TM, AVHRR (Fang et al. 1998; Motohka et al. 2009; Sun et al. 2009). Figure 2.10(a & b)

show that the original images from June 24 and July 10 are covered with about 30% cloud. In this study, Fmask was used to detect clouds and cloud shadows. Figure 2.10(g & h) show that Fmask worked well, but it overestimated the clouds. Therefore, these factors would result in the underestimation of paddy rice fields. Although 30 m Landsat-8 images were used in this study, it was still a challenge to remove the influence of the mixed pixels (e.g. vegetation and water). These pixels had the same characteristics as paddy rice fields during the flooding periods. Therefore, they might be identified as paddies if the ratio of vegetation and water satisfied the extraction algorithm: $LSWI - EVI \geq 0$ or $LSWI - NDVI \geq 0$. The confusion of paddy fields with other land cover types caused by mixed pixels is a common problem occurring in various sensors, including Landsat TM/ETM, SPOT, MODIS (Chen et al. 2011; Thi et al. 2012). Various agricultural practices would be another source of uncertainty. This research extracted flooded paddy rice fields with Landsat-8 images from June 24 and July 10, 2013. If some farmers deviated from the regular agricultural practice calendar, their paddy rice fields with earlier or later plants would not be detected from these two images, because flooding/transplanting signals would be weak or nonexistent. In addition, the rapid Land Use/Land Cover changes caused by urbanization and industrialization in this area from 2010 to 2013 was one of the reasons for the discrepancy between $Paddy_{Landsat\text{-}8}$ and $Paddy_{NLCD2010}$.

The results of this study have demonstrated the potential of multi-source remote sensing data (Landsat-8, MODIS and PALSAR) to map paddy rice planting areas in the wheat-rice double cropping system, using a pixel- and phenology-based algorithm. MODIS-based LST_{night} and VI dynamics make it possible to automatically select Landsat-

8 images within key time windows. PALSAR data can solve the mixture of croplands and forest. Landsat-8 images provide more details about the distribution of paddy rice fields, which is useful for the extraction of fragmented ones. As Landsat-8, MODIS and PALSAR Forest/Non-forest product are available to the public, there is a potential to develop 30 m paddy rice planting area maps across the two-crop zone using this approach.

2.5 Conclusion

Based on previous efforts in paddy rice mappings with MODIS vegetation indices time-series data, this paper aimed to estimate the potential of integrating time series optical images (Landsat-8, MODIS) from 2013 and radar images (PALSAR) for mapping paddy rice planting areas with a pixel-based and phenology-based algorithm. During the implementation of this algorithm, another criterion, the proportion of good quality observations, was introduced to generate masks, which made it possible to take advantage of each informative pixel. The accuracy assessment showed the results have an overall accuracy and Kappa coefficient of 89.81% and 0.79, respectively. Correlation analysis and comparison with reference databases ($Paddy_{NLC2010}$) also affirmed the quality of these results. Inherent in other optical sensors as well, there are some uncertainties from cloud/cloud shadow contamination, the limitation of spatial and temporal resolutions, and abnormal agricultural practices. However, Landsat-8 images with 30-m spatial resolution showed many advantages in the research area dominated by small cropland. It was possible to detect the flooded paddy rice fields in two-crop rotation agricultural systems using good Landsat-8 images. At large scales however, it is difficult to match the phenology of paddy rice with good Landsat-8 images based on one-year datasets. In the future, multi-year Landsat-8 data and other optical sensor data can be used for paddy rice

mappings at large scales. This work will be conducted via automatic algorithms. MODIS-based LST_{night} and VI dynamics will make it possible to automatically select Landsat-8 images within key time windows instead of relying on the investigation of local crop calendars. PALSAR data can help eliminate the impacts of forest, especially in areas with long growing seasons.

Chapter 3: Mapping the dynamics of eastern redcedar encroachment into grasslands during 1984-2010 through PALSAR and time series Landsat images

Abstract

Woody plant encroachment of eastern red cedar (*Juniperus virginiana*) into native grasslands in the U.S. Southern Great Plains has significantly affected the production of forage and livestock, wildlife habitats, as well as water, carbon, nutrient and biogeochemical cycles. However, time series maps are not available to document the continuously spatio-temporal dynamics of red cedar encroachment across landscape, watershed and regional scales. In this study, we developed a pixel and phenology-based mapping algorithm, and used it to analyze PALSAR mosaic data in 2010 and all the available Landsat 5/7 data during 1984-2010 with the Google Earth Engine (GEE) platform. This pilot study analyzed 4,233 images covering more than 10 counties in the central region of Oklahoma, and generated red cedar forest maps for 2010 and five historical time periods: the late 1980s (1984-1989), early 1990s (1990-1994), late 1990s (1995-1999), early 2000s (2000-2004), and late 2000s (2005-2010). The resultant maps for 2010, the late 2000s, early 2000s, and late 1990s were evaluated using validation samples collected from Google Earth's high-resolution images and geo-referenced field photos. The overall (producer and user) accuracy of these maps ranged from 88% to 96% (88% ~ 93%, and 96% ~ 99%). The resultant maps clearly illustrated an increase in red cedar encroachment within the study area at an annual rate of ~8% during 1984-2010. These maps can be used to support additional studies on the driving factors and consequences of red cedar encroachment. This study also demonstrated the potential to

trace the historical encroachment of red cedar into grasslands using time series Landsat images and PALSAR data.

3.1 Introduction

Woody plant encroachment has occurred globally across many ecosystems over the past century due to the effects of fire suppression, overgrazing, and climate changes (Archer et al. 1994; Barger et al. 2011; Van Auken 2000). The Southern Great Plains (SGPs) of the US has experienced five- to sevenfold greater woody plant expansion than other regions of the US (Zou et al. 2015). More than 20 documented woody species have encroached into the grassland and savanna ecosystems of North America over the past century (Barger et al. 2011). Juniper encroachment mainly threatens the tall- and mixed-grass prairies of the Great Plains (Barger et al. 2011). In Oklahoma, Juniperus virginiana L. (eastern red cedar) was reported to be encroaching into the grasslands and replacing the dominant oak trees in recent decades (DeSantis et al. 2010; Williams et al. 2013). The increased encroachment of eastern red cedar into native plant communities has threatened the sustainability, biodiversity, and productivity of native prairie ecosystems (Briggs et al. 2005; Engle et al. 1996). This shift in grassland species dominance has further affected ecosystem processes including water, carbon, nutrient, and biogeochemical cycles (Caterina et al. 2014; Williams et al. 2013; Zou et al. 2015).

Woody encroachment maps are vital for rangeland management, conservation planning, biodiversity assessment, and climate change studies. However, a time series of maps based on historically observed woody plant encroachment have not been produced at the regional scale (Gavier-Pizarro et al. 2012; Ge and Zou 2013), the absence of which constrains our capacity to understand the ecological consequences, environmental

impacts, and drivers of woody plant encroachment. For example, Ge and Zou (2013) simulated the impacts of eastern red cedar encroachment on regional climate in the SGPs. In their model simulation, the input maps of red cedar expansion were generated randomly, since the real maps of red cedar encroachment were not existent. In addition, the creation of regional-scale time series woody encroachment maps could reduce the uncertainty of continental-scale carbon budgets (Barger et al. 2011). Currently, it is hard to estimate the woody-plant expansion rate and describe the shapes of expansion curves for North America based on observations at two time points (Barger et al. 2011). Therefore, it is imperative to produce annual and multi-year maps of woody plant encroachment at regional and continental scales.

Traditional field survey approaches do not adequately document the expansive amount of data required to accurately map the spatio-temporal distribution and dynamics of woody plant encroachment at regional scales (Engle et al. 1996; Waser et al. 2008). Remote sensing images with long term data archives are alternative data sources to these studies. So far, most remote sensing studies have focused on (1) detecting trees in woodlands using very high spatial resolution (VHSR) aerial images (Anderson and Cobb 2004; Poznanovic et al. 2014; Strand et al. 2006) and Lidar data (Falkowski et al. 2006), and (2) calculating the woody coverage in grasslands or savannas using multiple data sources, including Landsat Thematic Mapper/Enhanced Thematic Mapper Plus (TM/ETM+), radar, and Lidar (Sankey and Glenn 2011; Urbazaev et al. 2015; Yang et al. 2012). These studies were conducted at small spatial scales (e.g., rangeland or landscape) for a single year. Furthermore, no work has been established on mapping the encroaching species in grassland or savanna ecosystems over several decades.

The Landsat program has provided continuous Earth observation since the first satellite launch in 1972 (Wulder et al. 2012; Wulder et al. 2008). Images from Landsat TM, ETM+, and Operational Land Imager (OLI) have been recording continuous land cover changes with consistent spatial (30m) and temporal (16 day) resolutions since 1984 (Wulder et al. 2015). An increasing number of land cover change studies have been conducted since the open access of the Landsat archive data in 2008 (Woodcock et al. 2008). However, optical remote sensing is sensitive to vegetation canopy (e.g., foliage cover), which may overestimate woody plant extent caused by the confusion with herbaceous vegetation or omit some woody plants with deciduous and semi-deciduous characteristics (Shimada et al. 2014). Synthetic Aperture Radar (SAR) sensors can penetrate clouds, and the longer wavelength SAR (L-band SAR) has better capability to obtain the vegetation structures (e.g., stem density, biomass.) (Baghdadi et al. 2009; Cloude and Papathanassiou 2003). The great volume scattering from leaves, trunks, and branches provides promising signatures for the classification of forest coverage (Chen et al. 2016; Qin et al. 2015a; Shimada et al. 2014). The Advanced Land Observing Satellite (ALOS) Phased Array type L-band Synthetic Aperture Radar (PALSAR) was launched by the Japan Aerospace Exploration Agency (JAXA) in January 2006 and stopped operation in April 2011. It provided numerous data for forest (Qin et al. 2015a; Shimada et al. 2014) and plantation (Dong et al. 2013; Miettinen and Liew 2011) mappings at the global and regional scales. Recent studies have shown that the combination of Landsat time series images and PALSAR data provides opportunities to monitor historical changes of forest resources (Lehmann et al. 2015).

The accuracy of land cover classification is impacted by both algorithms and remote sensing images (spatial, temporal and spectral resolutions). Broadband sensors have been widely used to generate regional or global land cover maps, which included vegetation types at the biome scale (Friedl et al. 2010; Gong et al. 2013; Loveland et al. 2000). Mapping at the plant species level has been mainly conducted using hyperspectral data with narrow bands (Clark et al. 2005; Martin et al. 1998) or VHSR images (IKONOS, WorldView-2, etc.) (Pu and Landry 2012). Nevertheless, there are not sufficient amounts of hyperspectral and VHSR data for monitoring the long-term land cover changes at the species level. Several studies used time series images to track land surface phenology and generate land cover maps for crop species and forest plantations (Dong et al. 2013; Xiao et al. 2005; Zhong et al. 2014), and separate cropland and pasture in complicated savanna landscapes (Mueller et al. 2015). These studies suggested the time series images can be used to extract seasonal, annual and multi-year phenological indicators for plant species of interest. For example, time series Landsat images have been used to classify crop types and map rubber plantations by generating phenological metrics (Zhong et al. 2014) or selecting unique phenological windows (Dong et al. 2013) at regional scales. It is still unknown about the potential of 30m Landsat images to recognize the species of trees (e.g., eastern red cedar) which has encroached into the grassland ecosystem.

This study proposes an approach to map the historical encroachment of eastern red cedar forest back to the 1980s by integrating PALSAR data in 2010 and long-term Landsat TM/ETM+ images during 1984-2010 using Google Earth Engine (GEE) cloud computing platform. Our three objectives were: (1) to develop a pixel and phenology-based algorithm to map the eastern red cedar encroachment into the grasslands based on

PALSAR and Landsat time series images; (2) to quantify the dynamics of eastern red cedar encroachment by using remote sensing observations in five historical time periods of the late 1980s (1984-1989), early 1990 (1990-1994), late 1990s (1995-1999), early 2000s (2000-2004), and late 2000s (2005-2010); and (3) to quantitatively evaluate the recognition capability of moderate spatial resolution images of Landsat and PALSAR at the species scale using the pixel and phenology-based algorithm.

3.2 Data and methods

3.2.1 Study area

The study area (35°12'N ~ 36°44'N, 96°25'W ~ 98°59'W) covers more than 10 counties (~28,303 km^2) across central and western Oklahoma (Fig. 3.1). It has a temperate continental climate. The annual mean air temperature is near 16 ^oC. The average annual precipitation is ~810 mm, and the northwestern regions are drier than the southeastern parts. The topography is generally flat with elevation ranging from 215m to 612m above sea level (Fig. S3.1a). The majority of this area is in the Central Great Plains ecoregion, with some small patches in the Cross Timbers and Flint Hills ecoregions (Fig. S3.1b) (Woods et al. 2005). Croplands, grasslands, and forests are the major land cover types, the combination of which accounted for about 90% of the study area. The spatial extent of urban areas were very small as captured on VHSR imagery dated 03/01/2011 from Google Earth (GE) (Fig. 3.1).

The study area is in the ecotone that connects the eastern deciduous forest and the tallgrass prairie, which includes a gradient from woody to non-woody vegetation (Hoagland 2000; Myster 2009). According to early vegetation investigations (Johnson and Risser 1975), the latest Oklahoma Ecosystem Map (OKESM) (Diamond and Elliott

2015), and our field survey in 2015 (Fig. 3.1), the deciduous forests in our study area are dominated by oaks, especially post oak (*Quercus stellata*) and blackjack oak (*Q. marilandic*a). Eastern red cedar is the dominant evergreen species in forest and woodland/shrubland areas, while other evergreen tree species (e.g. pine) are few. In addition, bottomland hardwood forests (e.g., elms, pecan) can be seen along rivers or creeks. Eastern red cedar is evergreen without leaf color changes in fall. The species in post oak-blackjack and bottomland hardwood forests are deciduous types, which have seasonal leaf emergence and leaf fall (http://www.forestry.ok.gov/ok-tree-guide). The leaf phenology can be detected by time series optical remote sensing signals, which facilitates the separation of eastern red cedar forest from deciduous forests of oaks and other hardwood species.

Substantial eastern red cedar encroachment has occurred in this forest-prairie ecotone over the last several decades (Engle et al. 1996; Williams et al. 2013). Nearly no eastern red cedar was observed in the 1950s (Rice and Penfound 1959). Forest surveys were conducted during the 2000s using standard dendrochronological methods covering our study area (DeSantis et al. 2011). The results showed that the eastern red cedar number increased from the 1960s to 1970s, and became the primary recruitment species from the mid-1970s to the 2000s. Also, the eastern red cedar basal area increased from 0% to 43% and tree density increased from 2% to 56% between the 1950s to the 2000s (DeSantis et al. 2011).

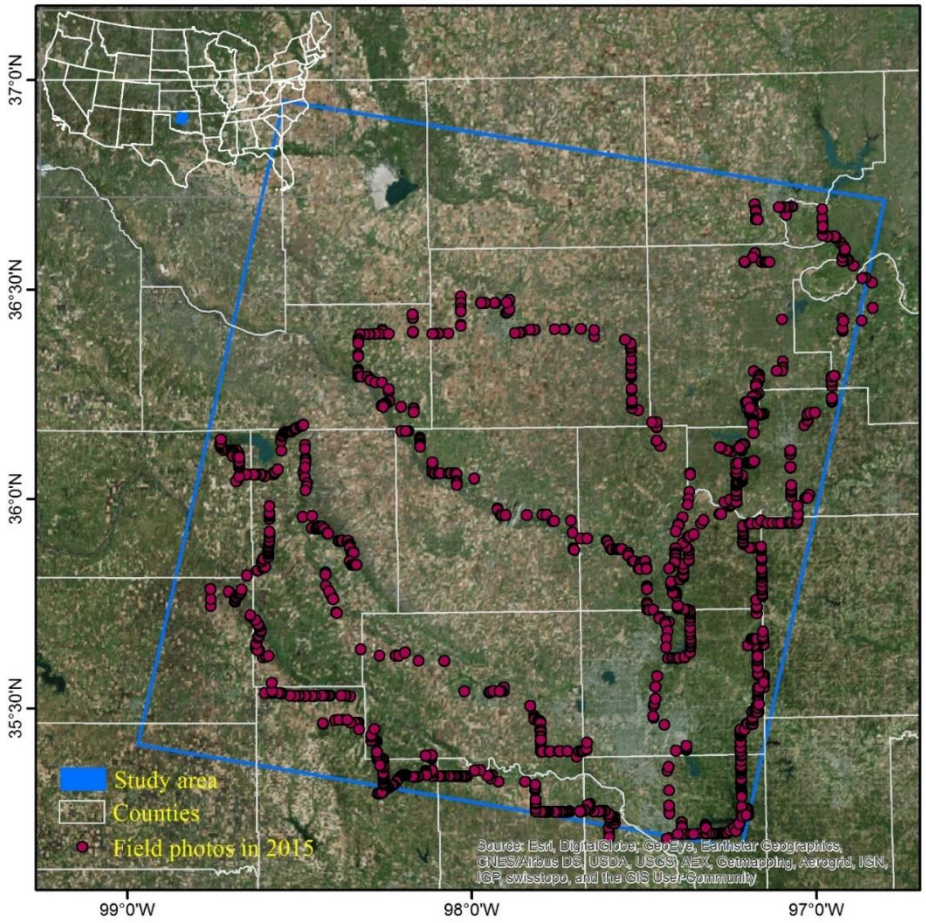

Figure 3.1 The location of the study area and the counties it covers. A very high spatial resolution image dated 03/01/2011 from Google Earth and the field photos taken in 2015 are shown in this figure.

3.2.2 Data

3.2.2.1 PALSAR data and pre-processing

The PALSAR datasets provided by the Earth Observation Research Center, JAXA, offer opportunities to develop forest maps at regional and global scales (Shimada et al. 2014a). The 25m PALSAR orthorectified mosaic datasets from 2007 to 2010 were generated from the annual HH and HV data acquired between June and October with Fine Beam Dual (FBD) polarization mode. The HH and HV data have been processed by geometric correction using a 90m digital elevation model and radiometric calibration

(Shimada et al. 2009; Shimada and Ohtaki 2010). The mosaic data of HH and HV were expressed by gamma-naught (γ^o), due to the normalization of backscatter by the realistic illumination area (Shimada et al. 2014a).

We downloaded all the 25m PALSAR orthorectified mosaic data for Oklahoma in 2010. The Digital Number (DN) values (amplitude) of HH and HV were converted into backscattering coefficient (gamma-naught) in decibel using the following calibration coefficient (Shimada et al. 2009).

$$\gamma^o = 10 \times log_{10} < DN^2 > +CF \tag{3.1}$$

where γ^o is the backscattering coefficient in decibel; DN is the digital number value of pixels in HH or HV; and CF is the absolute calibration factor of -83.

3.2.2.2 Time series Landsat data and pre-processing

The GEE platform was used to collect and process all the Landsat images in this study. We used all the available standard U.S. Geological Survey Center (USGS) surface reflectance products of Landsat 5/7 covering the study area over Jan. 1984 to Mar. 2011, which have been collected in the GEE platform. The surface reflectance data were generated from the Landsat Ecosystem Disturbance Adaptive Processing System (LEDAPS), which includes the calibration from at-sensor radiance to the top of atmosphere (TOA) reflectance and the atmospheric correction from TOA reflectance to surface reflectance (Masek et al. 2006; Vermote et al. 1997). The study area is located within the Landsat scene of path/row 28/35. The pixels near the boundary of the study area had more observations due to the overlap of neighboring Landsat scenes (paths/rows of 27/35, 27/36, 28/34, 28/36, 29/34, 29/35). We constructed the 3-dimensional data cube of land surface reflectance using these seven overlapping Landsat scenes. Fig. 3.2 shows

the annual distributions of all the available Landsat TM/ETM+ surface reflectance data over the study period by Landsat path/row (Fig. 3.2a), by months (Fig. 3.2b), and by sensors (Landsat 5/7) (Fig. 3.2c).

The quality of all observations for individual pixels in the data cube was assessed. The bad observations from clouds, cloud shadows, snow/ice and scan-line corrector (SLC)-off gaps were identified as NODATA according to the Fmask (Zhu and Woodcock 2012) and metadata. Fmask had good performance to detect cloud and cloud shadows from Landsat 5/7 images with overall accuracy greater than 90% (Zhu and Woodcock 2012). The number of individual pixels from good Landsat 5/7 observations were counted during the winter (including Dec. Jan. and Feb.) for each year (Fig. S3.2). In 1984 and 1986, about 2% pixels in the study area had zero good observations in the winter season, while in the other years, all the pixels had at least one good observation during the winter (Fig. 3.3).

We calculated three vegetation indices (VIs) based on the surface reflectance data with good observations: Normalized Difference Vegetation Index (NDVI) (Tucker 1979), Enhanced Vegetation Index (EVI) (Huete et al. 2002), and Land Surface Water Index (LSWI) (Xiao et al. 2005b). NDVI and EVI are related to the vegetation greenness, and LSWI is sensitive to the vegetation water content. The times series data of these three VIs can be used to analyze the vegetation phenology (Huete et al. 2002; Xiao et al. 2006b).

$$NDVI = \frac{\rho_{NIR} - \rho_{red}}{\rho_{NIR} + \rho_{red}} \tag{3.2}$$

$$EVI = 2.5 \times \frac{\rho_{NIR} - \rho_{red}}{\rho_{NIR} + 6 \times \rho_{red} - 7.5\rho_{blue} + 1} \tag{3.3}$$

$$LSWI = \frac{\rho_{NIR} - \rho_{SWIR}}{\rho_{NIR} + \rho_{SWIR}} \quad (3.4)$$

where ρ_{blue}, ρ_{red}, ρ_{NIR} and ρ_{SWIR} are the surface reflectance values of blue (450-520nm), red (630-690nm), near-infrared (760-900nm), and shortwave-infrared bands (1550-1750nm).

3.2.2.3 Field survey data

Field surveys were carried out three times during November 7-21 in 2015 to collect ground truth data for training and validation samples. These field surveys mainly focused on the species (e.g. red cedar, oaks, and bottomland hardwoods) of forests and woodlands. We also noted other land cover types including shrubland, grassland, and cropland. The regions with large vegetation coverage were chosen as sampling sites. At each site, we took at least five photos with GPS cameras and recorded the vegetation characteristics (e.g. growth stage, composition of community). Field photos were taken following the rules described in-detail in previous publications (Qin et al. 2015b; Wang et al. 2015). Fig. 3.1 shows the distribution of the field photos, with a total number of 1970. These photos can be accessed freely at the global data portal at the Earth Observation and Modeling Facility (EOMF), University of Oklahoma (http://www.eomf.ou.edu/photos/) (Xiao et al. 2011). The training Region of Interests (ROIs) were digitized according to these field photos and the GE images during the winter and early spring over 2005-2010. Although the ground truth photos were taken in 2015, they offered important references on vegetation types for the visual interpretation. We collected training ROIs stratified randomly across the red cedar and non red cedar forest areas (with plots/pixels of 46/11,712 for red cedar and 30/10,698 for other trees). The

distributions of the training ROIs and the boundaries of all the used GE VHSR images are shown in Fig. S3.3. In this study, the phrase ‘other trees’ refers to those non red cedar species, mainly composed of oaks and bottomland hardwoods.

3.2.3 Algorithm to identify red cedar forest

Forest is defined as land (> 0.5 ha) with tree canopy cover larger than 10% and minimum tree height of 5m, according to the United Nations Food and Agriculture Organization (FAO) (FAO 2012). The workflow for mapping long-term (1984-2010) red cedar forest included three sections (Fig. 3.4). First, a baseline forest map in 2010 was produced using a decision tree algorithm based on 25m 2010 PALSAR data. Second, the 2010 red cedar forest map was produced using a pixel and phenology-based algorithm based on the 2010 forest map and the Landsat images in the winter of 2010 (Dec.2010 - Feb.2011). Finally, a red cedar forest stand-age map in 2010 was produced based on the historical red cedar forest maps. The historical red cedar forest distributions were generated based on the 2010 forest map and Landsat times series images in 1984-2010 using the pixel and phenology-based algorithm. The red cedar forest maps were produced for the late 1980s (1984-1989), early 1990s (1990-1994), late 1990s (1995-1999), early 2000s (2000-2004) and late 2000s (2005-2010). The detailed workflow is described in the following paragraphs.

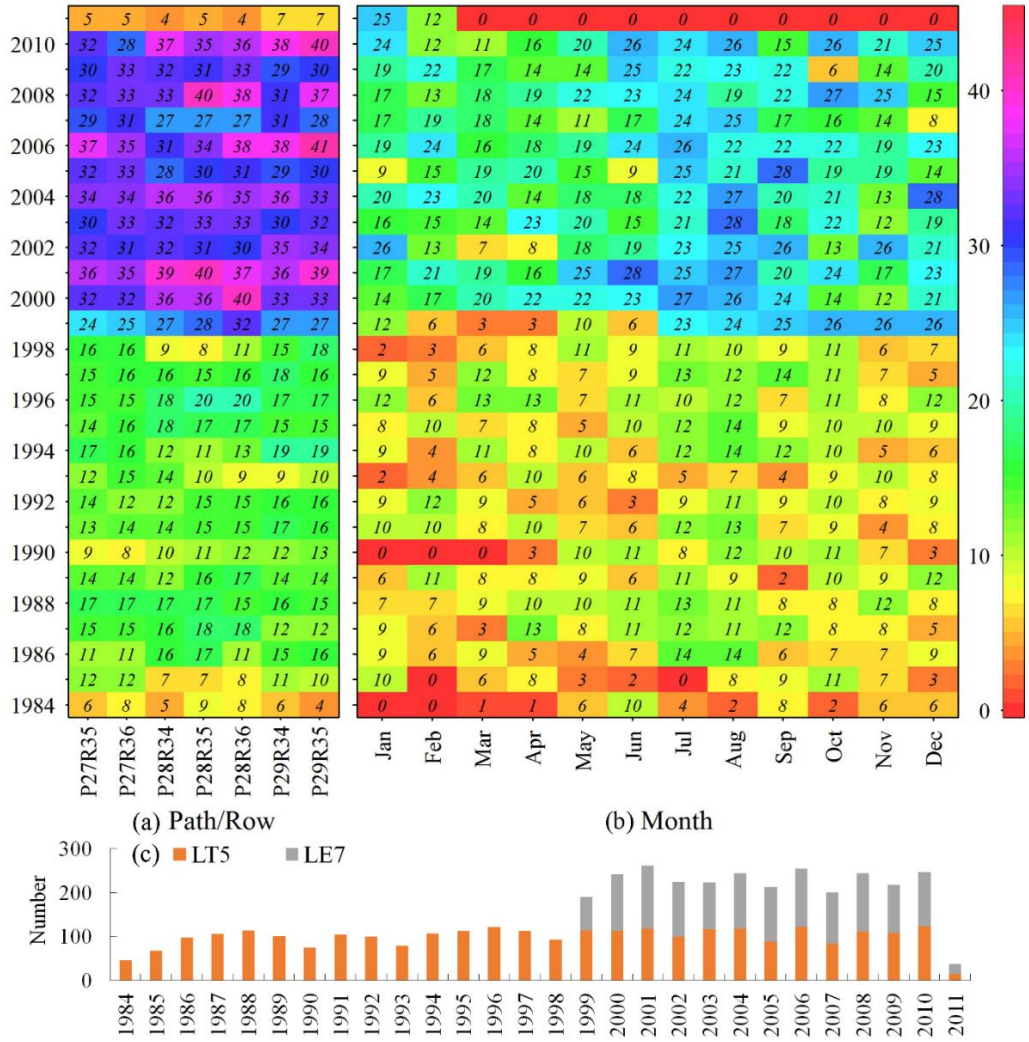

Figure 3.2 The annual distribution of Landsat images used in this study. Statistics were conducted by (a) path/row, (b) month and (c) sensors.

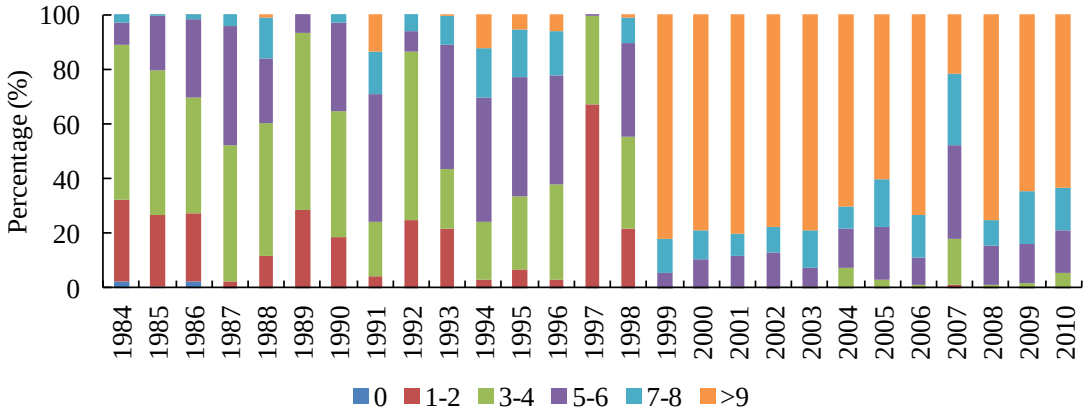

Figure 3.3 Percentage of pixels with various good observation counts in the annual winter (Dec-Feb) from 1984 to 2010.

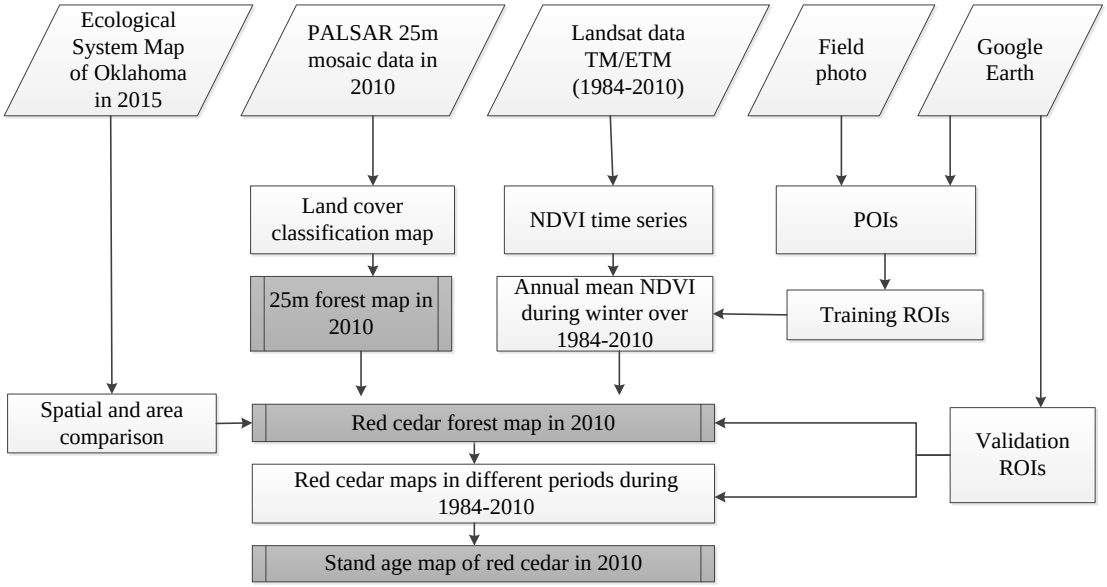

Figure 3.4 Workflow of red cedar forest mapping using 25m PALSAR mosaic data in 2010 and Landsat time-series images over 1984-2010. A detailed workflow for forest mapping was shown in previous publication (Qin et al. 2016a).

3.2.3.1 Phenology and signature analysis of red cedar and non red cedar trees

We selected three sites (Fig. S3.4a) with a largely homogeneous vegetation extent that represented red cedar, oak and bottomland hardwood forest types, according to the landscapes from the GE images and the field photos (Fig. S3.4b-g). Time series of three VIs (NDVI, EVI and LSWI) at these three sites were created using Landsat 5/7 data from 2005 to 2011 to examine the phenological characteristics of the forest types (Fig. 4.5). Oak and bottomland hardwood forests had more significant seasonal variations in the three VIs than did the evergreen red cedar forest. In comparison, red cedar forest had significantly lower VIs in summer and higher VIs in winter, which suggests the potential to separate red cedar forest from other forest types. In winter, NDVI and LSWI showed larger differences between red cedar and other forest types than EVI did. However, LSWI

tended to be influenced by ice and/or snow cover, which have a higher reflectance in the visible and near infrared bands than vegetation (Xiao et al. 2004a).

To map the red cedar at regional scale over multiple years, we analyzed the seasonal characteristics of NDVI based on the training ROIs of red cedar (11,712 pixels) and other trees (10,698 pixels) over a period of 2005-2010. We calculated the monthly mean NDVI (NDVImean) for individual pixels based on the Landsat 5/7 NDVI time series with a 8-day interval. We analyzed the mean values and standard deviations of monthly NDVImean for all the pixels of red cedar and non red cedar forests, in each year (Fig. S3.5) and in multiple years together over 2005-2010 (Fig. 3.6). The comparison of monthly NDVImean in summer and in winter suggested NDVImean in winter has a better ability to separate red cedar trees from other trees, as the monthly NDVImean of red cedar forests in winter was much higher than that of other forest types. These results also suggested that a threshold of about 0.4 can be used to extract the red cedar forest based on the winter NDVImean.

To confirm this information, we analyzed the signature distribution in HH, HV, and NDVImean in summer and in winter based on 2010 PALSAR data, 2010 Landsat 5/7 NDVI time series, and training ROIs of red cedar and non red cedar forests (Fig. 3.7). Fig. S3.6 shows these individual images and their spectral data. Red cedar and non red cedar forests had similar backscatter signature in PALSAR HH and HV, which can be used to extract a boundary of forests mixed with red cedar and non red cedar. In contrast, the spectral signature from NDVImean in summer and in winter showed some differences between red cedar and non red cedar forests. NDVImean in winter had the maximum between-class variance, which had the highest discrimination ability. Statistical analysis

showed that using a threshold of 0.40 can separate 95% of red cedar pixels (>0.4) from 99% of the pixels of non red cedar forest (<0.4) (Fig. 3.7d).

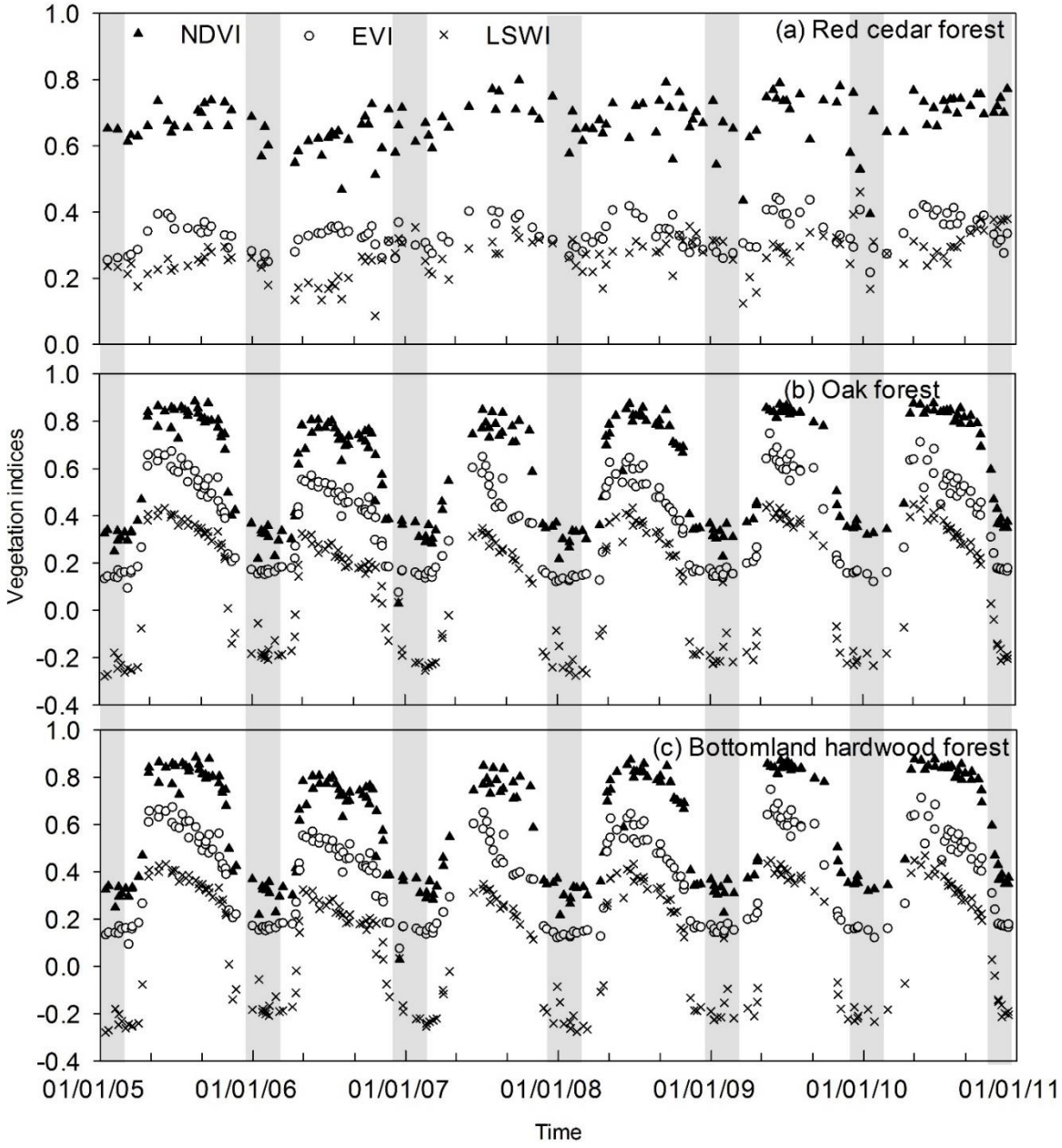

Figure 3.5 Seasonal and interannual variations of Landsat (TM/ETM+)-derived vegetation indices (NDVI, EVI and LSWI) for forest samples of (a) red cedar, (b) oak and (c) bottomland hardwood during 2005-2010. The winter in each year were delineated by grey boxes. The landscapes of these tree forest samples were shown in Fig. S3.4.

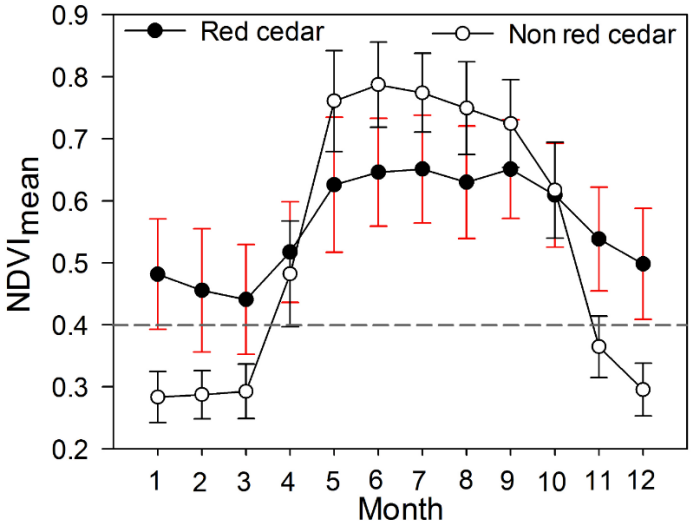

Figure 3.6 The monthly mean and standard deviation (SD) of NDVI of red cedar and non red cedar forests. These values were calculated based on the training ROIs over years of 2005-2010. The monthly mean and SD of NDVI of red cedar and other trees for individual years during 2005-2010 were shown in Fig. S3.5.

3.2.3.2 Algorithm of red cedar forest mapping

We have developed a decision classification algorithm for mapping forest based on 50m PALSAR mosaic data (Dong et al. 2012a), the integrated data of 50m PALSAR and MODIS (Qin et al. 2015a; Qin et al. 2016b), and the integrated data of 25m PALSAR and Landsat images (Chen et al. 2016). Previous studies showed forests, water, cropland, and other land cover types had different backscatter signature in HH, HV, HH/HV (Ratio), and HH-HV (Difference), which can be used to identify these land cover types (Chen et al. 2016; Dong et al. 2012a; Dong et al. 2012b; Qin et al. 2015a). We recalculated the frequency distributions of HH, HV, HH/HV and HH-HV for five main land cover types in this area (Fig. S3.7), based on 25m PALSAR data in 2010 and land cover samples (Fig. S3.8). To generate a forest and non-forest map, this study followed the PALSAR-based forest mapping algorithm using 25m PALSAR mosaic data in 2010 with updated thresholds of -16<HV<-8 & 2<Difference<8 & 0.3<Ratio<0.85 (Qin et al. 2016a). Then,

this PALSAR-based 25m forest map in 2010 was resampled to 30m to match Landsat spatial resolution. This forest map composed by red cedar and non red cedar types provided a baseline forest mask to overlay with the phenology characteristics from the time series Landsat data for the red cedar forest mapping.

A pixel and phenology-based algorithm was developed to map the red cedar forest in 2010 and five historical time periods. According to the analysis in section 2.3.1, Landsat images in winter were used to calculate the NDVI time series and generate the mean NDVI map in winter. The mean NDVI in winter larger than 0.4 was used to separate red cedar forest from other forest types.

In summary, we first produced the red cedar forest map in 2010 based on the 25m PALSAR data in 2010 and the Landsat-derived NDVI time series in the winter of 2010 using the rules of (1) -16<HV<-8, and 2 < Difference <8, and 0.3 <Ratio<0.85, and (2) the winter NDVImean>0.4. Second, following these rules, we produced the annual red cedar maps over 1984-2009 based on the 2010 PALSAR data and the annual time series Landsat data in the winter. Then, the annual red cedar maps were combined into 5 historical time periods using frequency combination to reduce the uncertainties caused by image quality or other factors. The 5 time periods were defined with 5 or 6 years as a group, including the late 1980s (1984-1989), early 1990s (1990-1994), late 1990s (1995-1999), early 2000s (2000-2004) and late 2000s (2005-2010). During each time period, we counted the number of individual pixels identified as red cedar based on the annual red cedar maps. A pixel with a number ≥ 3 (frequency $\geq 50\%$) was identified as red cedar. Third, the stand-age map of red cedar forest in 2010 was produced by examining the first red cedar occurrence time for individual pixels based on the red cedar map in 2010 and

the maps in five historical time periods. In this study, the 2010 PALSAR data was used to trace back the historical red cedar distribution, as long-term PALSAR data did not yet exist. We assumed that the 2010 PALSAR data provided the maximum red cedar distribution during 1984-2010, because the red cedar has encroached continuously into Oklahoma grasslands during recent decades (Williams et al. 2013; Zou et al. 2015).

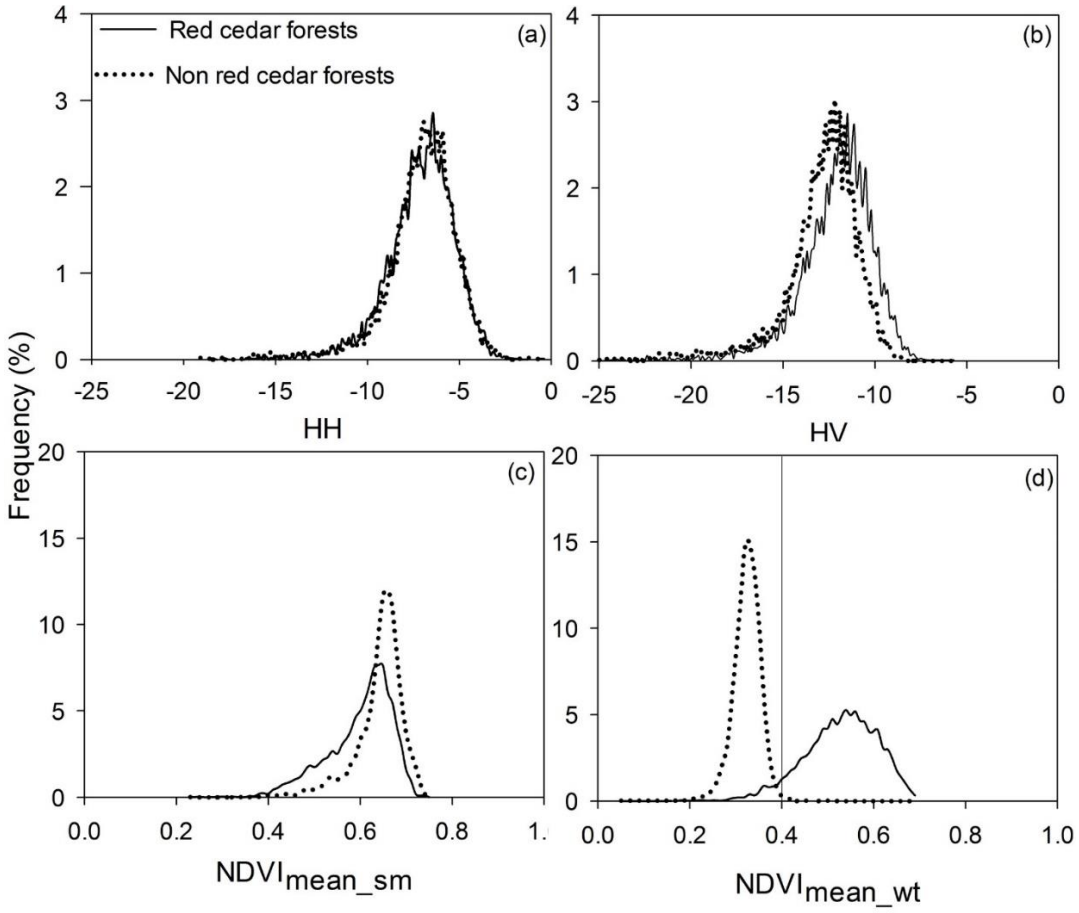

Figure 3.7 Frequency histograms of red cedar and non red cedar forests in 25m 2010 PALSAR (a) HH, (b) HV bands, and in the mean NDVI during (c) the summer and (d) winter of 2010. The solid line in (d) shows the threshold of 0.4 separating 95% of the red cedar pixels from 99% of the pixels of non red cedar forests. The statistics were based on the training regions of interests (ROIs) of red cedar and non red cedar forests.

3.2.4 Accuracy assessment of red cedar forest maps

A stratified random sampling design was used to acquire validation samples to estimate the accuracies of the red cedar forest maps. We stratified two classes of red cedar and non red cedar forests. Good practices for assessing accuracy of land cover changes suggested that the allocated sample size in each stratum in proportion to the area of the stratum can receive smaller standard errors for producer's and overall accuracies. At the same time, the comparison between user's versus producer's and overall accuracies should be considered by increasing the sample size in the rare classes (Olofsson et al. 2014). Non red cedar forest types occupied much larger areas than red cedar forests, therefore we collected more ROIs for non red cedar forests and increased the ROIs proportion of red cedar forests for good practices. The ROIs were collected manually through visual interpretation based on ground-truth photos and VHSR images in winter from GE. The validation ROIs were digitized after 1995, due to the available GE images in winter within the study area beginning in 1995. We collected validation ROIs for the year 2010 and three time periods of the late 1990s, early 2000s, and late 2000s. We acquired plots/pixels of red cedar and non red cedar forests of 24/5,072 and 43/7,326 in 2010, 44/4,877 and 34/6,853 over 2005-2010, 48/3,546 and 37/5,527 over 2000-2004, and 27/2,829 and 38/4,734 over 1995-1999, respectively. The ROIs of these four periods have different spatial distributions determined by the locations of the available GE images (Fig. S3.9a-d). Fig. S3.9e,f show the zoom-in landscapes of red cedar and non red cedar forests in winter from GE images. These ROIs were used to assess the accuracy of the red cedar maps in different periods. We calculated the adjusted accuracies and area estimates with 95% confidence intervals using the methods presented by Olofsson et al. (2013).

3.2.5 Comparison with other available red cedar datasets

The Oklahoma Ecological System Mapping (OKESM) project was launched in 2012, and finished by the summer of 2015 (Diamond and Elliott 2015). The OKESM map was produced to describe the current statewide vegetation distribution. This product was created based on multiple data sources of remote sensing, digital soils, slope, and streams using a decision tree classification approach. The remote sensing images used for the OKESM map were between Dec. 2010 and Aug. 2011 for the eastern regions of Oklahoma, and between Apr. 2013 and Jan. 2014 for the western regions of Oklahoma. It includes 165 vegetation types with 10m spatial resolution. The overall user's accuracy was 85%, according to the accuracy assessment with the ground-collected data (Diamond and Elliott 2015). This product can be downloaded freely from the Oklahoma department of wildlife conservation website (http://www.wildlifedepartment.com/facts_maps/ecoregions.htm).

We compared the 2010 red cedar map (PALSAR/Landsat-RC2010) with the optical image-based OKESM red cedar map in 2015 (OKESM-RC2015). In the OKESM map, the eastern red cedar appeared in multiple vegetation type legends including eastern red cedar forest, woodland, shrubland, and the mixed ecosystems of red cedar and other trees. The OKESM_RC2015 was generated by selecting the vegetation types related to the red cedar forest or woodland. We aggregated the 10m OKESM-RC2015 two-value map into a 30m OKESM-RC2015 percentage map. This comparison included two aspects: (1) the spatial distribution of red cedar and (2) the area assessment at the county scale. We visually compared the spatial differences of these two products at 30m spatial

resolution, and analyzed the area differences by linear regression. The areas were calculated based on these two products at the county level.

3.3 Results

3.3.1 The maps of eastern red cedar forest

We mapped *Juniperus virginiana* (eastern red cedar) distribution in 2010 and five historical periods from 1984 to 2010. Fig. 3.8 shows the resultant red cedar forest map (PALSAR/Landsat-RC map) in 2010. This map also shows the non red cedar forest extracted from the 2010 PALSAR-based forest map. The blank areas represented the non-forest areas which were not classified in this study. Within the study area, some counties had clear red cedar encroachment in 2010, including Caddo, Blaine, Deway, Logan and Payne counties. Fig. 3.9 shows the resultant red cedar maps during five phases from the late 1980s to the late 2000s, with an interval of five or six years. The forest of other trees shown in the five epoch maps were extracted from the 2010 PALSAR-based forest map.

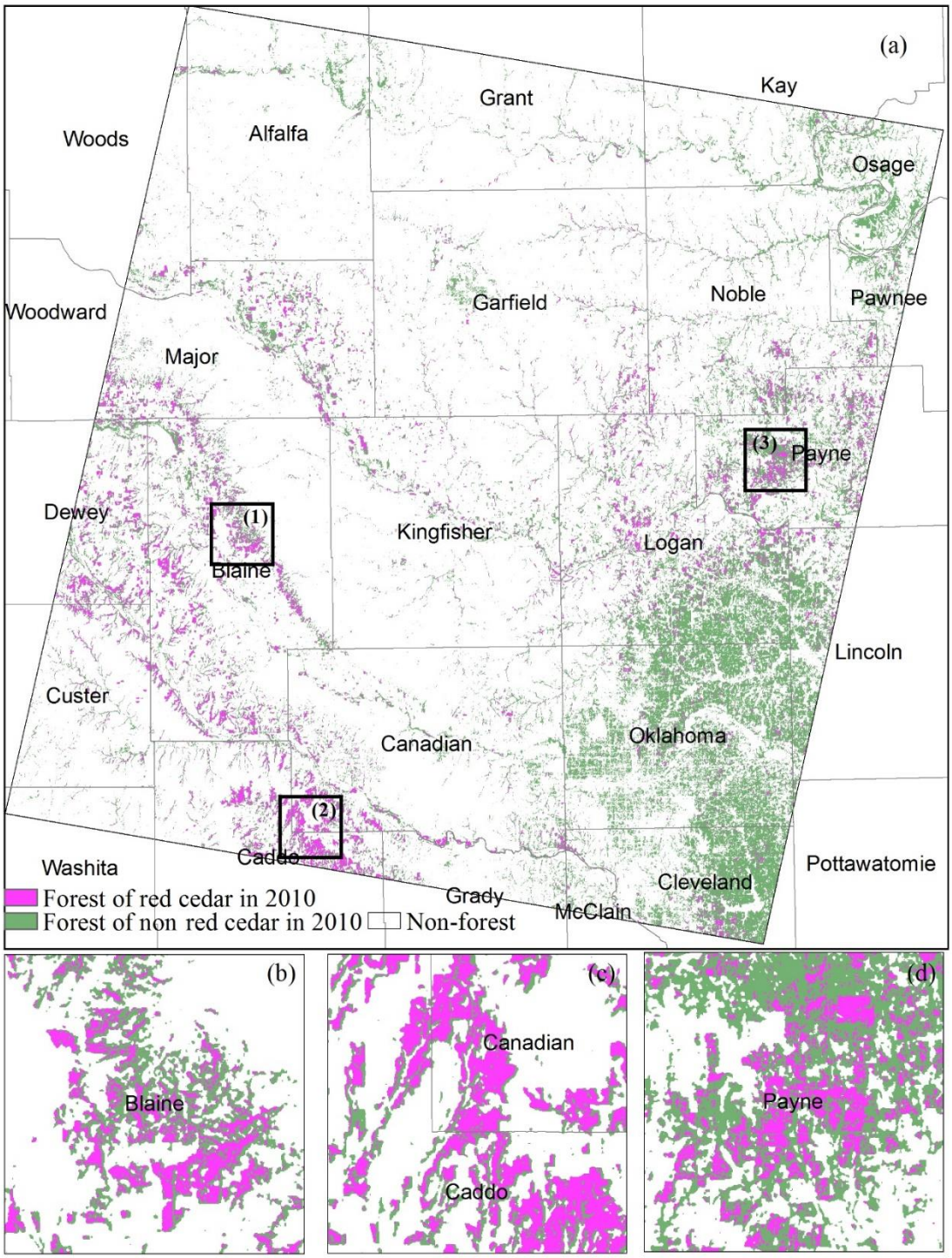

Figure 3.8 (a) The red cedar forest map in 2010. (b, c, d) are the zoom-in views of three regions labeled as 1,2,3 in (a), respectively.

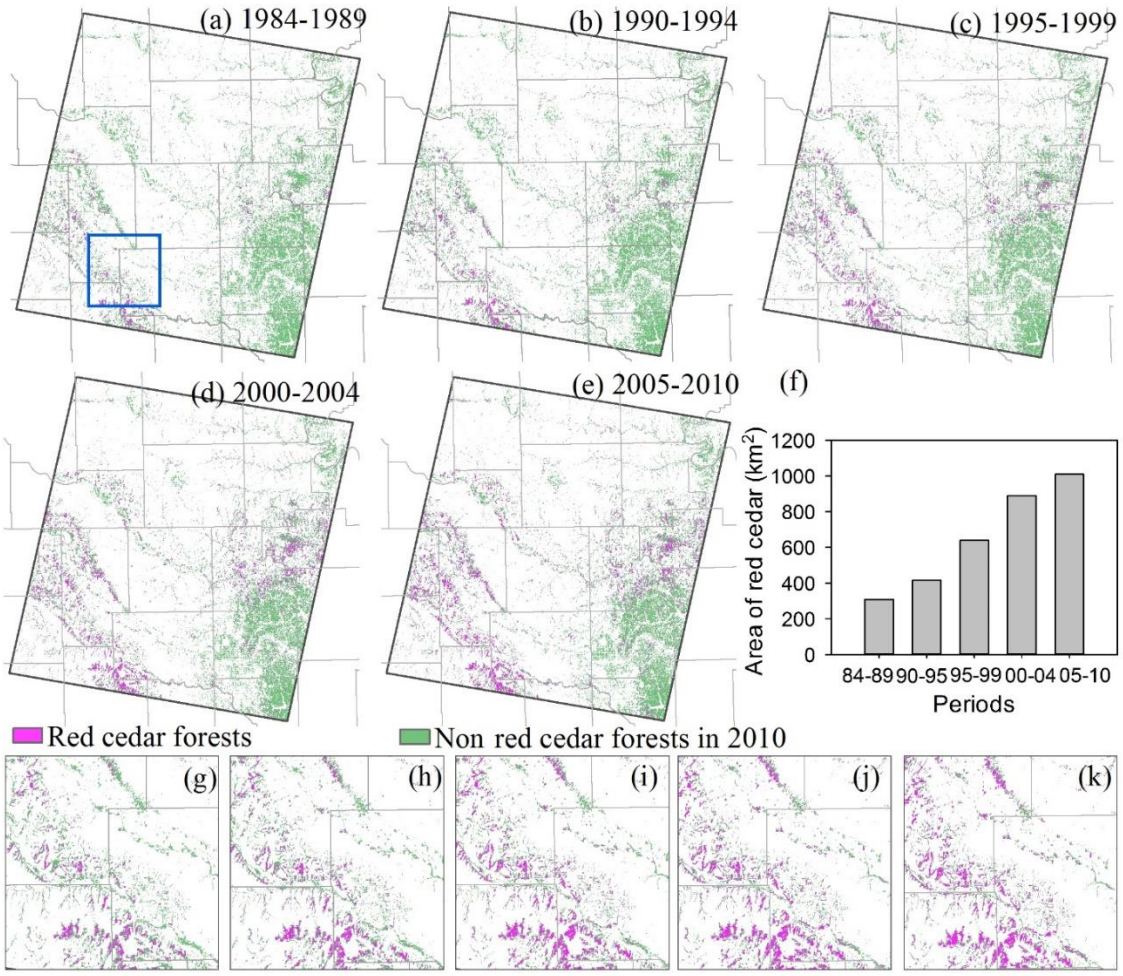

Figure 3.9 (a-e) The red cedar forest maps in five periods with 5-6 years as an interval. These maps showed the forest distribution in 2010 derived from the 2010 PALSAR data. (f) The red cedar areas in five different periods, (g-k) shows the zoom-in views for five periods from the late 1980s to the late 2000s for the region highlighted by the blue box in Fig. 3.9a.

3.3.2 Accuracy assessment

Accuracy assessments of these resultant maps was conducted for 2010 and three time periods of the late 1990s, early 2000s and late 2000s using the validation ROIs introduced in Section 2.4 (Fig. S3.9). The accuracy of the maps in the late 1980s and early 1990s was not assessed, because the VHSR images for validation from GE were not available until 1995. The assessment results demonstrated that the red cedar and non red

cedar maps had reasonably good accuracies (Table 3.1). The overall accuracies (OA) were 96%, 95%, 94% and 95%, and the Kappa coefficients were 0.91, 0.86, 0.88 and 0.91 in 2010, the late 2000s, early 2000s, and the late 1990s, respectively. The red cedar category had producer accuracies (PA) of 93%, 90%, 88%, and 90%, and user accuracies (UA) of 97%, 96%, 98%, and 99% in these resultant maps. This result suggested that the red cedar maps in different periods of time were comparable with each other, and it was possible to monitor red cedar encroachment from 1984 to 2010 based on the PALSAR/Landsat-RC maps in the five epochs.

The accuracies of PA, UA and OA were adjusted according to the mapped areas of red cedar and non red cedar forests (Table S3.1). These maps achieved adjusted OAs of 0.94-0.96. The red cedar type in these maps have adjusted PAs between 0.78 and 0.89, and adjusted UAs between 0.96 and 0.99. We estimated the red cedar forest areas in 2010, late 2000s, early 2000s and late 1990s with 95% confidence interval margins based on the validation ROIs. The adjusted areas increased from about 811 km^2 in the late 1990s to 1236 km^2 in 2010 (Table S3.1).

Table 3.1 Accuracy assessment of red cedar forest maps based on the validation regions of interests (ROIs) from field photos, and Google Earth images in different periods. More information about the ROIs was shown in Fig. S3.9.

Periods		Ground truth pixels in each period		Classified pixels	User Accuracy (UA)
		Red cedar	Non red cedar		
2010	Red cedar	4698	141	4839	97%
	Non red cedar	374	7185	7559	95%
	Ground truth pixels	5072	7326	12398	OA=96%
	Producer accuracy (PA)	93%	98%		Kappa=0.91
2005-2010	Red cedar	4402	170	4572	96%
	Non red cedar	475	6683	7153	93%
	Ground truth pixels	4877	6853	11730	OA=95%
	Producer accuracy (PA)	90%	98%		Kappa=0.86
2000-2004	Red cedar	3190	61	3170	98%
	Non red cedar	437	5466	5903	92%
	Ground truth pixels	3546	5527	9073	OA=94%
	Producer accuracy (PA)	88%	99%		Kappa=0.88

1995-1999	Red cedar	2553	29	4414	99%
	Non red cedar	276	4705	4407	94%
	Ground truth pixels	2829	4734	8821	OA=95%
	Producer accuracy (PA)	90%	99%		Kappa=0.91

3.3.3 Dynamics of red cedar encroachment and stand age analysis

In this chapter, *stand age* refers to the years of the eastern red cedar in each individual pixel after identified as forest based on Landsat images. There was significant red cedar encroachment in the study area from 1984 to 2010 according to the PALSAR/Landsat-RC maps (Fig. 3.9a-e) and the mapped red cedar area analysis (Fig. 3.9f). In the late 1980s, red cedar in the study area occupied ~300km^2. Then, the red cedar encroached slightly during the early 1990s, reaching an area of ~400km^2. The red cedar encroachment mainly happened in the counties of Caddo, Blaine, Dewey and Payne counties during this period. In the late 1990s, the red cedar expanded into Logan, Major and Canadian counties and the area increased to ~600km^2. Then, the red cedar continuously encroached in these counties during the 2000s, and the area reached ~900km^2 in the early 2000s and ~1000km^2 in the late 2000s. The PALSAR/Landsat-RC maps in the five historical time periods showed a continuous encroachment of red cedar, with the most significant encroachment occurring in the late 1990s and early 2000s. During the entire period of 1984-2010, the annual red cedar encroachment rate was about 8%. Further analysis of the geographical patterns of the red cedar encroachment at the county level was presented in supplementary data TS1 and Fig. S3.10.

The stand-age map of the red cedar forest in 2010 was generated by overlaying the historical red cedar forest maps in five time periods (Fig. 3.10a). Fig. 3.10d shows the percentage distributions of red cedar forest with different years after identified as forest including 1-5 (~20%), 6-10 (~23%), 11-15 (~22%), 16-20 (~11%) and larger than 20

(~24%) years old. Most of the red cedar forest (~57%) had a stand age larger than 10 years old, which agreed with the significant red cedar encroachment during the 1990s. 23% of the red cedar forest had a stand age of 6-10 years, and 20% of that had a stand age of less than 5 years, which coincides with the red cedar encroachment shown in the 2000s.

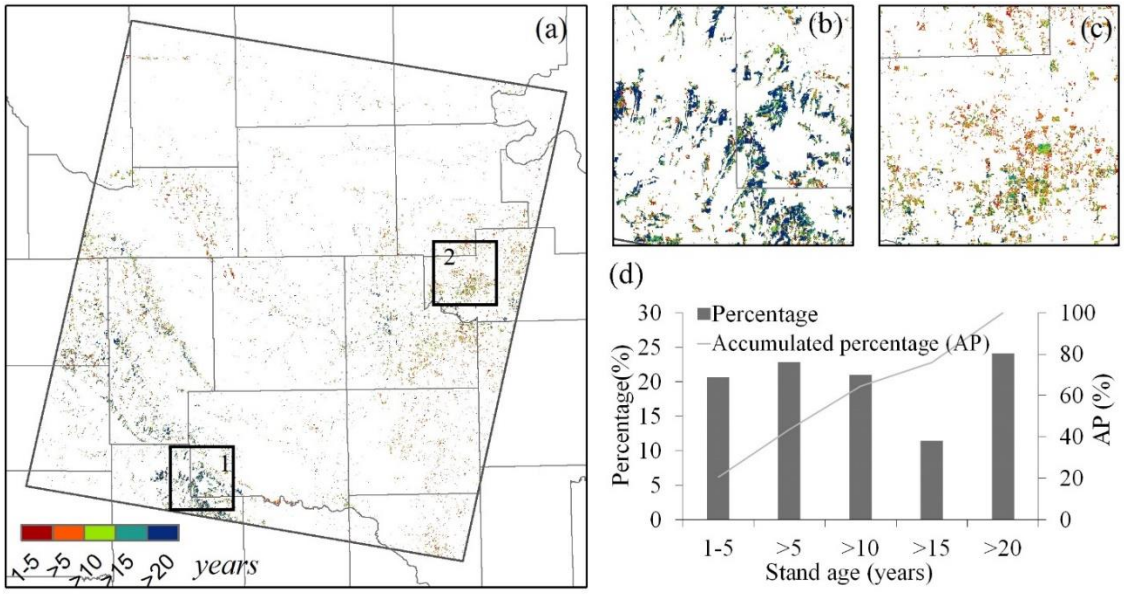

Figure 3.10 The years of eastern redcedar identified as forest (stand age map) (a) and two zoom-in views (b, c) for the case regions shown in black boxes of 1, 2 in (a). (d) shows the stand-age histogram of the red cedar forest in 2010.

3.3.4 A comparison of the PALSAR/Landsat-RC map with the OKESM-RC map

We compared the 2010 PALSAR/Landsat-RC map with the optical image-based red cedar map derived from the OKESM in 2015 (Fig. 3.11). The spatial distributions of the red cedar in these two maps were visually in high agreement (Fig. 3.11a and Fig. 3.11b). The red cedar areas derived from the two maps at county level had a significant linear relationship, with R^2 of 0.93 (Fig. 3.11c). The slope of 1.34 indicates that there is moderate difference in red cedar forest area estimates between these two map products

for our study area. Therefore, one case region (black boxes in Fig. 3.11a,b) was selected for zoom-in analysis on these two maps. The red cedar forest distributions derived from the two maps for the case region were shown in Fig. 3.11d,e. By comparison, we can see some inconsistent patches of red cedar in this case region. Therefore, another zoom-in view (black boxes in Fig. 3.11d,e) was selected for analysis based on the GE images. Fig. 3.11f and Fig. 3.11g show the red cedar distributions (pink areas) in the zoom-in view extracted from the PALSAR/Landsat-RC2010 map and the OKESM-RC2015 map, respectively. The background of Fig. 3.11f,g used the same image on 03/23/2011 from GE. This zoom-in view comparison revealed that OKESM-RC2015 missed some red cedar forests, which may result in some discrepancies of red cedar area estimations between these two products. The overall accuracy of 85% was reported for the OKESM map, but the specific accuracy for the red cedar forest in this area is unknown. In addition, the 2010 PALSAR/Landsat-RC map was developed based on the Landsat images from Dec. 2010 to Feb. 2011, while the OKESM-RC map was developed based on the images from 2013-2014. A real difference of red cedar forest cover in these two periods may exist, and it could contribute to the inconsistency between these two maps.

3.4 Discussion

3.4.1 Source errors of red cedar forest map in 2010 from PALSAR and Landsat images

It is a challenge to classify pixels with mixed vegetation types in land cover mapping or thematic object extractions (Gong et al. 2013; Herold et al. 2008; Sterling and Ducharne 2008). Considering the red cedar trees within each individual pixel, canopy coverage and tree height determined the classification accuracy in this study. This could be explained by the remote sensing data. The backscatter signals of low frequency SAR

(e.g. PALSAR) are related to the three dimensional structures (including crown and height) of forest (Cloude and Papathanassiou 2003). VIs developed from optical data were more sensitive to the canopy cover (Shimada et al. 2014a). These two factors have been confined in most of the forest definitions (FAO 2012; Friedl et al. 2010; Liu et al. 2005; Qin et al. 2015a; Shimada et al. 2014a). However, studies to quantitatively evaluate the roles of these two factors on the classification accuracy at the sub-pixel level are lacking. This study used the FAO definition of forests as lands with tree canopy coverage larger than 10%. The recognition capabilities of 2010 PALSAR/Landsat-RC map at different coverage levels of red cedar canopy in individual pixels is uncertain. The VHRS images from GE and the National Agriculture Imagery Program (NAIP) clearly show tree canopy coverage on the ground surface. We selected three case regions using the simple random design based on these VHRS images, and each region had an extent of about 1km×1km (Fig. 3.12a). The red cedar canopies were digitalized at individual pixels by visual interpretation based on the GE images in winter (Fig. 3.12b, Fig. S3.11). The boundaries of each pixel with shapefile format were obtained by generating a 30m fishnet based on the PALSAR/Landsat-RC maps. Then, we calculated the coverage of red cedar canopy within each individual pixel, and examined whether the specific pixel was recognized or not in the PALSAR/Landsat-RC maps. Fig. 3.12c shows the recognition capability of the 2010 PALSAR/Landsat-RC map at different coverage levels of red cedar trees within each pixel. There was 90% probability to recognize the pixels with red cedar coverage higher than 60%, and this probability decreases with decreasing red cedar coverage (Fig. 3.12c). There was 30% recognition probability in the sparse areas with red cedar canopy coverage ranging 10%-20%. One possible reason was that the unrecognized

pixels with red cedar coverage higher than 10% may have low red cedar height, which cannot be characterized as forests. Another explanation might be that red cedar forests were young with low backscatter signals. Previous studies showed that PALSAR-based forest products had good performance identifying mature forests, but it is possible to omit the sparse and/or low-height forests and woodlands (Qin et al. 2016b; Shimada et al. 2014a). If additional data becomes available, further studies will be conducted to evaluate the performance of the PALSAR/Landsat-RC maps with red cedar height, density, or biomass gradients at the sub-pixel scale.

3.4.2 Uncertainly analysis of red cedar forest stand age maps during 1984-2010 from Landsat images

The accuracy of mapping the dynamics of red cedar encroachment into grasslands could be potentially affected by factors within the data and algorithm. It is a challenge to collect good quality data within the phenological window of time to map the annual red cedar distribution and validate the results (Fig. 3.3, Fig. S3.2). Although the pixel-based algorithm increased the information input, amounts of pixels were short of sufficient good observations at annual scale, and the data availability showed significant inter-annual variations (Fig. 3.3, Fig. S3.2). The quality of input images (Gong et al. 2013) and the uneven availability of Landsat images at temporal and spatial scales (Hansen et al. 2016b) posed significant challenges to land cover mapping. Therefore, we produced multi-year red cedar maps in time periods of 5 or 6 years to reduce the uncertainties caused by the data availability.

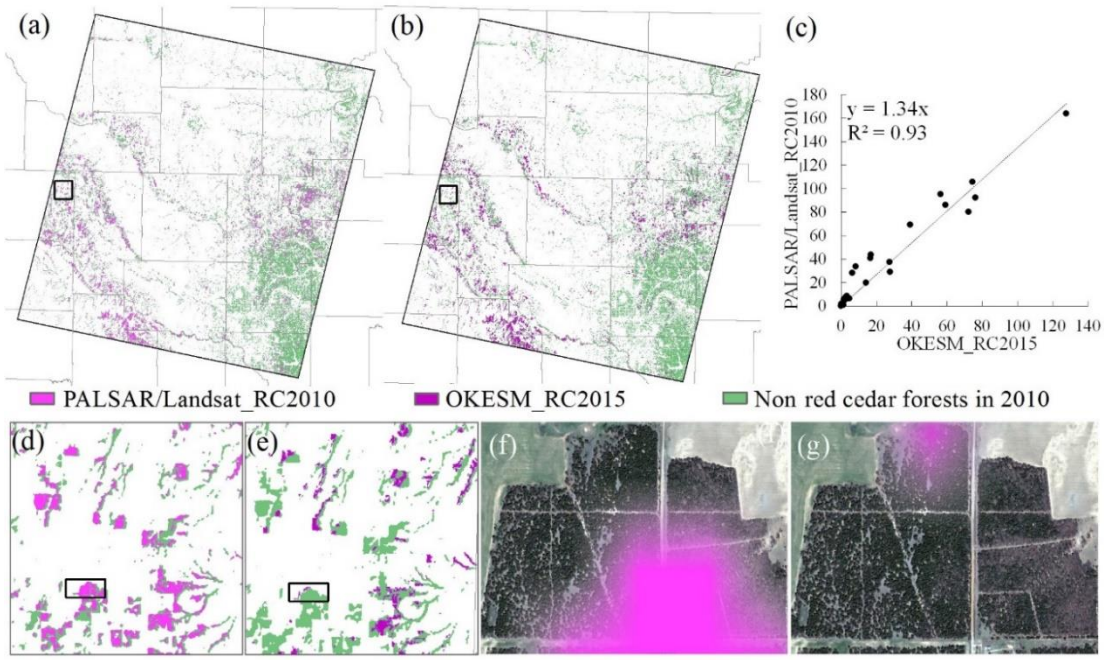

Figure 3.11 The comparison of the 2010 red cedar forest map produced in this study (PALSAR/Landsat_RC2010, Fig. 3.11a) and the red cedar map from the Oklahoma Ecosystem Map in 2015 (OKESM_RC2015, Fig. 3.11b). (c) Area comparison of PALSAR/Landsat_RC2010 and OKESM_RC2015 at the county level. (d) The zoom-in view of the region shown in black box in Fig. 3.11a. (e) The zoom-in view of the region shown in black box in Fig. 3.11b. (f) the zoom-in red cedar map from PALSAR/Landsat_RC2010 for the case region in Fig. 3.11d. (g) the zoom-in red cedar map from OKESM_RC2015 for the case region in Fig. 3.11e. The background of Fig. 3.11f,g was the Google Earth image on 03/23/2011. The pink areas in Fig. 3.11f, g show the red cedar forests from maps of PALSAR/Landsat_RC2010 and OKESM_RC2015, respectively.

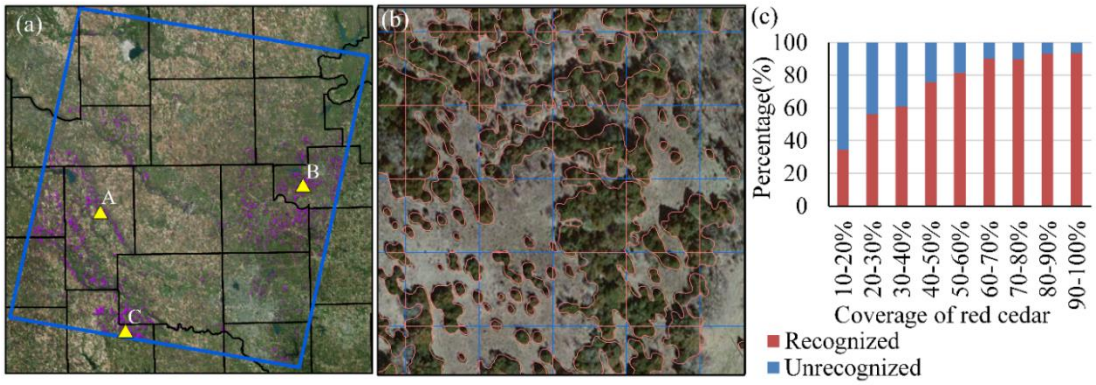

Figure 3.12 (a) Spatial distributions of three sample regions with total number of 2838 pixels. The red cedar canopy within each pixel was visually drawn (Fig. S3.11). (b) The zoom-in visual interpretation of red cedar canopy in each pixel. (c) The percentage of recognized and unrecognized red cedar pixels at different pixel-based red cedar coverage levels.

Accuracy assessments of the red cedar maps had some uncertainties resulting from the limited ground truth data and available VHSR images over time. We only evaluated the red cedar maps in three time periods, the late 1990s, the early 2000s, the late 2000s and the one in 2010. The accuracies of red cedar maps in the late 1980s and the early 1990s were still uncertain, although red cedar distribution patterns agreed with the maps produced by survey questionnaires (Engle et al. 1996). In addition, the spatial distributions of validation ROIs (Fig. S3.9) for different time periods were confined by the available VHSR images. For example, the ROIs in 2000-2004 (Fig. S3.9c) were only obtained in the eastern part of the study area, therefore some uncertainties may be caused in the accuracy assessment by the incomprehensively spatial representatives of the validation ROIs.

The phenology feature of red cedar trees having green foliage in the winter is also true for other evergreen trees. Due to the differences from canopy structure, leaf compositions, and phenological phases, the threshold used in this study could exclude some evergreen trees, but could not eliminate the confusions caused by the species with similarly spectral signature (Friedl et al. 2010; Herold et al. 2008). In this study, the commission errors did not affect the resultant maps too much (Table 3.1), which could be explained by the tree compositions in the grassland ecosystem as discussed in Section 3.4.3.

3.4.3 Potential for mapping long-term red cedar encroachment at regional scale

This study presented the potential of mapping the dynamics of red cedar encroachment to grassland at the regional scale through combining PALSAR data and time series Landsat data by using a pixel and phenology-based algorithm. Although the

red cedar forest maps in the late 1980s and early 1990s were not validated, these maps showed consistent red cedar distribution with the maps obtained by survey questionnaires in 1985 and 1995 (Engle et al. 1996). These two resultant maps also showed the eastern red cedar expanded along river drainages, which provides remote sensing evidence for the study by Engle et al. (1996). The red cedar forest maps in other periods had reasonable producer accuracies of 88%-93%. The successful practice in this study could be explained by data availability, algorithm, and vegetation types.

The L-band PALSAR images have shown good performance on mapping forest (Shimada et al. 2014a) and plantations (Chen et al. 2016; Dong et al. 2013b; Miettinen and Liew 2011). The release of 25m PALSAR mosaic images offered improved spatial resolution datasets for forest mapping (Shimada et al. 2014a). The Landsat data provided a long term (since the 1970s) data source at 30m spatial resolution for time series analysis (Woodcock et al. 2008; Wulder et al. 2012). Using all good observation data of individual pixels from both the TM and ETM+ images improved the description of phenology information (Dong et al. 2016; Dong et al. 2015b) and increased the temporal range of the study. The GEE platform facilitated the collection and processing of all the surface reflectance data from 1984 to 2011. A recent study on paddy rice mapping has shown the efficient capability of the GEE platform for the land cover mapping based on thousands of images (Dong et al. 2016).

The different phenological characteristics between red cedar trees and other trees (e.g. oaks) in the study area could be represented by vegetation indices of NDVI/EVI/LSWI (Fig. 3.5, Fig. 3.6). For example, in the winter, the red cedar trees have canopies with green leaves, while other dominant trees have significant defoliation. Thus,

the red cedar can be identified effectively with the images in the winter. Based on this analysis, this study proposed the pixel- and phenology-based algorithm with all good observations of Landsat 5/7 at a given pixel as input. This algorithm has better potential for time series analysis than traditional image- and statistics-based algorithms for two major reasons: (1) pixel-based algorithms increase the data input to describe the phenology (Fig. S3.2), and (2) phenology-based algorithms can be used repeatedly at a given area with similar climate and ecosystem types over time (Dong et al. 2015b; Zhong et al. 2014b).

Deciduous forest and prairies, which include tall, mixed, and short grasses, are two plant communities in western Oklahoma (Bruner 1931). This study examined the dynamics of red cedar encroachment into native grasslands in the ecotone between deciduous forests and grass prairie. Red cedar trees had unique phenology spectra which differed from that of the dominant deciduous trees. Therefore, the phenological characteristics of red cedar and deciduous trees could be successfully used to map the red cedar forest in grassland regions by remote sensing images using the phenology-based algorithm in this study.

3.4.4 Implications for extensive applications and future development

To our knowledge, this is the first attempt to monitor the dynamics of red cedar encroachment to native grasslands using remote sensing approaches at the regional scale. The pixel- and phenology-based algorithm based on PALSAR and time series Landsat images may have the potential to be applied widely (1) to other grassland regions, and (2) to extract other invasive tree species by adjusting the threshold used in this study. Detailed and long-term red cedar maps provide important data sources for the management of

grasslands, and for the exploring of causes and consequences of woody plant encroachment at the regional scale (Barger et al. 2011; Gavier-Pizarro et al. 2012; Ge and Zou 2013; Turner et al. 2003). Currently, this work was limited at both the spatial extent and the temporal range. We will apply this approach to map the dynamics of red cedar encroachment across the grasslands in Oklahoma and the Southern Great Plains. The release of the PALSAR2 data (Shimada et al. 2014a) provides an opportunity to map the red cedar patterns after 2010. Limited by the quality and quantity of the input data, this study produced the multi-year red cedar maps. The annual red cedar time series maps could be generated in the future through improving the mapping algorithms and using more data sources (e.g. Landsat 8, Sentinel-2).

3.5 Conclusion

Woody plant encroachment is occurring globally in multiple ecosystems, especially in the grassland of the Southern Great Plains of the USA. The lack of long-term red cedar maps at the regional scale severely limits our understanding of the ecosystem and climate feedbacks on woody plant encroachment, rangeland management and biodiversity conservation. Landsat data provided the possibility to trace back the regional land cover changes to the 1980s at 30m spatial resolution. This study integrated 4,233 Landsat 5/7 images from 1984 to 2010 with the PALSAR data in 2010 to monitor the red cedar dynamics in the central region of Oklahoma by a pixel and phenology-based algorithm. The Landsat-based time series vegetation indices can capture the phenological differences of red cedar and other trees, which facilitated the red cedar mapping in this study. The moderate spatial resolution images of Landsat and PALSAR had good performance to identify the regions with red cedar coverage larger than 50%, and the

identification capability reduced with the decreasing of red cedar coverage. The uneven image qualities at spatial and temporal scales and algorithm could cause some uncertainties that occurred on the resultant red cedar maps. Further studies are needed to apply this pixel- and phenology-based algorithm using PALSAR and time series Landsat images to other grassland regions.

Supplementary materials

Text S3.1 Geographical patterns of red cedar encroachment

For the entire study area (~28,303 km^2), the red cedar coverage increased at an annual rate of ~8% (~25km^2/year) during 1984-2010. The time series maps in Fig. 3.9a-e show the red cedar encroachment in the study area had significantly spatial patterns. According to the boundaries of the study area and counties, we calculated the red cedar coverage maps in five historical time periods (Fig. S3.10a-e) and the annual encroachment rate map of red cedar forest during 1984-2010 (Fig. S3.10f) to examine the geographical patterns of red cedar encroachment at the county level. In the late 1980s, majority of counties had red cedar coverage less than 2%. Only the counties of Dewey, Blain and Caddo had higher coverage larger than 2%. In the 1990s, all the counties within the study area had increased red cedar coverage and the coverage was over 2% in Logan, Major and Canadian, and over 4% in Payne and Blaine, and over 6% in Dewey and Caddo. In the 2000s, the red cedar coverage was over 8% in Dewey, Caddo and Payne, and the counties of Custer, Lincoln, and Cleveland also showed significant increase. The annual rate of red cedar encroachment varied among counties from less than 10% to higher than 40% (Fig. S3.10f). Compared with the red cedar coverage maps, the annual encroachment rate map showed a different geographical pattern with highest encroachment rates

occurred in counties of Woods, Oklahoma and Cleveland. The counties of Caddo and Dewey with highest red cedar coverage had lower annual encroachment rates of less than 10%. Most of the counties experienced eastern redcedar spread at an annual rate of less than 10% (Fig. S3.10f), consistent with the red cedar encroachment magnitude of 2% reported in the Loess Canyons region of Lincoln County, Nebraska (Walker and Hoback 2007). Over 20-year data at the Konza prairie biological station in Kansas suggested that woody plant abundance increased by a range of two to 40-fold under different fire and grazing regimes. Due to the expansion of woody plants in grasslands have to do with the changes of resource availability and disturbance regimes (Briggs et al. 2005), woody plant encroachment had substantial spatial difference. More studies on driven factors are imperative to explain the geographical patterns of the red cedar coverage dynamics and the annual encroachment rate at the county level.

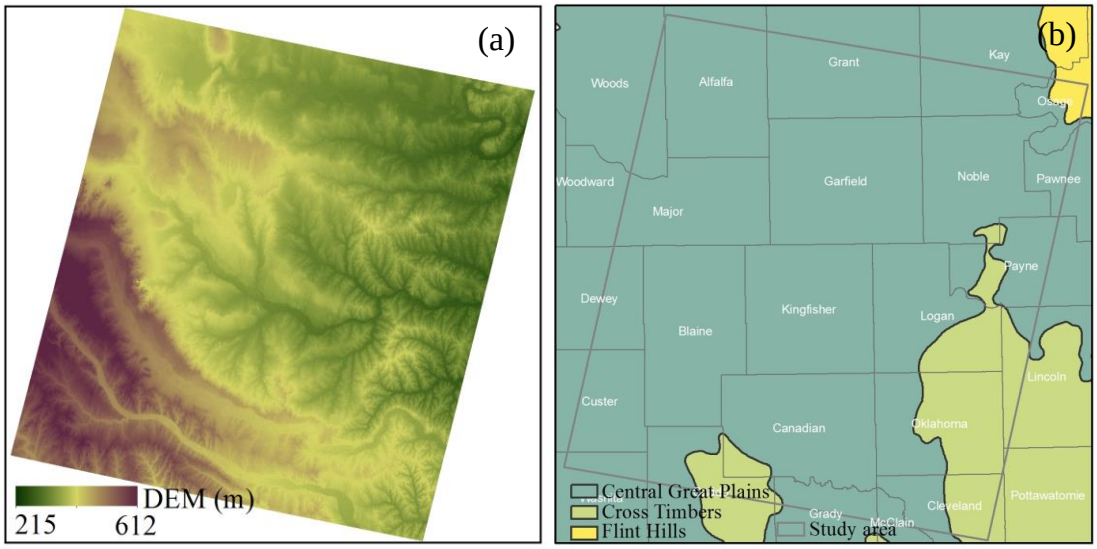

Figure S3.1 (a) The Digital Elevation Model (DEM), and (b) the ecoregions in the study area.

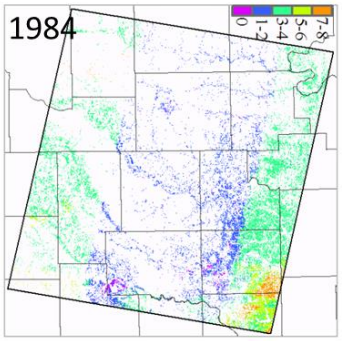
1984
0
1-2
3-4
5-6
7-8
9-11

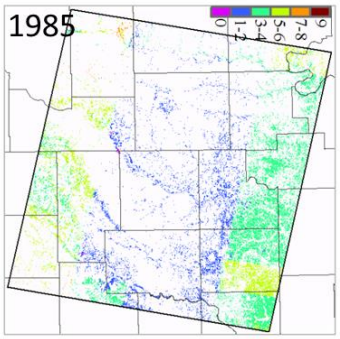
1985
0
1-2
3-4
5-6
7-8
9-11

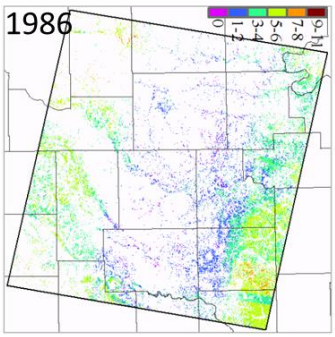
1986
0
1-2
3-4
5-6
7-8
9-11

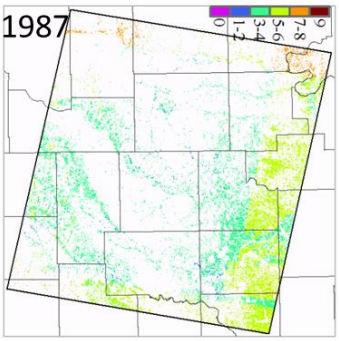
1987
0
1-2
3-4
5-6
7-8
9

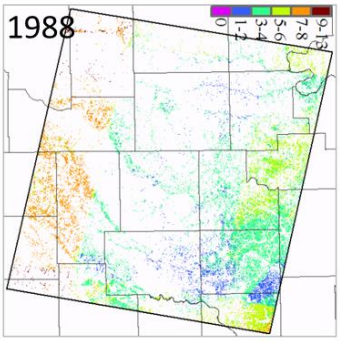
1988
0
1-2
3-4
5-6
7-8
9-13

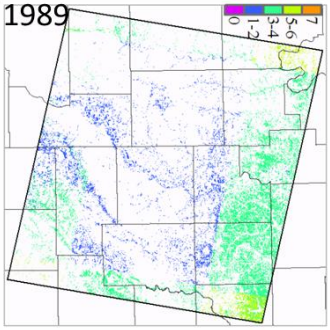
1989
0
1-2
3-4
5-6
7

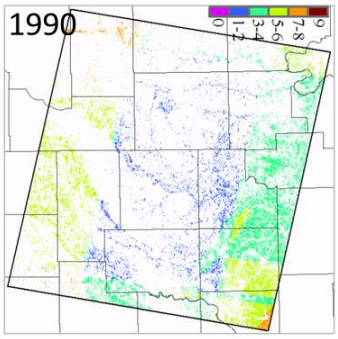
1990
0
1-2
3-4
5-6
7-8
9

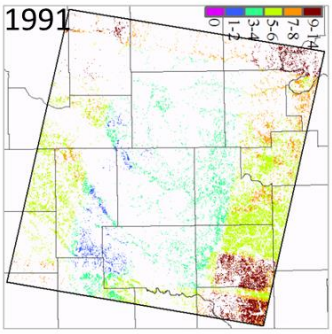
1991
0
1-2
3-4
5-6
7-8
9-14

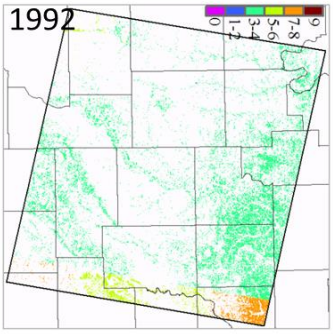
1992
0
1-2
3-4
5-6
7-8
9

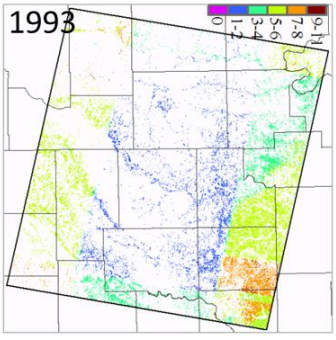
1993
0
1-2
3-4
5-6
7-8
9-14

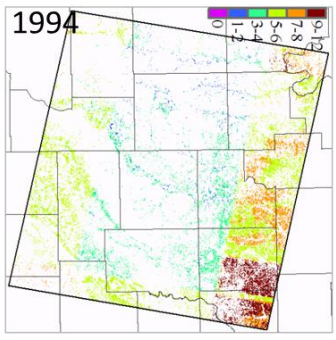
1994
0
1-2
3-4
5-6
7-8
9-12

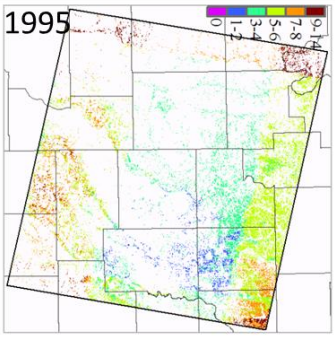
1995
0
1-2
3-4
5-6
7-8
9-14

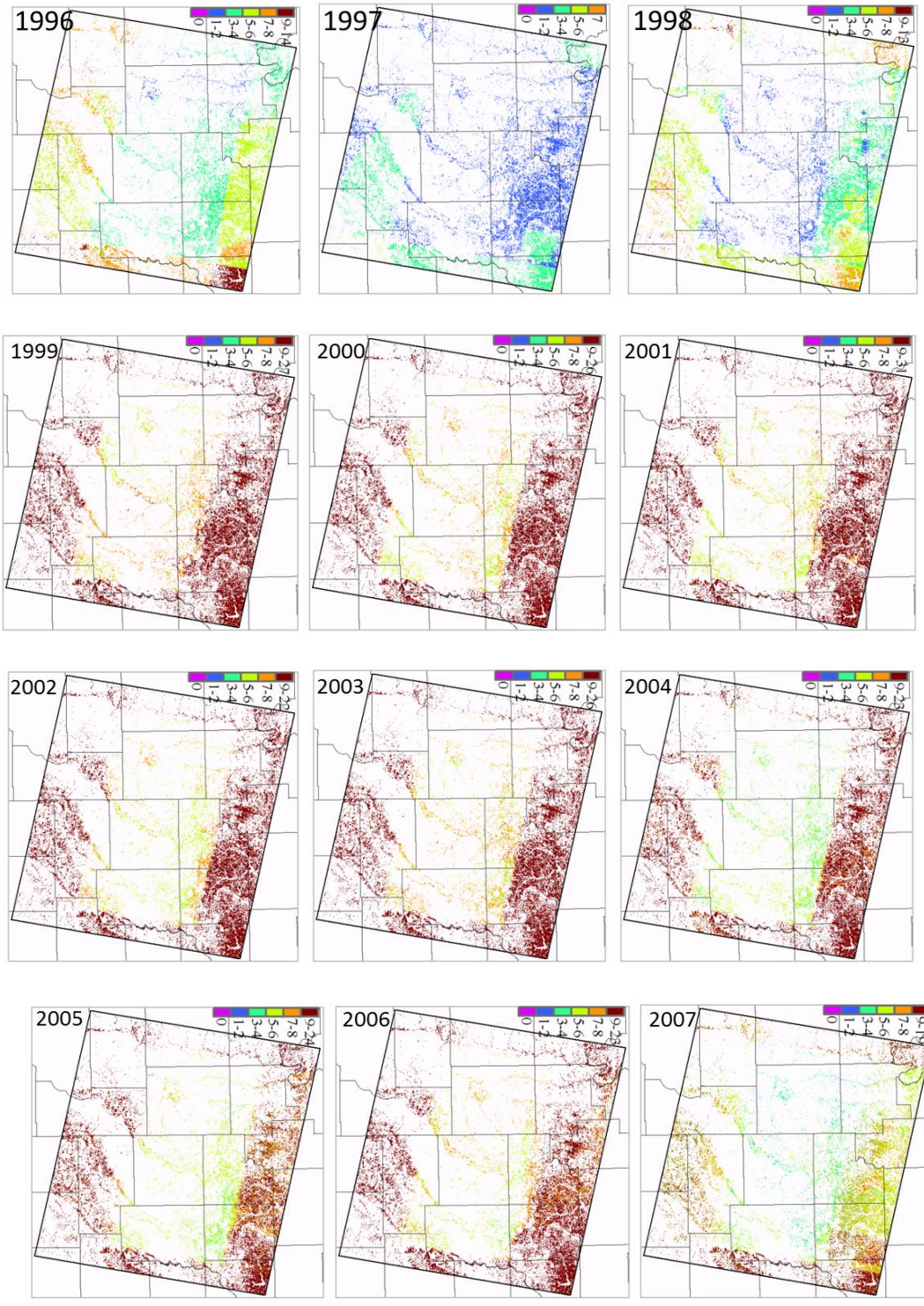
1996
1997
1998
1999
2000
2001
2002
2003
2004
2005
2006
2007

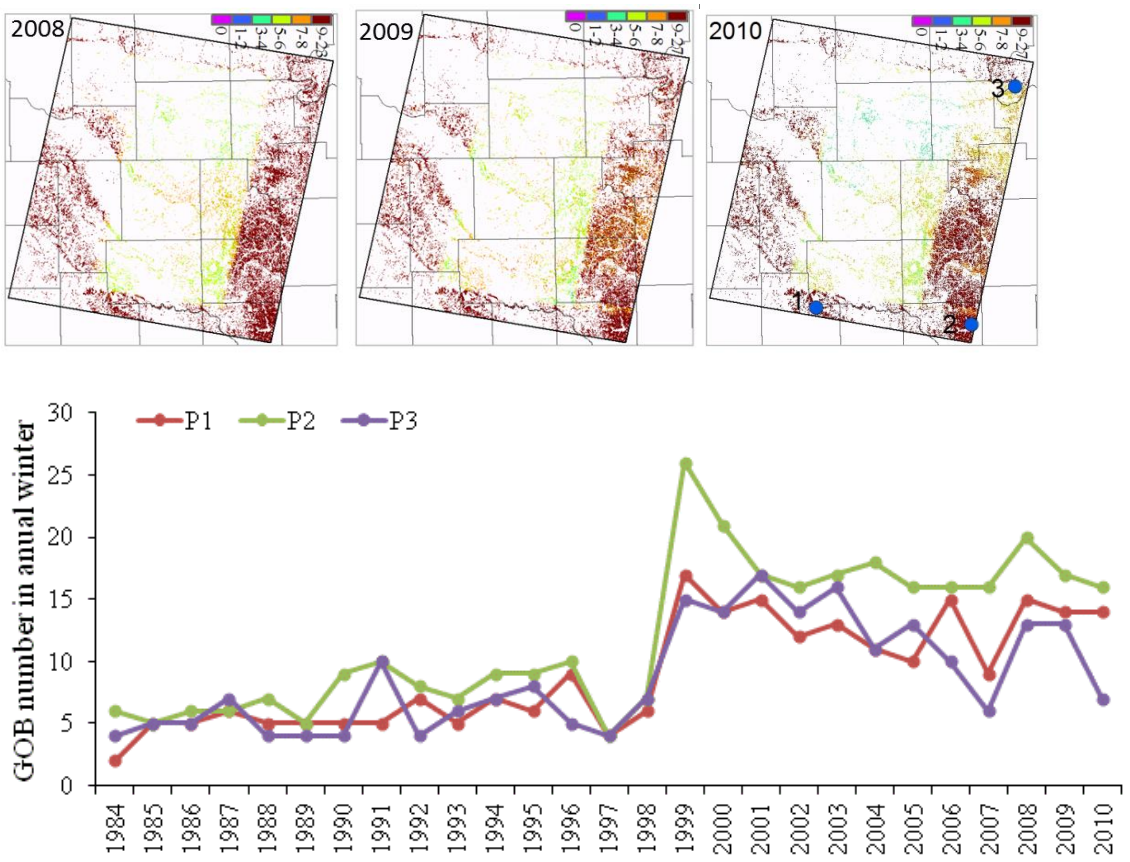

Figure S3.2 Good observation (GOB) number for individual pixels during the winter of each year from 1984 to 2010. The 2-D line figure shows the GOB number in annual winter for three sample points. Their locations were labeled by blue points in the 2010 figure about GOB number.

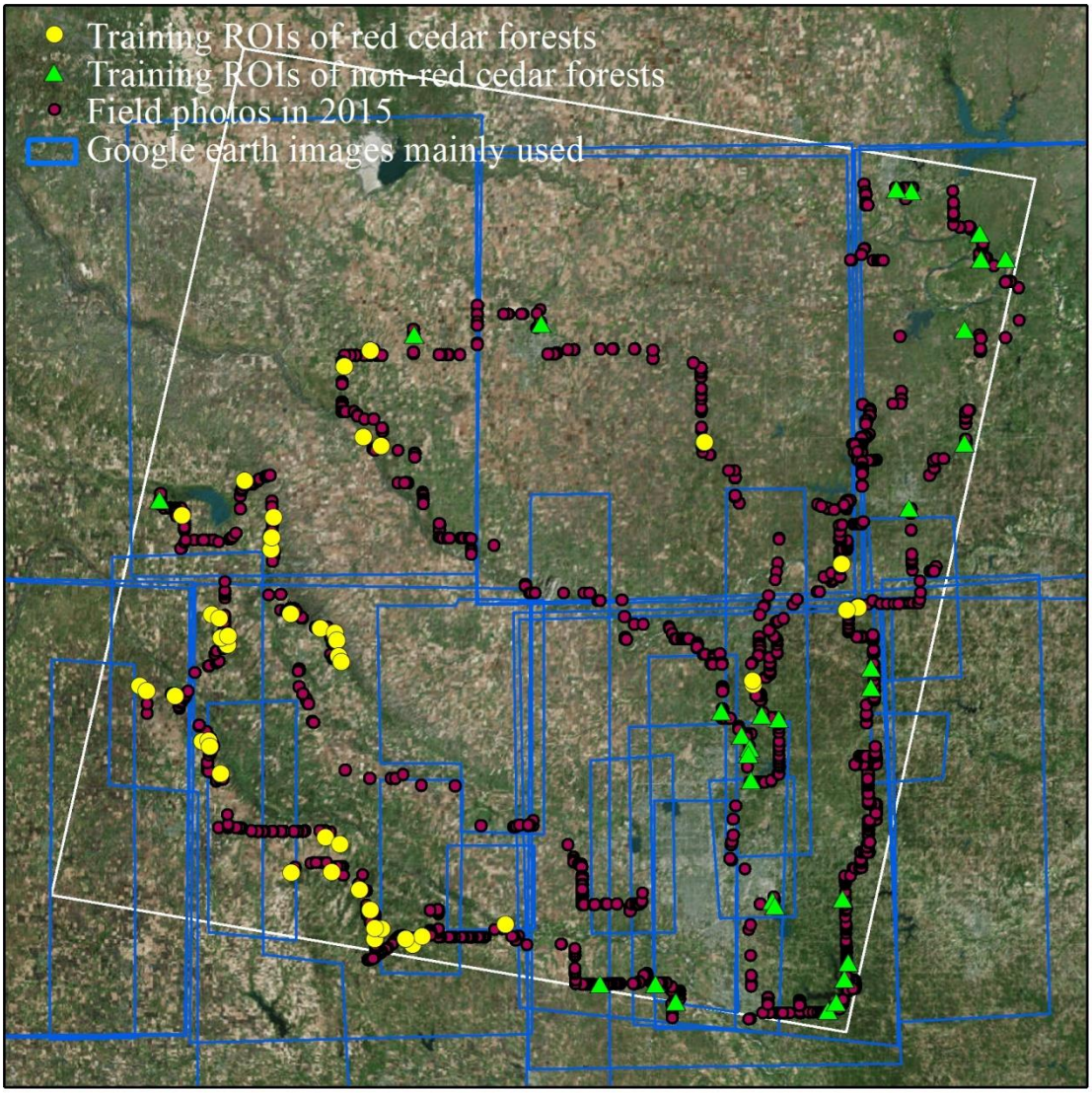

Figure S3.3 Spatial distributions of the training regions of interests (ROIs) for red cedar and non red cedar forests.

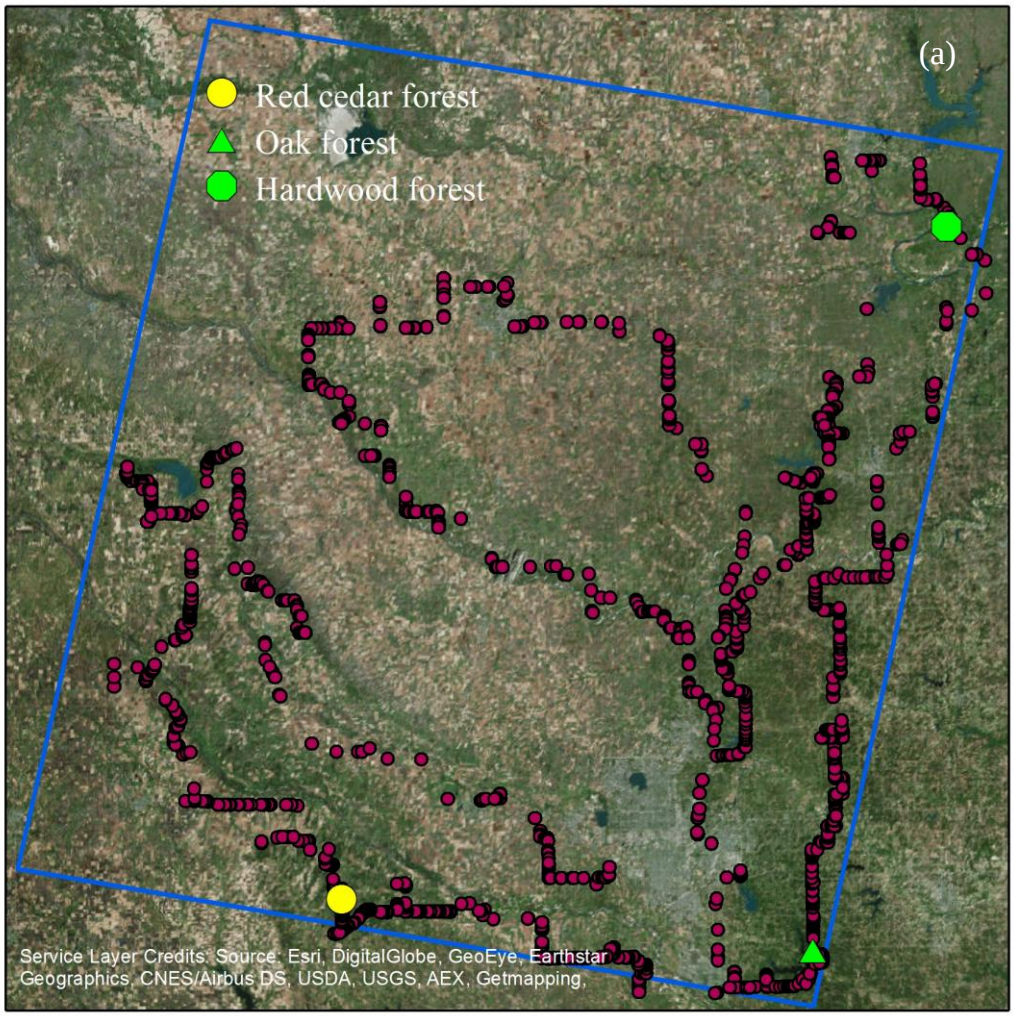
(a)
Red cedar forest
Oak forest
Hardwood forest
Service Layer Credits: Source: Esri, DigitalGlobe, GeoEye, Earthstar Geographics, CNES/Airbus DS, USDA, USGS, AEX, Getmapping,


(b)


(c)

Figure S3.4 The locations of three forest sites of red cedar (-98.2531°, 35.3574°), oak (-97.2134°, 35.2535°), and bottomland hardwood (-96.883, 36.559). It also shows the field photos taken in 2015 in the study area. (b, c, d) The zoom-in landscapes in the Google Earth image (03/01/2011) for three forest sites, respectively. (e, f, g) The field photos taken at three sites in the November 2015. Red cedar forest (b, e), oak forest (c, f), and bottomland hardwood forest (d, g).

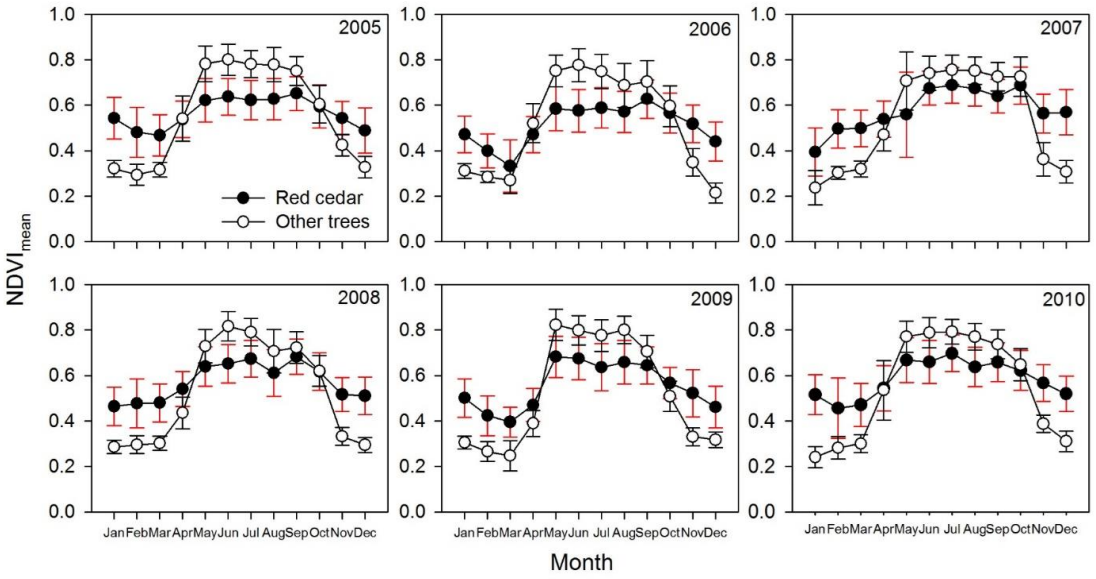

Figure S3.5 The monthly mean and deviation of NDVI of red cedar and other trees (non red cedar) forests for each year over 2005-2010.

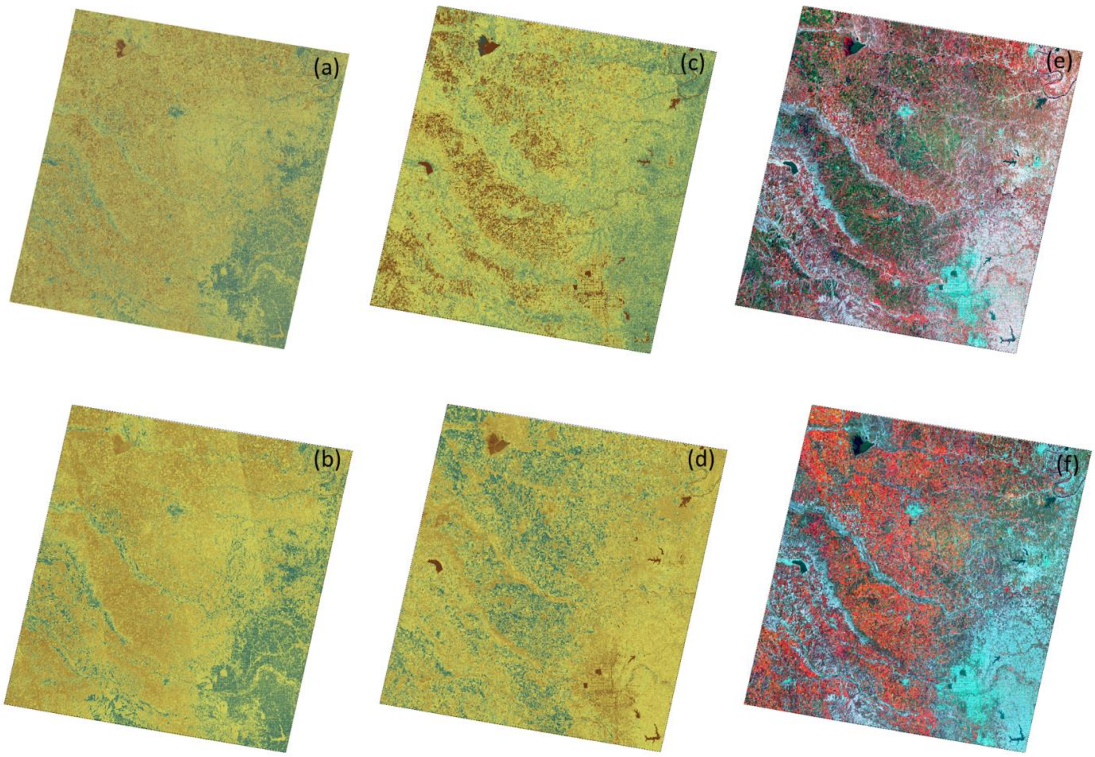

Figure S3.6 The data of PALSAR and Landsat in 2010. (a) the HH of PALSAR, (b) the HV of PALSAR, (c) the mean NDVI in the summer, (d) the mean NDVI in the winter, (e) R/G/B combination of Fig. S3.6c,a,b, (f) R/G/B combination of Fig. S3.6d,a,b.

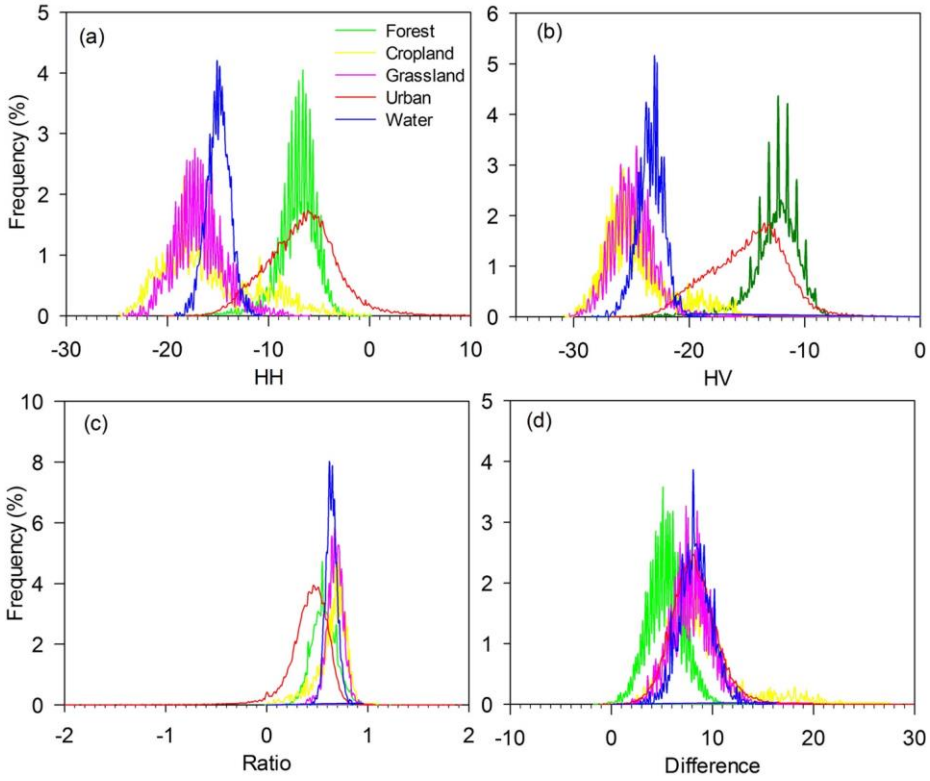

Figure S3.7 Frequency distributions of the backscatter signatures of five land cover types in the 2010 PALSAR images (a) HH, (b) HV, (c) Ratio (HH/HV), and (d) Difference (HH-HV) band. The training ROIs of the five land cover types were shown in Fig. S3.8.

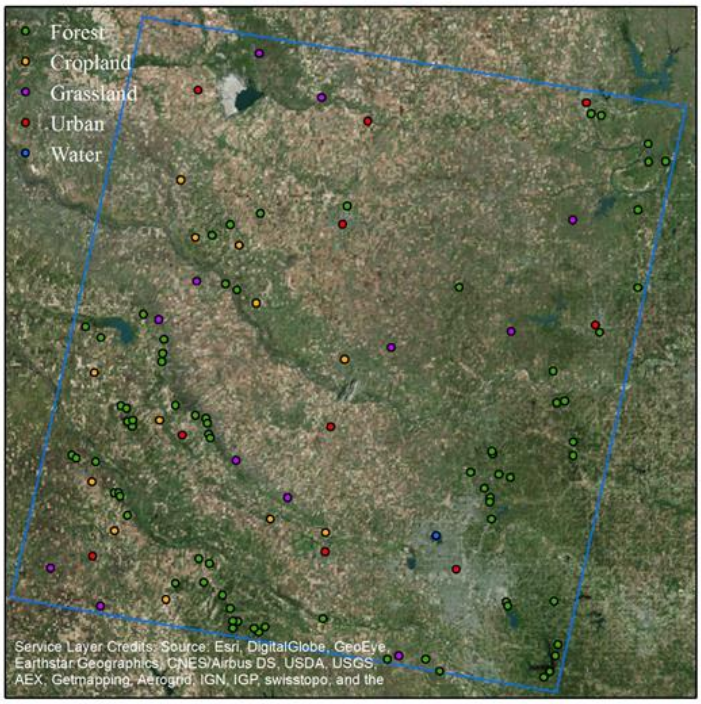

Figure S3.8 The spatial distributions of the training Region of Interests (ROIs) of five land cover types. The ROIs were generated randomly based on the 2010 Google Earth images, including pixels of forests (24,535), croplands (4,325), grasslands (4,680), water (3,780), and urban (6,222).

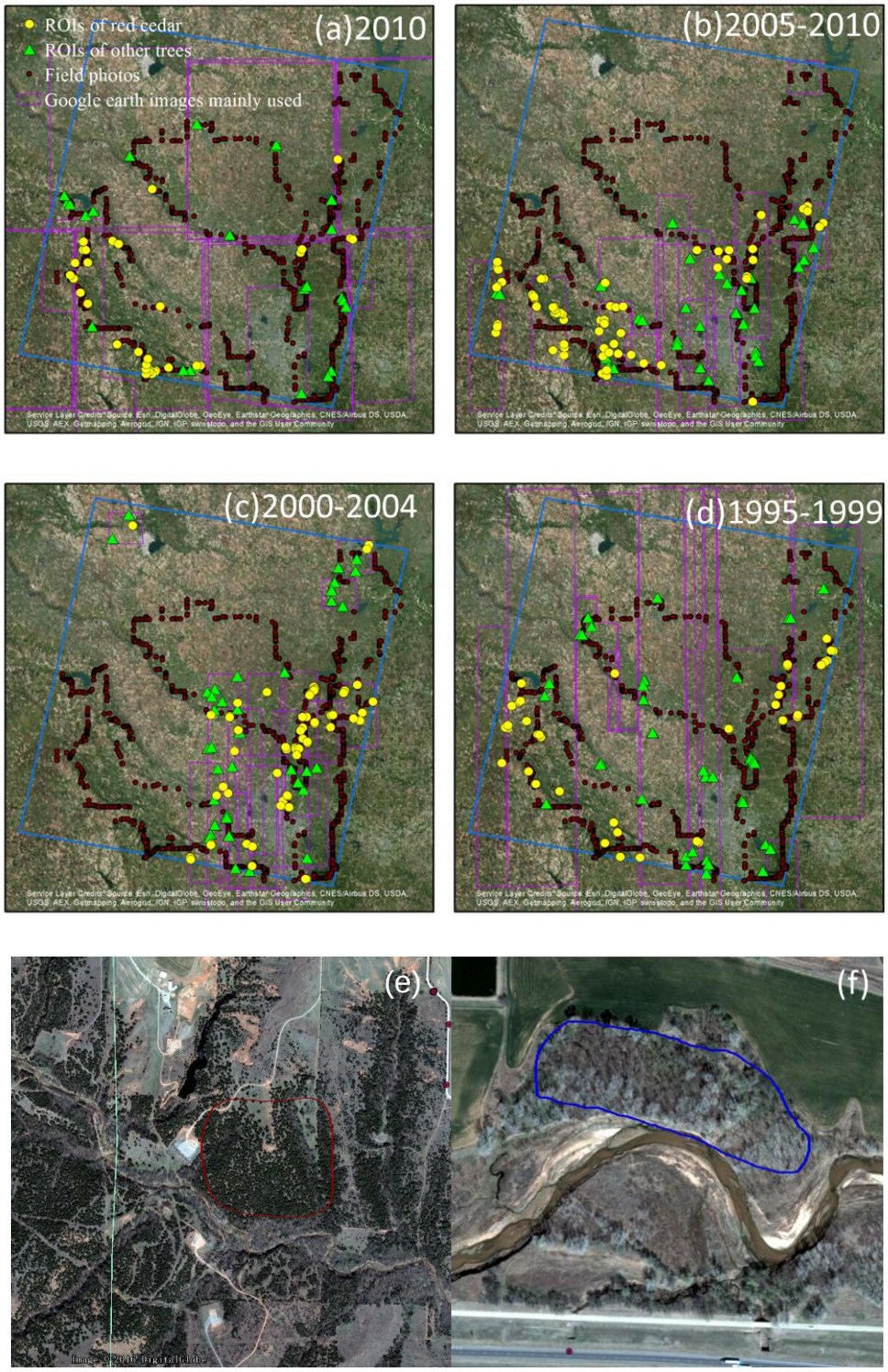

Figure S3.9 Spatial distributions of the validation regions of interests (ROIs) for (a) 2010, (b) 2005-2010, (c) 2000-2004, (d) 1995-1999. Examples of zoom-in ROIs of red cedar forest (e) and non red cedar forest (f) from the Google Earth image dated 03/23/2011.

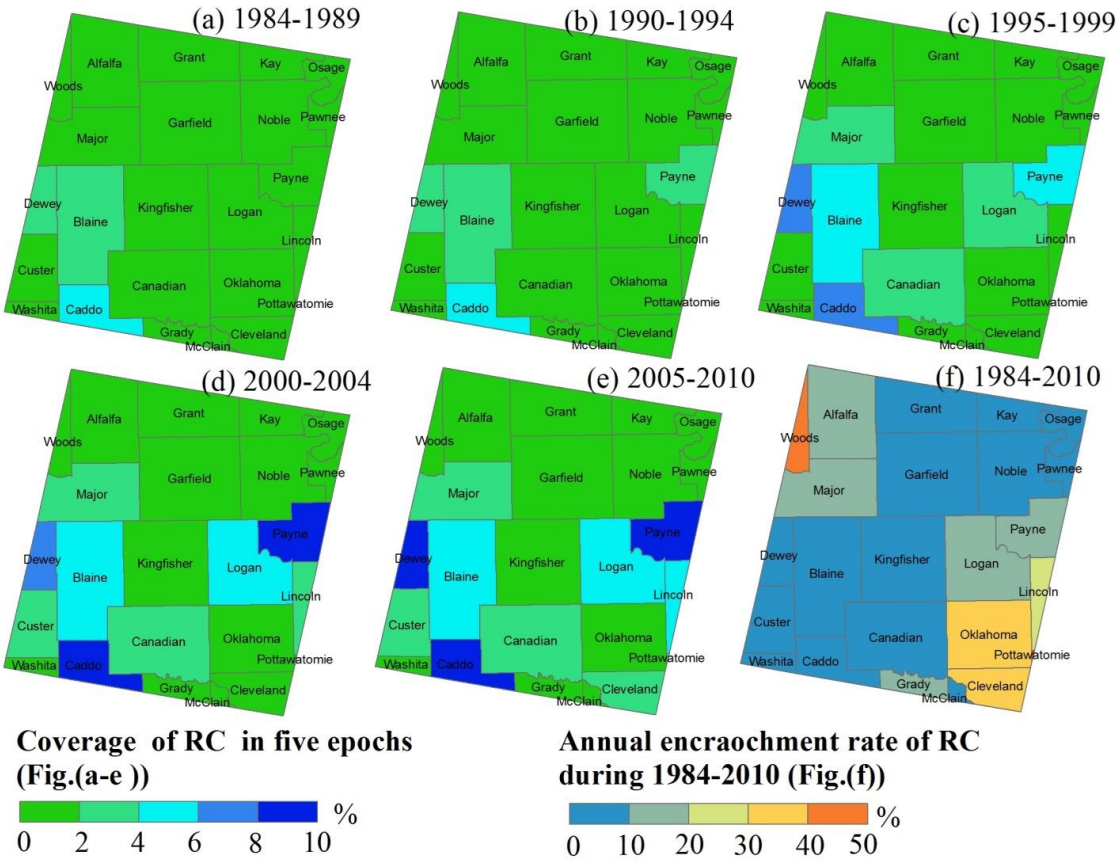

Figure S3.10 (a-e) The red cedar (RC) forest coverage maps in five historical periods at each county. The coverage of RC at each county was calculated by $\frac{Area_{RC}}{Area_{county}} \times 100$ **. (f) The annual encroachment rate of red cedar during 1984-2010 at the county level. For the incomplete counties, we just considered the parts within the study area. The annual encroachment rate of RC at each county was calculated by** $\frac{Area_{RC2005-2010} - Area_{RC1984-1989}}{26 \times Area_{RC1984-1989}} \times 100$ **.**

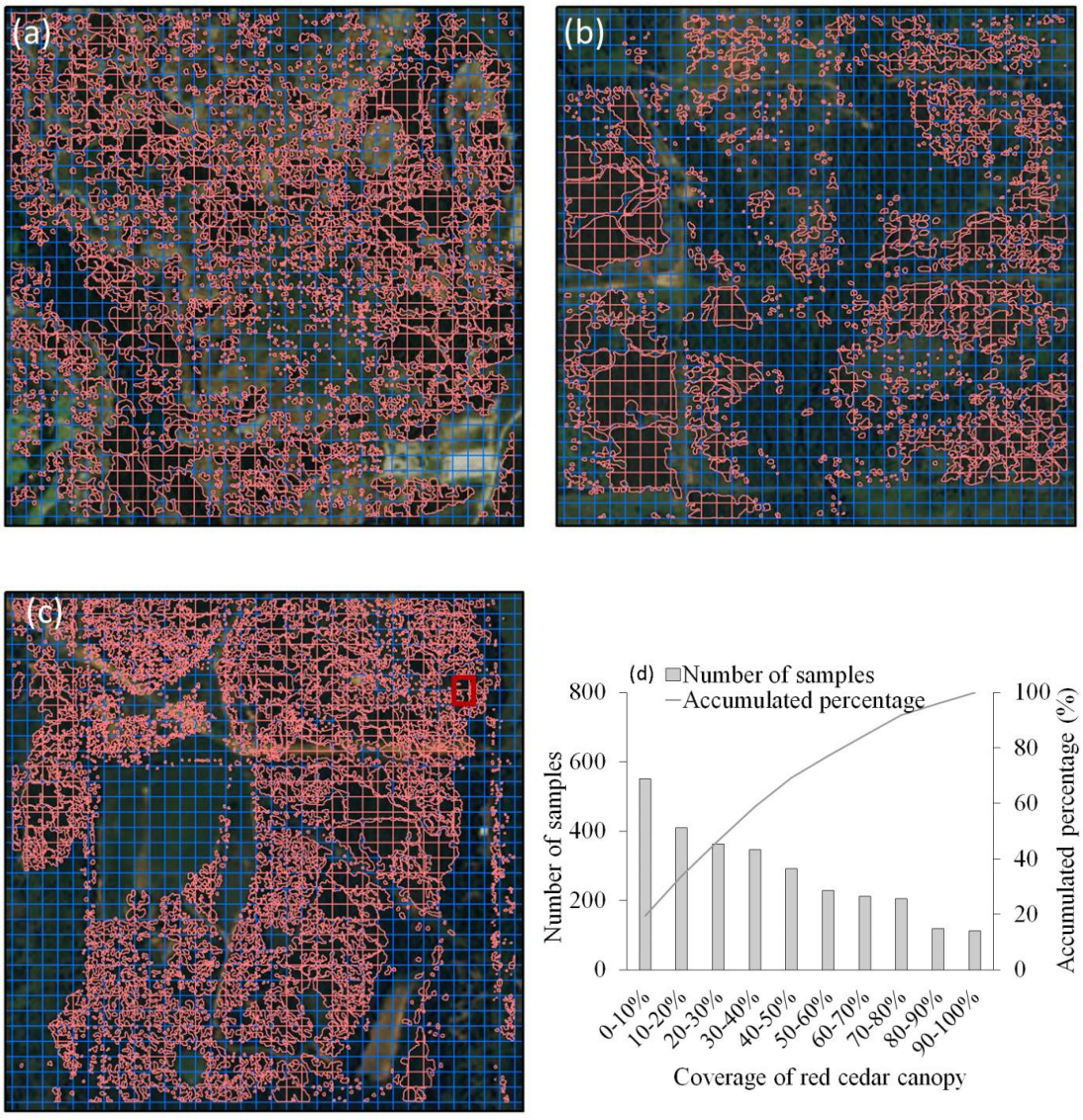

Figure S3.11 Spatial distributions of the visual interpretations of red cedar canopy in three test areas (A, B, and C) in Fig. 3.12a . Fig. S3.11a, b and c are related to the test areas of A, B, and C, respectively. The red box in Fig. S3.11c shows the zoom-in area in Fig. 3.12b. Fig. S3.11d shows the sample distributions at different coverage of red ceda canopy.

Table S3.1 Non-adjusted and adjusted producer's (PA/APA), user's (UA/AUA) and overall (OA/AOA) accuracies for the red cedar forest maps in 2010, late 2000s, early 2000s, and late 1990s. This table also shows the mapped areas (Area) and estimated areas (EArea) with 95% confidence interval margins for red cedar forests in 2010, late 2000s, early 2000s, and late 1990s (Olofsson et al. 2014; Olofsson et al. 2013).

Periods	Class	PA	APA	UA	AUA	OA	AOA	Area(km2)	EArea(km2)
2010	Red cedar	0.93	0.89	0.97	0.97	0.96	0.96	1,143	1236±15
	Non red cedar	0.98	0.99	0.95	0.95				
2005-2010	Red cedar	0.90	0.83	0.96	0.96	0.95	0.94	1008	1163±18
	Non red cedar	0.98	0.99	0.93	0.93				
2000-2004	Red cedar	0.88	0.80	0.98	0.98	0.88	0.94	890	1096±21
	Non red cedar	0.99	0.99	0.93	0.93				
1995-1999	Red cedar	0.90	0.78	0.99	0.99	0.91	0.95	638	811±21
	Non red cedar	0.99	1.00	0.94	0.94				

Chapter 4: Spatio-temporal dynamics of juniper encroachment into grasslands during 1984-2010 based on PALSAR and Landsat images

Abstract

Over the past few decades, Eastern redcedar (*Juniperus virginiana*) and Ashe juniper (*Juniperus ashei*) have widely encroached on the grasslands of the Great Plains. This encroachment has negatively affected wildlife habitats, forage and livestock production, soil microbial communities, and pre-invasion biogeochemical cycles. Understanding these spatio-temporal dynamics of juniper encroachment requires time series maps of juniper expansion across landscape, watershed and regional scales. This study investigates the dynamics of juniper encroachment on the grasslands of Oklahoma by generating multi-period maps of juniper encroachment from 1984 to 2010 at a 30-m spatial resolution. A pixel and phenology-based mapping algorithm was used to produce the time series maps of juniper encroachment using a combination of Phased Array type L-band Synthetic Aperture Radar (PALSAR) mosaic data from 2010 and Landsat 5/7 data (10,871 images from 1984-2010). Based on these maps, we analyzed the area dynamics of juniper encroachment at state and county spatial scales and examined juniper occurrence by geographic region and soil setting. We also calculated the stand age of the juniper forests in 2010. In this chapter, *stand age* refers to the years of the juniper in each individual pixel after identified as forest based on Landsat images. We developed the maps of juniper forests in Oklahoma over five multi-year epochs from 1984 to 2010: the late 1980s (1984-1989), early 1990s (1990-1994), late 1990s (1995-1999), early 2000s (2000-2004), and late 2000s (2005-2010). In addition, we produced a juniper forest stand age map for 2010. This study found that (1) juniper expanded in western and central

Oklahoma at an annual rate of ~40 km^2/year; (2) the geographic distribution of juniper forests has notable spatial heterogeneity and varies significantly between counties; (3) northwestern counties in Oklahoma experienced the most juniper encroachment; (4) stand age analysis suggested that ~65% of the juniper forests in Oklahoma are less than 15 years old; and (5) juniper forests in Oklahoma are mainly distributed in sandy and loamy soils with relatively low available water storage. This study demonstrated the potential of combining a cloud computing platform (Google Earth Engine), time series optical images (Landsat), and microwave images to document the spatial-temporal dynamics of juniper encroachment into grasslands since the 1980s at the state scale. The resultant maps can be used to support studies on ecosystem processes, sustainability, and services.

4.1 Introduction

Woody plant encroachment into grasslands and savannas in arid, semi-arid, and sub-humid climates has been widely reported around the world in recent years (Archer et al., 2001; Saintilan & Rogers, 2015). The encroachment of juniper species into native plant communities has gained increasing attention due to its widespread expansion in the Great Plains and the western United States, which often results in negative economic and ecological effects (Engle et al., 1996; Anadon et al., 2014; Meneguzzo & Liknes, 2015). For example, the accelerated encroachment of eastern redcedar (Juniperus virginiana L.) severely threatened tall- and mixed-grass prairies of the Great Plains and reduced the productivity of forage and livestock (Engle et al., 1996; Briggs et al., 2005; Knapp et al., 2008). Several studies also reported that the eastern redcedar has encroached into Oklahoma grasslands and tends to replace the dominant oak species of the Cross Timbers, forest-prairie ecotone (DeSantis et al., 2010; Williams et al., 2013). The altered species

composition further affected ecosystem processes, including water, carbon, and nutrient cycles (Williams et al., 2013; Caterina et al., 2014; Zou et al., 2015).

Quantifying and understanding the drivers, impacts, encroachment dynamics, and future trends of juniper encroachment would provide insights into rangeland management, conservation planning, and biodiversity assessment, enabling reduction of the negative effects associated with juniper encroachment. Historical juniper maps would facilitate these studies by consistent recording of the dynamics of juniper encroachment over large spatial and temporal scales. However, research and practical management of juniper encroachment have been hindered by a lack of juniper maps at local to regional spatial scales over multiple decades. Dominant views about the causes of woody plant encroachment concentrate on fire suppression, overgrazing, and climate change (Briggs et al., 2002b; Kulmatiski & Beard, 2013). However, explanations for these changes in plant composition are still controversial (Archer et al., 1994; Hibbard et al., 2001; Saintilan & Rogers, 2015). One reason is that these explanations are based on localized, historical descriptions or accounts that are often conflicting (Archer et al., 1994). Another reason refers to the variance in drivers of woody plant encroachment among ecoregions (Barger et al., 2011; Saintilan & Rogers, 2015). A number of studies have aimed to understand the impacts of woody encroachment on hydrology (Caterina et al., 2014; Zou et al., 2015), carbon (Barger et al., 2011; Pinno & Wilson, 2011), and nutrient cycles (Hughes et al., 2006; McCulley & Jackson, 2012). However, most of those studies were conducted at specific sites with field experiments, and the effects of woody plant encroachment on carbon and water budgets at a regional scale poorly understood (Pacala et al., 2001; Barger et al., 2011; Zou et al., 2015). In a study on the impacts of eastern

redcedar encroachment on regional climate by Ge and Zou (2013), eastern redcedar expansion was assumed to be random due to a lack of information on eastern redcedar encroachment. Without continuous historical data at the regional scale, it remains difficult to estimate the woody plant expansion rate, describe the shapes of expansion curves, and predict the density and distribution of woody plants in the future (Barger et al., 2011). Describing the magnitude of woody plant encroachment also proves confounding, as it varies largely among geographic areas despite within the similar ecosystems (Buitenwerf et al., 2012).

Time series maps of woody plant encroachment at regional scales are extremely helpful, as these maps can be used to widely and comprehensively examine the potential drivers and consequences of encroachment and document the spatial-temporal encroachment dynamics. Previous studies have been conducted to estimate the distribution of the encroachment species (e.g. eastern redcedar) by using field surveys or questionnaires (Schmidt & Leatherberry, 1995; Engle et al., 1996; Meneguzzo & Liknes, 2015). However, most of these studies were conducted within the sub-state scale and in one or two time periods (Meneguzzo & Liknes, 2015). Further, traditional field survey approaches are labor-intensive and cost prohibitive, making it difficult to collect enough data to accurately map the spatio-temporal distributions of the invasive plants over large regions. Currently, woody plant encroachment maps generated from historical observations over multiple decades at regional scales are not available (Gavier-Pizarro et al., 2012; Ge & Zou, 2013).

Remote sensing images with multi-decade data archives could be used to quantify spatial-temporal patterns of woody plant encroachment (Symeonakis & Higginbottom,

2014). The Landsat archive from Thematic Mapper (TM), Enhanced Thematic Mapper Plus (ETM+), and Operational Land Imager (OLI) has recorded continuous land cover changes at consistent spatial and temporal resolutions since 1984 (Wulder et al., 2008; Wulder et al., 2012; Wulder et al., 2016). Landsat time series data have been widely used to monitor long-term changes in forests, croplands, and grasslands from local to national spatial scales (Hansen et al., 2013; Zhong et al., 2014; Dong et al., 2015; Mueller et al., 2015). However, woody vegetation coverage may be overestimated by confusion with grasslands or omitted due to the absence of canopy foliage based on optical remote sensing data (Shimada et al., 2014; Qin et al., 2016b). Nevertheless, the cloud-free Synthetic Aperture Radar (L-band SAR) penetrates well into forest canopies to document forest structure (Baghdadi et al., 2009). Global and regional forests have been mapped based on the volume scatter signatures from leaves, trunks, and branches within forests (Shimada et al., 2014; Qin et al., 2015; Chen et al., 2016). The Japan Aerospace Exploration Agency (JAXA) provides multiple resolution datasets from the Advanced Land Observing Satellite Phased Array type L-band Synthetic Aperture Radar (ALOS/PALSAR) (Shimada et al., 2009; Shimada & Ohtaki, 2010). These datasets have been utilized by many studies to map forests (Shimada et al., 2014; Qin et al., 2015) and plantations (Miettinen & Liew, 2011; Dong et al., 2013; Chen et al., 2016) at regional and global scales. However, remote sensing datasets have not yet been utilized to study the spatio-temporal dynamics of woody plant encroachment into grasslands and changes in forest species composition at large spatial scales.

The overall goal of this study is to understand the current and historical patterns of juniper encroachment on tall- and mixed grasslands in Oklahoma during 1984-2010.

The juniper in Oklahoma comprises mainly eastern redcedar and ashe juniper (Engle et al., 1996). The specific objectives of this study are to: (1) generate a map of juniper forests in Oklahoma in 2010 at 30-m spatial resolution through analyses of PALSAR and Landsat images taken in 2010 and then determine the years of the juniper as identified as forest in 2010 through analysis of time series Landsat images from 1984 to 2010; (2) quantify the spatio-temporal dynamics of juniper encroachment at the state and county level from 1984 to 2010 using juniper forest maps produced for each period; and (3) characterize the geographical patterns and soil settings of the juniper encroachment during 1984-2010 based on the resultant maps. We report the results in five multi-year periods: the late 1980s (1984-1989), early 1990 (1990-1994), late 1990s (1995-1999), early 2000s (2000-2004), and late 2000s (2005-2010).

4.2 Materials and methods

4.2.1 Study area

The state of Oklahoma is located in the southern Great Plains, USA (33.4°N ~ 37.1°N, 94°W ~ 103.2°W). Oklahoma consists of 77 counties with a total land area of about 181,035 km2 (Fig. 4.1). It has a temperate continental climate, where the annual mean air temperature ranges from 13 oC in the north to 17 oC in the south. The average annual precipitation ranges from ~410 mm in the northwest to ~1700 mm in the southeast according to the PRISM (Parameter-elevation Relationships on Independent Slopes Model) precipitation datasets of 1980-2010 (http://prism.oregonstate.edu/) (Fig. 4.1). The PRISM climate datasets are developed based on climate observations from weather stations, and more information can be found in previous publications (Daly et al., 2008; Daly et al., 2015). Elevation ranges from 88 m to 1520 m above sea level according to

the 30m Shuttle Radar Topography Mission Digital Elevation Model (SRTM/DEM) (Fig. S4.1a). Oklahoma's diverse soil types have a wide range of texture from clay to sand. According to the 2011 National Land Cover Database (2011 NLCD), grasslands, croplands, deciduous forest, and pasture are the main land cover classes and account for 36%, 18%, 17%, and 11% of the total area, respectively (Fig. S4.1b). Evergreen forests occupy 3% of the total land area, mostly distributed in the southeast and dominated by pine plantations. The deciduous forests are mostly dominated by oak tree species (Diamond & Elliott, 2015).

Level I and level II ecoregion classifications from the U.S. Environmental Protection Agency (https://www.epa.gov/eco-research/ecoregions-north-america) were used to ecologically and geographically characterize the forest and prairie assemblages of natural communities and species in Oklahoma (Fig. 4.1). There are two distinct ecoregions of eastern temperate forest and western prairie. The forest region covers several eastern counties and has relatively high annual precipitation. The prairie region covers a majority of Oklahoma and has relatively low annual precipitation. There are three primary sub-ecoregions (level III) in this area; from east to west they are: the Cross Timbers, the Central Great Plains, and the High Plains and Southwestern Tablelands of the panhandle region. Early field surveys indicated that juniper species had widely encroached on the Cross Timbers and especially the Central Great Plains (Coppedge et al., 2001; DeSantis et al., 2011; Williams et al., 2013). Eastern redcedar (Juniperus virginiana) is the main invasive juniper species, followed by ashe juniper. Redberry juniper (J. pinchotii) and other juniper species (J. monosperma and J. scopulorum) are distributed only locally within Oklahoma (Engle et al., 1996). Juniper encroachment into

grasslands is the focus of this study, so we selected the counties within the prairie ecoregion and the transition zone between prairies and eastern forests. The transition zone consists of the counties located in the Eastern Temperate Forest ecoregion and have relatively low annual precipitation. We excluded eight eastern counties located in the same forest ecoregion that have relatively high annual precipitation (Fig. 4.1).

4.2.2 Data

4.2.2.1 PALSAR 25 m orthorectified image data

The 25m PALSAR orthorectified mosaic datasets from 2007 to 2010 at Fine Beam Dual (FBD, HH, HV) polarization mode were generated from data acquired between the months of June and October (Shimada et al., 2014). The HH and HV backscatter data were processed by geometric correction and radiometric calibration (Shimada et al., 2009; Shimada & Ohtaki, 2010). We downloaded all of the 25m PALSAR orthorectified mosaic data for Oklahoma in 2010 from the Earth Observation Research Center, JAXA (http://www.eorc.jaxa.jp/ALOS/en/palsar_fnf/fnf_index.htm). The Digital Number (DN) values (amplitude) of HH and HV were converted into backscattering coefficients (gamma-naught) in decibels using the following calibration coefficient (Shimada et al., 2009).

$$\gamma^o = 10 \times log_{10} < DN^2 > +CF \tag{4.1}$$

where γ^o is the backscattering coefficient in decibel; DN is the digital number value of pixels in HH or HV; and CF is the absolute calibration factor of -83.

4.2.2.2 Landsat data and pre-processing

We processed all available surface reflectance products of Landsat 5/7 accessible in the Google Earth Engine (GEE), a cloud computing platform. The surface reflectance

data were generated from the Landsat Ecosystem Disturbance Adaptive Processing System (LEDAPS) through radiance calibration and atmospheric correction (Vermote et al., 1997; Masek et al., 2006). The study area is covered by 23 path/row Landsat scenes (Fig. S4.1b). We collected a total number of 14,086 Landsat 5/7 images from January 1984 to March 2011 to construct a 3-dimensional data cube of land surface reflectance. Fig. S4.2 shows the annual distributions of all available Landsat TM/ETM+ surface reflectance data over the study period by sensors (Landsat 5/7) (Fig. S4.2a), by Landsat path/row (Fig. S4.2b), and by month (Fig. S4.2c).

We evaluated the observation quality of the 3-D data cube at the pixel level in two steps. First, the bad observations (clouds, cloud shadows, snow/ice and scan-line corrector (SLC)-off gaps) were identified as NODATA according to the Fmask (Zhu & Woodcock, 2012) and metadata. Then, we counted the number of good observations for individual pixels during each whole year and each winter (December, January, and February) (Fig. S4.3). Fig. S4.3 and Fig. 4.2 show the spatial distribution and frequency histogram of the observation quality of the time series Landsat data cube.

We used the surface reflectance data with good observations to calculate the Normalized Difference Vegetation Index (NDVI) (Tucker, 1979) and Land Surface Water Index (LSWI) (Xiao et al., 2005). We used the times series data of NDVI and LSWI to analyze the vegetation phenology, as NDVI is related to vegetation greenness and LSWI is sensitive to leaf and soil water (Xiao et al., 2006).

$$NDVI = \frac{\rho_{NIR} - \rho_{red}}{\rho_{NIR} + \rho_{red}} \tag{4.2}$$

$$LSWI = \frac{\rho_{NIR} - \rho_{SWIR}}{\rho_{NIR} + \rho_{SWIR}} \tag{4.3}$$

where ρ_{blue}, ρ_{red}, ρ_{NIR} and ρ_{SWIR} are the surface reflectance values of blue (450-520nm), red (630-690nm), near-infrared (760-900nm), and shortwave-infrared bands (1550-1750nm).

4.2.2.3 Oklahoma ecological system map

The OKESM product (Diamond & Elliott, 2015) was generated from multiple datasets including remote sensing, digital soils, slope, and streams using a decision tree classification approach. Remote sensing images between December 2010 and August 2011 were used for the map in the eastern regions, and images between April 2013 and January 2014 were used to map the western regions. A user's accuracy of 85% was reported for this product (Diamond & Elliott, 2015). This dataset can be downloaded freely from the Oklahoma department of wildlife conservation website (http://www.wildlifedepartment.com/facts_maps/ecoregions.htm).

4.2.2.4 Soil survey geographic database

Soil is a primary environmental factor that influences ecosystem stability in many regions (Maestas et al., 2016). We examined the physical and hydrological properties of soils to identify the soil environments for juniper encroachment, including soil texture (% sand, silt, clay), soil depth to restrictive layer for crop roots (crop root zone depths) (Staff, 2016a), and available water storage (AWS) at four depths: 0-25 cm, 0-50 cm, 0-100 cm and 0-150 cm. The 10-m gridded Soil Survey Geographic (gSSURGO) database for Oklahoma was downloaded from the United States Department of Agriculture (USDA) (Staff, 2016b). This soil data product contains information about soil components and properties collected by the National Cooperative Soil Survey. We resampled this product

by the nearest neighbor method to 30 m to match the spatial resolution of the juniper maps.

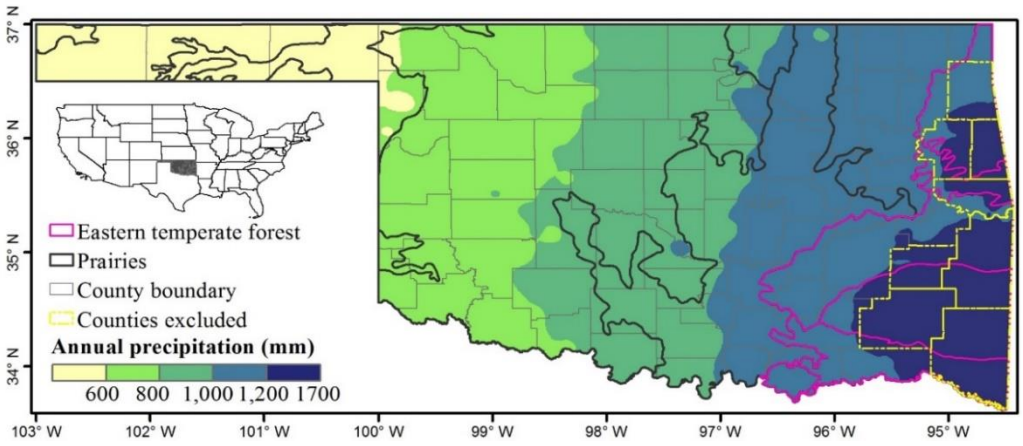

Figure 4.1 The location of the study area. The ecoregions, annual precipitation and counties are shown in the figure. The 8 counties located in eastern temperate forest ecoregion with high annual precipitation were not included in the study area.

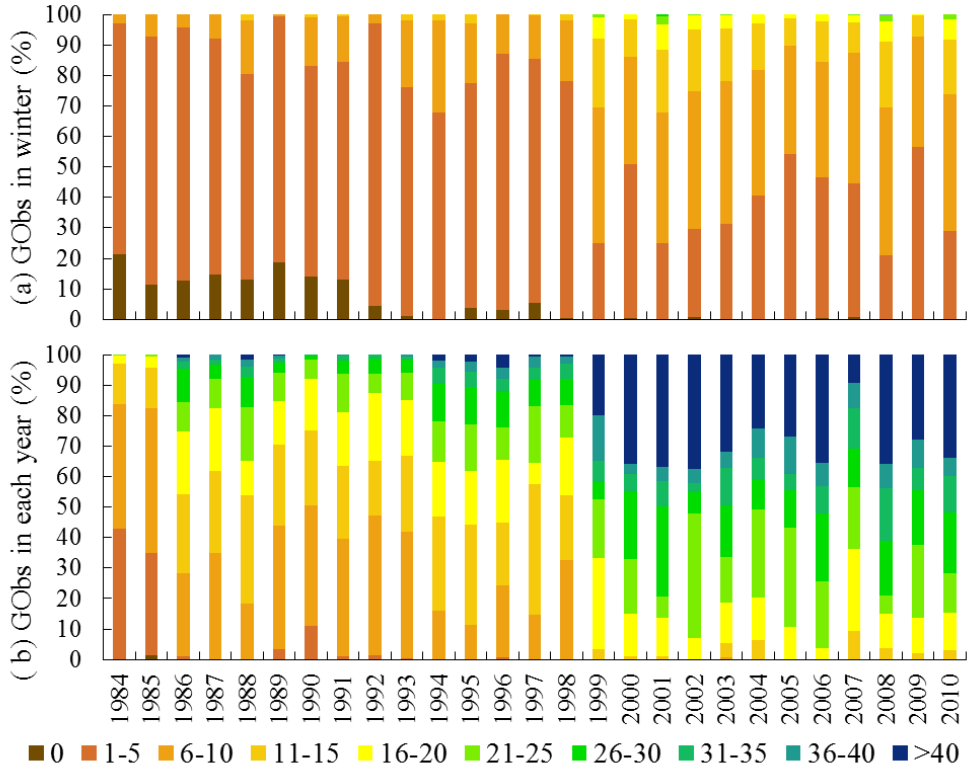

Figure 4.2 Percentage of good observations (GObs) in annual (a) winter (Dec-Feb) and (b) whole year from 1984 to 2010.

4.2.3 Methods

This study generates three map products, as shown in the workflow (Fig. 4.3). First, the baseline 2010 forest map was produced using a decision tree algorithm based on PALSAR and Landsat data in 2010. Second, the map of juniper forests in 2010 was produced using a pixel and phenology-based algorithm, the 2010 forest map, and the Landsat images for the winter of 2010 (December 2010 – February 2011). Finally, a juniper forest stand-age map in 2010 was produced based on the historical juniper forest maps. These historical maps were generated in five epochs including the late 1980s (1984-1989), early 1990s (1990-1994), late 1990s (1995-1999), early 2000s (2000-2004) and late 2000s (2005-2010). A detailed workflow for each set of map products is described in the following paragraphs.

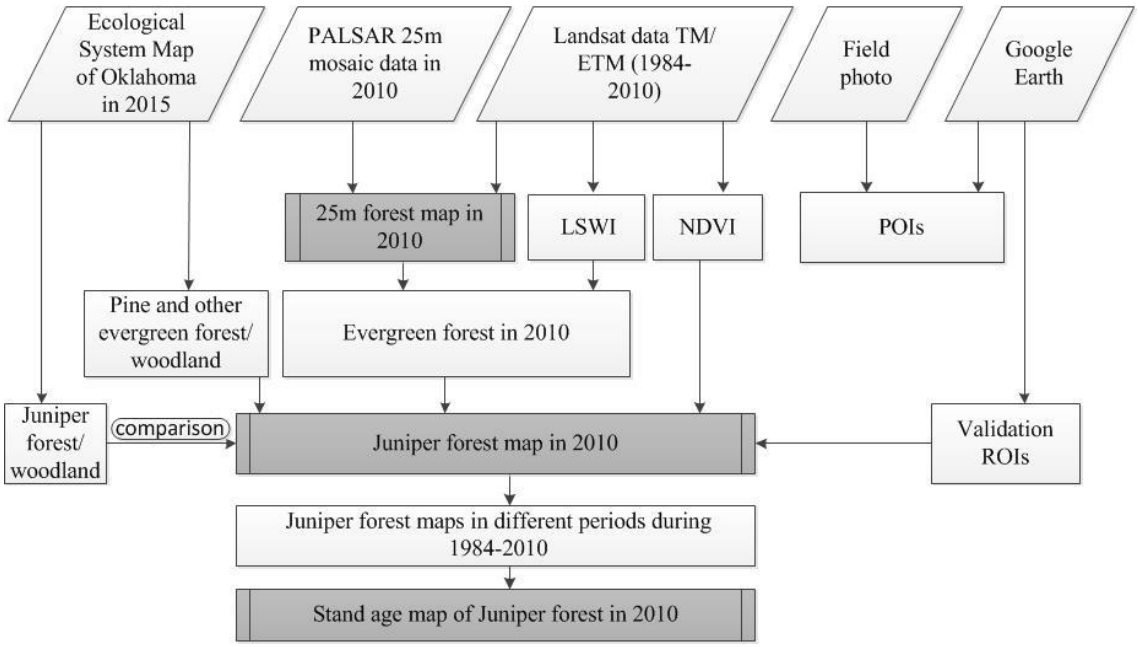

Figure 4.3 Work flow of this study. It includes three main sections shown in dark grey boxes.

4.2.3.1 Algorithm of juniper forest mapping

Juniper is a type of evergreen tree. To map the juniper forest, we developed an algorithm composed of three sequential steps including forest mapping, evergreen forest extraction, and juniper forest identification. The following paragraphs describe the algorithm development for each step and a summary of the rules used for juniper forest mapping.

Forests have a different backscatter signature than other land cover types (e.g. grasslands, croplands, water, etc.) in HH, HV, HH/HV (Ratio), and HH-HV (Difference) that can be used to identify forests (Qin et al., 2015; Qin et al., 2016a). Our previous studies have developed a decision classification algorithm for forest mapping based on 50m PALSAR mosaic data (Dong et al., 2012) and the integrated data of 50m PALSAR and MODIS (Qin et al., 2015; Qin et al., 2016b). This study used 25m PALSAR data to produce the 2010 Oklahoma forest as shown in our recent publication (Qin et al., 2016a). This PALSAR-based forest map used the United Nations Food and Agriculture Organization (FAO) forest definition as land (> 0.5 ha) with tree canopy cover greater than 10% and minimum tree height of 5 meter (FAO, 2012).

Evergreen forests keep green leaves throughout a year, while deciduous forests shed leaves in winter. Green leaves have higher reflectance in the NIR band than SWIR band, which results in positive LSWI. In contrast, senescent leaves and soil have lower NIR reflectance than SWIR, which produces negative LSWI. A simple algorithm of LSWI>0 for all good observations in a whole year was developed to separate evergreen forest from deciduous in tropical regions (Xiao et al., 2009). This algorithm has been successfully implemented to map evergreen forests in temperate regions (Qin et al., 2016b). In this study, the Landsat-derived LSWI time series of eastern redcedar, ashe

juniper, and deciduous forests at site level suggested the applicability of this method to extract evergreen forests in Oklahoma (Fig. 4.4).

Phenology analysis of greenness-based Landsat-derived NDVI time series revealed that eastern redcedar and ashe juniper had significantly lower VIs in summer and higher VIs in winter than did deciduous forest (Fig. 4.4). We analyzed the monthly mean NDVI (NDVImean) at the regional scale using training region of interests (ROIs) of eastern redcedar, ashe juniper, and deciduous forests (Fig. S4.4a) based on Landsat 5/7 images from 2009-2010. The monthly NDVImean time series (Fig. S4.4b) suggested that the NDVImean in winter is more able to separate juniper trees from deciduous species, as the monthly NDVImean of juniper in winter reached higher values than deciduous forests. This study extracted juniper forests based on the winter NDVImean using a threshold of 0.4 in accordance with the method proposed in our recent publication (Wang et al, 2017). A statistical analysis of the winter NDVImean spectral signature suggested the 0.4 threshold can separate 95% of eastern redcedar pixels (>0.4) from 99% pixels of other trees (<0.4) (Wang et al, 2017).

In summary, we first produced the forest map (Forest-2010) based on PALSAR from 2010 following the decision rule of 16<HV<-8, and 2 < Difference <8, and 0.3 <Ratio<0.85, which is documented in detail in a previous study in Oklahoma (Qin et al., 2016a). This map serves as the baseline forest map and is overlaid with the time series Landsat data to identify and map evergreen and deciduous forests based their phenology characteristics. Second, we counted the number of LSWI>0 in all the good observations within a year as the frequency of LSWI>0 (FrqLSWI) for individual pixels. Pixels that meet the criteria of FrqLSWI>=0.9 were identified as evergreen forest. In this study, we

extended the threshold of 1.0 used in early studies (Xiao et al., 2009; Qin et al., 2016b) to 0.9 to identify the potential maximum evergreen forest area and thus reduce the omission of evergreen pixels caused by short term disturbances (e.g., drought). Third, we followed the criteria of winter season, NDVImean>0.4, to extract the juniper from the evergreen forest map.

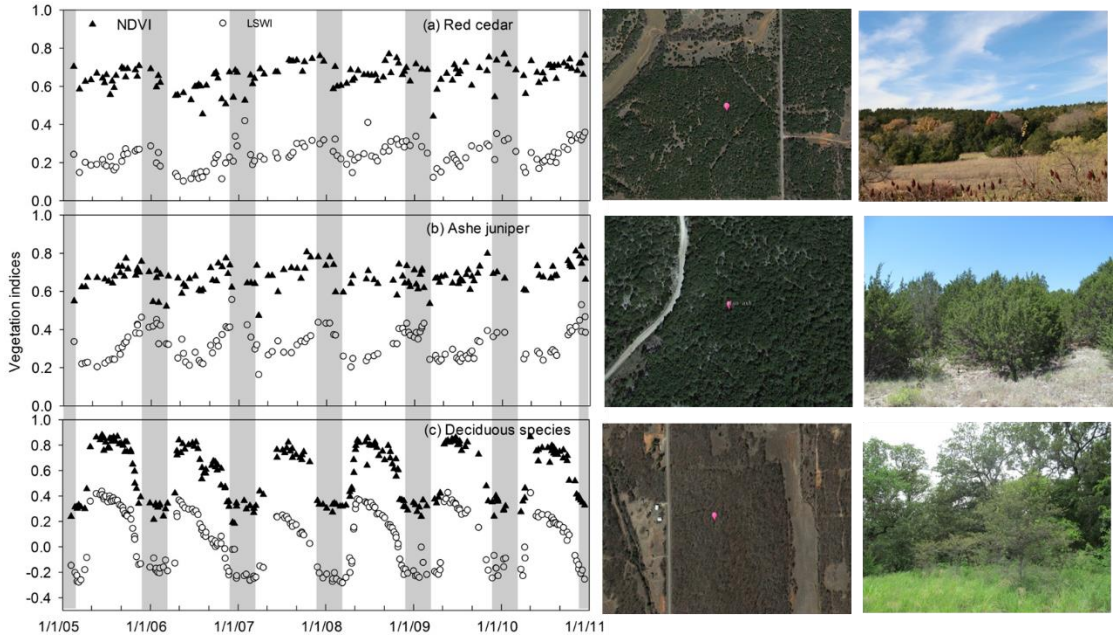

Figure 4.4 Time series of vegetation indices (a-c) of red cedar, ashe juniper and oak forests, and the landscapes in Google Earth images and field photos.

4.2.3.2 Regional implementation of the juniper forest mapping algorithm

Although forests in Oklahoma are dominated by deciduous species, some pine plantations, natural pine forest, and other evergreen species occur in the eastern counties of Oklahoma. These evergreen species may cause uncertainties in the implementation of the juniper forest mapping algorithm. Therefore, we generated a non-juniper evergreen forest mask from the 10-m OKESM dataset. We merged the pine plantation classification with shortleaf pine forest and other evergreen forest (non-juniper and non-pine) from the

OKESM and resampled it to 30m to match the resolution of the Landsat images using the nearest neighbor method (Fig. S4.5). The juniper forest encroachment map for 2010 was generated after masking out the non-juniper evergreen forests.

4.2.3.3 Stand age analysis

The stand age of juniper forest is a useful indicator for juniper encroachment over time, which shows the established time of the juniper forest pixels in 2010. For each individual juniper pixel in 2010, we analyzed LSWI and NDVI data from Landsat images in a year and determined whether it has evergreen forest characteristics or not. If the data had evergreen forest characteristics, we could assume the pixel remained juniper forest. We repeated this process for all juniper pixels to generate annual juniper maps from 1984 to 2009. These annual juniper forest maps were combined into five multi-year periods using frequency combination to reduce uncertainties caused by image quality or other factors (e.g. drought). The five periods comprised the late 1980s (1984-1989), early 1990s (1990-1994), late 1990s (1995-1999), early 2000s (2000-2004) and late 2000s (2005-2010). During each period, we counted the number of individual pixels identified as juniper based on the annual juniper forest maps. A pixel with a number $\geqslant 3$ (frequency $\geqslant$50%) was identified as juniper forest for each time period. The stand-age map of juniper forest in 2010 was produced using the time of first juniper forest occurrence for individual pixels in the juniper map for 2010 and the juniper maps in the five time periods, defined as <=5 (first time as juniper forest in 2010-2005), <=10, <=15, <=20, and >=20 years old (first time as juniper forest in 1989-1984).

4.2.3.4 Accuracy assessment and comparison

The strata random sampling method was used to collect the ground reference ROIs for the accuracy assessment (Olofsson et al., 2014). First, we generated random points in each stratum of juniper forest (150 points) and other land cover types (including 250 non-juniper forest points and 600 non-forest points) based on the OKESM map. Second, 100m*100m square buffers were generated according to the random points. Finally, these random square buffers were overlaid with the high resolution images in Google Earth (GE). In accordance with the GE images for winters during 2009-2011, we selected the ROIs with large juniper coverage (>80%) as validation samples for the juniper forest class. Similarly, we checked the ROIs of non-juniper forest and non-forest types using all available GE images and ground reference data. The non-juniper forest ROIs covered deciduous and non-juniper evergreen forests, and the non-forest ROIs covered cropland, grassland, water, and other land cover types. Fig. S4.6 shows the spatial distribution of the validation ROIs we collected for juniper forest, non-juniper forest and non-forest land cover types in 2010. These ROIs (including 1,402 juniper forest pixels and 8,742 other land cover pixels) were used to calculate the confusion matrix to assess the accuracy of the juniper forest map in 2010 following the best practices described by Olofsson et al. (2014).

We selected the vegetation classes related to the juniper species from OKESM to produce the juniper woodland/forest map (OKESM-JWF). We aggregated the 10m OKESM-JWF map (binary 0 and 1) into a 30m OKESM-JWF percentage map. We compared the 2010 juniper forest map (PALSAR/Landsat-JF2010) with the OKESM-JWF map in terms of the pixel-based spatial agreement and total area at the county level.

4.2.3.5 Spatiotemporal dynamic analysis of juniper encroachment

We analyzed the spatio-temporal dynamics of the juniper forest area and stand age at state and county scales. The total area and mean stand age of the juniper forest were calculated at each spatial scale. To understand the geographical patterns of juniper encroachment, we further examined the juniper area dynamics by (1) geographic regions divided by latitude (0.1° interval), longitude (0.1° interval), and elevation (50-m interval); and (2) the soil physical and hydrological properties including texture, depth, and AWS.

4.3 Results

4.3.1 The juniper forest map in 2010

We sequentially produced maps of 2010 forest (Fig. S4.6), evergreen forest (Fig. S4.7), and juniper forest (Fig. 4.5). The resultant juniper forest map in 2010 (PALSAR/Landsat-JF) suggests that juniper encroachment in Oklahoma has not occurred uniformly in space. Extensive juniper encroachment occurred mainly in western and central Oklahoma forming three encroachment clusters (labeled 1, 2, and 3 in Fig. 4.5). The western encroachment cluster included Woodward, Dewey, Major, Blaine, Canadian and Caddo counties. The northcentral encroachment cluster mainly covered Logan, Payne, and Pawnee counties. The southcentral cluster covers Murray, Johnston and Marshall counties. In the remaining counties, juniper forests are distributed either widely or sparsely.

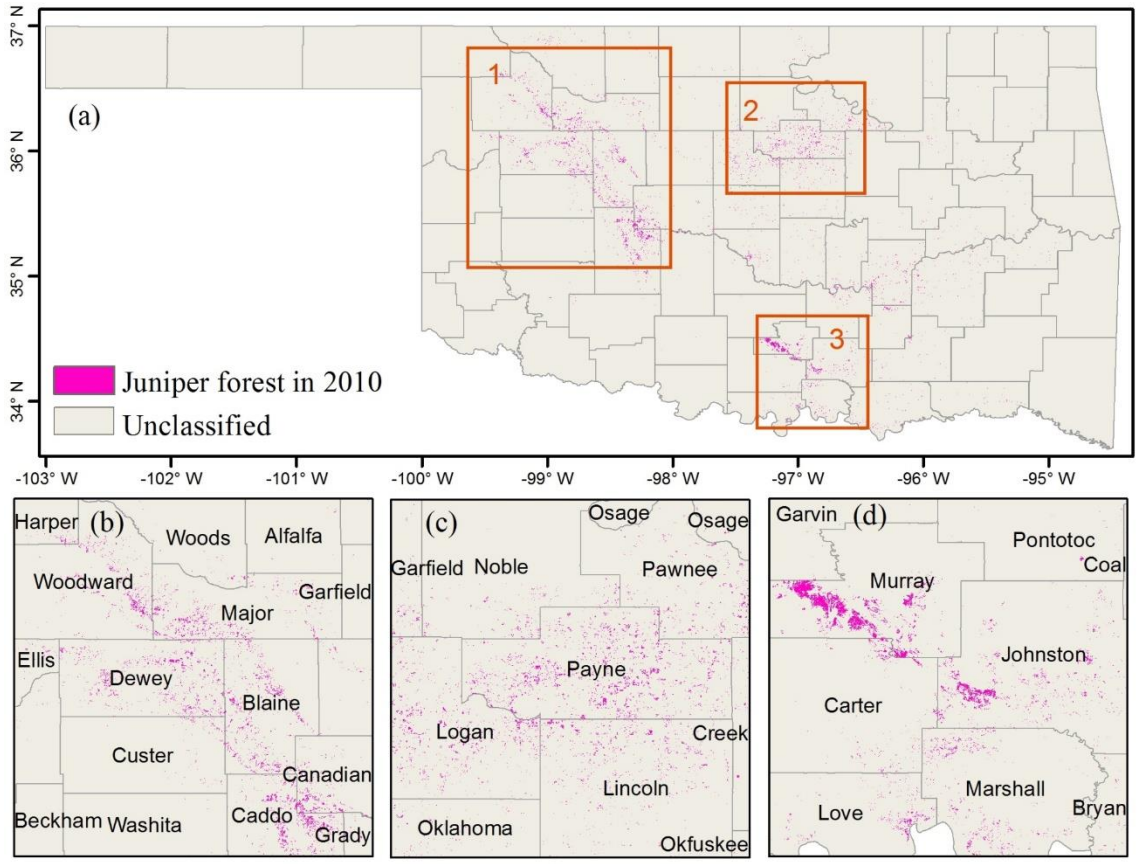

Figure 4.5 Map of Juniper forest in 2010 and three zoom-in regions.

4.3.2 Accuracy assessment and inter-comparison of the juniper forest map in 2010

The accuracy of the resultant PALSAR/Landsat-JF map in 2010 was assessed using a confusion matrix based on the validation ROIs introduced in Section 2.4 (Fig. S4.8). This juniper forest map had an overall accuracy (OA) of 0.99 and the juniper forest category had producer's accuracy (PA) of 0.95±0.01 and user's accuracy (UA) of 0.92±0.01 (Table 4.1).

The comparison between the PALSAR/Lansat-JF (Fig. 4.6a) and the OKESM-JWF map (Fig. 4.6b) showed good spatial consistency between these two products. Some differences occured in two western counties highlighted by the black box in Fig. 4.6a,b. The area estimation at the county scale showed that these two products have a statistically

significant linear correlation with R^2 of 0.74 (Fig. 4.6c). Two counties with large discrepancies are shown in red circles in Fig. 4.6c, which corresponds to Woods and Woodward counties shown in the black box in Fig. 4.6a, b. We zoomed-in on these two counties (Fig. 4.6d,e), selected three case regions, and examined the landscapes using the GE high resolution images dated 03/23/2011 in Fig. 4.6f, g, h. These GE images show that PALSAR/Landsat-JF may miss some pixels with small proportions of juniper trees within one Landsat pixel (Fig. 4.6f) or woodlands with sparse juniper tree coverage (Fig. 4.6g,h). The OKESM-JWF map found juniper woodlands and forests, whereas the PALSAR/Landsat-based juniper forest map identified only the forests, thus causing some discrepancies between these two products as shown in Fig. 4.6g,h.

Table 4.1 Accuracy assessment of juniper forest map in 2010 based on the validation regions of interests (ROIs) from field photos, and Google Earth images.

		Reference		
		Juniper	Non-juniper	Total
Map	Juniper	0.092	0.008	0.1
	Non-juniper	0.005	0.895	0.9
	Total	0.097	0903	
User's Accuracy (UA)		0.92±0.01	0.99±0.01	
Producer's accuracy (PA)		0.95±0.01	0.99±0.00	
Overall accuracy (OA)		0.99±0.00		

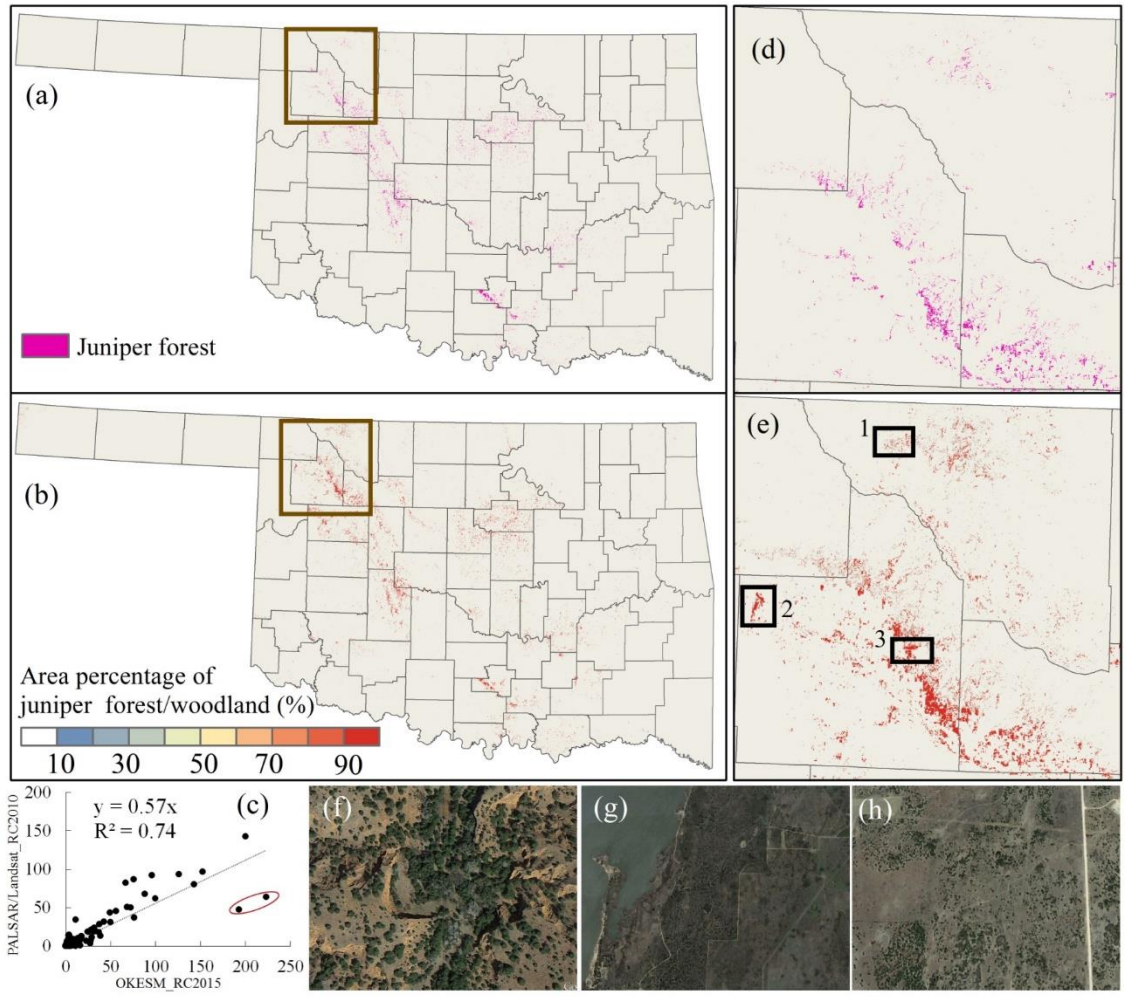

Figure 4.6 Comparison of PALSAR/Landsat-based juniper forest and OKESM-based juniper woodland/forest.

4.3.3 Area dynamics and stand age analysis at state and county levels during 1984-2010

Fig. 4.7 shows the juniper forest maps during five epochs from the late 1980s to the late 2000s, with an interval of five or six years. From 1984 to 2010, substantial juniper encroachment occurred in Oklahoma, particularly in three clusters in western, northcentral, and southcentral Oklahoma. Juniper forest area increased from ~350 km^2 in the late 1980s to ~500 km^2 during the early 1990s. The juniper encroachment mainly occurred in the western and northcentral counties during this period. In the late 1990s,

juniper forest expanded continuously, and the area increased to ~800 km^2. In the early and late 2000s, the area reached ~1100 km^2 and ~1300 km^2, respectively. During 1984-2010, the increase in juniper forest area was strongly linear with an encroachment rate of ~48 km^2 per year at the state level.

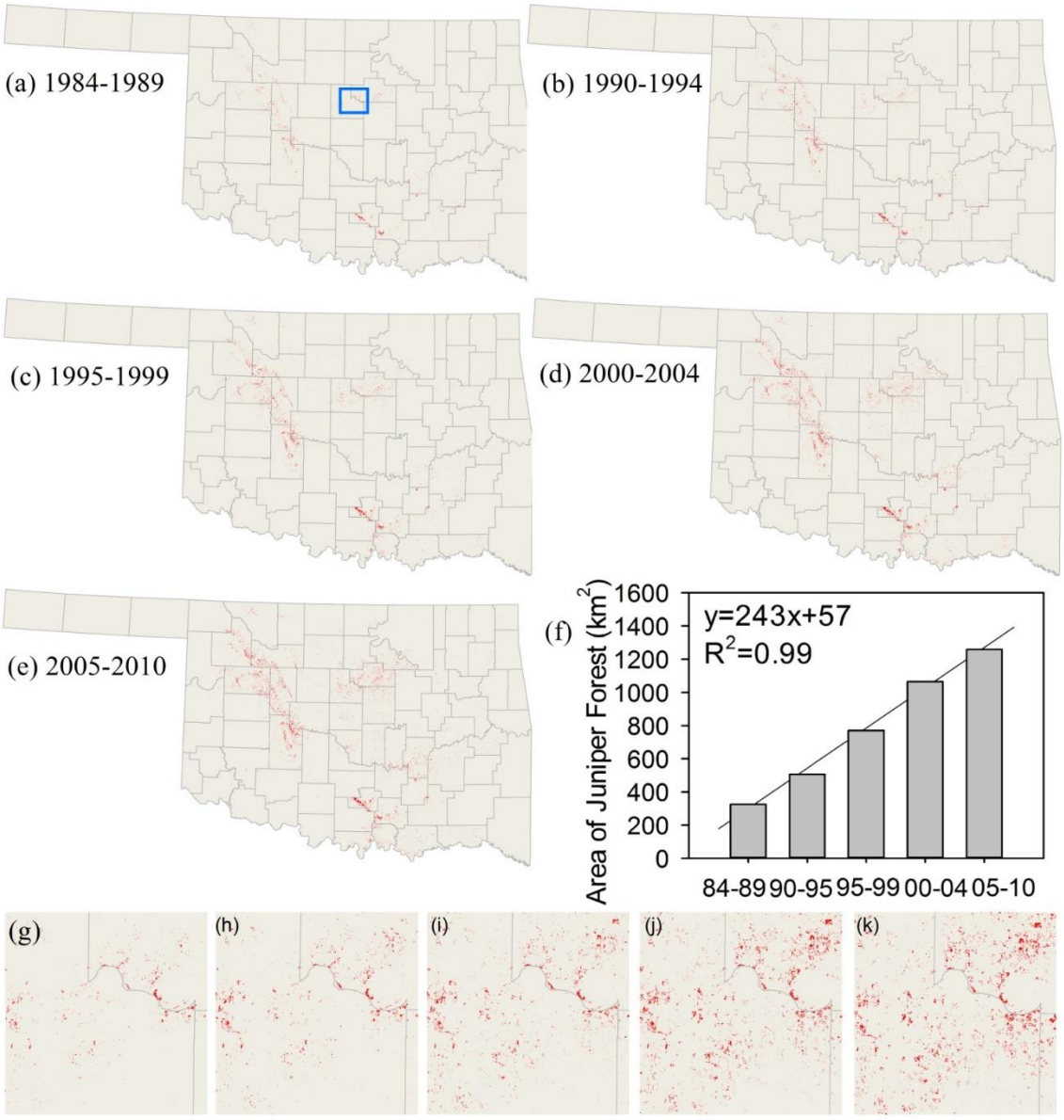

Figure 4.7 Spatial distribution of Juniper forest at five periods during 1984-2010.

Fig. 4.8 shows the stand-age map of the juniper forest in 2010. The juniper stands are composed of ages 1-5 (~24%), 6-10 (~22%), 11-15 (~18%), 16-20 (~15%), and larger than 20 (~21%) years old. Most of the juniper forest (~64%) had a stand age less than 15 years, reflecting juniper encroachment after the 1990s. Juniper stands of 20 years or older comprise 21% of the total, which demonstrates juniper encroachment prior to or in the early 1980s. Collectively, stand-ages suggest that the juniper in Oklahoma is still young at present.

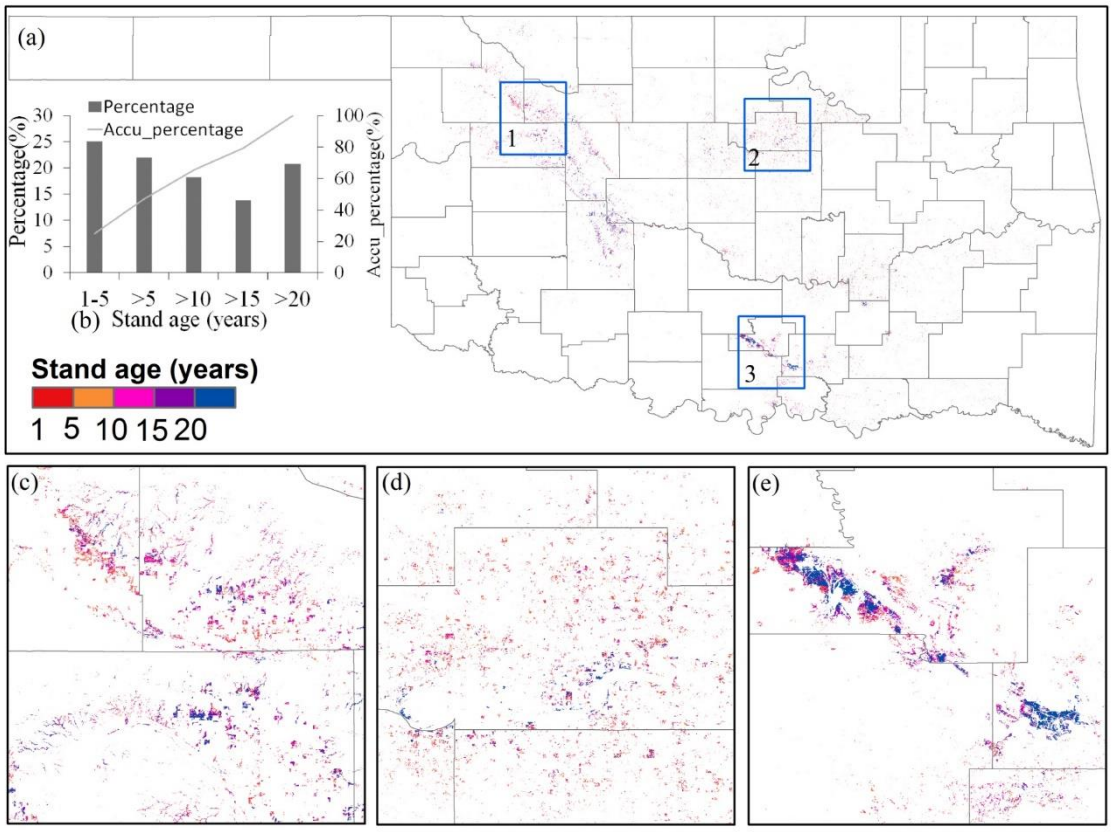

Figure 4.8 Years of juniper in each individual pixel after identified as forest (Stand-age map) in 2010.

The historical juniper forest maps demonstrate that the counties of Oklahoma have experienced various degrees of juniper encroachment. The juniper area in the five study

epochs and the mean stand age in 2010 were calculated for each county (Fig. 4.9). Total land area is different for each county in Oklahoma, so we standardized the juniper forest area of each county using a ratio of the juniper forest area to the total county land area in each time period. This ratio provides more reasonable comparisons of juniper encroachment at the county level. Fig. 4.10 shows that the western and central counties experienced the most substantial encroachment of juniper (e.g. Payne, Dewey, Blaine, and Murray). Payne and Murray counties experienced the relatively strongest juniper encroachment during 1984-2010, with the average annual juniper forest encroachment occupying larger than 1‰ of the county land areas (Fig. 4.11). The mean stand age of the juniper forests in 2010 ranged from 5 to 18 years at the county level (Fig. 4.9). In 2010, twenty-five counties had mean juniper forest stand ages less than 10 years, 8 counties had mean stand ages larger than 15 years, and the remaining 36 counties between 10 and 15 years.

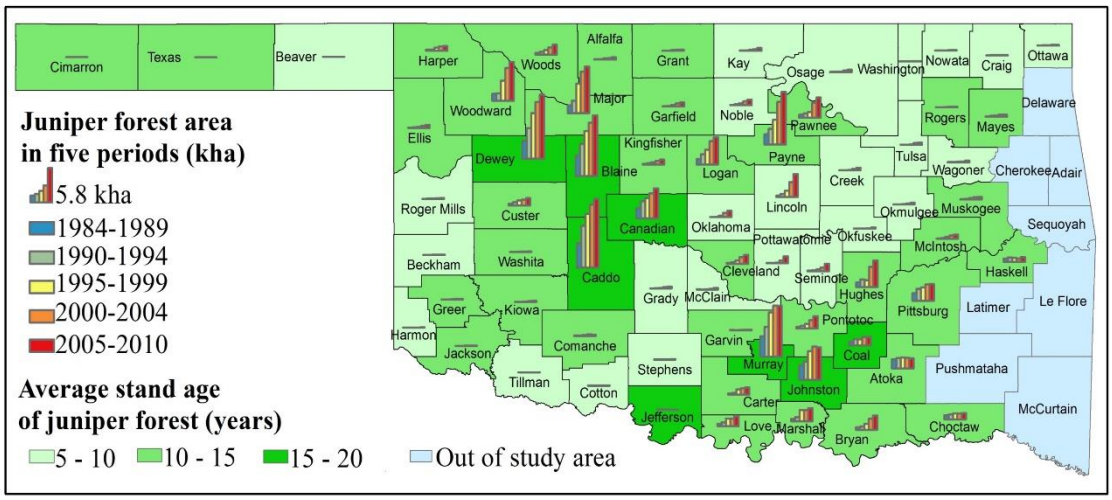

Figure 4.9 Dynamics of juniper forest areas in five periods and average stand age for each county.

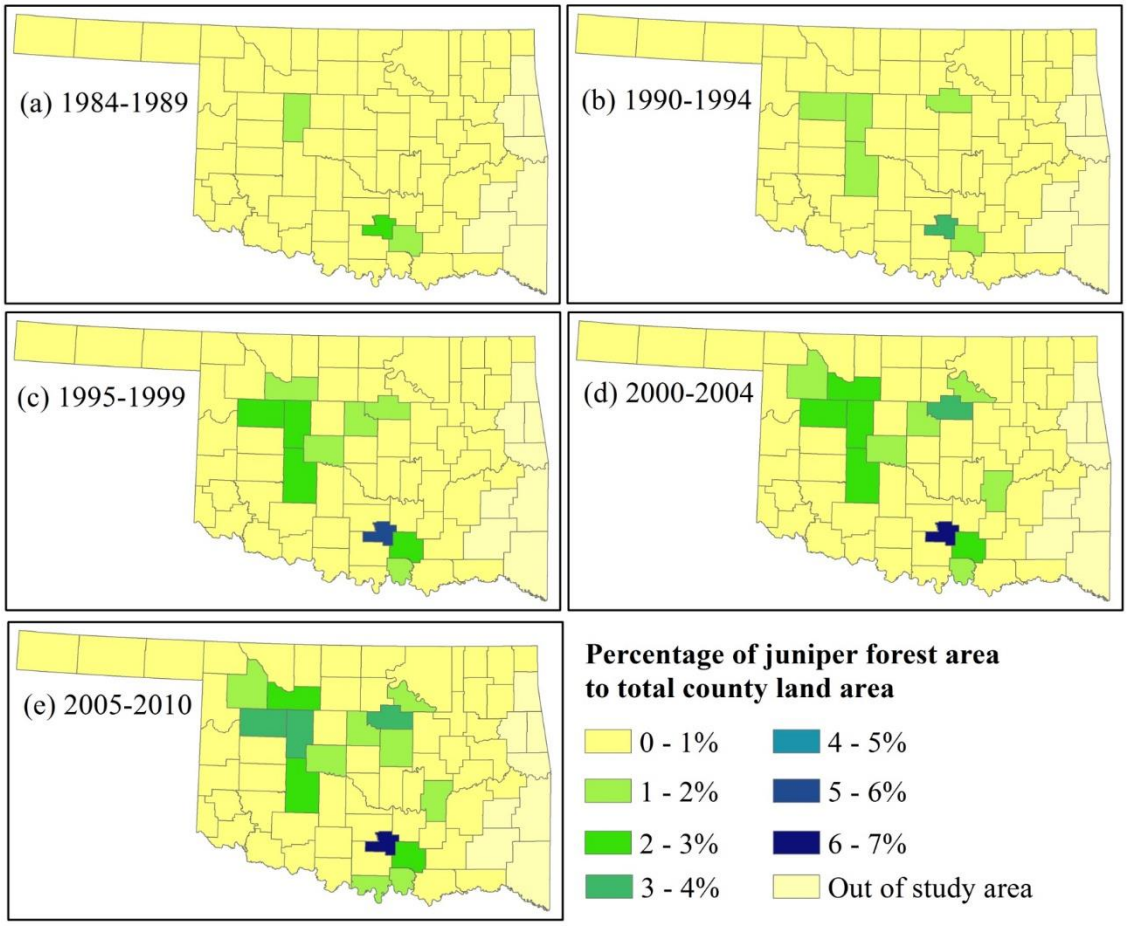

Figure 4.10 Dynamics of the percentage of the juniper forest area to the total county land area in five historical periods.

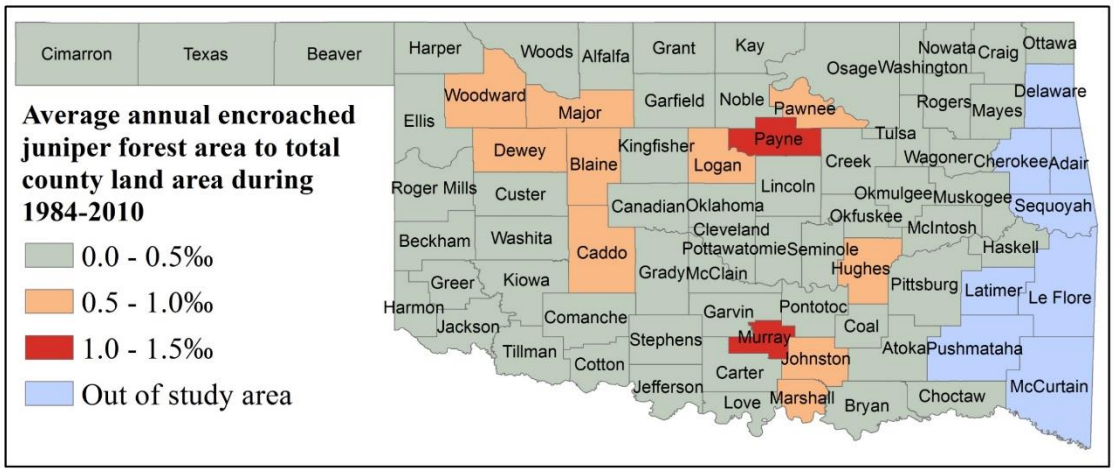

Figure 4.11 The ratio of average annual encroached juniper forest area to total county land area during 1984-2010 at county level.

4.3.4 Geographic characteristics of juniper encroachment

The geographic characteristics of the juniper encroachment were investigated along longitude, latitude, and elevation gradients (Fig. 4.12). From west to east, the juniper forests were mainly concentrated between -100° E ~ -98° E and -97.5° E ~ -95° E (Fig. 4.12a). From the late 1980s to the late 2000s, these two regions had a comparable distribution of juniper forests and rate of encroachment. For example, in the late 1980s the total juniper coverage was 160 km^2 for both regions, and in the late 2000s, the area expanded to 570 km^2 and 590 km^2 for the west and east regions, respectively. The juniper forest encroachment rate was about 18 km^2 per year for both regions.

In terms of latitudinal patterns, juniper encroachment was concentrated in three regions with latitudes of 33.7° N ~ 34.6° N, 34.6° N ~ 35.7° N and 35.7° N ~ 37° N. Juniper encroachment varied along latitude gradients (Fig. 4.12b). During 1984-2010, the region within 35.7° N ~ 37° N experienced the fastest rate of juniper encroachment. The juniper area in this region increased from 130 km^2 to 630 km^2 and the area proportion increased from 37% to 50%. The central region between 35° N ~ 35.7° N experienced moderate juniper encroachments. The juniper area expanded from 11 km^2 to 38 km^2, while area proportion decreased from 33% to 30%. The lower region within 33.7° N ~ 35° N had the lowest juniper encroachment. Although the juniper forest area increased from 100 km^2 to 250 km^2, the area proportion decreased significantly from 30% to 20%.

There are two clear regions of juniper encroachment following an elevation gradient from 90m to 750m. A threshold of about 300m can be used to divide juniper encroachment into low elevation and high elevation clusters. Both clusters experienced notable juniper encroachment from 1984 to 2010. In the late 1980s, the area proportions

were 41% and 58% for high and low clusters, respectively. These proportions changed to 44% and 56% in the late 2000s.

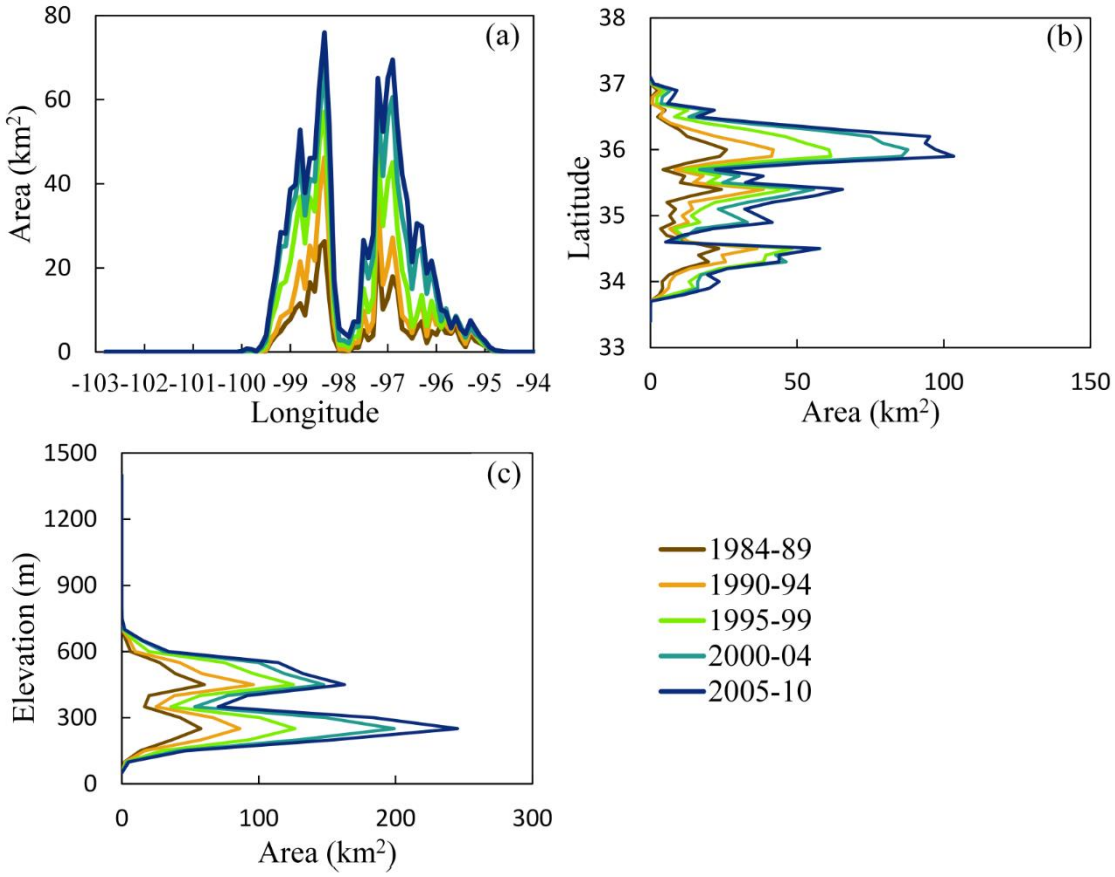

Figure 4.12 Area dynamics in five epochs analyzed by geographic regions of longitude, latitude and elevation.

4.3.5 The potential role of soils in juniper encroachment

Soil water potential, content, and available water storage (AWS) varies among different soil types and affects tree and grass competition. Therefore, we examined the relationships between juniper encroachment and soil texture, depth, and AWS during 1984-2010 (Fig. 4.13-4.15). In Oklahoma, juniper encroachment occurred more frequently on soils of sand and loam than clay soils (Fig. 4.13). Based on the available

soil texture data, juniper cover was largest in sandy loam soils throughout the entire study period of 1984-2010, (Fig. 4.13f).

Fig. 4.14 shows that juniper encroachment occurred widely on various soil depths in Oklahoma during 1984-2010. After the late 1990s, the regions with soil depth > 100 cm had more juniper than did the regions with lower soil depth. Fig. 4.15 shows the percentages of juniper forest area during five periods estimated based on soils characterized by AWS from the top soil (0cm) to different depths of 25cm, 50cm, 100cm and 150cm. This result suggests more juniper encroachment occurred in the soils with lower AWS (Fig. 4.15).

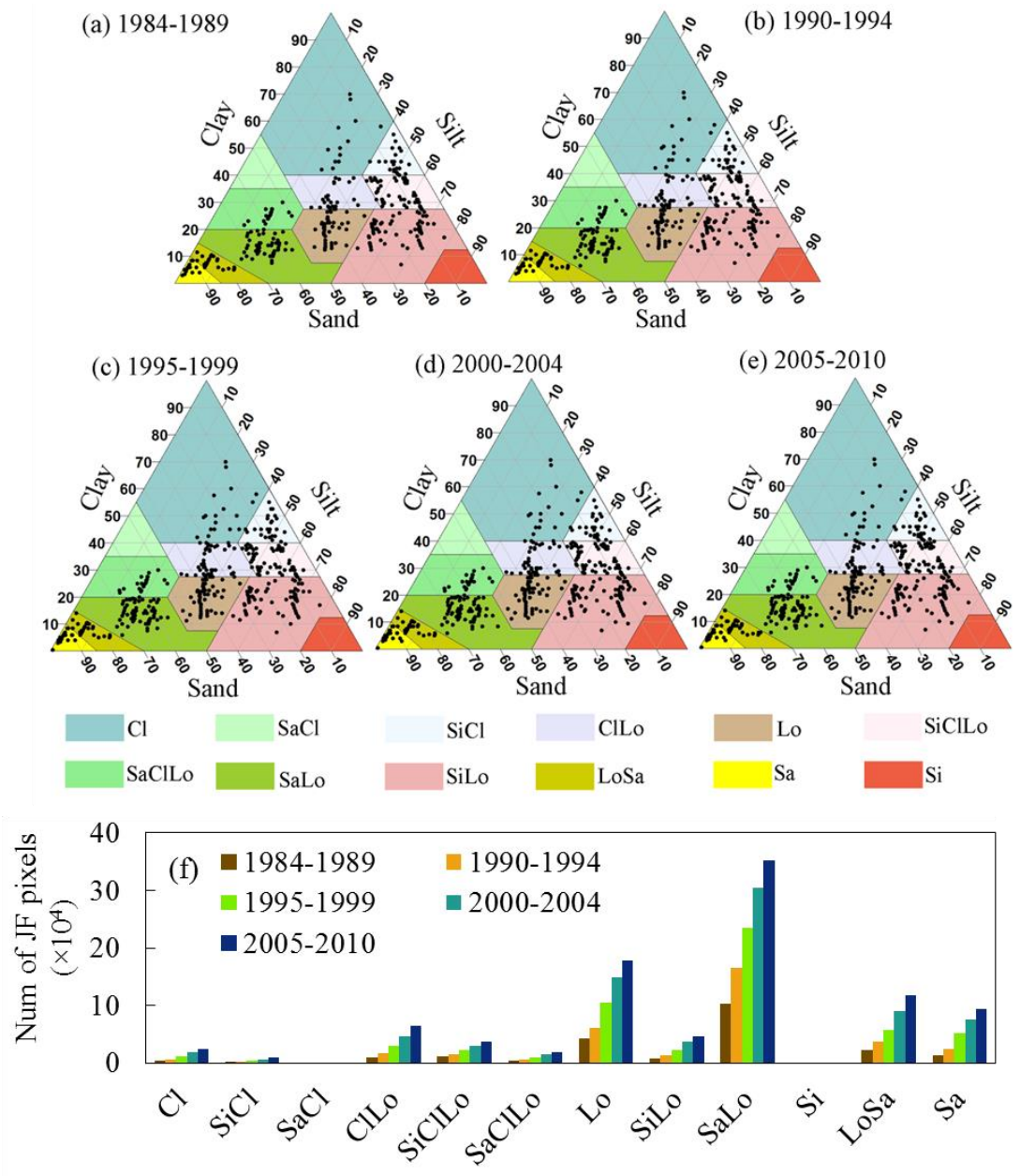

Figure 4.13 (a-e) Juniper forest pixel distribution at different soil texture in five historical periods. The background used the soil classification system of USDA, including clay (Cl), silty clay (SiCl), sandy clay (SaCl), clay loam (ClLo), silty clay loam (SiClLo), sandy clay loam (SaClLo), loam (Lo), silty loam (SiLo), sandy loam (SaLo), silt (Si), loamy sand (LoSa), and sand (Sa). (f) number of Juniper forest (num of JF) pixels at each soil type in five periods.

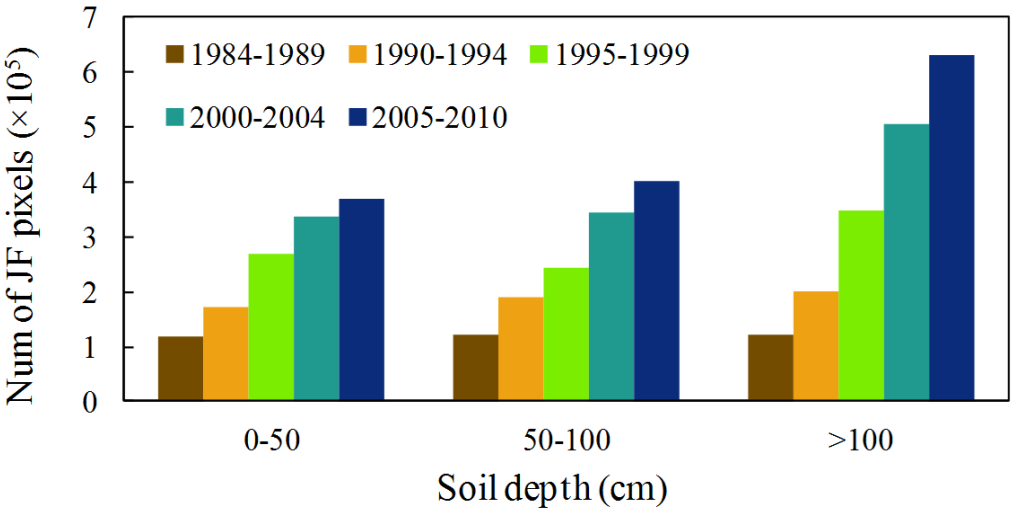

Figure 4.14 The number of Juniper forest (num of JF) pixels at different soil depths during five periods. We used crop root zone depths indicate soil depths, as these depths are generated according to the root-limiting criteria.

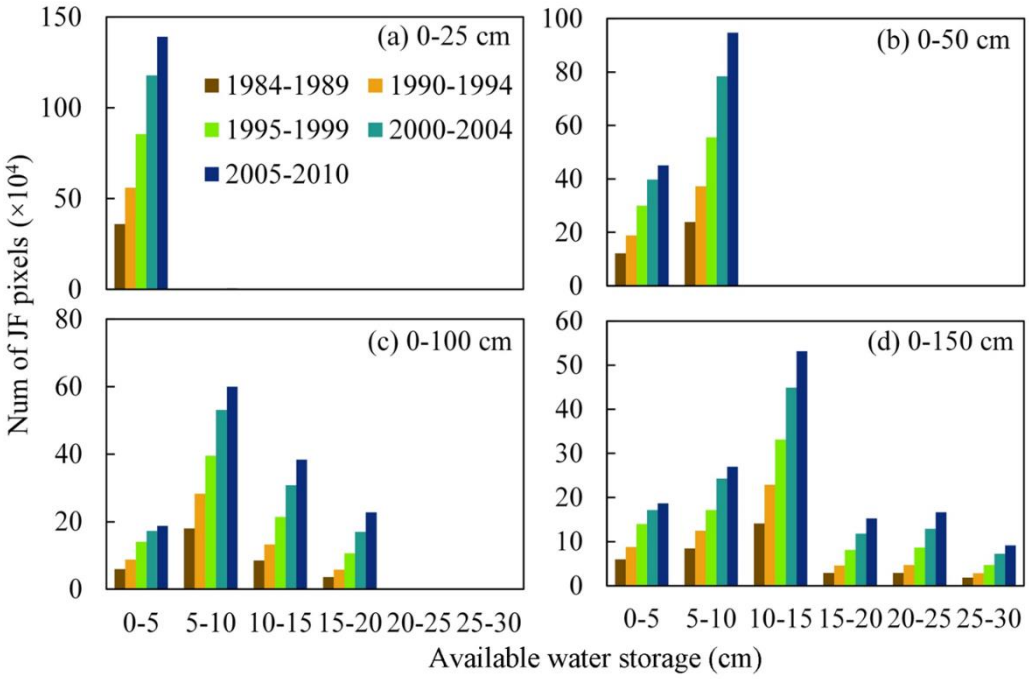

Figure 4.15 Juniper forest encroachment in different soil types examined (a-d) Available Water Storage from the top soil (0cm) to different depths of 25cm (0-25), 50cm (0-50), 100cm (0-100) and 150cm (0-150) .

4.4 Discussion

4.4.1 Uncertainty analysis of juniper forest maps

Some uncertainties could be caused potentially by data quality and algorithm implementations during juniper mapping at the regional scale across complex landscapes. Previous studies suggested some challenges in land cover mapping include the inconsistent quality of input images at temporal and spatial scales (Gong et al. 2013; Hansen et al. 2016a). In this study, data quality analysis at the pixel level showed that good observation data had notable inter-annual variations and ~10% of the pixels did not have good quality data during the winter seasons from 1984 to 1991 (Fig. 4.2). It is possible that some uncertainties exist in the juniper forest maps caused by the uneven availability of Landsat images at temporal and spatial scales. To alleviate the potential uncertainties in data quality, this study generated multi-year juniper forest maps in time periods of 5 or 6 years using a frequency composition method.

A phenology-based algorithm was used to map the juniper forest in Oklahoma during 1984-2010. This algorithm was developed based on the juniper-specific phenological feature of green foliage in winter, which can be identified by NDVI time series data. Non-juniper evergreen species such as live oak (*Quercus virginiana* and *Q. fusiformis*) occur very rarely in this study area, but they might have had phenological features and spectral signatures similar to juniper, which could have caused some uncertainty in the resultant juniper maps. To reduce such potential uncertainty, this study produced a non-juniper evergreen forest map as a mask in the regional implementation of algorithms. This mask, generated from the OKESM, was used to eliminate the possible

confusions in the resultant juniper forest maps produced from the PALSAR/Landsat images.

4.4.2 Spatio-temporal dynamics of juniper encroachment

This study explored the spatial-temporal dynamics of juniper encroachment on the tall- and mixed-grass prairies of Oklahoma during 1984-2010 using PALSAR and long-term Landsat images. The resultant maps clearly show that juniper expanded continuously at the state level and that the encroachment varied significantly at the county level. Our results were consistent with the findings of the early field surveys (Engle et al. 1996). Geographical analysis suggested juniper encroachment expanded along latitudinal and longitudinal gradients to northern and western regions in Oklahoma. This result concurs with observations made by other studies, in that woody plants around the world have expanded latitudinally and that woody encroachment is occurring in water-limited grasslands (Saintilan and Rogers 2015).

From the early to late 2000s, the net juniper forest area increased by ~200 km^2 in Oklahoma. Our result is similar to those reported by Meneguzzo and Liknes (2015) on eastern redcedar (ERC) forest type expansion in eight states of the central United States in 2005 and 2012, which used Forest Inventory and Analysis (FIA) data. Their study showed that the net increase in ERC forest type was ~1160 km^2 from 2005 to 2012 for the entire study area (except North Dakota, for which data was not available). The average increasing area was ~130 km^2 at the state level. Nebraska increased the most with ~600 km^2, followed by Kansas with ~210 km^2, while South Dakota decreased ~24 km^2. The annual increases in ERC forest type ranged from -3 km^2 in South Dakota to ~85 km^2 in Nebraska. Our study estimated that juniper forest expanded 200 km^2 in Oklahoma from

the early 2000s to the late 2000s at a rate of ~40 km^2/year, which is about half the rate calculated for Nebraska and slightly higher than the rate of expansion in Kansas at ~30 km^2/year. Although juniper encroachment varies greatly among counties in Oklahoma, most of the counties had a similar encroachment magnitude (Fig. 4.9) with the reported rate of eastern redcedar expansion in the Loess Canyons region of Lincoln County, Nebraska, at an annual rate of 2% (Walker and Hoback 2007) (Walker and Hoback 2007).

We noticed some discrepancies in area estimates between our remote sensing-based study and the early field survey results in Oklahoma. A survey by the Soil Conservation Service found that eastern redcedar and ashe juniper had expanded from about 6,070 km^2 in 1950 to 14,164 km^2 by 1985 in Oklahoma (Engle et al. 1996). The invaded area was estimated to be more than 16,187 km^2 by 1989 (Grumbles 1989). A 1994 survey reported that over 24,281 km^2 of rangeland and forestland were occupied by these two juniper species (Engle et al. 1996). These numbers were acquired through questionnaire responses from all Natural Resources Conservation Service (NRCS) field offices in Oklahoma. Respondents encircled the regions having more than 50 eastern redcedar or ashe juniper trees per acre on a map of their county (~10 trees per pixel of Landsat) (Engle et al. 1996). These surveys used a classification system based on the number of trees without considering the canopy coverage. In contrast, our study focused on the dynamics of the juniper forest extracted from remote sensing images according to the FAO definition of forests as lands with tree canopy coverage larger than 10%. Therefore, the juniper forest maps produced in this study did not include the regions where juniper trees were present but insufficient for classification as the juniper forest type. In addition, the estimated accuracy of the field survey results, generated by using

questionnaire responses, is unknown. The discrepancy between our results and early field survey reports could be explained by the different classification systems and methodologies. Increasing juniper density and/or juniper growth is expected to convert current juniper woodlands into juniper forests in the future. Therefore, it is necessary to estimate the juniper woodlands using high resolution images (e.g. NAIP) in the next studies, so that we may better understand and predict future juniper encroachment.

4.4.3 Juniper encroachment with soil features

In addition to the dominant explanations for woody plant encroachment (e.g. fire suppression, reduced herbivory, elevated CO_2), some studies proposed that drought and increasing precipitation intensity drive woody plant encroachment into grasslands through changing soil water (DeSantis et al. 2011; Kulmatiski and Beard 2013; Ward et al. 2014). Our study on the spatio-temporal patterns and geographic characteristics of juniper encroachment has suggested that there had been substantial spatial heterogeneity during 1984-2010 in Oklahoma (Fig. 4.7, Fig. 4.9). More encroachment occurred in the central and northwestern counties, within a longitude of -100° E ~ -98° E, -97.5° E ~ -96° E, latitude of 35° N ~ 37° N, and an elevation of 90 ~ 750m. The inconsistent encroachment of juniper into native ecosystems could be attributed to multiple factors. The results of this study provide some remote-sensing evidence for the conclusion that drought may cause a rapid increase of eastern redcedar in Oklahoma (DeSantis et al. 2011). A literature review showed soil water is a factor controlling woody shrub encroachment into the mesic grasslands (Saintilan and Rogers 2015). A field experiment in a sub-tropical savannah ecosystem revealed increased precipitation intensity facilitated the woody plant encroachment (Kulmatiski and Beard 2013). Soil moisture availability

is regulated by precipitation, soil properties, and geomorphology (Eagleson and Segarra, 1985). Likewise, soil available water storage influences the partitioning of precipitation and the effect of water stress on plants during long drought periods, which was demonstrated by a study on the grasslands in Oklahoma (Weng and Luo 2008). Grasses and trees have different root systems, so the competition between them is affected by soil water availability (Wang et al. 2016). Our study reveals that juniper is concentrated more in sand and loam than clay soils and favors soils with relatively low available water storage. These studies suggest soil properties may be associated with the spatially uneven encroachment of juniper in Oklahoma. For example, one study in the Mojave Desert showed soil attributes moderate long-term plant responses to climate (Munson et al. 2015). Additional studies are required to evaluate the roles of soil in juniper encroachment on the tall- and mixed grasslands in Oklahoma. Currently, there remains uncertainty regarding the drivers of woody plant encroachment and predicting its consequences (Van Auken 2009; Williams et al. 2013; Wine et al. 2012). It is necessary to further examine the potential factors affecting the spatio-temporal patterns of juniper encroachment in the future. The results of this study provide new spatial-temporal data as a foundation for these relevant research questions. Our results describing the relationship between soil properties and juniper encroachment will allow land managers to assess encroachment risk using soil data.

4.5 Conclusion

Woody plants are rapidly encroaching on multiple ecosystems, thereby causing many negative effects on water and nutrients cycles, rangeland management, and biodiversity conservation. Long-term juniper encroachment maps were unavailable at the

regional scale, limiting our ability to understand the spatial and temporal dynamics of juniper encroachment and predict encroachment trends. Our study resolved this problem by developing a pixel and phenology-based algorithm to map juniper forests in Oklahoma from 1984 to 2010 by using 14,086 Landsat 5/7 images and PALSAR data. We generated juniper forest maps for five historical epochs during 1984-2010. Based on these maps, we analyzed the spatial dynamics of encroachment at state and county spatial scales and characterized the juniper encroachment by geographic region and soil environment. In addition, the stand age of the juniper forests in 2010 was examined to indicate the current status of encroachment in Oklahoma. The resultant maps clearly indicate that between 1984 and 2010, juniper encroachment occurred at an average annual rate of ~48 km^2/year. Substantial encroachment took place in the western and central counties of Oklahoma. Stand age analysis suggested that the juniper forests in 2010 were young: 45% of juniper stands under 10 years old. Further studies are needed to examine the drivers and potential consequences of juniper encroachment using the produced juniper forest maps.

Supplementary materials

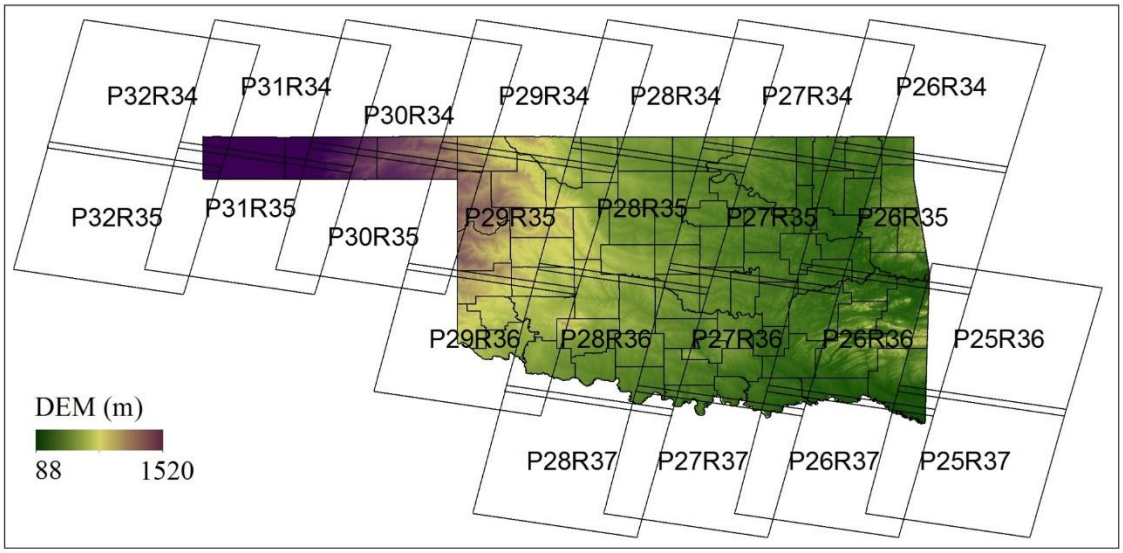

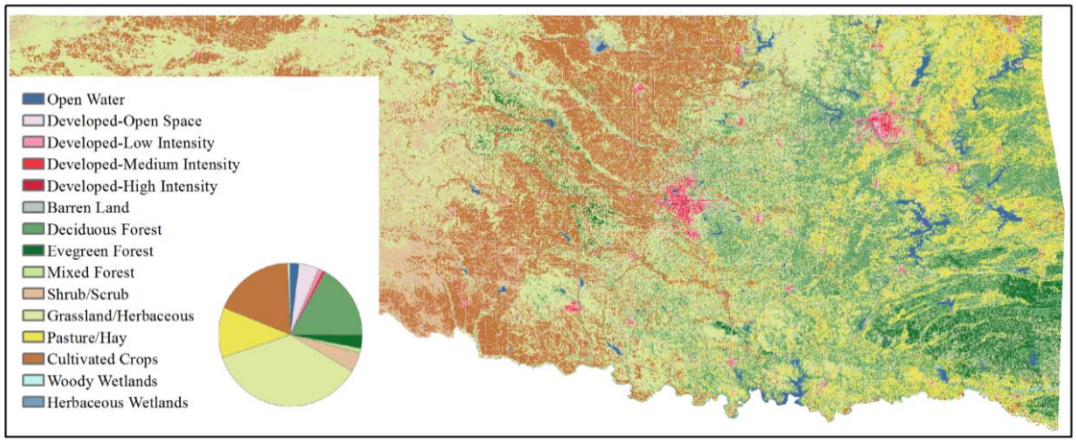

Figure S4.1 (a). The location of the study area. The Digital Elevation Model (DEM) and counties are shown in the figure. (b) The land cover map in Oklahoma from the 2011 National Land Cover Database (2011 NLCD). The pie figure shows the area percentage of different land cover types.

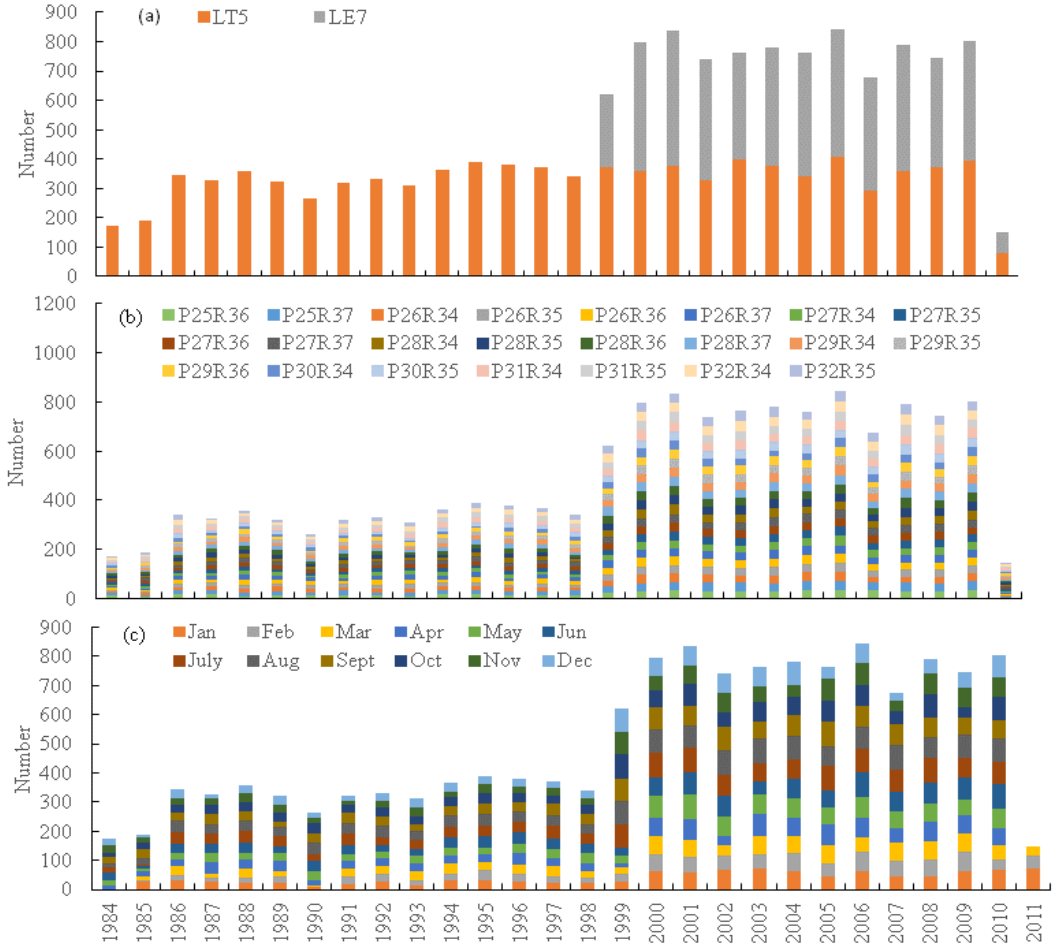

Figure S4.2 The annual distribution of Landsat images in the study area. Statistics was conducted by (a) sensors, (b) path/row and (c) months.

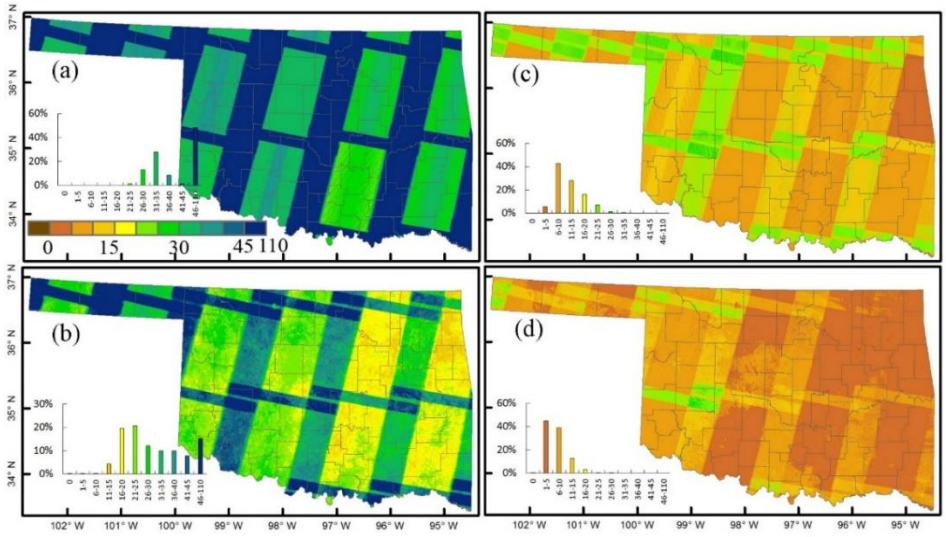

Figure S4.3 Image quality in 2010. (a) the total observation, (b) the good observation, (c) the total observation in winter, (d) the good observation in winter.

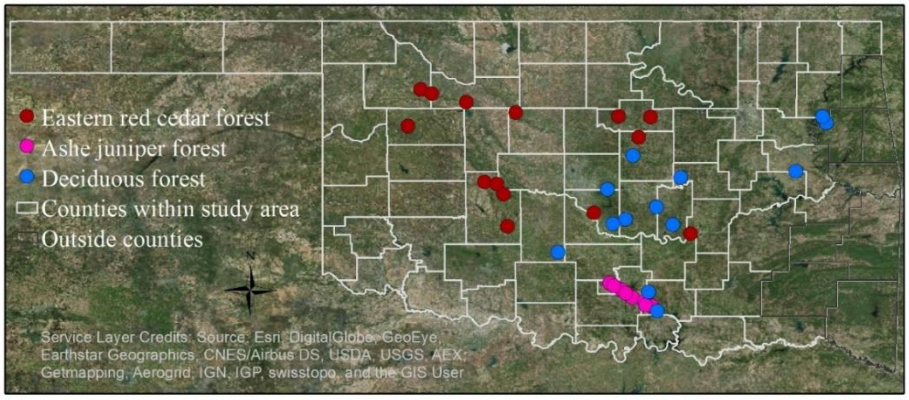

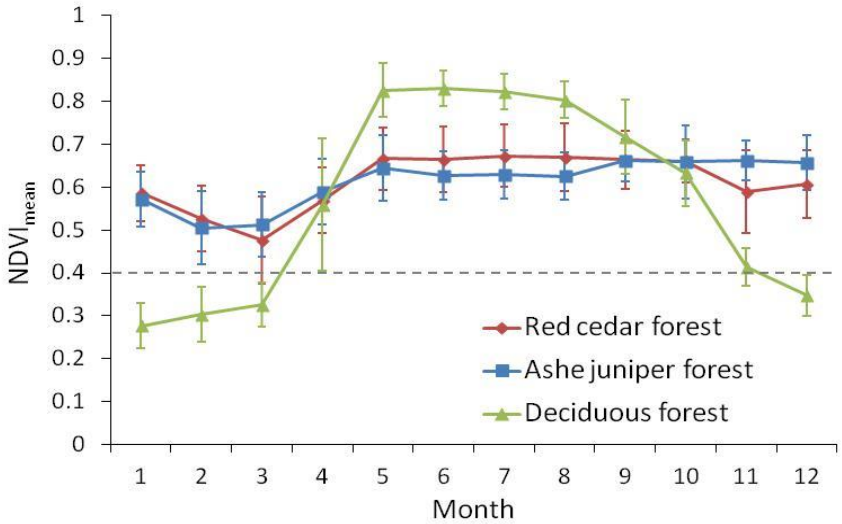

Figure S4.4 (a). Distribution of training region of interests (ROIs) for forests of red cedar, ashe juniper and deciduous. (b). Mean NDVI and standard deviation (SD) in

winter calculated from Landsat5/7 images in winters of 2009 and 2010 using the training ROIs for forests of red cedar, ashe juniper and deciduous.

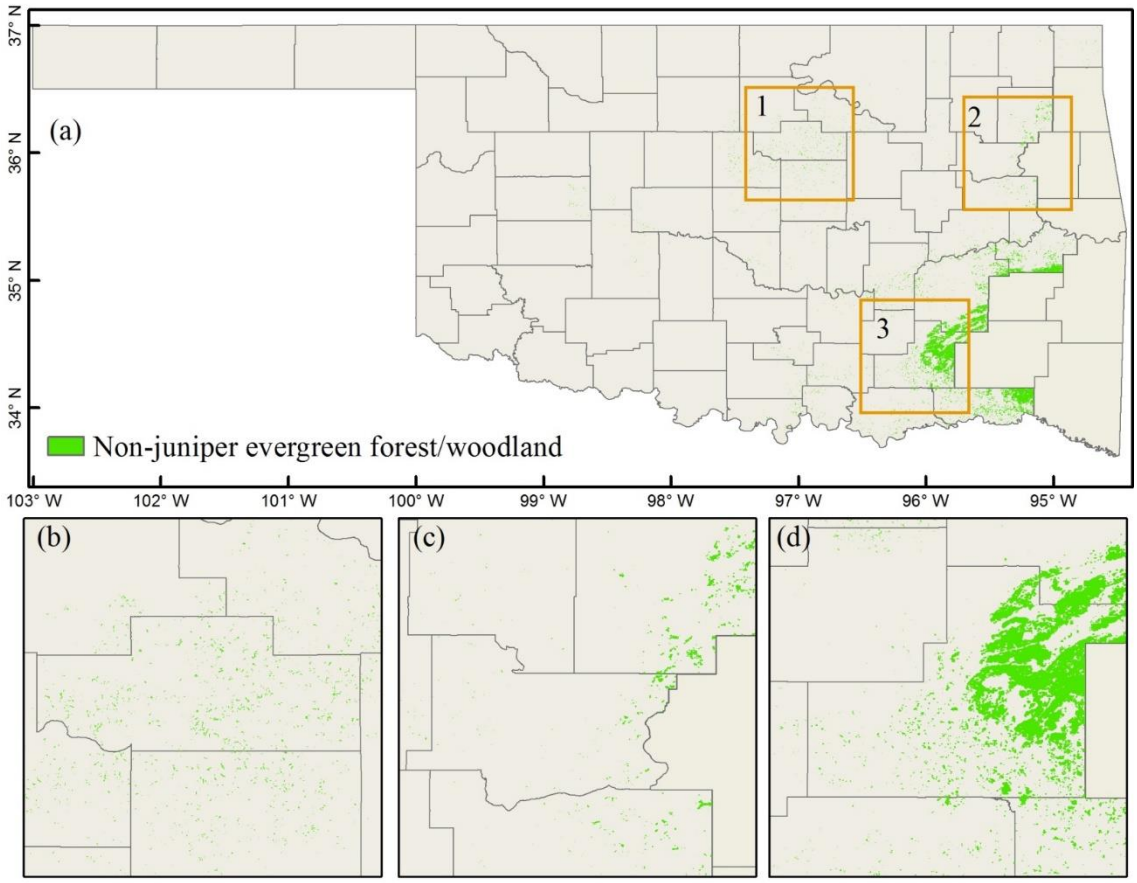

Figure S4.5 30m non-juniper evergreen forest/woodland from OKESM map.

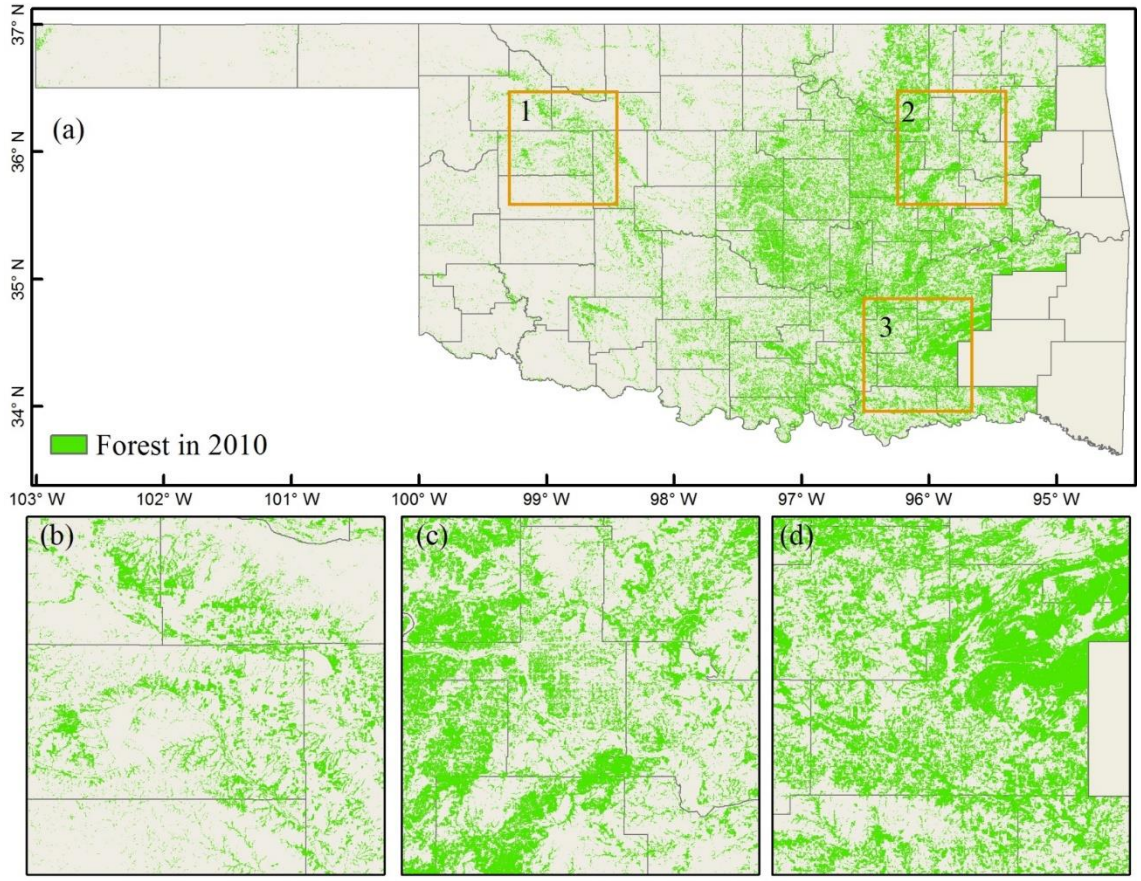

Figure S4.6 PALSAR-based forest map in 2010.

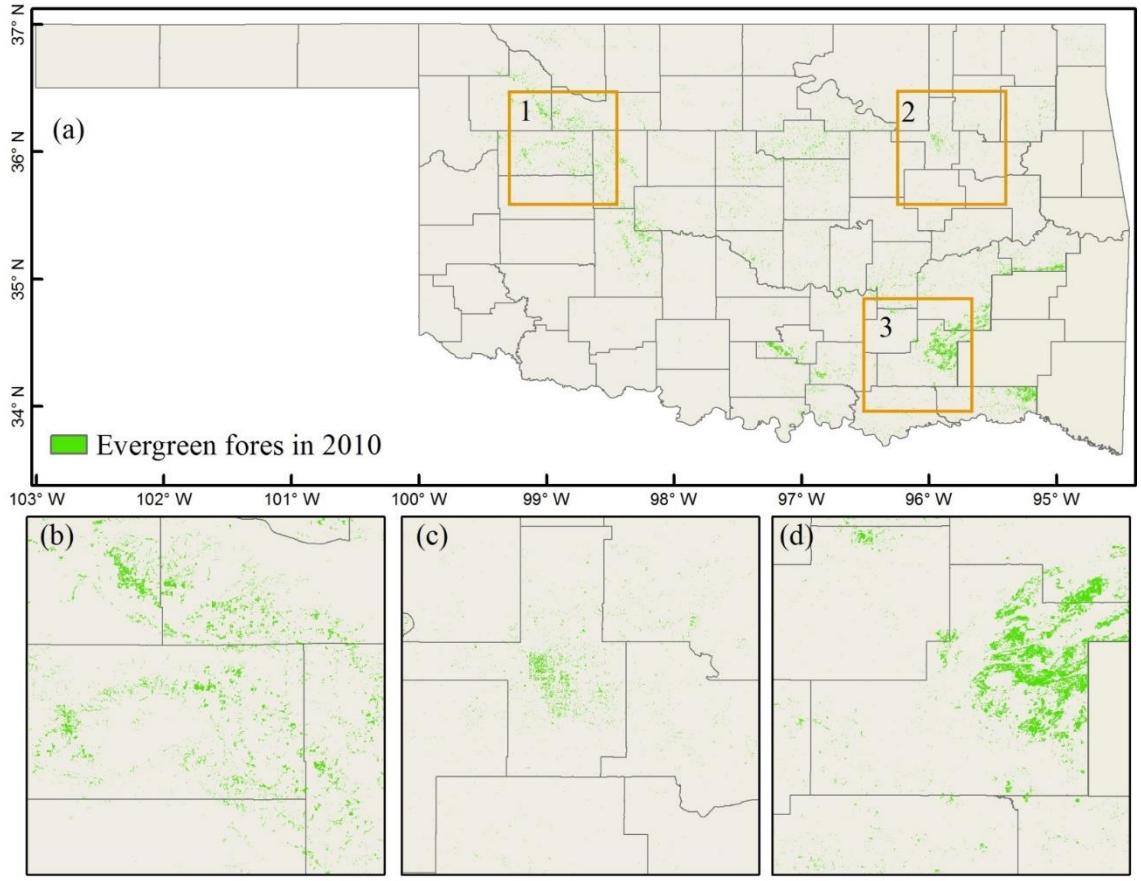

Figure S4.7 PALSAR/Landsat-based evergreen forest in 2010.

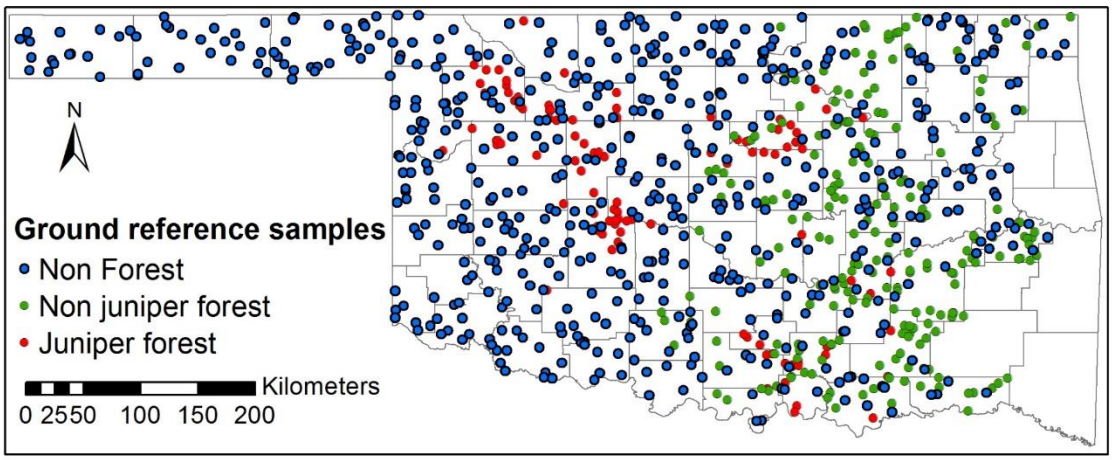

Figure S4.8 Ground reference samples from random points and high spatial resolution images in Google Earth in 2010-2011. The number of samples for juniper forest, non juniper forest and non forest are105, 218 and 612, respectively.

Chapter 5: Canopy and climate controls of gross primary production of deciduous and evergreen oak savannas under the Mediterranean climate

Abstract

Understanding the interactions of climate, vegetation growth, and gross primary production (GPP) is critical for accurate estimation of GPP over years. The eco-physiological response of two functional savannas (deciduous and evergreen) to temporal variations in biophysical factors under similar Mediterranean climate is still unclear. In this study, we compared dynamics of major climatic variables, eddy covariance tower-based GPP (GPP_{EC}), and vegetation indices (VIs: normalized difference vegetation index (NDVI), enhanced vegetation index (EVI), and land surface water index (LSWI)) over the last decade in a deciduous savanna (Tonzi Ranch in California, USA) and an evergreen savanna (Las Majadas del Tietar in Caceres, Spain) under the Mediterranean climate. We also examined the relationships among VIs, GPP_{EC}, and major climatic variables in dry, normal, and wet hydrological years. Seasonal dynamics of climate and GPP_{EC} were similar in both savanna sites, but seasonal dynamics of VIs showed some differences. Both savannas' VIs and GPP_{EC} had similar responses to air temperature. The evergreen savanna showed larger variations in VIs and GPP_{EC} with respect to changes in annual precipitation than did the deciduous savanna. We simulated GPP of these two savanna sites using a light-use efficiency based Vegetation Photosynthesis Model (VPM). The modeled GPP (GPP_{vpm}) at both savanna sites agreed well with the seasonal and interannual dynamics of GPP_{EC} over the study period (slopes of 0.83-1.15 and R^2 values of 0.91-0.97). The LSWI-based water scalar parameter in VPM helped to accurately

estimate GPP under dry, normal, and wet years. The results of this study help better understanding the eco-physiological response of evergreen and deciduous savannas, and also suggest the potential of VPM to simulate interannual variations of GPP in different types of Mediterranean-climate savannas through the integration of vegetation activity and climate data.

5.1 Introduction

Mediterranean-climate savannas provide many ecological services with rich species and unique natural and human landscapes (Baldocchi et al., 2010; Correia et al., 2014). These savannas are composed of sparse trees and continuous understory herbaceous cover, shaped by both human activities and ecological factors (Bugalho et al., 2011; Kobayashi et al., 2013; Marañón et al., 2009). These savannas experience large interannual variations in temperature, rainfall, and soil moisture (Joffre et al., 1999; Ma et al., 2007). In addition, climate models have projected large changes in the Mediterranean climate in this century, including increased mean air temperature, significantly reduced precipitation, more concentrated rainfall events, and longer drought periods (Gao and Giorgi, 2008; Hertig and Jacobeit, 2008). These factors are likely to result in even more complicated interannual variations in gross primary production (GPP) of Mediterranean-climate savanna ecosystems than that of sub-tropical, temperate, and boreal ecosystems (Ma et al., 2007). An accurate estimation of GPP for Mediterranean-climate savannas is, therefore, critical to better understand the feedbacks of these savannas to climate change.

In past decades, production efficiency models (PEMs) based on the light use efficiency (LUE) concept (Monteith, 1972) have been widely used to estimate GPP of

terrestrial ecosystems (Goetz et al., 1999; Running et al., 2004; Turner et al., 2006; Veroustraete et al., 2002; Xiao et al., 2004a; Yuan et al., 2007). These PEMs estimate GPP as the product of photosynthetically active radiation (PAR), the fraction of absorbed PAR (FPAR), and LUE (Monteith, 1972; Potter et al., 1993). The tree-grass mixed and open canopies of Mediterranean-climate savannas present a challenge to accurate estimation of leaf area index and FPAR (Hilker et al., 2008; Ruimy et al., 1999; Ryu et al., 2010; Widlowski, 2010), which may in turn present a challenge for LUE-based GPP models to capture large interannual GPP variations due to year to year changes in temperature, rainfall, and soil moisture.

The LUE-based Vegetation Photosynthesis Model (VPM), which estimates GPP at temporal scales ranging from daily to 8-day, has successfully simulated GPP across a variety of terrestrial ecosystems including tropical savannas (Jin et al., 2013), croplands (Kalfas et al., 2011; Wagle et al., 2015b), grasslands (Wagle et al., 2014), and forests (Xiao et al., 2005a; Xiao et al., 2005b). VPM uses temperature (Tscalar) and water (Wscalar) down-regulation scalars to characterize the effects of these factors on LUE. Satellite-based land surface water index (LSWI) that can track drought-impacted vegetation (Bajgain et al., 2015; Wagle et al., 2014; Wagle et al., 2015b) is used in VPM to compute Wscalar. For these reasons, several GPP model comparison studies have shown VPM's performance to be better than several other commonly used GPP models in capturing the impacts of drought on GPP in grasslands (Dong et al., 2015; Wu et al., 2010). Based on the findings of previous studies and the development of VPM to estimate GPP, in this study, we evaluate the performance of VPM in estimating seasonal dynamics and interannual variability of GPP in two oak savannas sites (one deciduous savanna in

the United States and one evergreen savanna in Spain). These two sites have comparable Mediterranean climates, and in-situ climate and carbon flux data over ten years (Casals et al., 2009; Gilabert et al., 2015; Ma et al., 2007).

The goals of this study were to (1) examine the seasonal dynamics and interannual variations of climate and vegetation growth of the Mediterranean-climate savannas based on flux observations and remote sensing data during the last 10 years; and (2) estimate the potential of the LUE-based VPM to simulate GPP of the Mediterranean-climate savannas under different hydrological conditions. Three specific objectives of this study were to (1) understand the seasonal dynamics of major climatic variables (temperature, precipitation, and radiation), vegetation indices (VIs), and carbon flux of two dominant functional (evergreen and deciduous) savannas under the Mediterranean climate; (2) examine the relationships among temperature, precipitation, VIs, and GPP dynamics; and (3) simulate seasonal dynamics and interannual variations of GPP over dry, normal, and wet hydrological years, using VPM.

5.2 Materials and methods

5.2.1 Study sites

5.2.1.1 Tonzi Ranch (US-Ton) site

The Tonzi Ranch site is located in California, USA (38.4316°N, 120.9660°W, Fig. 5.1a). Dominant species are deciduous blue oaks (*Quercus douglasii*) and understory C_3 grasses, with tree canopy cover of about 40%. This site has a Mediterranean climate with dry and hot summers (little summer precipitation), and wet and mild winters. The mean annual air temperature is 16.5 ^{o}C and the mean annual precipitation is 562 mm. The landscape features and relevant information of this site are shown in Fig. 5.1b and Table

5.1. Detailed information on the site can be found in an earlier publication (Ma et al. 2007).

5.2.1.2 Las Majadas del Tietar (ES-LMa) site

The Las Majadas del Tietar site is located at Caceres, Spain (39.9415°N, 5.7734°W Fig. 5.1a). Dominant species are evergreen holm oak trees (*Quercus ilex ssp ballota Lam.*) and annual C_3 grasses, with tree canopy cover of about 20%. This site experiences a Mediterranean climate and has a mean annual air temperature of 16.7 ^{o}C and mean annual precipitation of 528 mm with summer precipitation comprising less than 6%. The landscape features and relevant information of this site are shown in Fig. 5.1c and Table 5.1. Detailed information on the site can be found in an earlier publication (Casals et al. 2009).

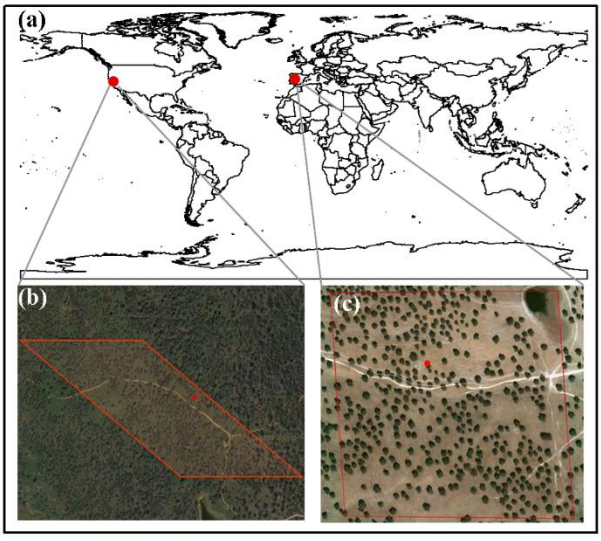

Figure 5.1 Geolocation of two savanna flux tower sites in USA and Spain (a); landscapes at the US-Ton site, USA (b); and landscapes at the ES-LMa site, Spain (c). The red square line in Figures b and c corresponds to the size of one MODIS pixel at 500 m spatial resolution, and the red dot represents the location of the flux tower.

Table 5.1 Summary of two savanna study sites

Site code	Site name	Country	Lat	Lon	Dominant species	MAP (mm)	MAT (˚C)	Flux data used	References
US-Ton	Tonzi Ranch	US.	38.4316	-120.966	Deciduous blue oak, C3 grass	562	16.5	2002-2013	Ma et al. (2007)
ES-LMa	Las Majadas del Tietar	Spain	39.9403	-5.7746	Evergreen holm oak, C3 grass	528	16.7	2004-2012	Casals et al. (2009)

5.2.2 Data

5.2.2.1 CO_2 flux and meteorological data

The climate and carbon flux data used in this study were downloaded from the AmeriFlux website (http://ameriflux.ornl.gov/) for the US-Ton site and European Fluxes Database Cluster (http://www.europe-fluxdata.eu/) for the ES-LMa site. We acquired the gap-filled half-hourly level 2 data over twelve years (2002-2013) for the US-Ton site. For the ES-LMa site, we acquired level 4 weekly data over 8 years (2004-2011) and half-hourly level 2 data for 2012. We aggregated half hourly eddy covariance tower-based GPP (GPP_{EC}) and meteorological data into 8-day intervals to match the temporal resolution of MODIS-derived VIs.

5.2.2.2 MODIS surface reflectance, vegetation indices, and GPP product

This study used the MODIS 8-day land surface reflectance product (MOD09A1) at 500 m spatial resolution. It includes seven spectral bands: red (620-670 nm), blue (459-479 nm), green (545-565 nm), NIR1 (841-876 nm), NIR2 (1230-1250 nm), SWIR1 (1628-1652 nm), and SWIR2 (2105-2155 nm). Three vegetation indices: NDVI (Tucker 1979), EVI (Huete et al. 2002; Huete et al. 1997b), and land surface water index (LSWI)) (Xiao et al. 2004a; Xiao et al. 2005c) were calculated using the blue, red, NIR1, and

SWIR1 spectral bands as shown in equations 1-3. The MOD09A1 data were downloaded from the Earth Observation and Modeling Facility (EOMF) data portal at the University of Oklahoma (http://eomf.ou.edu/visualization/).

$$NDVI = \frac{\rho_{NIR} - \rho_{Red}}{\rho_{NIR} + \rho_{Red}} \tag{5.1}$$

$$EVI = 2.5 \times \frac{\rho_{NIR} - \rho_{Red}}{\rho_{NIR} + 6 \times \rho_{Red} - 7.5 \times \rho_{Blue} + 1} \tag{5.2}$$

$$LSWI = \frac{\rho_{NIR} - \rho_{SWIR}}{\rho_{NIR} + \rho_{SWIR}} \tag{5.3}$$

The MODIS land science team provides the global standard MODIS GPP (GPP_{mod}) product (MOD17A2) at 1 km spatial resolution and 8-day temporal resolution (Running et al. 2004; Zhao and Running 2010; Zhao et al. 2005). MOD17A2 data (version-55 of 2002-2012, version-5 of 2013) were downloaded from NASA LAADS website (https://ladsweb.nascom.nasa.gov/data/search.html) for the model comparison.

5.2.3 Analysis of climate, vegetation indices, and carbon flux data

We examined the seasonal and interannual dynamics of PAR, mean air temperature (T_{air}), mean precipitation (Precip), soil water content (SWC), VIs, and GPP_{EC}. We computed annual precipitation (AP_{hyd}), mean annual precipitation (MAP_{hyd}), and standard deviation of annual precipitation (SD_{hyd}) over each hydrological (hyd) year (hydrological year begins in September and ends in August of the following year) across the study period. There is not a universal physical variable to quantitatively describe the types of the hydrological years (dry, normal, and wet years) at the annual scale. Precipitation is a main variable determining the humidity and dryness (Chang and Kleopa 1991; Heim 2002). In addition, drought indices are usually used to monitor different types

of hydrological systems (McKee et al. 1993; Palmer 1965; Vicente-Serrano et al. 2010). The Standardized Precipitation Evapotranspiration Index (SPEI) is the difference between precipitation (P) and Potential Evapotranspiration (PET) (Vicente-Serrano et al. 2010). This climatic water balance-based drought index includes the effects of precipitation and temperature variations on drought assessment. A global assessment showed good performance of the SPEI to capture drought impacts on agriculture, ecology, and hydrology (Vicente-Serrano et al. 2012). More information about the SPEI was shown in SI Appendix. To explore the responses of these two savannas to the interannual variations of precipitation, and to evaluate the performance of VPM under different hydrological conditions, we classified the study period into three types of hydrological years (dry, normal, and wet) based on annual precipitation and the SPEI.

We performed simple regression analysis between VIs (NDVI and EVI) and GPP_{EC} over the growing season to understand how vegetation greenness is related to canopy photosynthesis in these two savanna ecosystems. The growing season was defined as the period when $GPP_{EC} > 1$ g C m^{-2} day^{-1} as in previous studies (Dong et al. 2015a; Jin et al. 2013; Wagle et al. 2014).

The responses of EVI and GPP to daytime mean air temperature ($T_{air\_daytime}$) were examined to determine the optimal temperature (T_{opt}) parameter for GPP simulation in VPM. We categorized 8-day EVI and GPP_{EC} from both sites into different temperature classes at 1°C interval and computed mean EVI and GPP_{EC} in all years for each temperature bin. Similarly, we also computed mean EVI and GPP_{EC} only in wet years for each temperature bin to exclude the potential influence of water stress in dry years on

determining T_{opt}. The $T_{air\_daytime}$ at the maximum turning point (the inflection point) of the EVI and GPP_{EC} curves was selected as T_{opt}.

5.2.4 GPP simulation from VPM

The satellite-based VPM was developed to estimate vegetation GPP over the photosynthetically active period (Xiao et al. 2004a; Xiao et al. 2004b). The VPM estimates GPP as the product of *LUE*, $FPAR_{chl}$, and *PAR*.

$$GPP_{VPM} = \varepsilon_g \times FPAR_{chl} \times PAR \tag{5.4}$$

where ε_g is the LUE (g C mol^{-1} photosynthetic photon flux density, PPFD), $FPAR_{chl}$ is the fraction of PAR absorbed by chlorophyll, and PAR is the photosynthetically active radiation.

$FPAR_{chl}$ is estimated as a linear function of EVI (Eq. 5), and the coefficient a is set to be 1.0 following previous studies (Xiao et al. 2005a; Xiao et al. 2004b).

$$FPAR_{chl} = a \times EVI \tag{5.5}$$

ε_g is estimated as the down-regulation of maximum light use efficiency ε_0 (g C mol^{-1} PPFD) with temperature and water scalars to account for temperature and water stresses as shown in Eq. (6).

$$\varepsilon_g = \varepsilon_0 \times T_{scalar} \times W_{scalar} \tag{5.6}$$

ε_0 varies based on vegetation functional types (C_3 or C_4 biomes) in the VPM. The estimation methods include literature surveys and site-based analysis of NEE and photosynthetic photon flux density (PPFD) (Xiao 2006). In this study, ε_0 was determined from the NEE-PPFD relationship as shown in previous studies (Wagle *et al.*, 2014, Wagle *et al.*, 2015). The Michaelis-Menten function (Eq. 7) was used to estimate ε_0 at an

ecosystem level based on two weeks of half-hourly flux data during peak savanna growth (May 13-26, 2010 for the US-Ton site, May 3-16, 2010 for the ES-LMa site). These periods were selected based on the maximum 8-day NEE or GPP values for the study sites. Based on this analysis, we used the ε_0 value of 0.042 mol CO_2 mol^{-1} PPFD or 0.5 g C mol^{-1} PPFD (Fig. 5.2) for both sites across all site-years.

$$NEE = \frac{\varepsilon_0 \times GPP_{max} \times PPFD}{\varepsilon_0 \times PPFD + GPP_{max}} + ER \tag{5.7}$$

where GPP_{max} is the maximum canopy CO_2 uptake rate ($\mu molm^{-2}\ s^{-1}$) at light saturation and ER is ecosystem respiration.

T_{scalar} was estimated at each time step based on the relationship between stomatal conductance and air temperature (Jarvis, 1976) following the equation used in the Terrestrial Ecosystem Model (Raich *et al.*, 1991).

$$T_{scalar} = \frac{(T - T_{min})(T - T_{max})}{(T - T_{min})(T - T_{max}) - (T - T_{opt})^2} \tag{5.8}$$

where T_{min}, T_{max}, and T_{opt} are minimum, maximum, and optimal temperatures for photosynthetic activities, respectively. We set T_{min} and T_{max} values to be 0°C and 50°C considering the lethal effects of cold temperature (frost) and extreme heat on plant growth and development. T_{min} and T_{max} are generally selected in such a way that the sites do not experience that level of too low or high temperature during the growing season. T_{opt} for photosynthesis varies widely among different vegetation types (Baldocchi et al. 2001; Medlyn et al. 2002; Sims et al. 2008). Two sites had different portions of grass and tree covers which might alter T_{opt}. In this study, the site-specific T_{opt} was, therefore, estimated using the method described in section 5.2.3. As photosynthesis occurs in daytime, we

used daytime mean air temperature instead of the daily mean air temperature to calculate the T_{scalar}.

W_{scalar} was estimated based on the satellite-derived land surface water index (LSWI) as:

$$W_{scalar} = \frac{1+LSWI}{1+LSWI_{\max}} \tag{5.9}$$

Where $LSWI_{max}$ is the maximum LSWI within the growing season for individual pixels.

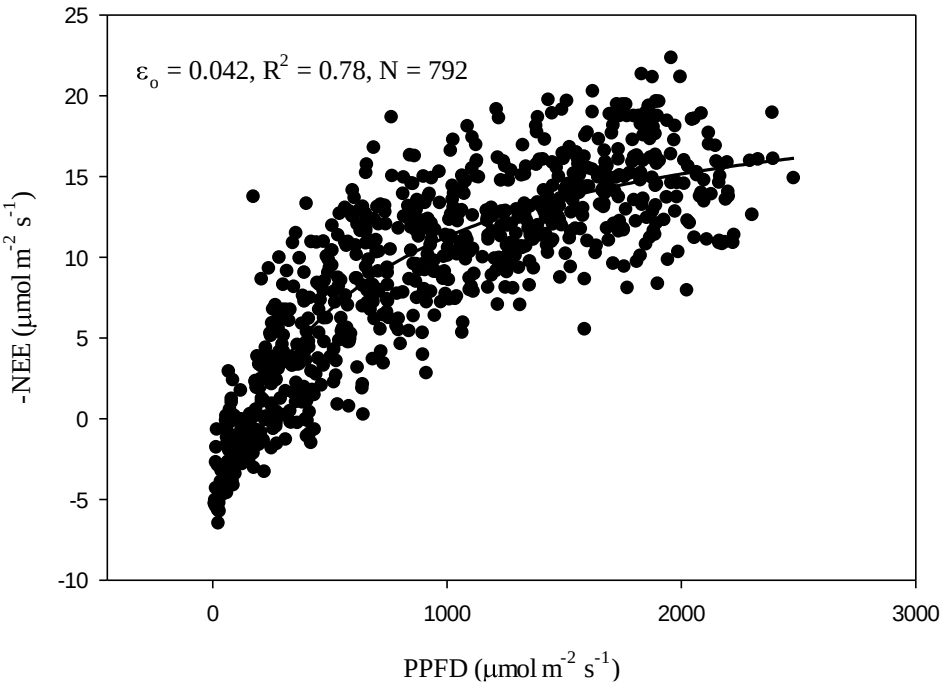

Figure 5.2 Light-response curve function based on two weeks of flux tower measurements during the selected time periods (May 13-26, 2010 for the US-Ton site, May 3-16, 2010 for the ES-LMa site). Data points represent 30-minute daytime net ecosystem CO2 exchange (NEE) values and data were pooled for both sites. PPFD is photosynthetic photon flux density. ε0 is the apparent quantum yield (mol CO2mol−1 of photon) from the initial slope of the light-response curve.

5.3 Results

5.3.1 Seasonal dynamics and interannual variations of climate, vegetation indices, and GPP_{EC}

The seasonal dynamics and interannual variations of PAR, T_{air}, SWC, and Precip at two savanna sites are shown in Fig. 5.3 and Table 5.2. Both sites had similar seasonal dynamics of PAR and T_{air}, with PAR ranging from 10 to 70 mol m^{-2} day^{-1} and T_{air} ranging from 4 to 35 °C. SWC at the US-Ton site ranged from 10% to 40% and dropped significantly below 15% in dry seasons, while SWC at the ES-LMa site ranged from 2% to 40% and was approximately 5% in dry seasons. In general, rainfall mainly occurred in autumn, winter, and the next spring at both sites (Fig. 5.3d). Over the study period, the US-Ton site had a MAP_{hyd} of 549 mm (Fig. S5.1a, Table 5.2) with summer precipitation less than 1%. And the ES-LMa site had a MAP_{hyd} of 633 mm (Fig. S5.1b, Table 5.2) with summer precipitation about 5%. The monthly SPEI time series for both sites were shown in Fig. S5.1c and Fig. S5.1d. We identified the wet, normal and dry years based on the intensity and duration of the monthly SPEI and the annual precipitation. We identified four dry years (2006-2007, 2007-2008, 2008-2009, and 2012-2013), three normal years (2002-2003, 2003-2004, 2009-2010), and four wet years (2004-2005, 2005-2006, 2010-2011, and 2011-2012) at the US-Ton site. Similarly, at the ES-LMa site, we identified four dry years (2004-2005, 2007-2008, 2008-2009, and 2011-2012), one normal year (2005-2006), and three wet years (2006-2007, 2009-2010, and 2010-2011).

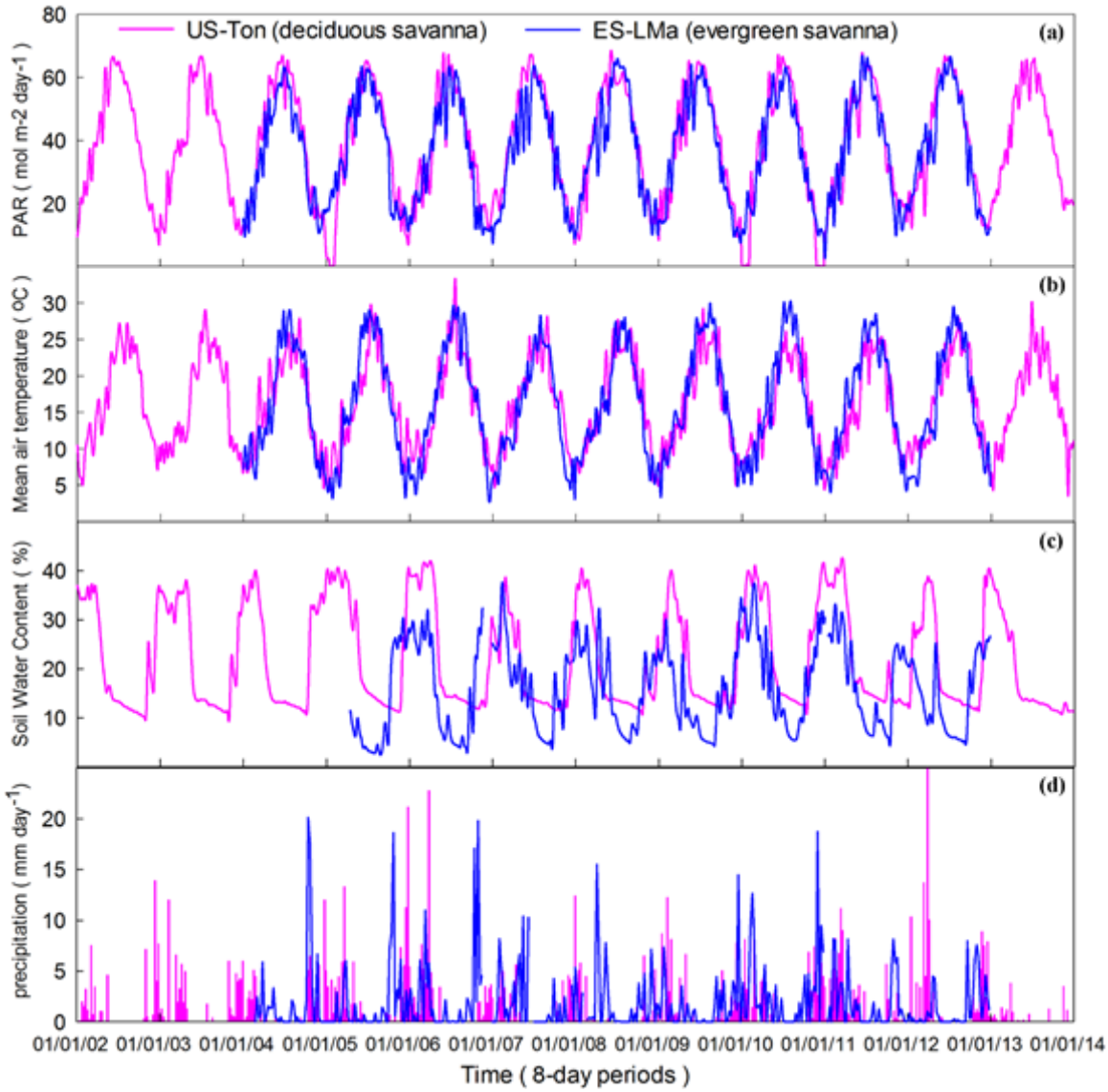

Figure 5.3 Seasonal dynamics and interannual variations (8-day values) of photosynthetically active radiation (PAR), daily mean air temperature, soil water content, and precipitation at two savanna sites over the study period.

Table 5.2 Summary of mean air temperature (Ta), mean photosynthetically active radiation (PAR), accumulated precipitation, and mean soil water content (SWC) at two ssavanna sites. Dry years are highlighted by red, normal years are highlighted by green and wet years are highlighted by blue.

Site	Year	Ta	PAR (mol m-2 day-1)	Precipitation (mm)	SWC (%)
US-Ton	2002-2003	17.3	42.3	391	22.3
	2003-2004	15.8	39.3	367	22.4

	2004-2005	15.0	35.7	723	28.9
	2005-2006	16.5	36.9	952	24.1
	2006-2007	16.0	40.2	381	19.9
	2007-2008	16.0	40.2	377	20.8
	2008-2009	15.6	39.3	508	21.6
	2009-2010	17.6	48.8	314	24.2
	2010-2011	15.2	40.6	886	25.8
	2011-2012	16.5	40.4	746	19.8
	2012-2013	16.8	40.2	393	21.1
	Average	16.2	40.3	549	22.8
	SD	0.7	3.0	212	2.5
ES-LMa	2004-2005	16.2	37.2	562	
	2005-2006	15.4	34.8	685	18.3
	2006-2007	15.2	33.5	876	18.6
	2007-2008	15.6	38.7	528	16.4
	2008-2009	15.9	37.6	403	14.7
	2009-2010	16.1	35.0	763	19.2
	2010-2011	15.7	35.4	839	19.4
	2011-2012	13.0	35.0	339	16.3
	Average	15.3	35.7	633	17.6
	SD	0.9	1.5	175	1.5

Seasonal dynamics of VIs (NDVI, EVI, and LSWI) and GPP_{EC} at both savanna sites varied from year to year depending on environmental drivers (Fig. 5.4). As both sites did not experience severe water stress in 2005-2006, 2009-2010 and 2010-2011, we compared the VIs and GPP_{EC} dynamics at two savanna sites during those three

hydrological years. At both sites, GPP_{EC} showed similar seasonal dynamics: started to increase and exceeded 1 g C m^{-2} day^{-1} during autumn, peaked in the following spring, then decreased to 1 g C m^{-2} day^{-1} or less in summer. This suggests that vegetation in these two savannas greened up during autumn and entered into senescence in summer. These GPP seasonal patterns showed close correspondence with the seasonal patterns of VIs, as VIs started to increase in autumn, declined rapidly before summer, and remained low throughout the summer. However, VIs at the ES-LMa site peaked in winter and exhibited a high plateau during the growing season from winter to next spring, while VIs at the US-Ton site peaked in spring and did not exhibit a high plateau during the entire growing season. Although VIs peaked in different periods at two sites, peak GPP_{EC} occurred at almost the same time (Fig. 5.4).

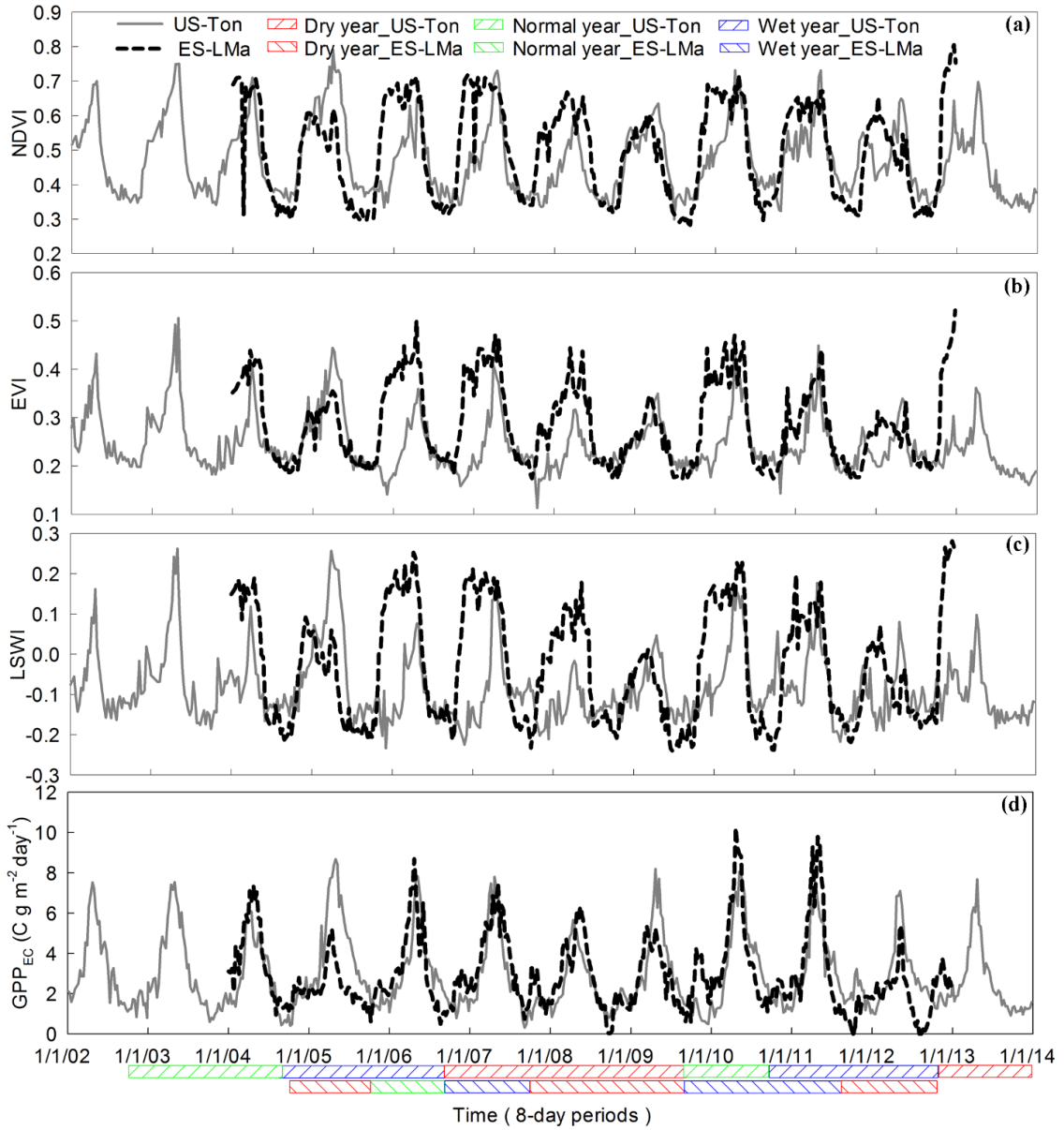

Figure 5.4 Seasonal and interannual variations in MODIS-derived vegetation indices (normalized difference vegetation index, NDVI, enhanced vegetation index, EVI, and land surface water index, LSWI) and tower-derived gross primary production (GPPEC) at two savanna sites.

5.3.2 The relationships among climate, vegetation indices, and GPP_{EC}

Relationships between VIs (NDVI and EVI) and GPP_{EC} during the plant growing season were examined under four scenarios: over the entire study period; dry years; normal years; and wet years (Fig. 5.5). NDVI and EVI accounted for more variabilities

of GPP_{EC} at the US-Ton site (R^2 = 0.36 and 0.55, respectively, Fig. 5.5 (a, b)) than at the ES-LMa site (R^2 = 0.20 and 0.33, respectively, Fig. 5.5 (e, f)) over the entire study period. Comparison of the relationships between GPP_{EC} and VIs in dry, normal, and wet years showed that the relationships were stronger in dry years at both sites (Fig. 5.5 (c, d, f)). These results indicated that GPP_{EC} was more sensitive to the variations in EVI at both savanna sites in dry years. In addition, EVI explained more variances of GPP_{EC} than did NDVI in each scenario at both sites.

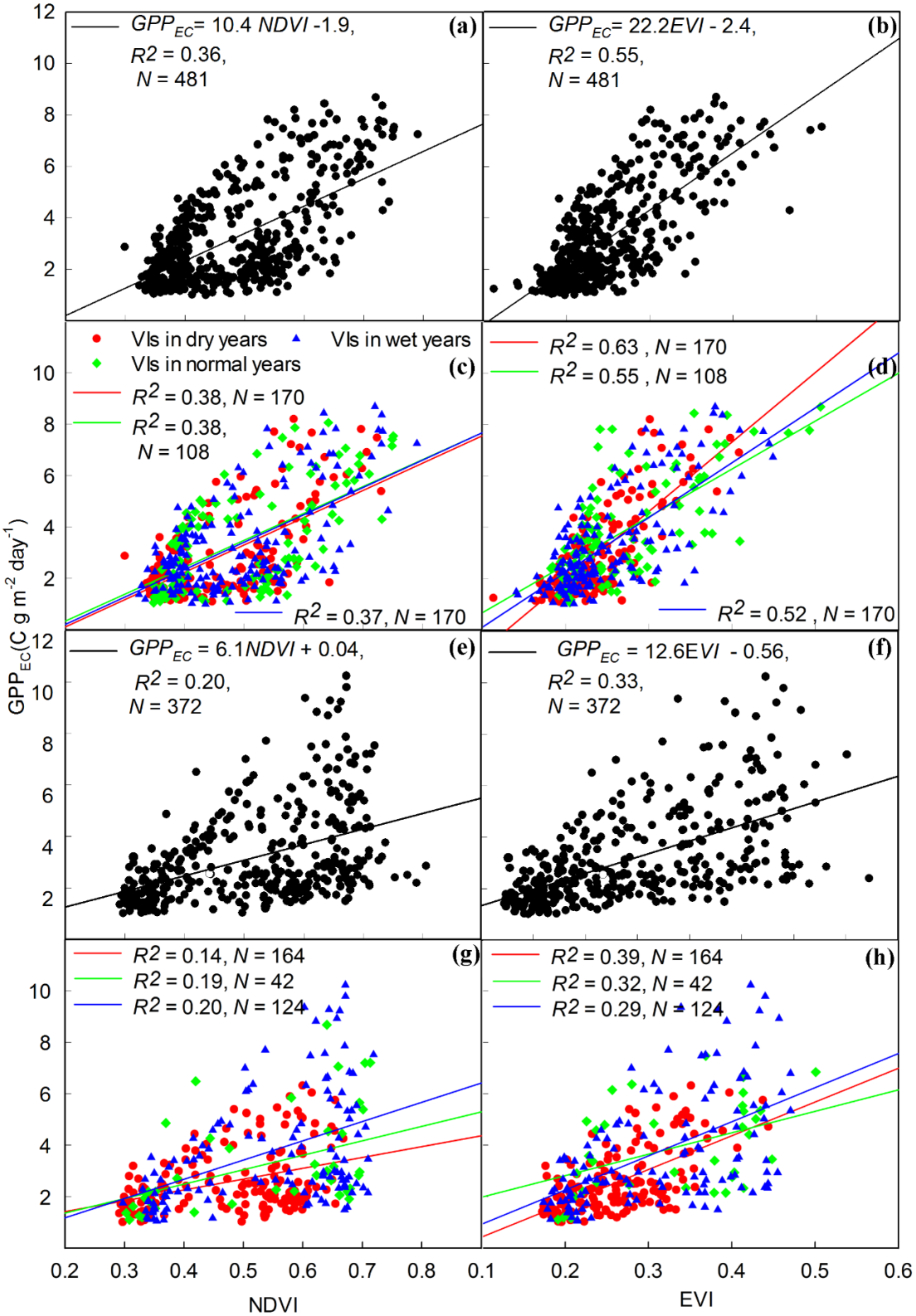

Figure 5.5 Simple liner regression between tower-derived gross primary production (GPPEC) and vegetation indices (NDVI and EVI) during the growing season: US-Ton site (Fig. 5.5a,b,c,d) and ES-LMa site (Fig. 5.5e,f,g,h).

Fig. 5.6 shows the responses of EVI and GPPEC to Tair_daytime during the plant growing season. Both GPPEC and EVI increased rapidly with increasing Tair_daytime up to a certain threshold then decreased as Tair_daytime increased. At the US-Ton site, when GPPEC and EVI in all years were plotted against Tair_daytime, maximum GPPEC and EVI occurred at 18 °C and 15°C, respectively (Fig. 5.6a,b). When GPPEC and EVI in wet years were plotted against Tair_daytime, GPPEC and EVI peaked at 18 °C (Fig. 5.6c,d). Similarly, at the ES-LMa site, the peak values of GPPEC and EVI occurred at 16 °C and 12 °C, respectively, when data for all years were used (Fig. 5.6e,f) and they occurred at 14°C when data in wet years were used (Fig. 5.6g,h). Based on these results, we used 18°C and 14°C as the Topt for the US-Ton site and the ES-LMa site, respectively, for the GPP simulation in VPM.

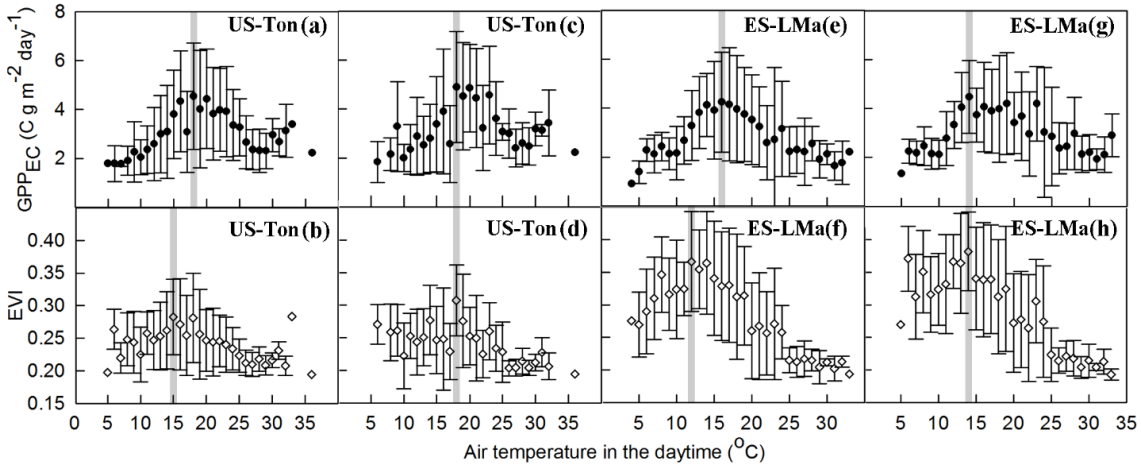

Figure 5.6 Responses of tower-derived gross primary production (GPPEC) and enhanced vegetation index (EVI) to daytime air temperature at two savanna sites. Figures 5.6a,b,e,f were based on all hydrological years' data and Figures 5.6c,d,g,h) were based on wet years' data. Grey boxes show the maximum GPP_{EC} or EVI.

We compared the responses of VIs and GPP_{EC} to the variations of hydrological conditions (dry, normal, and wet years) at the annual scale between these two savanna sites (Fig. 5.7). As shown, following a hydrological annual precipitation gradient from

dry to wet years, VIs and GPP_{EC} at the ES-LMa site increased substantially, while VIs and GPP_{EC} at the US-Ton site showed little change. LSWI had the largest sensitivity to the variations of annual hydrological conditions than did NDVI and EVI.

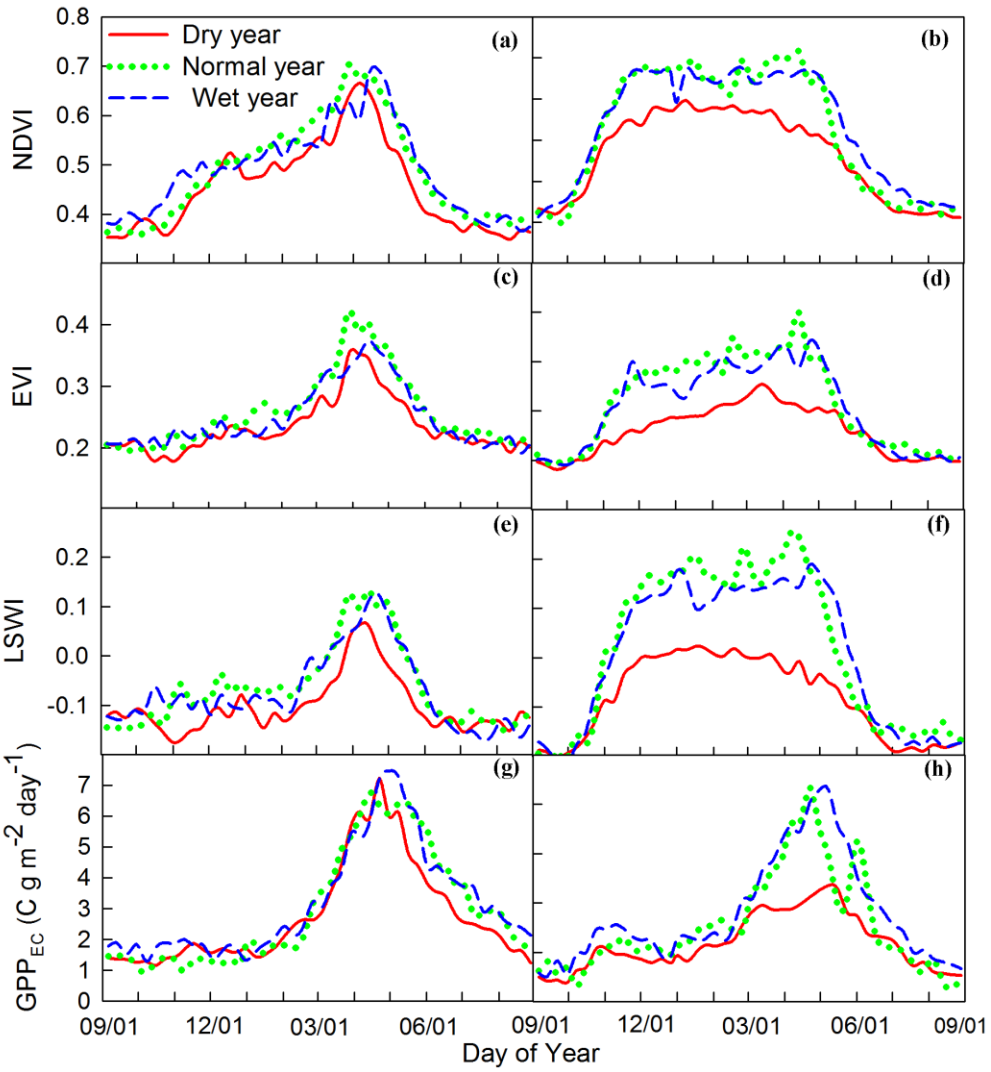

Figure 5.7 Mean seasonal variation (8-day values) of three MODIS-derived vegetation indices (NDVI, EVI, and LSWI) and tower-derived gross primary production (GPP_{EC}) at two savanna sites (Fig. 5.7a,c,e,g for US-Ton site; Fig. 5.7b,d,f,h for ES-LMa site). Data were averaged by day of year over dry, normal, and wet years.

5.3.3 GPP predicted by the VPM

Fig. 5.8 shows that GPP_{vpm} tracked the seasonal dynamics and interannual variations of GPP_{EC} reasonably well over the study period at both sites. A simple linear regression analysis showed a good correlation between GPP_{vpm} and GPP_{EC} for the entire study period and different hydrological (dry, normal, and wet) years with slopes of 0.91-1.06 and R^2 of 0.93-0.95 (Fig. 5.9). Linear regression coefficients for each year in Table 5.3 also showed that GPP_{vpm} was strongly correlated with GPP_{EC} at both sites with slopes > 0.83 and $R^2 > 0.90$. Comparison of the seasonally integrated GPP_{vpm} and GPP_{EC} at both sites showed that VPM slightly overestimated GPP in some normal and dry years (for example, in 2002-2003 at the US-Ton site and in 2011-2012 at the ES-LMa site) and slightly underestimated GPP in some wet years (for example, in 2004-2005 at the US-Ton site and in 2010-2011 at the ES-LMa site). At the US-Ton site, annual GPP_{EC} ranged from 822 to 1319 g C m^{-2} and GPP_{vpm} ranged from 885 to 1214 g C m^{-2} over the study period. At the ES-LMa site, annual GPP_{EC} ranged from 603 to 1328 g C m^{-2} and GPP_{vpm} ranged from 715 to 1222 g C m^{-2} over the study period.

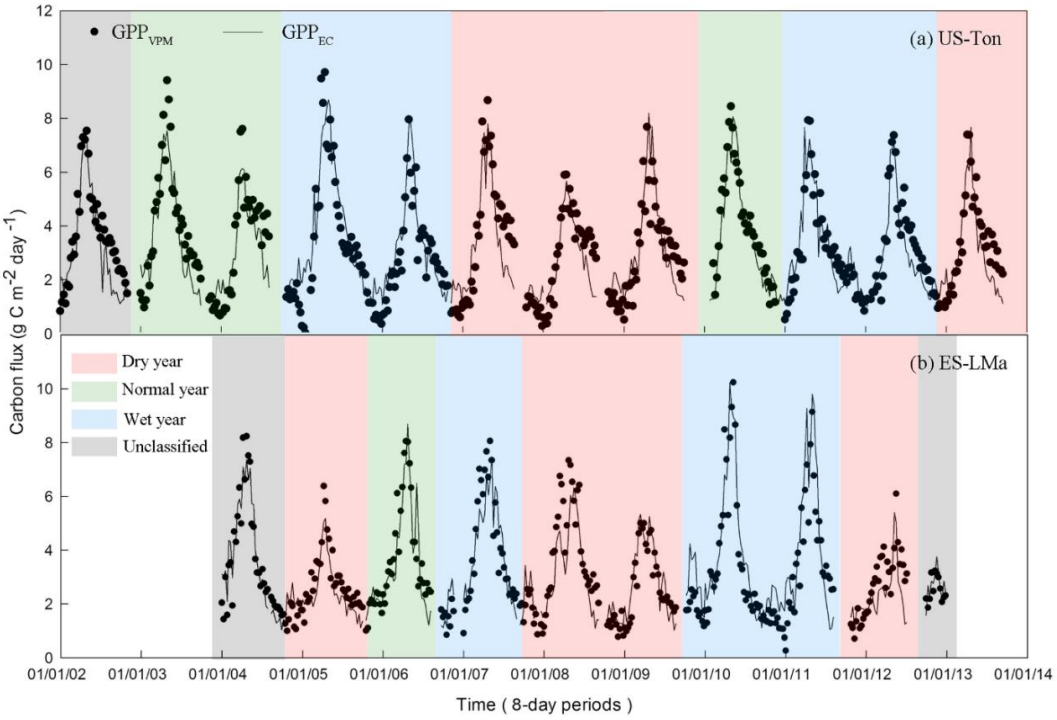

Figure 5.8 A comparison between seasonal dynamics and interannual variations of tower-derived gross primary production (GPP_{EC}) and simulated GPP (GPPvpm) at two savanna sites.

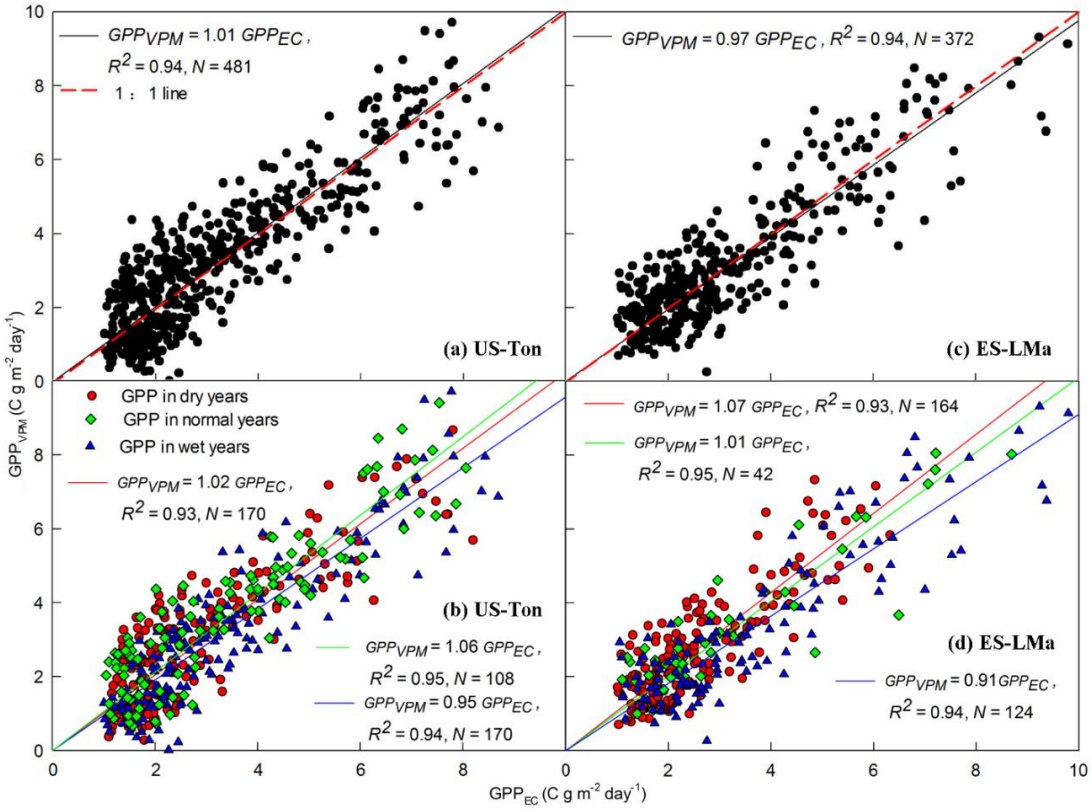

Figure 5.9 Linear relationship between tower-derived gross primary production (GPP_{EC}) and simulated GPP (GPPvpm) at two savanna sites: aggregated over the study period (Fig. 5.9a,c) and divided into different hydrological years (Fig. 5.9b,d).

Table 5.3 Linear regression coefficients (slope) and coefficients of determination (R2), and seasonally integrated values of simulated (GPPvpm) and tower-derived (GPP_{EC}) gross primary production for two savanna sites. Relative error in GPP sums (GPP%RE) were calculated by [(GPPvpm-GPP_{EC})/ GPP_{EC}]×100. RMSE is root mean square error (g C m-2day-1).

		GPPvpm = a × GPP_{EC}		GPP_{EC} (g C m-2)	GPPvpm (g C m-2)	GPP% RE	RMSE (g C m-2day-1)
Site	Year	slope	R^2				
US-Ton	2001-2002	1.05	0.96	906	978	7.9	0.88
	2002-2003	1.08	0.95	1082	1214	12.2	1.02
	2003-2004	1.09	0.93	895	986	10.1	1.01
	2004-2005	0.93	0.94	1319	1137	-13.8	1.16
	2005-2006	0.90	0.94	1117	1004	-10.1	0.85
	2006-2007	1.08	0.93	1068	1172	9.8	1.08
	2007-2008	1.07	0.93	822	885	7.7	0.85
	2008-2009	0.91	0.93	1023	971	-5.1	0.99
	2009-2010	1.02	0.97	1028	1074	4.5	0.85
	2010-2011	0.96	0.95	1131	1062	-6.1	0.86
	2011-2012	1.05	0.96	1022	1090	6.7	0.75
	2012-2013	1.04	0.93	1014	1094	7.9	0.89
ES-LMa	2003-2004	0.99	0.98	983	961	-2.2	0.67
	2004-2005	1.09	0.95	865	942	9.0	0.64
	2005-2006	1.01	0.95	1101	1162	5.5	0.86
	2006-2007	1.01	0.96	1249	1141	-8.6	0.86

2007-2008	1.14	0.95	1062	1222	15.1	1.04
2008-2009	0.91	0.97	873	804	-7.8	0.58
2009-2010	0.91	0.96	1328	1179	-11.2	0.96
2010-2011	0.83	0.93	1237	1063	-14.0	1.22
2011-2012	1.15	0.91	603	715	18.6	0.97

5.3.4 MODIS GPP (GPPmod) and flux tower GPP (GPP_{EC})

Fig. 5.10 shows the seasonal dynamics of GPP_{mod} and GPP_{EC} at two savanna sites. Although GPP_{mod} showed similar seasonal dynamics and interannual variations of GPP_{EC}, the magnitudes of GPP_{mod} were lower than those of GPP_{EC} at both sites in all hydrological years. GPP_{mod} underestimated GPP more at the US-Ton site (slope = 0.67, R^2 = 0.92) than at the ES-LMa site (slope = 0.78, R^2 = 0.92) (Table 5.4).

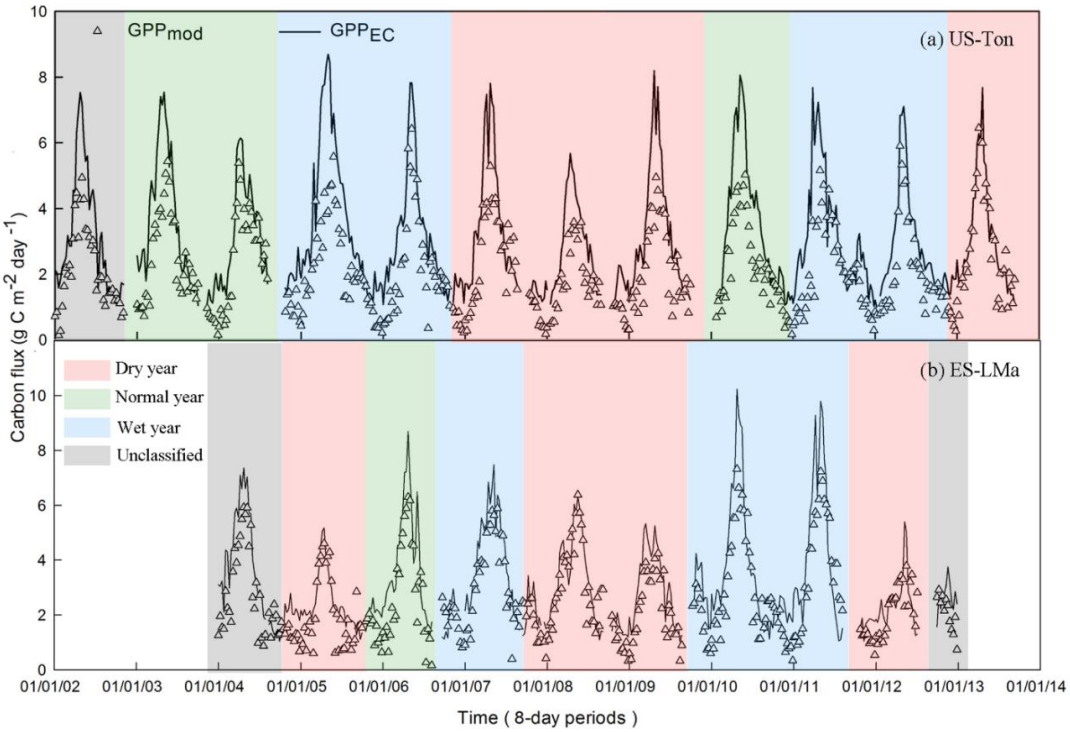

Figure 5.10 Comparison of MODIS-based gross primary production (GPPmod) and tower-derived gross primary production (GPP_{EC}) at two savanna sites.

Table 5.4 Linear regression coefficients (slope and coefficients of determination, R^2), seasonally integrated values of MODIS-based gross primary production (GPPmod) and tower-derived GPP (GPP_{EC}) for two savanna sites.

		GPPmod = a × GPP_{EC}		GPP_{EC}	GPPmod	GPP%	RMSE
Site	Year	slope	R2	(g C m^{-2})	(g C m^{-2})	RE	(g C $m^{-2}day^{-1}$)
US-Ton	2001-2002	0.64	0.95	906	578	-36.2	1.59
	2002-2003	0.64	0.93	1082	716	-33.8	1.58
	2003-2004	0.79	0.94	895	693	-22.6	0.94
	2004-2005	0.56	0.92	1319	751	-43.0	2.23
	2005-2006	0.70	0.93	1117	743	-33.5	1.22
	2006-2007	0.68	0.91	1068	755	-29.3	1.38
	2007-2008	0.63	0.92	822	518	-37.0	1.22
	2008-2009	0.63	0.94	1023	650	-36.5	1.47
	2009-2010	0.61	0.96	1028	650	-36.7	1.90
	2010-2011	0.64	0.86	1131	754	-33.4	1.64
	2011-2012	0.72	0.95	1022	714	-30.2	1.05
	2012-2013	0.87	0.95	1014	851	-16.1	0.77
	All years	0.67	0.92				
ES-LMa	2003-2004	0.74	0.96	983	715	-27.2	1.32
	2004-2005	0.81	0.89	865	672	-22.2	0.85
	2005-2006	0.74	0.91	1101	821	-25.4	1.35
	2006-2007	0.81	0.95	1249	1017	-18.6	1.02
	2007-2008	0.91	0.94	1062	976	-8.1	0.82
	2008-2009	0.76	0.95	873	655	-25.0	0.89
	2009-2010	0.75	0.95	1328	993	-25.2	1.39

2010-2011	0.79	0.90	1237	1054	-14.8	1.47
2011-2012	0.84	0.87	603	527	-12.5	0.88
All years	0.78	0.92				

5.4 Discussion

5.4.1 Seasonality of VIs, GPP_{EC} and savanna phenology

The deciduous savanna at the US-Ton site consists of four phenological stages for grasses and trees (Ma et al. 2007). Annual grasses germinate following the first autumn rainfall and grow slowly during the winter, grow and develop rapidly in the spring, and then die before the onset of the dry summer. Oak leaves emerge at the end of March and stay photosynthetically active during the summer, and fall down in the autumn and winter (Bartolome 1979; Ma et al. 2007; Xu and Baldocchi 2003). The savanna at the ES-LMa site is composed of evergreen holm oak trees and annual grasses. Holm oak trees emerge new leaves in spring and may have a weak leaf flushing in the autumn (Vaz et al. 2010; Wingate et al. 2015). The annual grasses also germinate after the autumn rains and die by the end of May, having a growing season of October to May (Casals et al. 2009; Figueroa and Davy 1991). VIs and GPP_{EC} at the US-Ton site increased slowly in the autumn and winter (Fig. 5.4 and Fig. 5.7), which can be attributed to the green up of the herbaceous layer (60% coverage). Comparing the VIs and GPP_{EC} in the autumn and winter with those in the dry summer also revealed the contributions of the herbaceous layer (80% coverage) to the seasonal dynamics of VIs and GPP_{EC} at the ES-LMa site. Assessment of the relative effects of tree layer and herbaceous layer could explain the influence of the savanna structure on carbon dynamics, which was not performed in this study due to the lack of separately ground-based observations of seasonality of VIs and GPP of trees and grasses.

5.4.2. Responses of two savannas to variations in annual precipitation

Our results show that interannual variations in precipitation influenced VIs and GPP_{EC} more at the evergreen savanna (ES-LMa) site than at the deciduous savanna (US-Ton) site. For example, Fig. 5.4d shows that a substantial reduction in GPP_{EC} only occurred in a few dry or normal years with low annual precipitation (2003-2004 and 2007-2008) at the US-Ton site, while at the ES-LMa site, it occurred in all dry years (2004-2005, 2007-2008, 2008-2009, and 2011-2012). Similarly, Fig. 5.7 shows that VIs and GPP_{EC} increased substantially in wet years at the ES-LMa site, but not at the US-Ton site. A meta-analysis for Mediterranean oak woodlands also showed that deciduous oak savannas were more resilient to drought and evergreen oak savannas were more sensitive to drought, as seen by a substantial reduction in ecosystem flux during drought (Vargas et al. 2013). Different tree canopy covers between two sites could be a possible reason for differences in responses of two savannas to precipitation. In savannas, grasses draw the upper soil water with shallow roots. This supply is exhausted quickly by grasses with high rate of transpiration (Walker and Noymeir 1982). Trees access to the deeper soil water with deep roots. This water source support trees living through the dry seasons (Walker and Noymeir, 1982). Tress can also use the percolating water from the upper layer soil which is unused by grasses (Eagleson and Segarra 1985). As well as, trees improve the soil nutrients and water-holding capacity, and control the water use of the understory vegetation by changing the microclimate (Jackson et al. 1990; Joffre and Rambal 1993; Scholes and Archer 1997). Studies of the Mediterranean savannas showed that the tree canopies improved the soil water storage and alleviated the water stress on vegetation in the ecosystem (Joffre and Rambal 1993; Joffre et al. 1999). The deciduous

savanna at the US-Ton site has higher tree canopy cover (about 40%) than that (about 20%) of the evergreen savanna at the ES-LMa site. Thus, higher tree cover could reduce the sensitivity of the US-Ton savanna to the water stress caused by the variations of precipitation. In Mediterranean ecosystems, plant photosynthesis is mostly limited by soil water availability (Gilabert et al. 2015; Niinemets and Keenan 2014; Nijland et al. 2011; Xu and Baldocchi 2004). Soil moisture availability was controlled by rainfall, soil properties, and geomorphology (Eagleson and Segarra, 1985). Differences in soil hydrological properties (i.e., SWC, Fig. 5.3c) may be another possible reason for the different responses of these two savannas to precipitation changes. A modeling study on grassland ecosystems demonstrated that soil available water capacity can alter the partitioning of precipitation and influence the buffer of water stress during long drought periods (Weng and Luo 2008). As vegetation responses to precipitation are complicated at ecosystem scales, further studies of Mediterranean-climate savannas are needed to explore the mechanisms at different spatial and temporal scales.

5.4.3. Model comparison

At these two savanna sites, GPP_{vpm} showed good agreement with GPP_{EC}, and GPPmod was lower than GPP_{EC} in all years (Fig. 5.9, Fig. 5.10). The underestimations of GPP_{mod} have been reported in other biomes such as the African savanna (Jin et al. 2013; Sjöström et al. 2013), deciduous forests (Wu et al. 2010a), and grasslands (Wagle et al. 2014). Previous studies have shown that the discrepancies between GPP_{mod} and GPP_{EC} are mainly due to estimation errors of LUE in those models (Sims et al. 2008; Sims et al. 2006). The ε_0 value used in this study was about 0.5 g C/mol PAR (~1.04 g C MJ^{-1}). This value is almost the same as that of 1.03 g C MJ^{-1} for savannas used by the MOD17A2

product in Collection 5.0 (Kanniah et al. 2009) and lower than 1.21 g C MJ^{-1} used in Collections 5.1 and 6 (Running and Zhao 2015; Sjöström et al. 2013; Zhao and Running 2010). This value is also lower than the maximum LUE inferred by the site specific estimations in tropical savannas, such as 1.26±0.03 g C MJ^{-1} (Kanniah et al. 2009) in Northern Australia and 1.66 g C MJ^{-1} in Africa (Sjöström et al. 2013). This comparison showed the maximum LUE used in GPP_{mod} may be reasonable for Mediterranean-climate savannas and other factors should be examined to explain the underestimation of GPP_{mod}.

Another simple way to compare simulations of GPP models is to evaluate (1) the length of plant phenology and (2) maximum GPP value in plant growing season. Recent studies shows that annual GPP can be explained by the integrated controls of plant phenology (Carbon Uptake Period (CUP)) and physiological processes (seasonal maximal capacity of CO_2 uptake, GPP_{max}) (Wagle et al. 2015a; Wagle et al. 2015b; Xia et al. 2015). As the CUP (number of days of carbon uptake by the ecosystem) term is generally used for analysis of NEE data (Churkina et al. 2005; Wagle et al. 2015a), here we use Active Photosynthesis Period (APP) for analysis of GPP data, and APP is defined as the period of daily GPP >= 1 g C m^2 d^{-1}. We compared the interannual dynamics of APP and GPP_{max} estimated from EC ($APP_{EC,}$ GPP_{max_EC}), VPM ($APP_{VPM,}$ GPP_{max_VPM}), and the standard MODIS GPP product ($APP_{mod,}$ GPP_{max_mod}) at these two savanna sites, respectively (Fig. 5.11). Fig. 5.11a,b show that APP_{mod} was significantly shorter than APP_{EC}, and GPP_{max_mod} was much lower than GPP_{max_EC}. APP_{VPM} and GPP_{max_VPM} were more comparable with APP_{EC} and GPP_{max_EC}. The simple linear regression analyses show that at these two savanna sites, the ratio α (slope in the linear regression model) between annual GPP (including GPP_{EC}, GPP_{mod} and GPP_{VPM}) and the product of APP × GPPmax

over years ranges from 0.43 to 0.52 (Fig. 5.11c), which is much lower than the value of $\alpha = 0.68$ reported for the savanna sites by Xia et al. (2015).

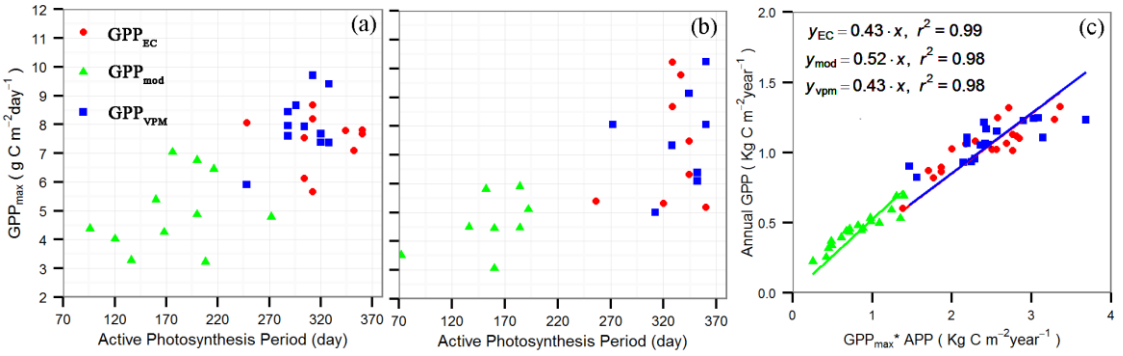

Figure 5.11 Comparison of active photosynthesis period (APP) and the annual maximum gross primary production (GPPmax) estimated from tower-derived gross primary production (GPP_{EC}), MODIS-based gross primary production (GPPmod) and simulated GPP by vegetation photosynthesis model (GPPvpm) at two savannas sites (Fig. 5.11a for US-Ton site; Fig. 5.11b for ES-LMa site). Fig. 5.11c shows the relationship between annual GPP (including GPP_{EC}, GPPmod and GPPVPM) and the product of GPPmax and APP at two savanna sites.

5.4.4. Parameter estimation in the VPM model

This study proposed an approach to estimate the T_{opt} at ecosystem level. We demonstrated that consistent values of T_{opt} based on the Ta-EVI and Ta-GPP_{EC} relationships can be achieved by excluding the influence of water stress on EVI and GPP_{EC} in dry years (i.e., using data only from wet years instead of all years, Fig. 5.6). It follows the assumption that maximum EVI and GPP_{EC} values represent optimal growth conditions (Singh et al. 2003; Yang et al. 2013). T_{opt} for photosynthesis varies widely with species at leaf and canopy scales (Baldocchi et al. 2001; Medlyn et al. 2002). At site or ecosystem scales, a specific T_{opt} may not be applicable to all sites and various growth conditions, especially for savannas with various canopy proportions (Cui 2013; Sims et al. 2008). Considering the influence of water stress on VIs for the estimation of T_{opt} may improve the model's performance, as the maximum NDVI values are used to estimate the

optimal weather at ecosystem scale (Singh et al. 2003) and T_{opt} is used in process-based and LUE-based GPP models (Raich et al. 1991; Tao et al. 2005; Yang et al. 2013). Topt for photosynthesis of Mediterranean plants ranged from 15°C to 30°C according to the studies under controlled conditions, and Mediterranean trees had higher Topt (~22°C) than did C_3 grasses (Charles-Edwards et al. 1971; Larcher 2000; Ogaya and Penuelas 2003). Both savanna sites are mixed ecosystems of C_3 grasses and trees, with tree coverage of 40% at the US-Ton site and 20% at the ES-LMa site. Our analysis showed that Topt was 18 ^{o}C at the US-Ton site and 14 ^{o}C at the ES-LMa site. This result is reasonable based on the Topt of Mediterranean trees and C_3 grasses, and the ecosystem structures of these two savanna sites. This result is consistent with the Topt range of 10-20 °C for photosynthesis of Mediterranean plants under field conditions (Flexas et al., 2014). More studies are required to evaluate our Topt estimation approach in other terrestrial ecosystems.

The seasonal dynamics of VIs showed some differences at two sites (Fig. 5.4) and the US-Ton site had better correlation between GPP_{EC} and NDVI/EVI compared to the ES-LMa site (Fig. 5.5). However, GPP_{VPM} were comparable with GPP_{EC} at both sites (Fig. 5.9). To further investigate the agreement of GPP, we compared observed and simulated GPP and each parameter of VPM at both sites (Fig. 5.12) by selecting a period from Sept. 2005 to Jun. 2006. During this period, two sites showed significantly different VIs seasonality and consistent GPP seasonality (Fig. 5.4). Although EVI of the ES-LMa site was higher than that of the US-Ton site from winter to the following spring (Fig. 5.12b), low radiation and temperature (Fig. 5.12c,d,e) at this time severely reduced the GPP of both sites (Fig. 5.12a). Therefore, similar seasonal dynamics of PAR and air

temperature at study sites resulted in occurrence of peak GPP almost at the same time (late April or early May) (Fig. 5.12a). Some studies reported radiation as a critical driver of GPP in tropical savannas (Whitley et al. 2011), but further study is needed to partition the individual effects of PAR and temperature on GPP seasonal dynamics in Mediterranean-climate savannas.

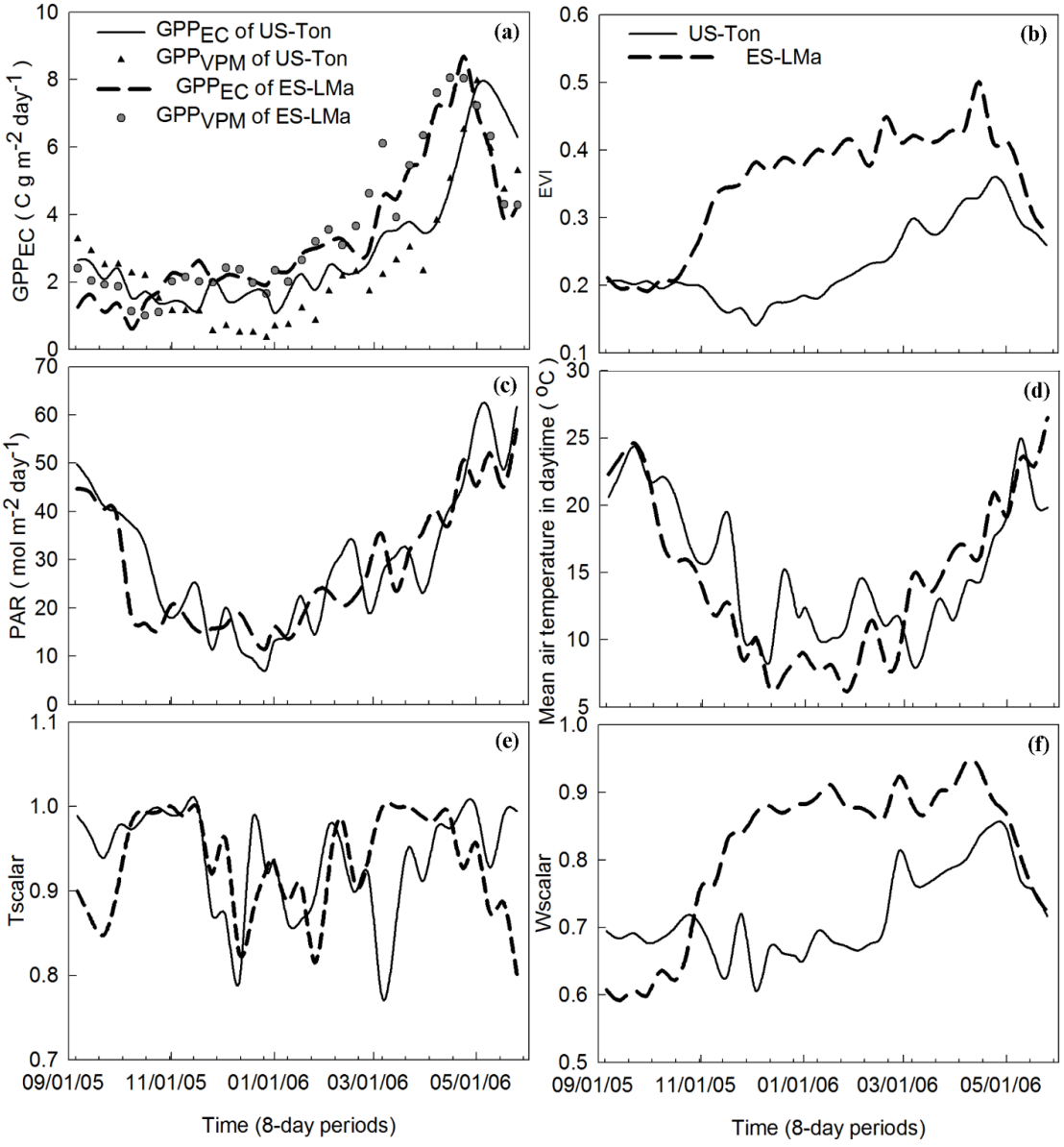

Figure 5.12 Comparison of the seasonal dynamics of tower-derived gross primary production (GPP_{EC}) and simulated GPP (GPPvpm), enhanced vegetation index (EVI), photosynthetically active radiation (PAR), mean daytime air temperature,

and temperature and water scalars in vegetation photosynthesis model (VPM) for the period of Sept.2005-Jun. 2006 at two savanna sites.

In addition, we examined the contributions of the water scalar and temperature scalar to the simulation of GPP at these savannas under different hydrological years. Fig. 5.13 compares GPP_{EC}, GPP_{vpm}, GPP_{vpm} without T_{scalar} and GPP_{vpm} without W_{scalar}. The results show that VPM can estimate GPP in the green-up stage without T_{scalar} or W_{scalar} at both sites. However, to accurately estimate GPP in peak growth and senescence periods, it is essential to add W_{scalar} and T_{scalar} regardless of it being a dry or wet year. W_{scalar} is more relevant than T_{scalar} in the simulation of GPP at these savanna sites. This study demonstrates that the mechanism of the LSWI-based water scalar used in VPM is applicable to sparse savannas in the Mediterranean climate for multi-year GPP simulation. Previous studies also showed that LSWI-based VPM was sensitive to droughts in croplands and tallgrass prairie (Dong et al. 2015a; Wagle et al. 2014; Wagle et al. 2015b). Although there are trade-offs between meteorology and satellite-based parameters in satellite-based GPP models (Gitelson et al. 2006; Sims et al. 2008; Yang et al. 2013), our results illustrate that it is critical to use vegetation canopy characteristics (eg. VIs) and climate factors (eg. PAR, temperature, water) to simulate multi-year GPP for sparse savannas (with low LAI and high gap canopies) in the Mediterranean climate.

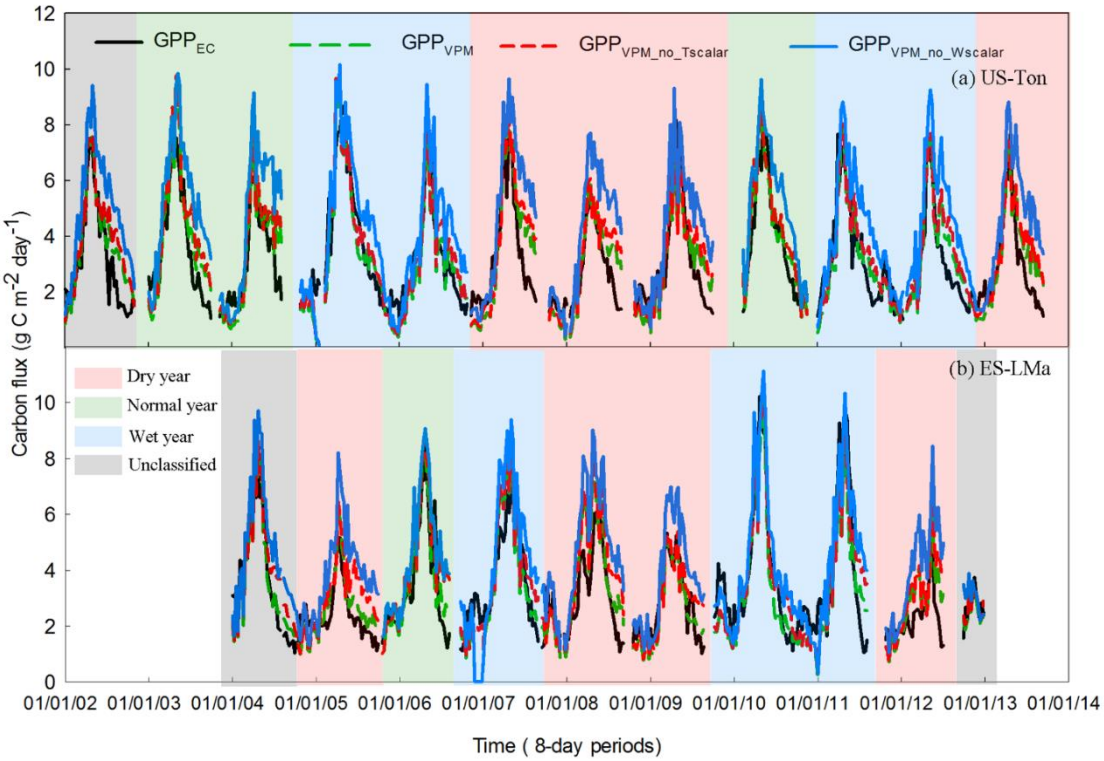

Figure 5.13 Comparison of simulation scenarios: (1) Vegetation Photosynthesis Model (VPM) with both Tscalar and Wscalar (GPPvpm), (2) VPM without Tscalar (GPPvpm_no_Tscalar), and (3) VPM without Wscalar (GPPvpm_no_Wscalar).

5.5 Conclusion

This study compared the seasonal dynamics of climate, VIs, and GPP_{EC}, and their interactions at two dominant functional oak savannas (deciduous and evergreen) under the Mediterranean climate. GPP simulation of these savannas is challenging because these ecosystems experience large variations in seasonal and interannual rainfall and soil moisture, and they have sparse trees with open canopies and low LAI. We used VPM to simulate multi-year GPP under various hydrological conditions (dry, normal, and wet years) and evaluated its performance by comparing the simulations with GPP_{EC} and the MODIS GPP product. This study demonstrates that the two savannas had similar seasonal dynamics of climate and GPP_{EC} despite different VI seasonal dynamics. EVI and GPP_{EC} had similar responses to daytime mean air temperature at both savanna sites. VIs and

GPP_{EC} of the ES-LMa site (evergreen savanna) were more sensitive to precipitation variation from dry years to wet years than those of the US-Ton site (deciduous savanna). VPM simulated seasonal dynamics and interannual variations of GPP reasonably well at both savanna sites in all hydrological conditions. The results of this study highlight the potential of integrating both EC technique and satellite remote sensing for better understanding and managing savanna ecosystems under the Mediterranean climate.

Supplementary materials

Text S5.1 Material and methods

The Standardized Precipitation Evapotranspiration Index (SPEI) is a climatic drought index and is the difference between precipitation (P) and Potential Evapotranspiration (PET) (Vicente-Serrano et al. 2010). This climatic water balance-based drought index includes the effects of precipitation and temperature variations on drought assessment. It also describes the multiscalar character of drought with time scales between one and 48 months. This different time scale droughts represent the deficits of different usable water sources (Vicente-Serrano et al. 2010). A global assessment showed good performance of the SPEI to capture drought impacts on agriculture, ecology, and hydrology (Vicente-Serrano et al. 2012). The SPEI has been widely used to examine the frequency, severity and changes of drought, and other climatic characteristics (Paulo et al. 2012; Yu et al. 2014).

The responses of different land biomes to drought occurred at different time scales (Vicente-Serrano et al. 2013). According to the geographical patterns analysis, there is a strong correlation between short-scale SPEI and vegetation activity at these two savanna sites. Therefore, in this study, monthly SPEI at two savanna sites was taken into account

to classify the types of hydrological years over the study period. The time series site-specific monthly SPEI data were downloaded from the global SPEI database (http://sac.csic.es/spei/database.html).

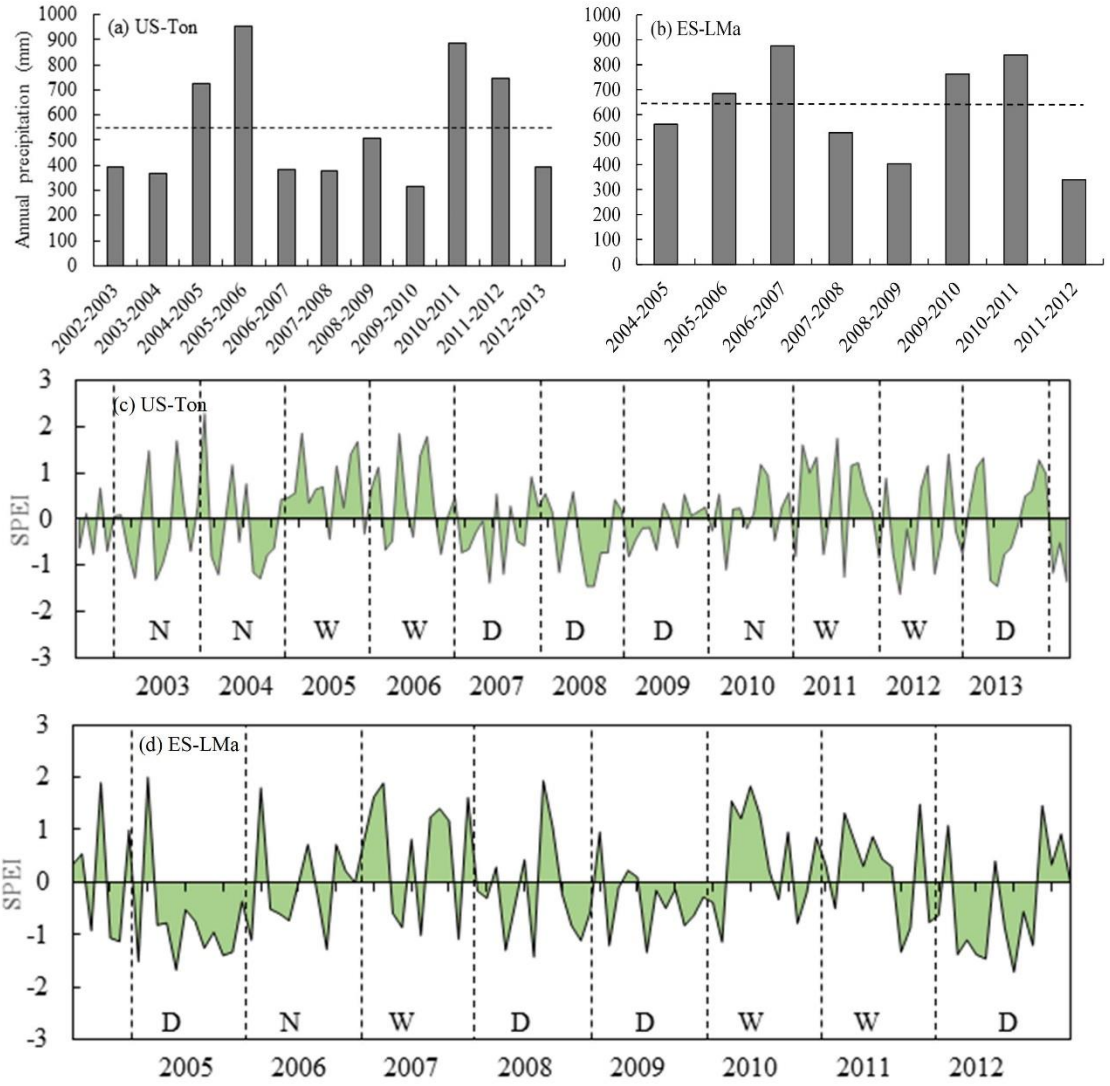

Figure S5.1 Precipitation sums (a, b) during the hydrological years (September to August) and time series of the monthly SPEI (c, d) at US-Ton and ES-LMa sites. The dash lines in (a) and (b) show the average precipitation over the study period. The dash lines in (c) and (d) show the start and end of each hydrological year. Dry, normal, and wet hydrological years are represented by D, N, and W, respectively.

Chapter 6: Conclusions and perspectives

Remote sensing has been widely used to map land use and land cover changes, examine the structure and process changes of ecosystem, and investigate the interactions between vegetation activities and climate. This dissertation used remote sensing data to map the vegetation distribution and dynamics at species level in agriculture and grassland ecosystems of Southeastern China and South central US. In addition, this dissertation used remote sensing data to examine the relationships of climate, vegetation indices and GPP in different types of savannas from Southwestern Spain and Southwestern USA. A remote sensing-based vegetation photosynthesis model was used to simulate the GPP in two savanna ecosystems. My dissertation extends the application of moderate spatial resolution images into land use and land cover change studies from biome scale to species scale. My dissertation strengthens the ecological problems premised by land cover changes, such as the different responses of different function savannas to climate change, and the woody encroachment caused by species shits in grasslands.

The results of the study in Chapter 2 have demonstrated the potential of multi-source remote sensing data (Landsat-8, MODIS and PALSAR) to map paddy rice planting areas in the wheat-rice double cropping system, using a pixel- and phenology-based algorithm. Future studies will use multi-year Landsat-8 data and other optical sensor data to map paddy rice mappings at large scales within multiple agricultural ecosystems. MODIS-based LST_{night} and VI dynamics will make it possible to automatically select Landsat-8 images within key time windows instead of relying on the investigation of local crop calendars. In addition to paddy rice, other crop species extraction will be explored based on moderate remote sensing images in future.

Chapter 3 first demonstrated the potential of long-term Landsat images to document the historical woody plant encroachment into the grasslands using a pixel and phenology-based algorithms at regional scales. The moderate spatial resolution images of Landsat and PALSAR had good performance to identify the regions with red cedar coverage larger than 50%, and the identification capability reduced with the decreasing of red cedar coverage. Further studies will apply this pixel- and phenology-based algorithm to other grasslands or detect other encroached woody species from regional to global scales.

Chapter 4 improved the algorithms developed in Chapter 3 to track the juniper species (Eastern redcedar and Ashe juniper) encroachment into grassland ecosystem at state scale (Oklahoma, US.). Historical juniper forest maps have been generated in this chapter at 30-m spatial resolution using Landsat and PALSAR data. This chapter examined the spatial and temporal dynamics, geographic patterns, and soil settings of juniper forest encroachment. Further studies are needed to examine the drivers and potential consequences of juniper encroachment using the produced juniper forest maps.

It is challenge to simulate the GPP of the savannas because these ecosystems experience large variations in seasonal and interannual rainfall and soil moisture, and they have sparse trees with open canopies and low LAI. Chapter 5 compared the seasonal dynamics of climate, VIs, and GPP_{EC}, and their interactions at two dominant functional oak savannas (deciduous and evergreen) under the Mediterranean climate. The VPM was used to simulate multi-year GPP under various hydrological conditions (dry, normal, and wet years) and it had good performance. The results of this chapter highlight the potential of integrating both EC technique and satellite remote sensing for better understanding and

managing savanna ecosystems under the Mediterranean climate. Future studies will assess the relative effects of tree layer and herbaceous layer to explain the influence of the savanna structure on carbon dynamics. In addition, further studies of Mediterranean-climate savannas are needed to explore the mechanisms of vegetation responses to precipitation at different spatial and temporal scales.

References

Akbari, M., Mamanpoush, A.R., Gieske, A., Miranzadeh, M., Torabi, M., & Salemi, H.R. (2006). Crop and land cover classification in Iran using Landsat 7 imagery. *International Journal of Remote Sensing, 27*, 4117-4135

Aselmann, I., & Crutzen, P.J. (1989). Global distribution of natural freshwater wetlands and rice paddies, their net primary productivity, seasonality and possible methane emissions. *Journal of atmospheric chemistry, 8*, 307-358

Bachelet, D. (1995). Rice paddy inventory in a few provinces of China using AVHRR data. *Geocarto International, 10*, 23-38

Baldocchi, D., Falge, E., Gu, L., Olson, R., Hollinger, D., Running, S., Anthoni, P., Bernhofer, C., Davis, K., & Evans, R. (2001). FLUXNET: A new tool to study the temporal and spatial variability of ecosystem-scale carbon dioxide, water vapor, and energy flux densities. *Bulletin of the American Meteorological Society, 82*, 2415-2434

Barger, N.N., Archer, S.R., Campbell, J.L., Huang, C.Y., Morton, J.A., & Knapp, A.K. (2011). Woody plant proliferation in North American drylands: A synthesis of impacts on ecosystem carbon balance. *Journal of Geophysical Research-Biogeosciences, 116*

Bartolome, J.W. (1979). Germination and seedling establishment in California annual grassland. *The Journal of Ecology*, 273-281

Berger, M., Moreno, J., Johannessen, J.A., Levelt, P.F., & Hanssen, R.F. (2012). ESA's sentinel missions in support of Earth system science. *Remote sensing of environment, 120*, 84-90

Biradar, C.M., & Xiao, X. (2011). Quantifying the area and spatial distribution of double- and triple-cropping croplands in India with multi-temporal MODIS imagery in 2005. *International Journal of Remote Sensing, 32*, 367-386

Bouvet, A., & Thuy, L.T. (2011). Use of ENVISAT/ASAR wide-swath data for timely rice fields mapping in the Mekong River Delta. *Remote sensing of environment, 115*, 1090-1101

Bridhikitti, A., & Overcamp, T.J. (2012). Estimation of Southeast Asian rice paddy areas with different ecosystems from moderate-resolution satellite imagery. *Agriculture, Ecosystems & Environment, 146*, 113-120

Briggs, J.M., Knapp, A.K., Blair, J.M., Heisler, J.L., Hoch, G.A., Lett, M.S., & McCARRON, J.K. (2005). An ecosystem in transition: causes and consequences of the conversion of mesic grassland to shrubland. *Bioscience, 55*, 243-254

Brisco, B., Li, K., Tedford, B., Charbonneau, F., Yun, S., & Murnaghan, K. (2013). Compact polarimetry assessment for rice and wetland mapping. *International Journal of Remote Sensing, 34*, 1949-1964

Bruner, W.E. (1931). The Vegetation of Oklahoma. *Ecological Monographs, 1*, 100-188

Casals, P., Gimeno, C., Carrara, A., Lopez-Sangil, L., & Sanz, M. (2009). Soil CO2 efflux and extractable organic carbon fractions under simulated precipitation events in a Mediterranean Dehesa. *Soil Biology and Biochemistry, 41*, 1915-1922

Chang, T.J., & Kleopa, X.A. (1991). A Proposed Method for Drought Monitoring. *Water Resources Bulletin, 27*, 275-281

Charles-Edwards, D., Charles-Edwards, J., & Cooper, J. (1971). The influence of temperature on photosynthesis and transpiration in ten temperate grass varieties grown in four different environments. *Journal of Experimental Botany, 22*, 650-662

Chen, B., Li, X., Xiao, X., Zhao, B., Dong, J., Kou, W., Qin, Y., Yang, C., Wu, Z., & Sun, R. (2016). Mapping tropical forests and deciduous rubber plantations in Hainan Island, China by integrating PALSAR 25-m and multi-temporal Landsat images. *International Journal of Applied Earth Observation and Geoinformation, 50*, 117-130

Chen, C.F., Huang, S.W., Son, N.T., & Chang, L.Y. (2011). Mapping double-cropped irrigated rice fields in Taiwan using time-series Satellite Pour l'Observation de la Terre data. *Journal of Applied Remote Sensing, 5*

Churkina, G., Schimel, D., Braswell, B.H., & Xiao, X. (2005). Spatial analysis of growing season length control over net ecosystem exchange. *Global Change Biology, 11*, 1777-1787

Cloude, S.R., & Papathanassiou, K.P. (2003). Three-stage inversion process for polarimetric SAR interferometry. *Iee Proceedings-Radar Sonar and Navigation, 150*, 125-134

Cohen, W.B., Yang, Z.G., & Kennedy, R. (2010). Detecting trends in forest disturbance and recovery using yearly Landsat time series: 2. TimeSync - Tools for calibration and validation. *Remote Sensing of Environment, 114*, 2911-2924

Cui, Y.P. (2013). Preliminary Estimation of the Realistic Optimum Temperature for Vegetation Growth in China. *Environmental Management, 52*, 151-162

Dayton, L. (2014). Agribiotechnology: Blue-sky rice. *Nature, 514*, S52-S54

DeSantis, R.D., Hallgren, S.W., & Stahle, D.W. (2011). Drought and fire suppression lead to rapid forest composition change in a forest-prairie ecotone. *Forest Ecology and Management, 261*, 1833-1840

Diamond, D.D., & Elliott, L.F. (2015). *Oklahoma ecological systems mapping interpretive booklet: Methods, short type descriptions, and summary results*. Norman: Oklahoma Department of Wildlife Conservation

Dong, J., Xiao, X., Chen, B., Torbick, N., Jin, C., Zhang, G., & Biradar, C. (2013a). Mapping deciduous rubber plantations through integration of PALSAR and multi-temporal Landsat imagery. *Remote Sensing of Environment, 134*, 392-402

Dong, J., Xiao, X., Menarguez, M.A., Zhang, G., Qin, Y., Thau, D., Biradar, C., & Moore Iii, B. (2016). Mapping paddy rice planting area in northeastern Asia with Landsat 8 images, phenology-based algorithm and Google Earth Engine. *Remote Sensing of Environment*

Dong, J., Xiao, X., Wagle, P., Zhang, G., Zhou, Y., Jin, C., Torn, M.S., Meyers, T.P., Suyker, A.E., & Wang, J. (2015a). Comparison of four EVI-based models for estimating gross primary production of maize and soybean croplands and tallgrass prairie under severe drought. *Remote Sensing of Environment, 162*, 154-168

Dong, J.W., Xiao, X.M., Chen, B.Q., Torbick, N., Jin, C., Zhang, G.L., & Biradar, C. (2013b). Mapping deciduous rubber plantations through integration of PALSAR and multi-temporal Landsat imagery. *Remote Sensing of Environment, 134*, 392-402

Dong, J.W., Xiao, X.M., Kou, W.L., Qin, Y.W., Zhang, G.L., Li, L., Jin, C., Zhou, Y.T., Wang, J., Biradar, C., Liu, J.Y., & Moore, B. (2015b). Tracking the dynamics of paddy rice planting area in 1986-2010 through time series Landsat images and phenology-based algorithms. *Remote sensing of environment, 160*, 99-113

Dong, J.W., Xiao, X.M., Sheldon, S., Biradar, C., Duong, N.D., & Hazarika, M. (2012a). A comparison of forest cover maps in Mainland Southeast Asia from multiple sources: PALSAR, MERIS, MODIS and FRA. *Remote Sensing of Environment, 127*, 60-73

Dong, J.W., Xiao, X.M., Sheldon, S., Biradar, C., & Xie, G.S. (2012b). Mapping tropical forests and rubber plantations in complex landscapes by integrating PALSAR and MODIS imagery. *Isprs Journal of Photogrammetry and Remote Sensing, 74*, 20-33

Doraiswamy, P.C., Sinclair, T.R., Hollinger, S., Akhmedov, B., Stern, A., & Prueger, J. (2005). Application of MODIS derived parameters for regional crop yield assessment. *Remote sensing of environment, 97*, 192-202

Drusch, M., Del Bello, U., Carlier, S., Colin, O., Fernandez, V., Gascon, F., Hoersch, B., Isola, C., Laberinti, P., Martimort, P., Meygret, A., Spoto, F., Sy, O., Marchese, F., & Bargellini, P. (2012). Sentinel-2: ESA's Optical High-Resolution Mission for GMES Operational Services. *Remote Sensing of Environment, 120*, 25-36

Eagleson, P.S., & Segarra, R.I. (1985). Water-Limited Equilibrium of Savanna Vegetation Systems. *Water Resources Research, 21*, 1483-1493

Engle, D.M., Bidwell, T.G., & Moseley, M.E. (1996). *Invasion of Oklahoma rangelands and forests by eastern redcedar and ashe juniper*. Oklahoma Cooperative Extension Service, Division of Agricultural Sciences and Natural Resources, Oklahoma State University

Fang, H.L., Wu, B.F., Liu, H.Y., & Huang, X. (1998). Using NOAA AVHRR and landsat TM to estimate rice area year-by-year. *International Journal of Remote Sensing, 19*, 521-525

FAO (2012). Forest Resources Assessments (FRA2010). In. Rome: Food and Agricultural Organization of the United Nations.

Figueroa, M., & Davy, A. (1991). Response of Mediterranean grassland species to changing rainfall. *The Journal of Ecology*, 925-941

Friedl, M.A., Sulla-Menashe, D., Tan, B., Schneider, A., Ramankutty, N., Sibley, A., & Huang, X.M. (2010). MODIS Collection 5 global land cover: Algorithm refinements and characterization of new datasets. *Remote sensing of environment, 114*, 168-182

Frolking, S., Qiu, J., Boles, S., Xiao, X., Liu, J., Zhuang, Y., Li, C., & Qin, X. (2002). Combining remote sensing and ground census data to develop new maps of the distribution of rice agriculture in China. *Global Biogeochemical Cycles, 16*, 1091

Gavier-Pizarro, G.I., Kuemmerle, T., Hoyos, L.E., Stewart, S.I., Huebner, C.D., Keuler, N.S., & Radeloff, V.C. (2012). Monitoring the invasion of an exotic tree (Ligustrum lucidum) from 1983 to 2006 with Landsat TM/ETM plus satellite data and Support Vector Machines in Cordoba, Argentina. *Remote Sensing of Environment, 122*, 134-145

Ge, J.J., & Zou, C. (2013). Impacts of woody plant encroachment on regional climate in the southern Great Plains of the United States. *Journal of Geophysical Research-Atmospheres, 118*, 9093-9104

Gilabert, M.A., Moreno, A., Maselli, F., Martínez, B., Chiesi, M., Sánchez-Ruiz, S., García-Haro, F.J., Pérez-Hoyos, A., Campos-Taberner, M., Pérez-Priego, O., Serrano-Ortiz, P., & Carrara, A. (2015). Daily GPP estimates in Mediterranean ecosystems by combining remote sensing and meteorological data. *Isprs Journal of Photogrammetry and Remote Sensing, 102*, 184-197

Gitelson, A.A., Vina, A., Verma, S.B., Rundquist, D.C., Arkebauer, T.J., Keydan, G., Leavitt, B., Ciganda, V., Burba, G.G., & Suyker, A.E. (2006). Relationship between gross primary production and chlorophyll content in crops: Implications for the synoptic monitoring of vegetation productivity. *Journal of Geophysical Research-Atmospheres, 111*

Gong, P., Wang, J., Yu, L., Zhao, Y.C., Zhao, Y.Y., Liang, L., Niu, Z.G., Huang, X.M., Fu, H.H., Liu, S., Li, C.C., Li, X.Y., Fu, W., Liu, C.X., Xu, Y., Wang, X.Y., Cheng, Q., Hu, L.Y., Yao, W.B., Zhang, H., Zhu, P., Zhao, Z.Y., Zhang, H.Y., Zheng, Y.M., Ji, L.Y., Zhang, Y.W., Chen, H., Yan, A., Guo, J.H., Yu, L., Wang, L., Liu, X.J., Shi, T.T., Zhu, M.H., Chen, Y.L., Yang, G.W., Tang, P., Xu, B., Giri, C., Clinton, N., Zhu, Z.L., Chen, J., & Chen, J. (2013). Finer resolution observation and monitoring of global land cover: first mapping results with Landsat TM and ETM+ data. *International Journal of Remote Sensing, 34*, 2607-2654

Goodwin, N.R., Collett, L.J., Denham, R.J., Flood, N., & Tindall, D. (2013). Cloud and cloud shadow screening across Queensland, Australia: An automated method for Landsat TM/ETM plus time series. *Remote sensing of environment, 134*, 50-65

Grumbles, J. (1989). Control of eastern redcedar and ashe juniper with soil spot applications of picloram. *Down to Earth, 45*, 13-16

Gumma, M.K., Nelson, A., Thenkabail, P.S., & Singh, A.N. (2011). Mapping rice areas of South Asia using MODIS multitemporal data. *Journal of Applied Remote Sensing, 5*

Gumma, M.K., Thenkabail, P.S., Maunahan, A., Islam, S., & Nelson, A. (2014). Mapping seasonal rice cropland extent and area in the high cropping intensity environment of Bangladesh using MODIS 500 m data for the year 2010. *Isprs Journal of Photogrammetry and Remote Sensing, 91*, 98-113

Hall, D.K., Riggs, G.A., & Salomonson, V.V. (1995). Development of Methods for Mapping Global Snow Cover Using Moderate Resolution Imaging Spectroradiometer Data. *Remote sensing of environment, 54*, 127-140

Hall, D.K., Riggs, G.A., Salomonson, V.V., DiGirolamo, N.E., & Bayr, K.J. (2002). MODIS snow-cover products. *Remote sensing of environment, 83*, 181-194

Hansen, M.C., Potapov, P.V., Goetz, S.J., Turubanova, S., Tyukavina, A., Krylov, A., Kommareddy, A., & Egorov, A. (2016a). Mapping tree height distributions in Sub-Saharan Africa using Landsat 7 and 8 data. *Remote Sensing of Environment, 185*, 221-232

Hansen, M.C., Potapov, P.V., Goetz, S.J., Turubanova, S., Tyukavina, A., Krylov, A., Kommareddy, A., & Egorov, A. (2016b). Mapping tree height distributions in Sub-Saharan Africa using Landsat 7 and 8 data. *Remote sensing of environment*

Heim, R.R. (2002). A review of twentieth-century drought indices used in the United States. *Bulletin of the American Meteorological Society, 83*, 1149-1165

Herold, M., Mayaux, P., Woodcock, C.E., Baccini, A., & Schmullius, C. (2008). Some challenges in global land cover mapping: An assessment of agreement and accuracy in existing 1 km datasets. *Remote Sensing of Environment, 112*, 2538-2556

Hoagland, B. (2000). The vegetation of Oklahoma: A classification for landscape mapping and conservation planning. *Southwestern Naturalist, 45*, 385-420

Huang, C.Q., Thomas, N., Goward, S.N., Masek, J.G., Zhu, Z.L., Townshend, J.R.G., & Vogelmann, J.E. (2010). Automated masking of cloud and cloud shadow for forest

change analysis using Landsat images. *International Journal of Remote Sensing, 31*, 5449-5464

Huete, A., Didan, K., Miura, T., Rodriguez, E.P., Gao, X., & Ferreira, L.G. (2002). Overview of the radiometric and biophysical performance of the MODIS vegetation indices. *Remote sensing of environment, 83*, 195-213

Huete, A.R., Liu, H.Q., Batchily, K., & vanLeeuwen, W. (1997a). A comparison of vegetation indices global set of TM images for EOS-MODIS. *Remote sensing of environment, 59*, 440-451

Huete, A.R., Liu, H.Q., Batchily, K., & vanLeeuwen, W. (1997b). A comparison of vegetation indices over a global set of TM images for EOS-MODIS. *Remote sensing of environment, 59*, 440-451

Huke, R.E. (1982). *Rice area by type of culture: South, Southeast, and East Asia*. Los Baños/Laguna/Philippine: International Rice Research Institute

Jackson, L.E., Strauss, R.B., Firestone, M.K., & Bartolome, J.W. (1990). Influence of Tree Canopies on Grassland Productivity and Nitrogen Dynamics in Deciduous Oak Savanna. *Agriculture Ecosystems & Environment, 32*, 89-105

Jin, C., Xiao, X.M., Merbold, L., Arneth, A., Veenendaal, E., & Kutsch, W.L. (2013). Phenology and gross primary production of two dominant savanna woodland ecosystems in Southern Africa. *Remote sensing of environment, 135*, 189-201

Joffre, R., & Rambal, S. (1993). How Tree Cover Influences the Water-Balance of Mediterranean Rangelands. *Ecology, 74*, 570-582

Joffre, R., Rambal, S., & Ratte, J.P. (1999). The dehesa system of southern Spain and Portugal as a natural ecosystem mimic. *Agroforestry Systems, 45*, 57-79

Johnson, F.L., & Risser, P.G. (1975). A quantitative comparison between an oak forest and an oak savannah in central Oklahoma. *The Southwestern Naturalist*, 75-84

Ju, J.C., Roy, D.P., Vermote, E., Masek, J., & Kovalskyy, V. (2012). Continental-scale validation of MODIS-based and LEDAPS Landsat ETM plus atmospheric correction methods. *Remote sensing of environment, 122*, 175-184

Kanniah, K., Beringer, J., Hutley, L., Tapper, N., & Zhu, X. (2009). Evaluation of Collections 4 and 5 of the MODIS Gross Primary Productivity product and algorithm improvement at a tropical savanna site in northern Australia. *Remote Sensing of Environment, 113*, 1808-1822

Khush, G.S. (2005). What it will take to feed 5.0 billion rice consumers in 2030. *Plant Molecular Biology, 59*, 1-6

Kulmatiski, A., & Beard, K.H. (2013). Woody plant encroachment facilitated by increased precipitation intensity. *Nature Climate Change, 3*, 833-837

Larcher, W. (2000). Temperature stress and survival ability of Mediterranean sclerophyllous plants. *Plant Biosystems, 134*, 279-295

Leff, B., Ramankutty, N., & Foley, J.A. (2004). Geographic distribution of major crops across the world. *Global Biogeochemical Cycles, 18*

Li, C.S., Frolking, S., Xiao, X.M., Moore, B., Boles, S., Qiu, J.J., Huang, Y., Salas, W., & Sass, R. (2005). Modeling impacts of farming management alternatives on CO2, CH4, and N2O emissions: A case study for water management of rice agriculture of China. *Global Biogeochemical Cycles, 19*

Li, P., Feng, Z., Jiang, L., Liu, Y., & Xiao, X. (2012). Changes in rice cropping systems in the Poyang Lake Region, China during 2004–2010. *Journal of Geographical Sciences, 22*, 653-668

Liu, J.Y., Kuang, W.H., Zhang, Z.X., Xu, X.L., Qin, Y.W., Ning, J., Zhou, W.C., Zhang, S.W., Li, R.D., Yan, C.Z., Wu, S.X., Shi, X.Z., Jiang, N., Yu, D.S., Pan, X.Z., & Chi, W.F. (2014). Spatiotemporal characteristics, patterns, and causes of land-use changes in China since the late 1980s. *Journal of Geographical Sciences, 24*, 195-210

Liu, J.Y., Liu, M.L., Tian, H.Q., Zhuang, D.F., Zhang, Z.X., Zhang, W., Tang, X.M., & Deng, X.Z. (2005). Spatial and temporal patterns of China's cropland during 1990-2000: An analysis based on Landsat TM data. *Remote Sensing of Environment, 98*, 442-456

Liu, Z., Li, Z., Tang, P., Li, Z., Wu, W., Yang, P., You, L., & Tang, H. (2013). Change analysis of rice area and production in China during the past three decades. *Journal of Geographical Sciences, 23*, 1005-1018

Long, H., Liu, Y., Wu, X., & Dong, G. (2009). Spatio-temporal dynamic patterns of farmland and rural settlements in Su–Xi–Chang region: Implications for building a new countryside in coastal China. *Land Use Policy, 26*, 322-333

Luedeling, E., & Buerkert, A. (2008). Typology of oases in northern Oman based on Landsat and SRTM imagery and geological survey data. *Remote sensing of environment, 112*, 1181-1195

Ma, S., Baldocchi, D.D., Xu, L., & Hehn, T. (2007). Inter-annual variability in carbon dioxide exchange of an oak/grass savanna and open grassland in California. *Agricultural and Forest Meteorology, 147*, 157-171

Masek, J.G., Vermote, E.F., Saleous, N.E., Wolfe, R., Hall, F.G., Huemmrich, K.F., Gao, F., Kutler, J., & Lim, T.K. (2006). A Landsat surface reflectance dataset for North America, 1990-2000. *Ieee Geoscience and Remote Sensing Letters, 3*, 68-72

Matthews, E., Fung, I., & Lerner, J. (1991). Methane emission from rice cultivation: Geographic and seasonal distribution of cultivated areas and emissions. *Global Biogeochemical Cycles, 5*, 3-24

McKee, T.B., Doesken, N.J., & Kleist, J. (1993). The relationship of drought frequency and duration to time scales. In, *Proceedings of the 8th Conference on Applied Climatology* (pp. 179-183): American Meteorological Society Boston, MA, USA

Medlyn, B., Dreyer, E., Ellsworth, D., Forstreuter, M., Harley, P., Kirschbaum, M., Le Roux, X., Montpied, P., Strassemeyer, J., & Walcroft, A. (2002). Temperature response of parameters of a biochemically based model of photosynthesis. II. A review of experimental data. *Plant, Cell & Environment, 25*, 1167-1179

Miettinen, J., & Liew, S.C. (2011). Separability of insular Southeast Asian woody plantation species in the 50 m resolution ALOS PALSAR mosaic product. *Remote Sensing Letters, 2*, 299-307

Miyaoka, K., Maki, M., Susaki, J., Homma, K., Noda, K., & Oki, K. (2013). Rice-Planted Area Mapping Using Small Sets of Multi-Temporal SAR Data. *Geoscience and Remote Sensing Letters, IEEE, 10*, 1507-1511

Monfreda, C., Ramankutty, N., & Foley, J.A. (2008). Farming the planet: 2. Geographic distribution of crop areas, yields, physiological types, and net primary production in the year 2000. *Global Biogeochemical Cycles, 22*

Montesano, P.M., Nelson, R., Sun, G., Margolis, H., Kerber, A., & Ranson, K.J. (2009). MODIS tree cover validation for the circumpolar taiga-tundra transition zone. *Remote sensing of environment, 113*, 2130-2141

Motohka, T., Nasahara, K.N., Miyata, A., Mano, M., & Tsuchida, S. (2009). Evaluation of optical satellite remote sensing for rice paddy phenology in monsoon Asia using a continuous in situ dataset. *International Journal of Remote Sensing, 30*, 4343-4357

Munson, S.M., Webb, R.H., Housman, D.C., Veblen, K.E., Nussear, K.E., Beever, E.A., Hartney, K.B., Miriti, M.N., Phillips, S.L., Fulton, R.E., & Tallent, N.G. (2015). Long-term plant responses to climate are moderated by biophysical attributes in a North American desert. *Journal of Ecology, 103*, 657-668

Myster, R.W. (2009). Tree seedling survivorship, growth, and allocation in the Cross Timbers ecotone of Oklahoma, USA. *Plant Ecology, 205*, 193-199

Niinemets, Ü., & Keenan, T. (2014). Photosynthetic responses to stress in Mediterranean evergreens: mechanisms and models. *Environmental and Experimental Botany, 103*, 24-41

Nijland, W., Jansma, E., Addink, E., Domínguez Delmás, M., & De Jong, S. (2011). Relating ring width of Mediterranean evergreen species to seasonal and annual variations of precipitation and temperature. *Biogeosciences Discussions, 8*, 355-383

Ogaya, R., & Penuelas, J. (2003). Comparative seasonal gas exchange and chlorophyll fluorescence of two dominant woody species in a Holm Oak Forest. *Flora, 198*, 132-141

Olofsson, P., Foody, G.M., Herold, M., Stehman, S.V., Woodcock, C.E., & Wulder, M.A. (2014). Good practices for estimating area and assessing accuracy of land change. *Remote sensing of environment, 148*, 42-57

Olofsson, P., Foody, G.M., Stehman, S.V., & Woodcock, C.E. (2013). Making better use of accuracy data in land change studies: Estimating accuracy and area and quantifying uncertainty using stratified estimation. *Remote sensing of environment, 129*, 122-131

Ou, W.Y., Guishan; LI, Hengpeng; Yv, Xingxiu (2004). Spatio-temporal Variation and Driving Forces of Landscape Patterns in the Coastal Zone of Yancheng, Jiangsu. *SCIENTIA GEOGRAPHICA SINICA, 24*, 610-615

Palmer, W.C. (1965). Meteorological Drought. In (p. 55). Weather Bureau, Washington, D. C.

Panigrahy, S., & Parihar, J.S. (1992). Role of Middle Infrared Bands of Landsat Thematic Mapper in Determining the Classification Accuracy of Rice. *International Journal of Remote Sensing, 13*, 2943-2949

Paulo, A.A., Rosa, R.D., & Pereira, L.S. (2012). Climate trends and behaviour of drought indices based on precipitation and evapotranspiration in Portugal. *Natural Hazards and Earth System Sciences, 12*, 1481-1491

Peng, D.L., Huete, A.R., Huang, J.F., Wang, F.M., & Sun, H.S. (2011). Detection and estimation of mixed paddy rice cropping patterns with MODIS data. *International Journal of Applied Earth Observation and Geoinformation, 13*, 13-23

Qin, Y., Xiao, X., Dong, J., Zhang, G., Shimada, M., Liu, J., Li, C., Kou, W., & Moore, B. (2015a). Forest cover maps of China in 2010 from multiple approaches and data sources: PALSAR, Landsat, MODIS, FRA, and NFI. *Isprs Journal of Photogrammetry and Remote Sensing, 109*, 1-16

Qin, Y., Xiao, X., Wang, J., Dong, J., Ewing, K., Hoagland, B., Hough, D., Fagin, T., Zou, Z., Geissler, G., Xian, G., & Loveland, T. (2016a). Mapping Annual Forest Cover in Sub-Humid and Semi-Arid Regions through Analysis of Landsat and PALSAR Imagery. *Remote Sensing, 8*, 933

Qin, Y.W., Xiao, X.M., Dong, J.W., Zhang, G.L., Roy, P.S., Joshi, P.K., Gilani, H., Murthy, M.S.R., Jin, C., Wang, J., Zhang, Y., Chen, B.Q., Menarguez, M.A., Biradar, C.M., Bajgain, R., Li, X.P., Dai, S.Q., Hou, Y., Xin, F.F., & Moore, B. (2016b). Mapping forests in monsoon Asia with ALOS PALSAR 50-m mosaic images and MODIS imagery in 2010. *Scientific Reports, 6*

Qin, Y.W., Xiao, X.M., Dong, J.W., Zhou, Y.T., Zhu, Z., Zhang, G.L., Du, G.M., Jin, C., Kou, W.L., Wang, J., & Li, X.P. (2015b). Mapping paddy rice planting area in cold temperate climate region through analysis of time series Landsat 8 (OLI), Landsat 7 (ETM+) and MODIS imagery. *Isprs Journal of Photogrammetry and Remote Sensing, 105*, 220-233

Rahman, S., & Rahman, M. (2009). Impact of land fragmentation and resource ownership on productivity and efficiency: The case of rice producers in Bangladesh. *Land Use Policy, 26*, 95-103

Raich, J., Rastetter, E., Melillo, J., Kicklighter, D., Steudler, P., Peterson, B., Grace, A., Moore Iii, B., & Vörösmarty, C. (1991). Potential net primary productivity in South America: application of a global model. *Ecological Applications*, 399-429

Rice, E.L., & Penfound, W.T. (1959). The Upland Forests of Oklahoma. *Ecology, 40*, 593-608

Rosenzweig, C., Strzepek, K.M., Major, D.C., Iglesias, A., Yates, D.N., McCluskey, A., & Hillel, D. (2004). Water resources for agriculture in a changing climate: international case studies. *Global Environmental Change: Human and Policy Dimensions, 14*, 345-360

Running, S.W., Nemani, R.R., Heinsch, F.A., Zhao, M.S., Reeves, M., & Hashimoto, H. (2004). A continuous satellite-derived measure of global terrestrial primary production. *Bioscience, 54*, 547-560

Running, S.W., & Zhao, M. (2015). Daily GPP and Annual NPP (MOD17A2/A3) Products NASA Earth Observing System MODIS Land Algorithm

Saintilan, N., & Rogers, K. (2015). Woody plant encroachment of grasslands: a comparison of terrestrial and wetland settings. *New Phytologist, 205*, 1062-1070

Sakamoto, T., Van Phung, C., Kotera, A., Nguyen, K.D., & Yokozawa, M. (2009). Analysis of rapid expansion of inland aquaculture and triple rice-cropping areas in a coastal area of the Vietnamese Mekong Delta using MODIS time-series imagery. *Landscape and Urban Planning, 92*, 34-46

SAMAD, M., Merrey, D., Vermillion, D., Fuchs-Carsch, M., MOHTADULLAH, K., & Lenton, R. (1992). Irrigation management strategies for improving the performance of irrigated agriculture. *Outlook on agriculture, 21*, 279-286

Scholes, R., & Archer, S. (1997). Tree-grass interactions in savannas. *Annual review of Ecology and Systematics*, 517-544

Shao, Y., Fan, X.T., Liu, H., Xiao, J.H., Ross, S., Brisco, B., Brown, R., & Staples, G. (2001). Rice monitoring and production estimation using multitemporal RADARSAT. *Remote sensing of environment, 76*, 310-325

Shimada, M., Isoguchi, O., Tadono, T., & Isono, K. (2009). PALSAR Radiometric and Geometric Calibration. *Ieee Transactions on Geoscience and Remote Sensing, 47*, 3915-3932

Shimada, M., Itoh, T., Motooka, T., Watanabe, M., Shiraishi, T., Thapa, R., & Lucas, R. (2014a). New global forest/non-forest maps from ALOS PALSAR data (2007-2010). *Remote Sensing of Environment, 155*, 13-31

Shimada, M., Itoh, T., Motooka, T., Watanabe, M., Shiraishi, T., Thapa, R., & Lucas, R. (2014b). New global forest/non-forest maps from ALOS PALSAR data (2007–2010). *Remote sensing of environment*

Shimada, M., & Ohtaki, T. (2010). Generating Large-Scale High-Quality SAR Mosaic Datasets: Application to PALSAR Data for Global Monitoring. *Ieee Journal of Selected Topics in Applied Earth Observations and Remote Sensing, 3*, 637-656

Shiu, Y.S., Lin, M.L., Huang, C.H., & Chu, T.H. (2012). Mapping paddy rice agriculture in a highly fragmented area using a geographic information system object-based post classification process. *Journal of Applied Remote Sensing, 6*

Sims, D.A., Rahman, A.F., Cordova, V.D., El-Masri, B.Z., Baldocchi, D.D., Bolstad, P.V., Flanagan, L.B., Goldstein, A.H., Hollinger, D.Y., Misson, L., Monson, R.K., Oechel, W.C., Schmid, H.P., Wofsy, S.C., & Xu, L. (2008). A new model of gross primary productivity for North American ecosystems based solely on the enhanced vegetation index and land surface temperature from MODIS. *Remote Sensing of Environment, 112*, 1633-1646

Sims, D.A., Rahman, A.F., Cordova, V.D., El-Masri, B.Z., Baldocchi, D.D., Flanagan, L.B., Goldstein, A.H., Hollinger, D.Y., Misson, L., Monson, R.K., Oechel, W.C., Schmid, H.P., Wofsy, S.C., & Xu, L.K. (2006). On the use of MODIS EVI to assess gross primary productivity of North American ecosystems. *Journal of Geophysical Research-Biogeosciences, 111*

Singh, R.P., Roy, S., & Kogan, F. (2003). Vegetation and temperature condition indices from NOAA AVHRR data for drought monitoring over India. *International Journal of Remote Sensing, 24*, 4393-4402

Sjöström, M., Zhao, M., Archibald, S., Arneth, A., Cappelaere, B., Falk, U., De Grandcourt, A., Hanan, N., Kergoat, L., & Kutsch, W. (2013). Evaluation of MODIS gross primary productivity for Africa using eddy covariance data. *Remote Sensing of Environment, 131*, 275-286

Son, N.-T., Chen, C.-F., Chen, C.-R., Duc, H.-N., & Chang, L.-Y. (2014). A Phenology-Based Classification of Time-Series MODIS Data for Rice Crop Monitoring in Mekong Delta, Vietnam. *Remote Sensing, 6,* 135-156

Sterling, S., & Ducharne, A. (2008). Comprehensive data set of global land cover change for land surface model applications. *Global Biogeochemical Cycles, 22*

Sun, H.S., Huang, J.F., Huete, A.R., Peng, D.L., & Zhang, F. (2009). Mapping paddy rice with multi-date moderate-resolution imaging spectroradiometer (MODIS) data in China. *Journal of Zhejiang University-Science A, 10*, 1509-1522

Tan, S., Heerink, N., & Qu, F. (2006). Land fragmentation and its driving forces in China. *Land Use Policy, 23,* 272-285

Tao, F., Yokozawa, M., Zhang, Z., Xu, Y., & Hayashi, Y. (2005). Remote sensing of crop production in China by production efficiency models: models comparisons, estimates and uncertainties. *Ecological Modelling, 183*, 385-396

Thenkabail, P.S., Knox, J.W., Ozdogan, M., Gumma, M.K., Congalton, R.G., Wu, Z.T., Milesi, C., Finkral, A., Marshall, M., Mariotto, I., You, S.C., Giri, C., & Nagler, P. (2012). Assessing Future Risks to Agricultural Productivity, Water Resources and Food Security: How Can Remote Sensing Help? *Photogrammetric Engineering and Remote Sensing, 78,* 773-782

Thi, T.H.N., De Bie, C.A.J.M., Ali, A., Smaling, E.M.A., & Chu, T.H. (2012). Mapping the irrigated rice cropping patterns of the Mekong delta, Vietnam, through hyper-temporal SPOT NDVI image analysis. *International Journal of Remote Sensing, 33,* 415-434

Torbick, N., Salas, W.A., Hagen, S., & Xiao, X.M. (2011). Monitoring Rice Agriculture in the Sacramento Valley, USA With Multitemporal PALSAR and MODIS Imagery. *Ieee Journal of Selected Topics in Applied Earth Observations and Remote Sensing, 4*, 451-457

Tucker, C.J. (1979). Red and photographic infrared linear combinations for monitoring vegetation. *Remote Sensing of Environment, 8,* 127-150

Turner, W., Spector, S., Gardiner, N., Fladeland, M., Sterling, E., & Steininger, M. (2003). Remote sensing for biodiversity science and conservation. *Trends in Ecology & Evolution, 18,* 306-314

Van Auken, O.W. (2009). Causes and consequences of woody plant encroachment into western North American grasslands. *Journal of Environmental Management, 90*, 2931-2942

Vargas, R., Sonnentag, O., Abramowitz, G., Carrara, A., Chen, J.M., Ciais, P., Correia, A., Keenan, T.F., Kobayashi, H., & Ourcival, J.-M. (2013). Drought Influences the Accuracy of Simulated Ecosystem Fluxes: A Model-Data Meta-analysis for Mediterranean Oak Woodlands. *Ecosystems, 16*, 749-764

Vaz, M., Pereira, J.S., Gazarini, L.C., David, T.S., David, J.S., Rodrigues, A., Maroco, J., & Chaves, M.M. (2010). Drought-induced photosynthetic inhibition and autumn recovery in two Mediterranean oak species (Quercus ilex and Quercus suber). *Tree Physiology, 30*, 946-956

Vermote, E.F., ElSaleous, N., Justice, C.O., Kaufman, Y.J., Privette, J.L., Remer, L., Roger, J.C., & Tanre, D. (1997). Atmospheric correction of visible to middle-infrared EOS-MODIS data over land surfaces: Background, operational algorithm and validation. *Journal of Geophysical Research-Atmospheres, 102*, 17131-17141

Vicente-Serrano, S.M., Begueria, S., & Lopez-Moreno, J.I. (2010). A Multiscalar Drought Index Sensitive to Global Warming: The Standardized Precipitation Evapotranspiration Index. *Journal of Climate, 23*, 1696-1718

Vicente-Serrano, S.M., Begueria, S., Lorenzo-Lacruz, J., Camarero, J.J., Lopez-Moreno, J.I., Azorin-Molina, C., Revuelto, J., Moran-Tejeda, E., & Sanchez-Lorenzo, A. (2012). Performance of Drought Indices for Ecological, Agricultural, and Hydrological Applications. *Earth Interactions, 16*

Vicente-Serrano, S.M., Gouveia, C., Camarero, J.J., Begueria, S., Trigo, R., Lopez-Moreno, J.I., Azorin-Molina, C., Pasho, E., Lorenzo-Lacruz, J., Revuelto, J., Moran-Tejeda, E., & Sanchez-Lorenzo, A. (2013). Response of vegetation to drought time-scales across global land biomes. *Proceedings of the National Academy of Sciences of the United States of America, 110*, 52-57

Wagle, P., Xiao, X., Scott, R.L., Kolb, T.E., Cook, D.R., Brunsell, N., Baldocchi, D.D., Basara, J., Matamala, R., Zhou, Y., & Bajgain, R. (2015a). Biophysical controls on carbon and water vapor fluxes across a grassland climatic gradient in the United States. *Agricultural and Forest Meteorology, 214–215*, 293-305

Wagle, P., Xiao, X., Torn, M.S., Cook, D.R., Matamala, R., Fischer, M.L., Jin, C., Dong, J., & Biradar, C. (2014). Sensitivity of vegetation indices and gross primary

production of tallgrass prairie to severe drought. *Remote sensing of environment, 152*, 1-14

Wagle, P., Xiao, X.M., & Suyker, A.E. (2015b). Estimation and analysis of gross primary production of soybean under various management practices and drought conditions. *Isprs Journal of Photogrammetry and Remote Sensing, 99*, 70-83

Walker, B.H., & Noymeir, I. (1982). Aspects of the Stability and Resilience of Savanna Ecosystems. *Ecological Studies, 42*, 557-590

Walker, T.L., & Hoback, W.W. (2007). Effects of invasive eastern redcedar on capture rates of Nicrophorus americanus and other Silphidae. *Environmental Entomology, 36*, 297-307

Wang, J., Xiao, X.M., Qin, Y.W., Dong, J.W., Zhang, G.L., Kou, W.L., Jin, C., Zhou, Y.T., & Zhang, Y. (2015). Mapping paddy rice planting area in wheat-rice double-cropped areas through integration of Landsat-8 OLI, MODIS, and PALSAR images. *Scientific Reports*

Wang, J., Xiao, X.M., Wagle, P., Ma, S.Y., Baldocchi, D., Carrara, A., Zhang, Y., Dong, J.W., & Qin, Y.W. (2016). Canopy and climate controls of gross primary production of Mediterranean-type deciduous and evergreen oak savannas. *Agricultural and Forest Meteorology, 226*, 132-147

Ward, D., Hoffman, M.T., & Collocott, S.J. (2014). A century of woody plant encroachment in the dry Kimberley savanna of South Africa. *African Journal of Range & Forage Science, 31*, 107-121

Weng, E.S., & Luo, Y.Q. (2008). Soil hydrological properties regulate grassland ecosystem responses to multifactor global change: A modeling analysis. *Journal of Geophysical Research-Biogeosciences, 113*

Whitley, R.J., Macinnis-Ng, C.M.O., Hutley, L.B., Beringer, J., Zeppel, M., Williams, M., Taylor, D., & Eamus, D. (2011). Is productivity of mesic savannas light limited or water limited? Results of a simulation study. *Global Change Biology, 17*, 3130-3149

Williams, R.J., Hallgren, S.W., Wilson, G.W.T., & Palmer, M.W. (2013). Juniperus virginiana encroachment into upland oak forests alters arbuscular mycorrhizal abundance and litter chemistry. *Applied Soil Ecology, 65*, 23-30

Wine, M.L., Ochsner, T.E., Sutradhar, A., & Pepin, R. (2012). Effects of eastern redcedar encroachment on soil hydraulic properties along Oklahoma's grassland-forest ecotone. *Hydrological Processes, 26*, 1720-1728

Wingate, L., Ogee, J., Cremonese, E., Filippa, G., Mizunuma, T., Migliavacca, M., Moisy, C., Wilkinson, M., Moureaux, C., Wohlfahrt, G., Hammerle, A., Hortnagl, L., Gimeno, C., Porcar-Castell, A., Galvagno, M., Nakaji, T., Morison, J., Kolle, O., Knohl, A., Kutsch, W., Kolari, P., Nikinmaa, E., Ibrom, A., Gielen, B., Eugster, W., Balzarolo, M., Papale, D., Klumpp, K., Kostner, B., Grunwald, T., Joffre, R., Ourcival, J.M., Hellstrom, M., Lindroth, A., George, C., Longdoz, B., Genty, B., Levula, J., Heinesch, B., Sprintsin, M., Yakir, D., Manise, T., Guyon, D., Ahrends, H., Plaza-Aguilar, A., Guan, J.H., & Grace, J. (2015). Interpreting canopy development and physiology using a European phenology camera network at flux sites. *Biogeosciences, 12*, 5995-6015

Woodcock, C.E., Allen, R., Anderson, M., Belward, A., Bindschadler, R., Cohen, W., Gao, F., Goward, S.N., Helder, D., Helmer, E., Nemani, R., Oreopoulos, L., Schott, J., Thenkabail, P.S., Vermote, E.F., Vogelmann, J., Wulder, M.A., Wynne, R., & Team, L.S. (2008). Free access to Landsat imagery. *Science, 320*, 1011-1011

Woods, A., Omernik, J., Butler, D., Ford, J., Henley, J., Hoagland, B., Arndt, D., & Moran, B. (2005). Ecoregions of Oklahoma (color poster with map, descriptive text, summary tables, and photographs). *US Geological Survey (map scale 1: 1,250,000), Reston, Virginia*

Woolston, C. (2014). Rice. *Nature, 514*, S49-S49

Wu, C.Y., Munger, J.W., Niu, Z., & Kuang, D. (2010a). Comparison of multiple models for estimating gross primary production using MODIS and eddy covariance data in Harvard Forest. *Remote Sensing of Environment, 114*, 2925-2939

Wu, W.B., Shibasaki, R., Yang, P., Tang, H.J., & Sugimoto, K. (2010b). Modeling changes in paddy rice sown areas in Asia. *Sustainability Science, 5*, 29-38

Wulder, M.A., Masek, J.G., Cohen, W.B., Loveland, T.R., & Woodcock, C.E. (2012). Opening the archive: How free data has enabled the science and monitoring promise of Landsat. *Remote Sensing of Environment, 122*, 2-10

Xia, J., Niu, S., Ciais, P., Janssens, I.A., Chen, J., Ammann, C., Arain, A., Blanken, P.D., Cescatti, A., Bonal, D., Buchmann, N., Curtis, P.S., Chen, S., Dong, J., Flanagan, L.B., Frankenberg, C., Georgiadis, T., Gough, C.M., Hui, D., Kiely, G., Li, J., Lund, M., Magliulo, V., Marcolla, B., Merbold, L., Montagnani, L., Moors, E.J., Olesen, J.E.,

Piao, S., Raschi, A., Roupsard, O., Suyker, A.E., Urbaniak, M., Vaccari, F.P., Varlagin, A., Vesala, T., Wilkinson, M., Weng, E., Wohlfahrt, G., Yan, L., & Luo, Y. (2015). Joint control of terrestrial gross primary productivity by plant phenology and physiology. *Proceedings of the National Academy of Sciences, 112*, 2788-2793

Xiao, X., Boles, S., Frolking, S., Li, C., Babu, J.Y., Salas, W., & Moore, B. (2006a). Mapping paddy rice agriculture in South and Southeast Asia using multi-temporal MODIS images. *Remote sensing of environment, 100*, 95-113

Xiao, X., Boles, S., Frolking, S., Salas, W., Moore, B., Li, C., He, L., & Zhao, R. (2002a). Observation of flooding and rice transplanting of paddy rice fields at the site to landscape scales in China using VEGETATION sensor data. *International Journal of Remote Sensing, 23*, 3009-3022

Xiao, X., Dorovskoy, P., Biradar, C., & Bridge, E. (2011). A library of georeferenced photos from the field. *Eos, Transactions American Geophysical Union, 92*, 453-454

Xiao, X., Hagen, S., Zhang, Q., Keller, M., & Moore, B. (2006b). Detecting leaf phenology of seasonally moist tropical forests in South America with multi-temporal MODIS images. *Remote sensing of environment, 103*, 465-473

Xiao, X., Zhang, Q., Saleska, S., Hutyra, L., De Camargo, P., Wofsy, S., Frolking, S., Boles, S., Keller, M., & Moore, B. (2005a). Satellite-based modeling of gross primary production in a seasonally moist tropical evergreen forest. *Remote Sensing of Environment, 94*, 105-122

Xiao, X.M. (2006). Light absorption by leaf chlorophyll and maximum light use efficiency. *Ieee Transactions on Geoscience and Remote Sensing, 44*, 1933-1935

Xiao, X.M., Boles, S., Liu, J.Y., Zhuang, D.F., Frolking, S., Li, C.S., Salas, W., & Moore, B. (2005b). Mapping paddy rice agriculture in southern China using multi-temporal MODIS images. *Remote Sensing of Environment, 95*, 480-492

Xiao, X.M., Boles, S., Liu, J.Y., Zhuang, D.F., & Liu, M.L. (2002b). Characterization of forest types in Northeastern China, using multi-temporal SPOT-4 VEGETATION sensor data. *Remote Sensing of Environment, 82*, 335-348

Xiao, X.M., Hollinger, D., Aber, J., Goltz, M., Davidson, E.A., Zhang, Q.Y., & Moore, B. (2004a). Satellite-based modeling of gross primary production in an evergreen needleleaf forest. *Remote sensing of environment, 89*, 519-534

Xiao, X.M., Zhang, Q.Y., Braswell, B., Urbanski, S., Boles, S., Wofsy, S., Berrien, M., & Ojima, D. (2004b). Modeling gross primary production of temperate deciduous broadleaf forest using satellite images and climate data. *Remote sensing of environment, 91*, 256-270

Xiao, X.M., Zhang, Q.Y., Hollinger, D., Aber, J., & Moore, B. (2005c). Modeling gross primary production of an evergreen needleleaf forest using modis and climate data. *Ecological Applications, 15*, 954-969

Xiao, X.M., Zhang, Q.Y., Saleska, S., Hutyra, L., De Camargo, P., Wofsy, S., Frolking, S., Boles, S., Keller, M., & Moore, B. (2005d). Satellite-based modeling of gross primary production in a seasonally moist tropical evergreen forest. *Remote sensing of environment, 94*, 105-122

Xu, L., & Baldocchi, D.D. (2004). Seasonal variation in carbon dioxide exchange over a Mediterranean annual grassland in California. *Agricultural and Forest Meteorology, 123*, 79-96

Xu, L.K., & Baldocchi, D.D. (2003). Seasonal trends in photosynthetic parameters and stomatal conductance of blue oak (Quercus douglasii) under prolonged summer drought and high temperature. *Tree Physiology, 23*, 865-877

Yang, Y., Shang, S., Guan, H., & Jiang, L. (2013). A novel algorithm to assess gross primary production for terrestrial ecosystems from MODIS imagery. *Journal of Geophysical Research: Biogeosciences, 118*, 590-605

Yu, M.X., Li, Q.F., Hayes, M.J., Svoboda, M.D., & Heim, R.R. (2014). Are droughts becoming more frequent or severe in China based on the Standardized Precipitation Evapotranspiration Index: 1951-2010? *International Journal of Climatology, 34*, 545-558

Zhang, W., Yu, Y., Huang, Y., Li, T., & Wang, P. (2011). Modeling methane emissions from irrigated rice cultivation in China from 1960 to 2050. *Global Change Biology, 17*, 3511-3523

Zhang, Y., Wang, C.Z., Wu, J.P., Qi, J.G., & Salas, W.A. (2009). Mapping paddy rice with multitemporal ALOS/PALSAR imagery in southeast China. *International Journal of Remote Sensing, 30*, 6301-6315

Zhang, Z., Wang, X., Zhao, X., Liu, B., Yi, L., Zuo, L., Wen, Q., Liu, F., Xu, J., & Hu, S. (2014). A 2010 update of National Land Use/Cover Database of China at 1:100000 scale using medium spatial resolution satellite images. *Remote sensing of environment, 149*, 142-154

Zhao, M., & Running, S.W. (2010). Drought-Induced Reduction in Global Terrestrial Net Primary Production from 2000 Through 2009. *Science, 329*, 940-943

Zhao, M.S., Heinsch, F.A., Nemani, R.R., & Running, S.W. (2005). Improvements of the MODIS terrestrial gross and net primary production global data set. *Remote Sensing of Environment, 95*, 164-176

Zhong, L., Gong, P., & Biging, G.S. (2014a). Efficient corn and soybean mapping with temporal extendability: A multi-year experiment using Landsat imagery. *Remote sensing of environment, 140*, 1-13

Zhong, L., Hawkins, T., Biging, G., & Gong, P. (2011). A phenology-based approach to map crop types in the San Joaquin Valley, California. *International Journal of Remote Sensing, 32*, 7777-7804

Zhong, L.H., Gong, P., & Biging, G.S. (2014b). Efficient corn and soybean mapping with temporal extendability: A multi-year experiment using Landsat imagery. *Remote Sensing of Environment, 140*, 1-13

Zhu, Z., & Woodcock, C.E. (2012). Object-based cloud and cloud shadow detection in Landsat imagery. *Remote Sensing of Environment, 118*, 83-94

Zou, C.B., Qiao, L., & Wilcox, B.P. (2016). Woodland expansion in central Oklahoma will significantly reduce streamflows - a modelling analysis. *Ecohydrology*, 9, 807-816